UNIVERSITY OF CALIFORNIA SAN DIEGO
SAN DIEGO STATE UNIVERSITY

Enhancement and Validation of Ground Motion Simulations

A dissertation submitted in partial satisfaction of the
requirements for the degree
Doctor of Philosophy

in

Geophysics

by

Nan Wang

Committee in charge:

University of California San Diego

Professor Joel Conte
Professor Peter Shearer

San Diego State University

Professor Kim Olsen, Chair
Professor Steven Day
Professor Samuel Shen

2021

The dissertation of Nan Wang is approved, and it is acceptable in quality and form for publication on microfilm and electronically.

_____

_____

_____

_____

_____

Chair

University of California San Diego

San Diego State University

2021

DEDICATION

To my family

Wenfang, Yifan, and Zheng

EPIGRAPH

Scientia potentia est.

Knowledge is power.

— Francis Bacon

Veni, vidi, vici.

I came; I saw; I conquered.

— Gaius Julius Caesar

I believe that whatever we do or live for has its causality;

it is good, however, that we cannot see through to it.

— Albert Einstein

TABLE OF CONTENTS

LIST OF FIGURES

LIST OF TABLES

ACKNOWLEDGEMENTS

It is hard to believe my journey of being a student finally comes to an end. I guess time does fly when you are immersed in a cordial environment with incredible people and lots of interesting work to do. I am truly grateful for the opportunity to work, learn and gain inspiration from my excellent advisors, teachers, colleagues and fellow students. I would like to thank each of them for all the help and support throughout this journey.

First and foremost, I would like to extend my deepest gratitude to my advisor, Professor Kim Olsen, for his invaluable advice, continuous support and patience during my Ph.D. study. He was always there when I needed help. He taught me how to develop research projects, how to present research results, and how to write academic papers. He trained and treated me as an independent researcher; and his guidance during the past years has helped me become a better scientist. I would also like to express my sincere appreciation to Professor Steven Day, who has always been a role model not only as a great scientist but also as a great person. I am honored to have the chance to work together with someone as knowledgeable, caring, and elegant as him. He always makes time for students and provides suggestions and guidance to the most difficult problems. I thank my dissertation committee members for their mentorship, guidance and support. Professor Peter Shearer offered inspiring suggestions about my research and was always being encouraging and supportive. Professor Samuel Shen taught me about useful statistical approaches to conduct analysis on my research projects. Professor Joel Conte provided additional guidance and references on the structural engineering aspect of my research. I am grateful to all my dissertation committee members. Their feedback and suggestions were very helpful in improving my research.

During my graduate studies, I took many useful courses from excellent teachers. Special thanks to Professor Duncan Agnew, Professor Adrian Borsa, Professor Kevin Brown, Professor Catherine Constable, Professor Steven Constable, Professor Yuri Fialko, Professor Guy Masters, Professor David Sandwell, Professor Peter Shearer, and Professor Dave Stegman at Scripps

Institution of Oceanography at UCSD; Professor Ian Abramson, Professor Ery Arias-Castro, Professor Michael Holst, and Professor Dimitris Politis in Department of Mathematics at UCSD; Professor Shou Ma and Professor Kim Olsen at SDSU.

A lot of the research would not be done without my coauthors. I thank Kim Olsen, Steven Day, Daniel Roten, Rumi Takedatsu, James Pechmann, Marine Denolle, Rob Clayton, Laura Ermert, Julian Schmitt, and Tim Clements for their insightful research collaboration with me.

I appreciate the support and friendship from my incredible fellows: Zhifeng Hu, Qian Yao, Shiying Nie, Yongfei Wang, Wei Wang, Bill Savran, Kyle Withers, Evan Hirakawa, Xiaohua Xu, Kang Wang, Wenyuan Fan, Drake Singleton, Maya Becker, Yuval Levy, Susheel Adusumilli, Yuxiang Zhang, and Te-Yang Yeh. They have made my time in San Diego so enjoyable. In addition, many thanks to administrative advisors and staffs, including Gilbert Bretado, Wayne Farquharson, Paul Dean, and Sara Miceli at UCSD; Irene Occhiello, Pia Parrish, Heather Webb, Susan Langsford, Joan Kimbrough and Pat Walls at SDSU.

Finally, I want to extend a very special thanks to my parents, Wenfang and Yifan, for helping me get to where I am today. Their support, encouragement, and love were worth more than I can express in words. Their presence in my life made everything enjoyable and made me a better person. Lastly but most importantly, I thank Zheng for being at my side through all the ups and downs, for always believing in me, and for making my life much happier and easier.

Chapter 2, in full, is a reformatted version of the material as it appears in Final Technical Report for U.S. Geological Survey: Wang, N., D. Roten, K.B. Olsen, and J.C. Pechmann (2017). Rupture direction, hanging wall, basin, and distance effects on ground motions from large normal-faulting earthquakes, Final Technical Report, *U.S. Geological Survey*, Award Nos. G14AP00044 and G14AP00045, 44 pp. 05/19/2017. The dissertation author was the primary investigator and author of this report.

Chapter 3, in full, is a reformatted version of a paper currently being prepared: Wang, N., Schmitt, J., Denolle, M., Olsen, K.B., Clements, T., Ermert, L., Clayton, R. (2021). Signatures of

Seismic Waveguides in Los Angeles from Numerical Simulations and Noise Cross Correlations. The dissertation author was the primary investigator and author of this paper.

Chapter 4, in full, is a reformatted version of the material as it appears in Bulletin of the Seismological Society of America: Wang, N., Takedatsu, R., Olsen, K.B., and Day, S.M. (2019). Broadband ground-motion simulation with interfrequency correlations. *Bulletin of the Seismological Society of America*, 109(6), 2437-2446. The dissertation author was the primary investigator and author of this paper.

Chapter 5, in full, is a reformatted version of the material as it appears in Earthquake Spectra: Wang, N., Olsen, K.B., Day S.M. (2021). A frequency-dependent ground-motion spatial correlation model of within-event residuals for Fourier amplitude spectra. *Earthquake Spectra*. The dissertation author was the primary investigator and author of this paper.

VITA

2015	B.S. in Geophysics, University of Science and Technology of China
2015-2020	Graduate Teaching/Research Assistant, San Diego State University
2021	Ph.D. in Geophysics, University of California San Diego and San Diego State University

PUBLICATIONS

Wang, N., Roten, D., Olsen, K.B., and Pechmann, J.C. (2017). Rupture direction, hanging wall, basin, and distance effects on ground motions from large normal-faulting earthquakes, Final Technical Report, *U.S. Geological Survey*, Award Nos. G14AP00044 and G14AP00045, 44 pp.

Wang, N., Takedatsu, R., Olsen, K.B., and Day, S.M. (2019). Broadband ground-motion simulation with interfrequency correlations. *Bulletin of the Seismological Society of America*, 109(6), 2437-2446.

Wang, N., Olsen, K.B., Day, S.M. (2021). A frequency-dependent ground-motion spatial correlation model of within-event residuals for Fourier amplitude spectra. *Earthquake Spectra*. https://doi.org/10.1177/8755293020981995 (First Published January 7, 2021).

Wang, N., Schmitt, J., Denolle, M., Olsen, K.B., Clements, T., Ermert, L., Clayton, R. (2021). Signatures of Seismic Waveguides in Los Angeles from Numerical Simulations and Noise Cross Correlations. *In preparation*.

ABSTRACT OF THE DISSERTATION

Enhancement and Validation of Ground Motion Simulations

by

Nan Wang

Doctor of Philosophy in Geophysics

University of California San Diego, 2021
San Diego State University, 2021

Professor Kim Olsen, Chair

Accurate prediction of strong ground motion is central to seismic hazard analysis in order to estimate losses during major earthquakes. Ground motion simulations are essential to seismic ground motion prediction, especially for locations of infrequent observations, such as large magnitude and short distance events, where simulations can provide a viable alternative to data. Therefore, enhancement and validation of ground motion simulations, the primary goal of this dissertation, are highly desirable. In Chapter 2, we quantify the effects of four important factors on ground motions from large normal-faulting earthquakes on the Wasatch fault in the Salt Lake Basin: rupture direction, location on the hanging wall versus the footwall,

deep 3D basin structure, and the distance from the rupture in the near field range. In Chapter 3, we attempt to validate the presence of several proposed waveguides in the Los Angeles area using 3D simulations and observed data from ambient noise. Here, we compare the numerical and empirical surface-to-surface Green tensors for virtual sources located on the San Andreas Fault. The regions of large peak motions caused by waveguide focusing in the simulations show generally good agreement with increases in the Green tensor amplitudes, supporting the presence of two separate waveguides in greater Los Angeles. In Chapters 4 and 5, we develop an empirical frequency-dependent spatial ground motion correlation model and methods to rectify simulation techniques that otherwise produce synthetic time histories deficient in inter-frequency and spatial correlation structure. The methods are tested using a hybrid deterministic-stochastic broadband ground motion generation module, where our method reproduces the empirical correlations well for a large number of realizations without biasing the fit of the median of the spectral accelerations to data. We find that the best fit of the inter-frequency correlation to data is obtained assuming that the horizontal components are correlated with a correlation coefficient of about 0.7.

Chapter 1

Introduction

1.1 Motivation

Earthquakes can inflict tremendous damage to humans and property. There are approximately 55 earthquakes per day around the globe that are located by the National Earthquake Information Center. Every year, there are on average of about 16 major earthquakes including 15 earthquakes of magnitude 7 and one earthquake of magnitude 8 or greater. A significant earthquake can produce a number of hazards including damaging ground shaking, ground displacement, liquefaction, landslides, fires, flooding, and tsunamis.

A fundamental problem for civil engineers is to design structures that can withstand potential earthquakes in the region during their lifetime. Ground motion prediction studies thus play a significant role in seismology and earthquake engineering in order to perform accurate seismic hazard assessment. Ground motion simulations are essential to seismic ground motion prediction, especially for locations of infrequent observations, such as large magnitude and short distance events, where simulations can provide a viable alternative to data. Recent advances in simulation techniques due to improved source characterization, accuracy of numerical methods and available computational resources have increased potential benefits for seismic hazard

assessment.

Simulation techniques for ground motion can be broadly divided into two classes: (1) deterministic methods solving the elasto-dynamic equations (e.g., finite-difference, finite-element, and spectral-element methods), typically limiting the simulations to low frequencies (e.g., $<$ 1Hz) due to computational requirements; and (2) approximate simulation techniques that are used to simulate ground motions for higher frequencies (e.g., 1-10 Hz) , such as stochastic simulation methods, the empirical Green's function method, the composite source modelling method and semi-empirical technique methods.

An example of deterministic simulation techniques is the finite-difference method. This method is based on the numerical solution of the wave equation via partial differential equations. 2D finite-difference methods (Kelly et al., 1976; Virieux, 1984; Vidale et al., 1985; Virieux, 1986; Scrivner and Helmberger, 1994; Pitarka et al., 1994) demonstrated the approach as an important modeling tool for earthquake wave propagation, and increasing computer power then led to the extension of the method to 3D (Frankel and Vidale, 1992; Graves, 1993; Frankel, 1993; Yomogida and Etgen, 1993; Olsen et al., 1995; Olsen and Archuleta, 1996; Olsen et al., 1996; Pitarka and Irikura, 1996) with implementation of rheologies (Day and Minster, 1984; Emmerich and Korn, 1987; Robertsson et al., 1994; Igel et al., 1995; Robertsson and Holliger, 1997) and frictional boundary conditions (Andrews, 1976; Day, 1982; Olsen et al., 1997; Ohminato and Chouet, 1997; Madariaga et al., 1998). Today, finite-difference methods are among the most common methods used to simulate seismic ground motions in 3D earth models, in part due to simple mesh generation and computational efficiency.

An example of high-frequency simulation techniques is the composite source modelling method. This method is based on the fact that an earthquake source composes several subevents that are characterized by their size, seismic moment, stress drop, slip, and source-time function (Ruiz et al., 2011). Zeng et al. (1994) proposed a composite source modelling method that uses summation of the convolution of source time function and synthetic scattering Green's function

(Zeng et al., 1991; Zeng, 1993) of the corresponding subevents. This method produces realistic synthetic acceleration seismograms with statistical properties consistent with the observations (Zeng et al., 1995). In some cases, a hybrid broadband simulation technique which merges low-frequency deterministic and high-frequency stochastic synthetics is performed in order to obtain optimal ground motion predictions with a computationally-efficient approach (e.g., Graves and Pitarka, 2015; Olsen and Takedatsu, 2015).

Simulations need to be validated before they can be used for engineering applications. There have been many studies to validate ground motion simulations: (1) using simple ground motion intensity measures such as spectral acceleration and Modified Mercalli Intensity (Hartzell et al., 2005; Aagaard et al., 2008); (2) using some general "goodness of fit" metrics that measure the similarity between recorded and simulated time histories by a combination of parameters such as peak ground velocity, peak ground acceleration, spectral acceleration, and some other structural response parameters (e.g., Kristeková et al., 2006; Bielak et al., 2010; Olsen and Mayhew, 2010; Taborda and Bielak, 2014); (3) using a framework of metrics that act as proxies for more complicated parameters including correlation of spectral acceleration across periods, the ratio of maximum to median spectral acceleration across all horizontal orientations, and the ratio of inelastic to elastic spectral displacement (Burks and Baker, 2014); and (4) using cross-validation between numerical and empirical simulation methods when no available instrumental recordings exist (Denolle et al., 2020).

Enhancement and validation of ground motion simulations are central to help scientists to better understand seismic hazards. Some of these aspects will be introduced and studied in detail below.

1.2 Sedimentary Basins and Seismic Hazards

Sedimentary basins are regions of the Earth where long-term subsidence creates accumulation of sediments which are geologically younger and have slower seismic wave velocities than the underlying basement rock, and also decrease in thickness towards their margins. Seismic waves are often trapped and reflected due to their interactions with the basin structure and the associated variations in material properties, resulting in the generation of surface waves. In general, material properties and geometry of sedimentary basins control seismic amplification (e.g., Wald and Graves, 1998). The high compliance of soft sediments reduces the elastic wave speed and the shape of the basin causes the seismic waves to focus and amplify within the basin, often leading to focusing effects toward the center of the basin (Koketsu and Kikuchi, 2000). A sharp contrast between basin and bedrock elastic properties reflects the incident waves and generates converted phases that are often referred to as "basin-edge effects" (e.g., Kawase, 1996; Pitarka et al., 1998). Such basin effects are known from first-principles to depend on a complex series of factors related to three-dimensional basin geometry (shape, depth, etc.) and direction of the source-to-site path. Olsen and Schuster (1995) showed several mechanisms that can contribute significantly to the ground motion amplification in basins, including: (1) P-to-S wave conversion at the base of sedimentary layers; (2) surface-wave generation from body waves incident at the edges of basins; (3) impedance effects at the sediment-bedrock boundary; and (4) seismic resonance effects.

Many densely populated areas such as Los Angeles, Salt Lake Valley, Seattle, Mexico City, Tokyo, and Wenchuan are located near active faults and are subject to high seismic risk. The severe damages caused by the 1985 M 8 Mexico City earthquake, the 1989 M 6.9 Loma Prieta earthquake and 2008 M 7.9 Wenchuan earthquake can be attributed to basin effects. Accurate prediction of strong ground motion is central to seismic hazard analysis in order to estimate losses during earthquakes at these areas.

1.2.1 Sedimentary Basin Amplification in the Salt Lake Valley

Earthquake hazards in the Salt Lake Valley are a serious concern because the valley is a major urban center with a population of approximately 1.2 million people (35% of the population of Utah). The most prominent source of seismic hazard to the Salt Lake Valley is the Salt Lake City segment of the Wasatch fault (WFSLC), a major normal fault that separates the Salt Lake Basin from the Wasatch Mountains to the east (Machette et al., 1991; DuRoss, 2008). Paleoseismological studies of the Salt Lake City segment indicate that large, M$\sim$7, surface faulting earthquakes have occurred on the average of once every 1,350 $\pm$ 200 yrs during the last 6,000 yrs along this segment, with the last one occurring 1,230 $\pm$ 60 yrs ago (Black et al., 1995; McCalpin and Nishenko, 1996; McCalpin and Nelson, 2000). Based on this information, McCalpin and Nelson (2000) estimated the probability of such an event occurring during the next 100 years to be about 16% and Wong et al. (2002) estimated the probability during the next 50 years to be 6% to 9%. Other faults and fault segments such as the West Valley fault, the Great Salt Lake fault, the northern Oquirrh fault, and the Provo and Weber segments of the Wasatch fault also contribute significantly to the seismic hazard in the Salt Lake Valley, along with "background" earthquakes of M $\leq$ 6.5 $\pm$ 0.25 (e.g., Youngs et al., 2000; Wong et al., 2002; Lund, 2005).

A large, surface-faulting earthquake on the WFSLC is considered to be the worst-case future earthquake scenario for the State of Utah. Severe damage is expected because the rupture surface would underlie most of the heavily urbanized Salt Lake Valley and the surface break would run along the eastern side of the valley. A 2012 study by Robert Carey of the Utah Division of Homeland Security and Douglas Bausch of the Federal Emergency Management Agency estimated that an M$\sim$7 WFSLC earthquake would result in 1500 to 2500 deaths (depending on the time of day), 25,000 to 35,000 injuries requiring medical attention, 85,000 displaced households, and $25 billion in direct damage to buildings and contents, with 9% of the building stock in the affected region damaged beyond repair.

Roten et al. (2011) simulated 0-1 Hz 3D numerical simulations of ground motions from M7 earthquakes on the Salt Lake City segment of the Wasatch fault in Utah (WFSLC) for six different rupture scenarios. The simulations were carried out in the Wasatch Front Community Velocity Model (WFCVM), which includes the low-velocity sediments of the Salt Lake Basin adjacent to the WFSLC. These sediments have a strong influence on the ground shaking. For example, the 3D simulations show much larger 0-1 Hz spectral accelerations (SAs) on the sediments in the Salt Lake Valley, as compared to bedrock and thin sediment sites on the footwall, with highly variable patterns dependent on the specific scenario. Average ground motions from the six scenarios were generally consistent with values predicted by four next-generation attenuation (NGA-West1) models, but with some differences.

In Chapter 2, we build on the results by Roten et al. (2011) to separate and quantify the effects of four important factors on strong ground motions from large normal-faulting earthquakes on the WFSLC: rupture direction, location on the hanging wall versus the footwall, the deep 3D structure of the Salt Lake Basin, and the distance from the rupture in the near field range. To investigate these effects, we use six scenarios from Roten et al. (2011) as well as a 1D rock site velocity model. We use the two sets of simulations to analyze the relationships between SA-2s and SA-3s and basin depth, Vs30, source description, and directivity models. Finally, we compare the results to the more recent NGA-West2 models and discuss the differences.

1.2.2 Waveguides in the Greater Los Angeles Area

The greater Los Angeles (LA) region is a metropolitan area with 16 million inhabitants living adjacent to the San Andreas Fault (SAF) system, a major plate boundary between the Pacific and North America plates. The SAF accommodates a large portion of the plate motion and may host events as large as M8. The most recent events on the SAF near LA occurred in 1857, 1812, and around 1690 (Weldon et al., 2004) and since the recurrence times associated with the

respective segments of the fault are estimated at 86 (-18 $+23$), 146 ($+91$ -60) and 220 (± 13) years, respectively (2007 Working Group on California Earthquake Probabilities, 2008; Scharer et al., 2010), another major event is expected at any time. The LA area is also crosscut with internal faults which themselves are capable of M7+ earthquakes (e.g., Dolan et al., 1995; Shaw and Shearer, 1999; Fuis et al., 2001). In addition, the greater LA area sits on top of sedimentary basins, which range in thickness from 2 to 10 km. The downtown portion of the city is located on the edge of the largest of these basins – the LA Basin.

Waveguides are confined geological units capable of channeling and focusing seismic energy over long distances. Elongated basins have the capacity to funnel seismic energy from one end to the other. Of particular concern is the connectivity of the northern sedimentary basins (LA - San Gabriel – Chino – San Bernardino). 3D simulations in the LA area (e.g., Olsen et al., 2006; Olsen et al., 2009; Graves et al., 2011; Day et al., 2012) suggest that the presence of such waveguides caused by the connectivity of the sedimentary basins strongly increases ground motion predictions for large, northwestward ruptures on the southern San Andreas fault (SAF). However, the efficiency in focusing and increase in the simulated ground motions due to the waveguides depend critically on the accuracy of the basin structure in the velocity models.

In Chapter 3, we attempt to validate the presence of several waveguides in the LA region, as indicated by 3D earthquake simulations, with observed seismic data from ambient noise. Using correlation of over 700 temporary (nodal and broadband) and permanent (SCSN) stations as receivers, and 14 stations (located along the SAF) as virtual sources, we calculate and compare all 9 components (over $\sim$40,000 correlations) of the Green's function tensor. In addition, we generate the analogous synthetic Green's tensors using simulations in a state-of-the-art 3D earth model, and compare the numerical and empirical surface-to-surface Green tensors for virtual sources located along the SAF. The regions of large peak motions caused by waveguide focusing in the simulations show generally good agreement with increases in the Green tensor amplitudes obtained from ambient noise, supporting the presence of two separate waveguides in greater LA.

Analysis of the cross terms and particle motions confirm that 0.1-0.35 Hz ($\sim$2.5-10s) surface waves play the most important role in the waveguide focusing.

1.3 Broadband Simulation of Ground Motion Correlation

Seismic ground motions recorded from earthquakes reveal both inter-frequency and spatial correlations. A number of studies have been done over the past decades for the spatial correlations of intensity measures such as peak ground velocities, peak ground accelerations and peak spectral accelerations (i.e., response spectra) (e.g., Bycroft, 1980; Bolt et al., 1982; Abrahamson et al., 1991; Harichandran and Vanmarcke, 1986; Hao et al., 1989; Der Kiureghian, 1996; Wesson and Perkins, 2001; Kawakami and Mogi, 2003; Boore et al., 2003; Wang and Takada, 2005; Goda and Hong, 2008; Jayaram and Baker, 2009; Esposito and Iervolino, 2011; Sokolov et al., 2012; Sokolov and Wenzel, 2013; Loth and Baker, 2013; Markhvida et al., 2018; Heresi and Miranda, 2019) and inter-frequency correlations of response spectra (e.g., Baker and Cornell, 2006; Baker and Jayaram, 2008; Goda and Atkinson, 2009; Cimellaro, 2013; Akkar et al., 2014; Azarbakht et al., 2014; Abrahamson et al., 2014; Baker and Bradley, 2017), as well as some recent studies for inter-frequency correlations of Fourier spectra (e.g., Wharf, 2016; Stafford, 2017; Bayless and Abrahamson, 2019). In addition, many studies (e.g., Burks and Baker, 2014; Weatherill et al., 2015; Stafford, 2017; Bayless and Abrahamson, 2018a) have demonstrated how seismic hazard assessment from simulations without such correlations can lead to underprediction of the seismic risk.

1.3.1 Inter-Frequency Correlation

Ground motions generated by many broadband simulation methods (e.g., Atkinson and Assatourians, 2015; Graves and Pitarka, 2015; Olsen and Takedatsu, 2015; Crempien and

Archuleta, 2015) have been used as input for engineering applications. However, while these methods have been tuned to produce median spectral acceleration in good agreement with that from strong motion data, less attention has been paid to their correlation behavior compared with empirical data (Bayless and Abrahamson, 2018b).

Stafford (2017) and Bayless and Abrahamson (2018b) both proposed techniques to incorporate inter-frequency correlations into the Boore (2003) simulation method. The Boore (2003) method generates a windowed Gaussian noise, transformed into the frequency domain and shaped by the deterministic Fourier amplitude spectrum for a scenario. Stafford (2017) used a model that is developed using two as-recorded horizontal components of unsmoothed Fourier Amplitude Spectrum (FAS). Bayless and Abrahamson (2018b) used an inter-frequency correlation model that is developed using a smoothed and orientation-independent Fourier Amplitude Spectrum called the Effective Amplitude Spectrum (EAS). We choose to apply the model developed using the EAS, applied to each of the two horizontal components, as our simulations are performed separately for each component. In contrast to the two recent studies mentioned above, we optimize the results for the inter-frequency correlation based on assumptions about the correlation of the two horizontal orthogonal components. Specifically, we find that incorporating two correlated FAS components can lead to a more accurate correlation structure in EAS, as described in the following chapters.

Wang et al. (2019) in Chapter 4 develop a new approach for including inter-frequency correlation in stochastic ground motion simulations, and demonstrate and validate the approach on an established and validated ground motion simulation tool. We have selected the San Diego State University (SDSU) broadband ground-motion generation module (Olsen and Takedatsu, 2015) which is implemented on the Southern California Earthquake Center (SCEC) Broadband Platform (BBP) for this purpose. The SDSU BBP module participated in and passed the SCEC BBP validation exercise (Dreger et al., 2015; Goulet et al., 2015). The focus of this exercise was on validating simulated median pseudo-spectral accelerations for earthquakes in western and

eastern US and Japan, as well as Next Generation Attenuation (NGA) Ground Motion Prediction Equations (GMPEs). The stochastic component of the SDSU method has undergone extensive calibration with respect to pseudo-spectral acceleration (PSA) using GMPEs and strong motion data, aiming at improving the prediction of ground motions. However, the SDSU Module was designed to provide satisfactory fits to data for median ground motions only, lending itself as an appropriate testbed for incorporating inter-frequency correlation. Chapter 4 starts by reviewing the intensity measure and the empirical covariance matrix for inter-frequency correlations and then explains and verifies our approach to compute the correlation, and demonstrates how the inter-frequency correlation coefficients are applied to the SDSU Module.

1.3.2 Spatial Correlation

The accuracy of the seismic loss estimates in a region is critically dependent on the spatial correlation between the ground motion intensities at different sites during a single event, which can be significant at distances up to 50 km (e.g., Bycroft, 1980; Bolt et al., 1982; Abrahamson et al., 1991; Harichandran and Vanmarcke, 1986; Hao et al., 1989; Der Kiureghian, 1996). Strong motion data naturally include such correlation, but is often available in insufficient amounts for loss analysis, in particular for large events and close to the causative fault. Instead, numerical simulations can provide key information for seismic hazard analysis. However, while ground motion simulations produced from complex 3D rupture and crustal models may include realistic spatial correlation structure (e.g., Withers et al., 2019), those obtained by more simplified deterministic simulations (e.g., 1D) and, in particular, by stochastic approaches (e.g., Boore, 2003; Boore, 2009; Beresnev and Atkinson, 1997; Motazedian and Atkinson, 2005; Atkinson et al., 2009), oftentimes do not. The importance of including spatial correlation in ground motion simulations has been illustrated by many studies (e.g., Jayaram and Baker, 2010; Miller and Baker, 2015) for loss estimates, clearly showing that simulations without spatial correlation can

result in an under-estimation of seismic risk.

Pseudo-spectral acceleration (PSA) has traditionally been the preferred metric in earthquake engineering, and many studies have proposed spatial correlation models for PSA. However, each PSA ordinate depends (nonlinearly) on ground motion amplitudes over a range of frequencies, and therefore a correlation model for PSA does not provide a direct means to impose the correlation structure on numerically simulated time histories (or on other ground-motion metrics derived therefrom). On the other hand, the Fourier Amplitude Spectrum (FAS) provides a straightforward means to incorporate an empirical correlation model into simulated ground motion time histories, through frequency-domain multiplication, but its empirical estimation is complicated by the fact that its value depends upon recording-instrument orientation. The Effective Amplitude Spectrum (EAS) avoids this complication, and bears a simple relationship to the FAS.

Wang et al. (2021) in Chapter 5 (1) develop a new, empirical frequency-dependent spatial correlation model of EAS, and (2) describe and demonstrate its implementation into numerically simulated ground motion that otherwise lacks such correlation. In that implementation, the empirical EAS correlation model is used to generate separate but correlated FAS adjustments to the two horizontal components at a given site.

References

2007 Working Group on California Earthquake Probabilities (2008). *The uniform California earthquake rupture forecast, version 2 (UCERF 2),USGS Open-File Report 2007–1437*. Tech. rep. US Geological Survey.

Aagaard, B. T., Brocher, T. M., Dolenc, D., Dreger, D., Graves, R. W., Harmsen, S., Hartzell, S., Larsen, S., and Zoback, M. L. (2008). "Ground-motion modeling of the 1906 San Francisco earthquake, Part I: Validation using the 1989 Loma Prieta earthquake". In: *Bulletin of the Seismological Society of America* 98.2, pp. 989–1011.

Abrahamson, N., Schneider, J. F., and Stepp, J. C. (1991). "Spatial coherency of shear waves from the Lotung, Taiwan large-scale seismic test". In: *Structural Safety* 10.1-3, pp. 145–162.

Abrahamson, N. A., Silva, W. J., and Kamai, R. (2014). "Summary of the ASK14 ground motion relation for active crustal regions". In: *Earthquake Spectra* 30.3, pp. 1025–1055.

Akkar, S., Sandıkkaya, M. A., and Ay, B. Ö. (2014). "Compatible ground-motion prediction equations for damping scaling factors and vertical-to-horizontal spectral amplitude ratios for the broader Europe region". In: *Bulletin of Earthquake Engineering* 12.1, pp. 517–547.

Andrews, D. (1976). "Rupture velocity of plane strain shear cracks". In: *Journal of Geophysical Research* 81.32, pp. 5679–5687.

Atkinson, G. M. and Assatourians, K. (2015). "Implementation and validation of EXSIM (a stochastic finite-fault ground-motion simulation algorithm) on the SCEC broadband platform". In: *Seismological Research Letters* 86.1, pp. 48–60.

Atkinson, G. M., Assatourians, K., Boore, D. M., Campbell, K., and Motazedian, D. (2009). "A guide to differences between stochastic point-source and stochastic finite-fault simulations". In: *Bulletin of the Seismological Society of America* 99.6, pp. 3192–3201.

Azarbakht, A, Mousavi, M, Nourizadeh, M, and Shahri, M (2014). "Dependence of correlations between spectral accelerations at multiple periods on magnitude and distance". In: *Earthquake engineering & structural dynamics* 43.8, pp. 1193–1204.

Baker, J. W. and Bradley, B. A. (2017). "Intensity measure correlations observed in the NGA-West2 database, and dependence of correlations on rupture and site parameters". In: *Earthquake Spectra* 33.1, pp. 145–156.

Baker, J. W. and Cornell, C. A. (2006). "Spectral shape, epsilon and record selection". In: *Earthquake Engineering & Structural Dynamics* 35.9, pp. 1077–1095.

Baker, J. W. and Jayaram, N. (2008). "Correlation of spectral acceleration values from NGA ground motion models". In: *Earthquake Spectra* 24.1, pp. 299–317.

Bayless, J. and Abrahamson, N. A. (2018a). *An empirical model for Fourier amplitude spectra using the NGA-West2 database, PEER Report 2018/07*. Report. Pacific Earthquake Engineering Research Center, University of California, Berkeley.

— (2018b). "Evaluation of the Interperiod Correlation of Ground-Motion SimulationsEvaluation of the Interperiod Correlation of Ground-Motion Simulations". In: *Bulletin of the Seismological Society of America* 108.6, pp. 3413–3430.

— (2019). "An Empirical Model for the Interfrequency Correlation of Epsilon for Fourier Amplitude Spectra". In: *Bulletin of the Seismological Society of America* 109.3, pp. 1058–1070.

Beresnev, I. A. and Atkinson, G. M. (1997). "Modeling finite-fault radiation from the ω n spectrum". In: *Bulletin of the Seismological Society of America* 87.1, pp. 67–84.

Bielak, J., Graves, R. W., Olsen, K. B., Taborda, R., Ramírez-Guzmán, L., Day, S. M., Ely, G. P., Roten, D., Jordan, T. H., Maechling, P. J., Urbanic, J., Cui, Y., and Juve, G. (2010). "The ShakeOut earthquake scenario: Verification of three simulation sets". In: *Geophysical Journal International* 180.1, pp. 375–404.

Black, B. D., Lund, W. R., and Mayes, B. H. (1995). "Large Earthquakes on the Salt Lake City Segment of the Wasatch Fault Zone–Summary of New Information from the South Fork Dry Creek Site, Salt Lake County, Utah". In: *Environmental and Engineering Geology of theWasatch Front Region: 1995 Symposium and Field Conference*. Ed. by W. Lund. Utah Geological Association.

Bolt, B. A., Loh, C., Penzien, J, Tsai, Y., and Yeh, Y. (1982). *Preliminary report on the SMART 1 strong motion array in Taiwan, Report UCB/EERC-82/13*. Report. University of California, Earthquake Engineering Research Center.

Boore, D. M. (2003). "Simulation of ground motion using the stochastic method". In: *Pure and applied geophysics* 160.3, pp. 635–676.

— (2009). "Comparing stochastic point-source and finite-source ground-motion simulations: SMSIM and EXSIM". In: *Bulletin of the Seismological Society of America* 99.6, pp. 3202–3216.

Boore, D. M., Gibbs, J. F., Joyner, W. B., Tinsley, J. C., and Ponti, D. J. (2003). "Estimated ground motion from the 1994 Northridge, California, earthquake at the site of the Interstate 10 and La Cienega Boulevard bridge collapse, West Los Angeles, California". In: *Bulletin of the Seismological Society of America* 93.6, pp. 2737–2751.

Burks, L. S. and Baker, J. W. (2014). "Validation of ground-motion simulations through simple proxies for the response of engineered systemsvalidation of ground-motion simulations through simple proxies for the response of engineered systems". In: *Bulletin of the Seismological Society of America* 104.4, pp. 1930–1946.

Bycroft, G. N. (Aug. 1980). *El Centro, California, differential ground motion array, Report 80-919*. Tech. rep. US Geological Survey.

Cimellaro, G. P. (2013). "Correlation in spectral accelerations for earthquakes in Europe". In: *Earthquake Engineering & Structural Dynamics* 42.4, pp. 623–633.

Crempien, J. G. and Archuleta, R. J. (2015). "UCSB method for simulation of broadband ground motion from kinematic earthquake sources". In: *Seismological Research Letters* 86.1, pp. 61–67.

Day, S. M. (1982). "Three-dimensional simulation of spontaneous rupture: the effect of nonuniform prestress". In: *Bulletin of the Seismological Society of America* 72.6A, pp. 1881–1902.

Day, S. M. and Minster, J. B. (1984). "Numerical simulation of attenuated wavefields using a Padé approximant method". In: *Geophysical Journal International* 78.1, pp. 105–118.

Day, S. M., Roten, D., and Olsen, K. B. (2012). "Adjoint analysis of the source and path sensitivities of basin-guided waves". In: *Geophysical Journal International* 189.2, pp. 1103–1124.

Denolle, M., Schmitt, J., Ermert, L., Clements, T., Wang, N., and Olsen, K. B. (2020). "Illuminating seismic waveguides using noise cross correlations and numerical simulations". In: *AGU Fall Meeting 2020*. American Geophysical Union.

Der Kiureghian, A (1996). "A coherency model for spatially varying ground motions". In: *Earthquake engineering & structural dynamics* 25.1, pp. 99–111.

Dolan, J. F., Sieh, K., Rockwell, T. K., Yeats, R. S., Shaw, J., Suppe, J., Huftile, G. J., and Gath, E. M. (1995). "Prospects for larger or more frequent earthquakes in the Los Angeles metropolitan region". In: *Science* 267.5195, pp. 199–205.

Dreger, D. S., Beroza, G. C., Day, S. M., Goulet, C. A., Jordan, T. H., Spudich, P. A., and Stewart, J. P. (2015). "Validation of the SCEC broadband platform v14. 3 simulation methods using pseudospectral acceleration data". In: *Seismological Research Letters* 86.1, pp. 39–47.

DuRoss, C. B. (2008). "Holocene vertical displacement on the central segments of the Wasatch fault zone, Utah". In: *Bulletin of the Seismological Society of America* 98.6, pp. 2918–2933.

Emmerich, H. and Korn, M. (1987). "Incorporation of attenuation into time-domain computations of seismic wave fields". In: *Geophysics* 52.9, pp. 1252–1264.

Esposito, S. and Iervolino, I. (2011). "PGA and PGV spatial correlation models based on European multievent datasets". In: *Bulletin of the Seismological Society of America* 101.5, pp. 2532–2541.

Frankel, A. (1993). "Three-dimensional simulations of ground motions in the San Bernardino Valley, California, for hypothetical earthquakes on the San Andreas fault". In: *Bulletin of the Seismological Society of America* 83.4, pp. 1020–1041.

Frankel, A. and Vidale, J. (1992). "A three-dimensional simulation of seismic waves in the Santa Clara Valley, California, from a Loma Prieta aftershock". In: *Bulletin of the Seismological Society of America* 82.5, pp. 2045–2074.

Fuis, G., Ryberg, T., Godfrey, N., Okaya, D., and Murphy, J. (2001). "Crustal structure and tectonics from the Los Angeles basin to the Mojave Desert, southern California". In: *Geology* 29.1, pp. 15–18.

Goda, K. and Atkinson, G. M. (2009). "Probabilistic characterization of spatially correlated response spectra for earthquakes in Japan". In: *Bulletin of the Seismological Society of America* 99.5, pp. 3003–3020.

Goda, K. and Hong, H.-P. (2008). "Spatial correlation of peak ground motions and response spectra". In: *Bulletin of the Seismological Society of America* 98.1, pp. 354–365.

Goulet, C., Abrahamson, N., Somerville, P., and Wooddell, K. (2015). "The SCEC Broadband Platform validation exercise for pseudo-spectral acceleration: Methodology for code validation in the context of seismic hazard analyses". In: *Seismol. Res. Lett* 86.1, pp. 17–26.

Graves, R., Jordan, T. H., Callaghan, S., Deelman, E., Field, E., Juve, G., Kesselman, C., Maechling, P., Mehta, G., Milner, K., et al. (2011). "CyberShake: A physics-based seismic hazard model for southern California". In: *Pure and Applied Geophysics* 168.3, pp. 367–381.

Graves, R. and Pitarka, A. (2015). "Refinements to the Graves and Pitarka (2010) broadband ground-motion simulation method". In: *Seismological Research Letters* 86.1, pp. 75–80.

Graves, R. W. (1993). "Modeling three-dimensional site response effects in the Marina District Basin, San Francisco, California". In: *Bulletin of the Seismological Society of America* 83.4, pp. 1042–1063.

Hao, H, Oliveira, C., and Penzien, J (1989). "Multiple-station ground motion processing and simulation based on SMART-1 array data". In: *Nuclear Engineering and Design* 111.3, pp. 293–310.

Harichandran, R. S. and Vanmarcke, E. H. (1986). "Stochastic variation of earthquake ground motion in space and time". In: *Journal of engineering mechanics* 112.2, pp. 154–174.

Hartzell, S., Guatteri, M., Mai, P. M., Liu, P.-C., and Fisk, M. (2005). "Calculation of broadband time histories of ground motion, Part II: Kinematic and dynamic modeling using theoretical Green's functions and comparison with the 1994 Northridge earthquake". In: *Bulletin of the Seismological Society of America* 95.2, pp. 614–645.

Heresi, P. and Miranda, E. (2019). "Uncertainty in intraevent spatial correlation of elastic pseudo-acceleration spectral ordinates". In: *Bulletin of Earthquake Engineering* 17.3, pp. 1099–1115.

Igel, H., Mora, P., and Riollet, B. (1995). "Anisotropic wave propagation through finite-difference grids". In: *Geophysics* 60.4, pp. 1203–1216.

Jayaram, N. and Baker, J. W. (2009). "Correlation model for spatially distributed ground-motion intensities". In: *Earthquake Engineering & Structural Dynamics* 38.15, pp. 1687–1708.

— (2010). "Efficient sampling and data reduction techniques for probabilistic seismic lifeline risk assessment". In: *Earthquake Engineering & Structural Dynamics* 39.10, pp. 1109–1131.

Kawakami, H. and Mogi, H. (2003). "Analyzing spatial intraevent variability of peak ground accelerations as a function of separation distance". In: *Bulletin of the Seismological Society of America* 93.3, pp. 1079–1090.

Kawase, H. (1996). "The cause of the damage belt in Kobe:"The basin-edge effect," constructive interference of the direct S-wave with the basin-induced diffracted/Rayleigh waves". In: *Seismological Research Letters* 67.5, pp. 25–34.

Kelly, K. R., Ward, R. W., Treitel, S., and Alford, R. M. (1976). "Synthetic seismograms: A finite-difference approach". In: *Geophysics* 41.1, pp. 2–27.

Koketsu, K. and Kikuchi, M. (2000). "Propagation of seismic ground motion in the Kanto basin, Japan". In: *Science* 288.5469, pp. 1237–1239.

Kristeková, M., Kristek, J., Moczo, P., and Day, S. M. (2006). "Misfit criteria for quantitative comparison of seismograms". In: *Bulletin of the seismological Society of America* 96.5, pp. 1836–1850.

Loth, C. and Baker, J. W. (2013). "A spatial cross-correlation model of spectral accelerations at multiple periods". In: *Earthquake Engineering & Structural Dynamics* 42.3, pp. 397–417.

Lund, W. R. (2005). "Consensus preferred recurrence-interval and vertical slip-rate estimates: Review of Utah paleoseismic-trenching data by the Utah Quaternary Fault Parameters Working Group". In:

Machette, M. N., Personius, S. F., Nelson, A. R., Schwartz, D. P., and Lund, W. R. (1991). "The Wasatch fault zone, Utah—Segmentation and history of Holocene earthquakes". In: *Journal of Structural Geology* 13.2, pp. 137–149.

Madariaga, R, Olsen, K, and Archuleta, R (1998). "Modeling dynamic rupture in a 3D earthquake fault model". In: *Bulletin of the Seismological Society of America* 88.5, pp. 1182–1197.

Markhvida, M., Ceferino, L., and Baker, J. W. (2018). “Modeling spatially correlated spectral accelerations at multiple periods using principal component analysis and geostatistics”. In: *Earthquake Engineering & Structural Dynamics* 47.5, pp. 1107–1123.

McCalpin, J. and Nelson, C. V. (2000). *Long Recurrence Records from the Wasatch Fault Zone, Utah, Final Technical Report*. Report. US Geological Survey, National Earthquake Hazards Reduction Program.

McCalpin, J. and Nishenko, S. (1996). “Holocene paleoseismicity, temporal clustering, and probabilities of future large (M¿ 7) earthquakes on the Wasatch fault zone, Utah”. In: *Journal of Geophysical Research: Solid Earth* 101.B3, pp. 6233–6253.

Miller, M and Baker, J (2015). “Ground-motion intensity and damage map selection for probabilistic infrastructure network risk assessment using optimization”. In: *Earthquake Engineering & Structural Dynamics* 44.7, pp. 1139–1156.

Motazedian, D. and Atkinson, G. M. (2005). “Stochastic finite-fault modeling based on a dynamic corner frequency”. In: *Bulletin of the Seismological Society of America* 95.3, pp. 995–1010.

Ohminato, T. and Chouet, B. A. (1997). “A free-surface boundary condition for including 3D topography in the finite-difference method”. In: *Bulletin of the Seismological Society of America* 87.2, pp. 494–515.

Olsen, K., Day, S., Dalguer, L., Mayhew, J, Cui, Y, Zhu, J, Cruz-Atienza, V., Roten, D, Maechling, P, Jordan, T., and Chourasia, A (2009). “ShakeOut-D: Ground motion estimates using an ensemble of large earthquakes on the southern San Andreas fault with spontaneous rupture propagation”. In: *Geophysical Research Letters* 36.4.

Olsen, K., Day, S., Minster, J., Cui, Y., Chourasia, A., Faerman, M., Moore, R., Maechling, P., and Jordan, T. (2006). “Strong shaking in Los Angeles expected from southern San Andreas earthquake”. In: *Geophysical Research Letters* 33.7.

Olsen, K., Madariaga, R, and Archuleta, R. J. (1997). “Three-dimensional dynamic simulation of the 1992 Landers earthquake”. In: *Science* 278.5339, pp. 834–838.

Olsen, K. and Takedatsu, R. (2015). “The SDSU broadband ground-motion generation module BBtoolbox version 1.5”. In: *Seismological Research Letters* 86.1, pp. 81–88.

Olsen, K. B. and Archuleta, R. J. (1996). “Three-dimensional simulation of earthquakes on the Los Angeles fault system”. In: *Bulletin of the Seismological Society of America* 86.3, pp. 575–596.

Olsen, K. B., Archuleta, R. J., and Matarese, J. R. (1995). “Three-dimensional simulation of a magnitude 7.75 earthquake on the San Andreas fault”. In: *Science* 270.5242, pp. 1628–1632.

Olsen, K. B. and Mayhew, J. E. (2010). "Goodness-of-fit criteria for broadband synthetic seismograms, with application to the 2008 Mw 5.4 Chino Hills, California, earthquake". In: *Seismological Research Letters* 81.5, pp. 715–723.

Olsen, K. B., Pechmann, J. C., and Schuster, G. T. (1996). "An analysis of simulated and observed blast records in the Salt Lake basin". In: *Bulletin of the Seismological Society of America* 86.4, pp. 1061–1076.

Olsen, K. B. and Schuster, G. T. (1995). "Causes of low-frequency ground motion amplification in the Salt Lake Basin: the case of the vertically incident P wave". In: *Geophysical Journal International* 122.3, pp. 1045–1061.

Pitarka, A. and Irikura, K. (1996). "Modeling 3D surface topography by finite-difference method: Kobe-JMA station site, Japan, case study". In: *Geophysical Research Letters* 23.20, pp. 2729–2732.

Pitarka, A., Irikura, K., Iwata, T., and Sekiguchi, H. (1998). "Three-dimensional simulation of the near-fault ground motion for the 1995 Hyogo-ken Nanbu (Kobe), Japan, earthquake". In: *Bulletin of the Seismological Society of America* 88.2, pp. 428–440.

Pitarka, A., Takenaka, H, and Suetsugu, D (1994). "Modeling strong motion in the Ashigara valley for the 1990 Odawara, Japan, earthquake". In: *Bulletin of the Seismological Society of America* 84.5, pp. 1327–1335.

Robertsson, J. and Holliger, K (1997). "Modeling of seismic wave propagation near the earth's surface". In: *Physics of the Earth and Planetary Interiors* 104.1-3, pp. 193–211.

Robertsson, J. O., Blanch, J. O., and Symes, W. W. (1994). "Viscoelastic finite-difference modeling". In: *Geophysics* 59.9, pp. 1444–1456.

Roten, D, Olsen, K., Pechmann, J., Cruz-Atienza, V., and Magistrale, H (2011). "3D simulations of M 7 earthquakes on the Wasatch fault, Utah, Part I: Long-period (0–1 Hz) ground motion". In: *Bulletin of the Seismological Society of America* 101.5, pp. 2045–2063.

Ruiz, J., Baumont, D, Bernard, P, and Berge-Thierry, C (2011). "Modelling directivity of strong ground motion with a fractal, k- 2, kinematic source model". In: *Geophysical Journal International* 186.1, pp. 226–244.

Scharer, K. M., Biasi, G. P., Weldon, R. J., and Fumal, T. E. (2010). "Quasi-periodic recurrence of large earthquakes on the southern San Andreas fault". In: *Geology* 38.6, pp. 555–558.

Scrivner, C. W. and Helmberger, D. V. (1994). "Seismic waveform modeling in the Los Angeles Basin". In: *Bulletin of the Seismological Society of America* 84.5, pp. 1310–1326.

Shaw, J. H. and Shearer, P. M. (1999). "An elusive blind-thrust fault beneath metropolitan Los Angeles". In: *Science* 283.5407, pp. 1516–1518.

Sokolov, V. and Wenzel, F. (2013). "Further analysis of the influence of site conditions and earthquake magnitude on ground-motion within-earthquake correlation: analysis of PGA and PGV data from the K-NET and the KiK-net (Japan) networks". In: *Bulletin of Earthquake Engineering* 11.6, pp. 1909–1926.

Sokolov, V., Wenzel, F., Wen, K.-L., and Jean, W.-Y. (2012). "On the influence of site conditions and earthquake magnitude on ground-motion within-earthquake correlation: analysis of PGA data from TSMIP (Taiwan) network". In: *Bulletin of Earthquake Engineering* 10.5, pp. 1401–1429.

Stafford, P. J. (2017). "Interfrequency Correlations among Fourier Spectral Ordinates and Implications for Stochastic Ground-Motion SimulationInterfrequency Correlations among Fourier Spectral Ordinates and Implications". In: *Bulletin of the Seismological Society of America* 107.6, pp. 2774–2791.

Taborda, R. and Bielak, J. (2014). "Ground-motion simulation and validation of the 2008 Chino Hills, California, earthquake using different velocity models". In: *Bulletin of the Seismological Society of America* 104.4, pp. 1876–1898.

Vidale, J., Helmberger, D. V., and Clayton, R. W. (1985). "Finite-difference seismograms for SH waves". In: *Bulletin of the Seismological Society of America* 75.6, pp. 1765–1782.

Virieux, J. (1984). "SH-wave propagation in heterogeneous media: Velocity-stress finite-difference method". In: *Geophysics* 49.11, pp. 1933–1942.

— (1986). "P-SV wave propagation in heterogeneous media: Velocity-stress finite-difference method". In: *Geophysics* 51.4, pp. 889–901.

Wald, D. J. and Graves, R. W. (1998). "The seismic response of the Los Angeles basin, California". In: *Bulletin of the Seismological Society of America* 88.2, pp. 337–356.

Wang, M. and Takada, T. (2005). "Macrospatial correlation model of seismic ground motions". In: *Earthquake spectra* 21.4, pp. 1137–1156.

Wang, N., Olsen, K. B., and Day, S. M. (2021). "A frequency-dependent ground-motion spatial correlation model of within-event residuals for Fourier amplitude spectra". In: *Earthquake Spectra*.

Wang, N., Takedatsu, R., Olsen, K. B., and Day, S. M. (2019). "Broadband ground-motion simulation with interfrequency correlations". In: *Bulletin of the Seismological Society of America* 109.6, pp. 2437–2446.

Weatherill, G., Silva, V, Crowley, H, and Bazzurro, P (2015). "Exploring the impact of spatial correlations and uncertainties for portfolio analysis in probabilistic seismic loss estimation". In: *Bulletin of Earthquake Engineering* 13.4, pp. 957–981.

Weldon, R., Scharer, K., Fumal, T., and Biasi, G. (2004). "Wrightwood and the earthquake cycle: What a long recurrence record tells us about how faults work". In: *GSA today* 14.9, pp. 4–10.

Wesson, R. L. and Perkins, D. M. (2001). "Spatial correlation of probabilistic earthquake ground motion and loss". In: *Bulletin of the Seismological Society of America* 91.6, pp. 1498–1515.

Wharf, C. (2016). "Discrete multivariate representation of Fourier spectral ordinates, M.Sc. Thesis". MA thesis. Department of Civil and Environmental Engineering, London, United Kingdom: Imperial College London.

Withers, K. B., Olsen, K. B., Shi, Z., and Day, S. M. (2019). "Validation of Deterministic Broadband Ground Motion and Variability from Dynamic Rupture Simulations of Buried Thrust EarthquakesValidation of Deterministic Broadband Ground Motion and Variability". In: *Bulletin of the Seismological Society of America* 109.1, pp. 212–228.

Wong, I. G., Silva, W., Olig, S., Thomas, P., Wright, D., Ashland, F., Gregor, N., Pechmann, J., Dober, M., Christenson, G., and Gerth, R. (2002). *Earthquake scenario and probabilistic ground shaking maps for the Salt Lake City, Utah, metropolitan area*. Vol. 2. 5. Utah Geological Survey.

Yomogida, K. and Etgen, J. T. (1993). "3-D wave propagation in the Los Angeles basin for the Whittier-Narrows earthquake". In: *Bulletin of the Seismological Society of America* 83.5, pp. 1325–1344.

Youngs, R., Swan, F., Power, M., Schwartz, D., and Green, R. (Nov. 2000). "Probabilistic Analysis of Earthquake Ground-Shaking Hazards Along the Wasatch Front, Utah". In: *US Geological Survey Professional Paper*, pp. M1–M67.

Zeng, Y. (1993). "Theory of scattered P-and S-wave energy in a random isotropic scattering medium". In: *Bulletin of the Seismological Society of America* 83.4, pp. 1264–1276.

Zeng, Y., Anderson, J. G., and Su, F. (1995). "Subevent rake and random scattering effects in realistic strong ground motion simulation". In: *Geophysical research letters* 22.1, pp. 17–20.

Zeng, Y., Anderson, J. G., and Yu, G. (1994). "A composite source model for computing realistic synthetic strong ground motions". In: *Geophysical Research Letters* 21.8, pp. 725–728.

Zeng, Y., Su, F., and Aki, K. (1991). "Scattering wave energy propagation in a random isotropic scattering medium: 1. Theory". In: *Journal of Geophysical Research: Solid Earth* 96.B1, pp. 607–619.

Chapter 2

Rupture Direction, Hanging Wall, Basin, and Distance Effects on Ground Motions from Large Normal-Faulting Earthquakes

We have analyzed numerical simulations of six M7 earthquakes on the Salt Lake City segment of the Wasatch fault, Utah, to better understand the long-period ground motions that these simulations predict in the adjacent Salt Lake Valley (SLV). The peak spectral accelerations at 2s (SA-2s) and 3s (SA-3s) were calculated in the Wasatch Front Community Velocity Model (v3d) as well as in a 1D rock model using the same source descriptions. The SAs from the 1D model are generally smoother and smaller in amplitude due to the lack of underlying 3D basin structure. 3D/1D ratios of the SA values depict the 3D basin effects in the SLV, such as focusing, defocusing, and wave entrapment. We developed regression models for the 6-scenario ensemble ground motions as a function of depth to the isosurfaces of Vs=1.0 and 1.5 km/s in the SLV. These models show amplification factors of up to $\sim$2.7 and $\sim$3.7 above the deepest part of the basin for SA-2s and SA-3s, respectively. The individual scenario SAs show correlations with the underlying rupture parameters, in particular, the slip distribution. The directivity factors for the Bayless and

Somerville (2013) model, computed using a 10-section rupture surface approximation, increase the SAs by less than 20% for the scenarios and help little to increase the similarity between the SAs from the NGA-West2 GMPEs and the simulations. As compared to 4 NGA-West2 GMPEs, the long-period scenario ground motions for soil sites increase from Rrup (rupture distance) of 0 to 1-1.5 km and decrease from Rrup $\sim$4 to 10 km. The maximum in simulated ground motions for Rrup $\sim$1-4 km appears at least in part to be caused by basin-edge effects and entrapment of waves in the deeper basin, combined with scenario specific conditions not captured by the GMPEs. The GMPEs do a reasonably good job of predicting the increased ground motions over the hanging wall for the simulated SA-3s; however, for SA-2s, the simulations show minimal increase over the hanging wall and the GMPEs overpredict the simulations.

2.1 Introduction

Roten et al. (2011) simulated 0-1 Hz 3D numerical simulations of ground motions from M 7 earthquakes on the Salt Lake City segment of the Wasatch fault in Utah (WFSLC) for six different rupture scenarios. The simulations were carried out in the Wasatch Front Community Velocity Model (WFCVM), which includes the low-velocity sediments of the Salt Lake Basin adjacent to the WFSLC. These sediments have a strong influence on the ground shaking. For example, the 3D simulations show much larger 0-1 Hz Spectral Accelerations (SAs) on the sediments in the Salt Lake Valley, as compared to bedrock and thin sediment sites on the footwall, with highly variable patterns dependent on the specific scenario. Average ground motions from the six scenarios were generally consistent with values predicted by four next-generation attenuation (NGA-West1) models, but with some differences.

In this study, we build on the results by Roten et al. (2011) to separate and quantify the effects of four important factors on strong ground motions from large normal-faulting earthquakes on the WFSLC: rupture direction, location on the hanging wall versus the footwall, the deep 3D

structure of the Salt Lake Basin, and the distance from the rupture in the near field range. To investigate these effects, we simulate the six scenarios from Roten et al. (2011) with an updated version of the WFCVM, as well as with a 1D rock site velocity model. We use the two sets of simulations to analyze the relationships between SA-2s and SA-3s and basin depth, Vs30, source description, and directivity models. Finally, we compare the results to the more recent NGA-West2 models and discuss the differences.

2.2 Ground Motion Amplification Due to Basin Structure

2.2.1 Effects of Basin Depth and Vs30

We recalculated the six M7 Wasatch Fault (WF) scenario simulations by Roten et al. (2011) in an updated WF Community Velocity Model (WFCVM-v3d) for the Salt Lake City segment that corrects artifacts in the velocity distribution near borehole locations (WFCVM-v3c, see Figure 2.1). In addition, we have simulated visco-elastic rupture and wave propagation in a 1D rock model selected to be the WFCVM-v3d velocity-density values at the location -111.73070526°, 40.57409668°, which is marked by the star in the right panel of Figure 2.1. The 1D rock model (Figure 2.2) has constant depths to velocity isosurfaces and the same Vs30 everywhere (1,444 m/s). Figure 2.3 shows a map of the Quaternary surface faulting on the Wasatch fault zone and the 3D structure of the WFSLC rupture model used in the M7 earthquake simulations. The 1D simulations use the same source models (e.g., identical slip and peak slip rate distributions) used in the 3D simulations in Roten et al. (2011), and in this study. Since the 1D and 3D simulations used the same source models, the ground motion differences observed are due to differences in wave propagation effects that result primarily from the presence of the Salt Lake Basin in the WFCVM. The effects of the basin include amplification of seismic waves traveling into regions of lower seismic velocities within the basin, focusing and defocusing by

non-planar impedance contrasts, resonances, entrapment of waves in the basin, and generation of surface waves along the edges of the basin.

Figures 2.4 to 2.9 show comparisons between the SA-2s and SA-3s in the 1D and 3D models. Also, shown in these figures are slip and peak slip rate values. Figure 2.10 shows Vs30 values and depths to the Vs=1.0 km/s and 1.5 km/s isosurfaces for comparison with the SA-2s and SA-3s values. Notice that the ground motion intensities from the 1D model are generally smoother and smaller in amplitude due to the lack of underlying 3D structure and higher Vs30 values. The ratios of 3D/1D SA values shown in Figures 2.4-2.9 illustrate the 3D basin effects in SLV, such as focusing, defocusing, and entrapment of waves in 'pockets' of the basin. Such effects are observed above the deeper parts of the basin for all scenarios, such as just SW of South Salt Lake for scenario A (particularly for SA-2s), and just northwest of downtown SLC for scenario A', B and B'.

The isosurfaces of Vs=1.0 km/s and Vs=1.5 km/s show similar trends in the basin structure, namely the deepest part is just northwest of downtown SLC, with shallower sub-basins to the north of the Oquirrh Mountains and in the southern part of the Salt Lake Valley (near Midvale). The smallest Vs30 values of $\sim$200 m/s are located in the northern and east-central parts of the valley. The Vs30 values are negatively correlated with the associated depth to the isosurfaces (e.g., smaller Vs30 above larger depths to isosurfaces), but do not appear to be a good predictor of the areas of the largest long-period SA-3s and SA-2s values.

In order to quantify the correlation between the SAs and the basin structure, we calculated the 2D correlation coefficient (R) between the SA values from the six 3D simulations and the isosurface depths for Vs=1.0 km/s and 1.5 km/s as well as for Vs30 (Figure 2.11). The correlation coefficients are very similar for SA-2s and SA-3s and the two isosurfaces, with the largest values obtained for scenarios B', C and D (0.70-0.80) as compared to 0.60-0.68 for scenarios A, A' and B. The SAs show expectedly a negative correlation with the Vs30 distributions, with correlation coefficients between -0.33 and -0.57. Thus, the deep basin structure appears to be a slightly better

estimator of amplification than Vs30 at periods of 2 and 3 sec.

Figure 2.12 shows the average amplification effects derived from the 6-scenario ensemble of simulations, quantified as the mean 3D/1D ratio of SAs at periods of 3s and 2s, compared to the amplification factors from a representative NGA-West2 GMPE, Boore et al. (2014) (henceforth BSSA14). The BSSA14 amplification factors are functions of the variable depth to the Vs=1.0 km/s isosurface and Vs30 in the model domain. In general, the BSSA14 amplification factors have a smoother spatial distribution (as expected), but are also larger than the corresponding values from the 6-scenario simulation means. For example, the range of the BSSA14 values in the deeper northeastern part of the valley is $\sim$3.5-5.5, but only $\sim$2.5-4.5 for the simulation ensemble. This discrepancy is even larger for the southwestern (shallower) part of the valley, where the range for the simulation ensemble is 0.5-2.5, and 1.5-3.5 for BSSA14, a discrepancy that is analyzed further later. In the next subsection, we provide a more comprehensive and quantitative comparison of the basin amplification factors derived from the simulations with those predicted by 4 NGA-West2 GMPEs.

2.2.2 Regression of Amplification with Basin Depth

We have developed a regression model for basin amplification in the SLV as a function of basin depth, similar to the approach used by Day et al. (2008) for southern California. We first bin the depths (D) to a specified isosurface of Vs, either 1.0 km/s or 1.5 km/s. We define n_{bin} bins by specifying depths $D_n^{bin}, n = 1, ..., n_{bin}$, the bin centers, spaced at equal intervals $\Delta D = 100m$ and then form the binning matrix W,

$$W_{nj} = \begin{cases} 1, & if\ (D_n^{bin} - \Delta D/2) \leq D_j \leq (D_n^{bin} + \Delta D/2) \\ 0, & otherwise \end{cases} \tag{2.1}$$

where D_j is the depth at site j. We calculate the source-averaged basin response factor, $B(D_n, T_m)$,

for period T_m, by taking the natural logarithm and averaging over all N_{site} sites (3,411,094) and over all $N_{sn} = 6$ scenarios. For the ith scenario and jth site, we compute the ratio $\frac{SA_{ij}^{3d}(T_m)}{SA_{ij}^{1d}(T_m)}$, where $SA_{ij}^{3d}(T_m)$ are the SAs using the 3D WFCVM at period T_m and $SA_{ij}^{1d}(T_m)$ the SAs using the 1D velocity model at period T_m. The number of sites in the bins range between ~9,000 and 600,000.

$$B(D_n, T_m) = \left(N_{sn} \sum_{j=1}^{N_{site}} W_{nj} \right)^{-1} \sum_{i=1}^{N_{sn}} \sum_{j=1}^{N_{site}} W_{nj} ln \left[\frac{SA_{ij}^{3d}(T_m)}{SA_{ij}^{1d}(T_m)} \right] \tag{2.2}$$

We use the approximate representation constructed by Day et al. (2008) to provide a simple functional form for representing basin effects in regression modeling of ground motion:

$$A(D,T) = a_0(T) + a_1(T)[1 - exp(-D/300)] + a_2(T)[1 - exp(-D/4000)] \tag{2.3}$$

where

$$a_i(T) = b_i + c_i T, \quad i = 0, 1, 2$$

with T given in seconds and D n meters.

The parameters b_i and c_i are calculated in a two-step procedure. Separate least squares fits (at each period T_m) of $A(D,T)$ to $B(D_n, T_m)$ provided individual estimates of the $a_i(T_m)$ values for each period T_m. Then parameters b_i and c_i, for $i = 0, 1, 2$ were obtained by least-squares fits of these individual $a_i(T_m)$ estimates (although with only two periods, the linear fits are unique for this application). The resulting values for $D = Z_{1.0}$ and $Z_{1.5}$ are shown in Table 2.1.

The variances s^2 (s is standard deviation) of the logarithm of amplification as a function

of depth and period are:

$$s^2(D_n,T_m)=\left(N_{sn}\sum_{j=1}^{N_{site}}W_{nj}\right)^{-1}\sum_{i=1}^{N_{sn}}\sum_{j=1}^{N_{site}}W_{nj}\left\{ln\left[\frac{SA_{ij}^{3d}(T_m)}{SA_{ij}^{1d}(T_m)}\right]-B(D_n,T_m)\right\}^2 \tag{2.4}$$

Figure 2.13 shows the regression results for the natural log of amplification in the simulations as a function of the depth to the $Vs=1.0\ km/s$ and $Vs=1.5\ km/s$ isosurfaces. The regression for $Vs=1.5\ km/s$ shows similar amplification factors up to ∼3.15 ($ln[Amp]$ ∼1.15) at depths of ∼1.2 km/s for both SA-3s and SA-2s, with small de-amplification for depths less than ∼150 m (SA-2s) and ∼180 m (SA-3s). For $Vs=1.0\ km/s$, the regressions for SA-2s and SA-3s show larger differences, with larger amplifications for SA-2s than SA-3s for depths $<$ 500 m. The largest depth of 680 m shows amplifications of ∼2.7 for SA-2s and ∼3.7 for SA-3s.

To compare the basin depth amplification factors from four selected NGA-West2 GMPEs, we did the same regressions for the GMPEs as a function of the depth to the $Vs=1.0\ km/s$ isosurface, $Z_{1.0}$. Figure 2.14 shows the regression results for the natural log of amplification as a function of the depth to the $Vs=1.0\ km/s$ isosurface for BSSA14. Figures 2.15 and 2.16 show the regression results for the simulations and the four selected GMPEs: BSSA14 (Boore et al., 2014), ASK14 (Abrahamson et al., 2014), CB14 (Campbell and Bozorgnia, 2014), and CY14 (Chiou and Youngs, 2014). Table 2.2 lists the average amplification factors over the whole range of the depth to the $Vs=1.0\ km/s$ isosurface used in the regressions. The average 3D/1D amplification values for the GMPEs are much larger than those for the simulations. The GMPE overestimation of the amplification factors appears to be due primarily to inadequacies in the GMPE Vs30 scaling, most likely for the very high Vs30 value of 1,444 m/s in the 1D model. For this reason, we show an additional set of plots (Figures 2.17 and 2.18) with the GMPE regression curves normalized to 1 (natural log = 0) at $Z_{1.0}=0\ m$. With this normalization, it can be seen that the variation of the basin amplification with $Z_{1.0}$ in the simulations is matched fairly well by three

of the four GMPEs (CY14, ASK14, and BSSA14). Only CB14 shows a significantly different trend, namely a slower increase in amplification with depth. The relatively poor fit for CB14 is not surprising, because CB14 parameterizes basin depth with the depth to the $Vs = 2.5\ km/s$ isosurface, $Z_{2.5}$, whereas the other three GMPEs all parameterize basin depth with $Z_{1.0}$.

2.3 Source Effects on Ground Motions

2.3.1 Effects of Source Descriptions

Above, we have examined correlations of the ground motion distributions with depth measurements of the basin and Vs30 values for the SLV. Another factor strongly affecting ground motion patterns is the source description associated with the M7 WF scenario events. Here, we consider significant source parameters such as distributions of slip and peak slip velocity. In addition, rupture direction/hypocentral location is an important parameter that controls directivity, another possible factor in the final distribution of ground motions.

The first two panels in the bottom row of Figures 2.4-2.9 show the distributions of slip and peak slip rates for the scenarios. The largest asperities (defined as the areas of largest slip) tend to be located laterally opposite to and shallower than the hypocentral location for the unilateral ruptures (A, A', B, and B'), and updip from the hypocenters of the bilateral ruptures (C, D). There appears to be a correlation between the areas of the largest SA values for both the 3D and 1D simulations, and the immediately underlying slip concentrations. Examples include the southeastern part of the valley for scenarios A and B, and the east-central part of the valley for scenarios A' and D. However, there are also several cases where the largest ground motions are located above areas of limited slip, such as above the northern corner of the rupture (north of Salt Lake City) for scenarios B', and D. The range of correlation coefficients between the distributions of SAs and the underlying slip distributions is 0.70-0.87 in 3D and 0.55-0.82 in

1D (Figure 2.11). The correlation between peak slip rates and associated SAs in the valley immediately above is weaker, with the largest peak slip rates typically located at the edges of the asperities and/or the fault break, and near the hypocenter. The range of correlation coefficients between the distributions of SAs and the underlying peak slip rate distributions is 0.55-0.79 in 3D and 0.41-0.76 in 1D. The generally larger correlations between SAs and the underlying slip distributions in the 3D model suggest a possible enhancement of source effects by basin structure.

2.3.2 Rupture Direction Effects

Somerville et al. (1997) developed a (now widely used) directivity model dependent on the angle between the direction of rupture propagation and the direction of waves traveling from the fault to the site, and the fraction of the fault rupture surface that lies between the hypocenter and the site. Abrahamson (2000) modified the Somerville et al. (1997) model by adding distance and magnitude tapers. Bayless and Somerville (2013) further developed the model by removing normalization to the rupture length, using a different dependence on site azimuth, introducing azimuth tapers for dip-slip faults, and providing an extension of the model for geometrically complex faults. For dip-slip faults the Bayless and Somerville (2013) model, like the Somerville et al. (1997) model, considers only directivity effects from the updip component of the rupture propagation.

Here, we apply the directivity model of Bayless and Somerville (2013) for multi-section ("multi-segment") faults to quantify its effect on GMPE predictions of ground-motion SAs in the Wasatch fault zone. We considered three rupture models, which divide the fault into one, two, and ten sections along strike (Figure 2.19). The scenario hypocenter becomes the rupture initiation point on the first section. Following the Bayless and Somerville (2013) model, 'pseudo-hypocenters' for the rupture of successive sections are defined as the point on the edge of the fault section that is closest to the edge of the neighboring section, half way between the top and

bottom of the rupture. The directivity adjustment term f_D for each section of a dip-slip fault is expressed as:

$$\begin{aligned} f_D &= f_D\,(d, R_x, W, R_{rup}, M_w, A_z, T) \\ &= [C_0(T) + C_1(T) ln(d) cos(Rx/W)]\ T_{CD}(R_{rup}, W)\ T_{M_w}(M_w)\ T_{A_z}(A_z) \end{aligned} \tag{2.5}$$

where C_0 and C_1 are period (T) dependent coefficients, d is the width in km of the (dipping) fault section rupturing updip towards a site (minimum = 1 km and maximum = W; see also Somerville et al. (1997)), R_x is the horizontal distance from the top edge of the rupture measured perpendicular to the rupture strike, T_{CD} is a distance taper, R_{rup} is the closest distance to the fault rupture plane, W is the fault width, T_{M_w} is a magnitude taper, M_w is the moment magnitude of the earthquake (not the section), $T_{A_z} = sin^2(|A_z|)$ is an azimuth taper, and A_z is the NGA-defined source-to-site azimuth. The NGA azimuth is measured from the strike direction of the site's closest point on the surface projection of the top edge of the rupture Ancheta et al. (2013). This azimuth, d, and R_{rup} are measured from each rupture section to the site whereas R_x is measured from the closest rupture section to the site (Jeffrey R. Bayless, written communication, January 27, 2017). The total directivity adjustment term f_D is a weighted average of the segments' directivity adjustment terms, with the seismic moments of the individual segments as the weights. We modified the median spectral acceleration SA_{med} from four leading NGA-West2 GMPEs (calculated without directivity effects) to include f_D by setting $SA_{dir} = SA_{med}\ e^{f_D}$.

Maps of the directivity factors e^{f_D} for scenarios A and C at 2s and 3s periods are shown in Figures 2.20 and 2.21. It is evident that the Bayless and Somerville (2013) directivity factors depend strongly on how the fault plane is subdivided into segments, generally producing smaller directivity factors with a larger number of segments. Here, we apply the factors with the 1-segment WFSLC approximation to the GMPEs to estimate the largest possible directivity effects

from the model. Figures 2.22 - 2.25 show comparisons between SAs from 3D and 1D simulations for scenarios A and C to SAs predicted for the 3D model from the four selected NGA-West2 GMPEs, shown with and without the directivity factors from Bayless and Somerville (2013). It is clear that the largest effect of the directivity factors is to increase the ground motions almost uniformly next to the fault. These directivity factors do little to increase the similarity between the SAs from the GMPEs and the simulations because the rupture direction effects in the simulations vary strongly with distance along the fault. The directivity factors improve the match between the GMPEs and the simulations in only four of the eight cases examined for rupture scenario A (Figures 2.22 and 2.23) and only three of the eight cases examined for rupture scenario C (Figures 2.24 and 2.25).

2.4 Distance Dependence of the Ground Motions

Roten et al. (2011) compared mean simulated 3s-SAs and 2s-SAs and the values from the NGA08 ground motion prediction equations CB08 (Campbell and Bozorgnia, 2008), AS08 (Abrahamson and Silva, 2008), and CY08 (Chiou and Youngs, 2008) as a function of R_{rup}. For sites on the hanging wall at rupture distances larger than $\sim$4km, the average simulated SAs were below the values predicted by all three NGA models. At $R_{rup} = 10\ km$, the simulated 3s-SAs and 2s-SAs dropped below one standard deviation of the NGA predictions. In contrast, simulated long-period SAs on the footwall did not show such discrepancies with the NGA08 relations.

The bias between the simulated 3D SA distributions (geometric mean of six scenarios calculated in the WFCVM) and predicted SA distributions from 4 NGA-West2 GMPEs is shown by the maps in Figures 2.26-2.27 (3s) and 2.28-2.29 (2s), and as a function of R_{rup} in Figures 2.30 (3s) and 2.31 (2s) for soil and rock sites separately. All of the bias values are normalized by the standard deviations, σ, which range from $\sim$0.67 to $\sim$0.74 in natural log units. Because the bias is fairly constant in all of the GMPEs (within $\pm$ 5%), the apparent distance dependences

of the biases are not significantly affected by the normalization with the standard deviation. Comparisons for SAs calculated in the 1D model are shown as maps in Figures 2.32-2.33 (3s) and 2.34-2.35 (2s), and as a function of R_{rup} in Figures 2.36 (3s) and 2.37 (2s). Although all sites are rock sites in the 1D model, the sites are subdivided into soil or rock sites according to their 3D model classification to facilitate comparisons with the 3D results. In the 3D model, the soil sites (Vs30 $<$ 750 m/s) are primarily located on the hanging wall, whereas the rock sites (Vs30 $>$ 750 m/s) are located on both the footwall and the hanging wall in the mountain ranges surrounding the Salt Lake Valley (Figure 2.1).

Three pervasive distance trends are seen in the bias plots (Figures 2.30, 2.31, 2.36, and 2.37). The first trend is a gradual increase in bias from $R_{rup} = 0$ to $1 - 1.5$ km for all soil sites at 2s and 3s in both models, about twice as large in the 3D as compared to the 1D results. An increase in bias from $R_{rup} = 0$ to ~ 0.25 km for all rock sites is also seen at 2s and 3s in both 1D and 3D models. The second trend is a decrease in bias from R_{rup} $\sim$4 km to $\sim$10 km for all soil sites at 2s and 3s in both models, again about twice as large in the 3D results as in the 1D results. The result of these two trends is a relative high in the bias plots for R_{rup} $\sim$1-4 km on the hanging wall side of the fault, which is also evident in maps of geometric mean SAs from the six different scenarios (Figure 2.38). O'connell et al. (2007) found a similar pattern for 3D simulations of large earthquakes on the Teton fault where the highest peak ground velocities (PGVs) occurred at distances of 1-4 km from the surface trace of the fault, also on the hanging wall side. The third pervasive trend consists of an increase in bias for soil sites for both 2s and 3s SAs as R_{rup} increases from $\sim$12 to 20 km, with the amount of increase comparable for both the 1D and 3D models.

Because trend 1 is more pronounced in the 3D simulations, we interpret it as partly caused by the basin edge effect, as hypothesized by Roten et al. (2011). The basin edge effect is caused by constructive interference between basin-edge-generated surface waves and the direct S wave (e.g., Kawase, 1996; Pitarka et al., 1998), and is only present in the 3D model. Because a positive

bias near the fault occurs also in the 1D models, entrapment of waves by the horizontally layered structure may also be contributing to this amplification. Alternatively, the drop-off of the bias in SAs at distances less than 1.5 km from the fault trace could be related to velocity strengthening fault friction in the shallow part of the fault. Shallow velocity strengthening was emulated in the dynamic rupture simulations performed by Roten et al. (2011) in order to produce realistic ground motions, and consequently affects both the 3D and 1D simulations. The lower bias for near-fault rock sites is likely also caused by this source effect, but in a narrower zone because the fault dips below the valley sediments.

The gradual decrease in the bias for soil sites in the 3D model at distances of ∼4-10 km (trend 2) was previously noted by Roten et al. (2011) for the 2008 NGA-West1 relations. This decrease is evident for the 2014 GMPEs as well and is most pronounced for BSSA14 and CB14 and smallest in size for CY14 (Figures 2.30 and 2.31). In comparison, the 2014 GMPEs for rock sites generally show little to no change in the bias at these distances from the fault. For his reason, we interpret this trend to be at least in part due to the basin effects discussed previously, as well as directivity effects. Another possible cause of this trend is the westward termination of the WF as well as associated significant slip in the M7 scenarios. While the nature of the GMPEs imply a smooth distribution of slip on the fault, our scenarios produced the majority of the slip on the upper half of the fault, likely concentrating the highest ground motion amplitudes closer to the surface trace.

With trend 3 the bias increases with distance again at soil sites located within 12 to 20 km from the rupture (Figures 2.30 and 2.31). The bias maps for the 3D simulations (Figures 2.26-2.29) typically show the lowest values, generally between -0.5 σ and -2 σ in the southwestern part of the SLB, roughly to the SW of a line connecting West Valley City to Draper. In the NW part of the SLB, towards the Great Salt Lake, the bias tends to range between +0.5 σ and -1 σ. Therefore, we interpret trend 3 to be an artifact of the distribution of rupture distances in the basin in combination with azimuthal variations in ground motions. The apparent distance trend occurs

because the distance range between 12 and 20 km includes more points from the NW part of the basin than from the SW part. (For a map with rupture distances, refer to Figure 9 in Roten et al. (2011).

The simulations in Roten et al. (2011) used the Qs-Vs relation by Brocher (2006). In order to test whether a less attenuating Q distribution can account for the bias at Rrup ∼4-10 km, we simulated scenario A' using the relations $Qs = 0.1Vs$ (Vs in km/s) and $Qp = 2Qs$ (based on results from Withers et al. (2015)). The distributions of SA-2s for scenario A' simulated with the 2 different Q distributions are shown in Figure 2.39. The main differences between the SA-2s results are larger SA-2s values within ∼10 km to the west of the fault trace, in particular N and NW of SLC. Figure 2.40 shows the bias relative to BSSA14 and CB14 of SA-2s from simulations with the two different Q relations, suggesting that the Brocher (2006) Q relation provides slightly greater overall similarity to the GMPEs.

2.5 Hanging Wall Effects

The ASK14, CB14, and CY14 GMPEs have explicit factors to account for observed systematic ground motion differences between sites on the hanging wall and footwall located at the same distance from the closest part of the rupture (e.g., Abrahamson and Somerville, 1996). These "hanging wall factors" are all based in part on finite fault simulations by Donahue and Abrahamson (2014). The expectation of higher ground motions on the hanging wall is implicit in the distance definition used in BSSA14, which is the closest horizontal distance to the surface projection of the rupture. Chiou et al. (1999a), Chiou et al. (1999b) and Donahue and Abrahamson (2014) showed that the larger ground motions at hanging wall sites could be explained as a geometrical effect resulting from the fact that the average distance to the rupture from a hanging wall site is less than that for a footwall site at the same closest distance. Note that this hanging wall effect is independent of, and in addition to, any ground motion amplifications

that may be caused by low velocity sediments on the hanging wall.

The hanging wall factors in the 2008 and 2014 NGA equations are based primarily on data and simulations for reverse-faulting earthquakes. Consequently, the application of these hanging wall factors to normal-faulting earthquakes has been somewhat controversial. Here, we test the applicability of these factors to normal faulting earthquakes using the results of our simulations for the 1D rock model.

Figure 2.41 compares geometric mean SA-2s and SA-3s values from the six 1D simulations with GMPE predictions for sites within a 4-km-wide zone trending ENE-WSW across the center of the simulated WFSLC rupture. The horizontal axis in Figure 2.41 is R_x, the horizontal distance from the top of the rupture measured perpendicular to strike. R_x is defined as positive on the hanging wall side. All of the SAs shown are normalized to 1.0 at a footwall reference site where $R_x = -12.2$ km (40.7635°, -111.6972°). Each SA value plotted is a geometric mean for sites within a 1km R_x bin.

Figure 2.41 shows that the GMPEs do a reasonably good job of predicting the increased ground motions over the hanging wall for SA-3s, although the fit for BSSA14 is not as good as for the others. For SA-2s, the simulations show minimal increase over the hanging wall and the GMPEs overpredict the simulations. However, the overpredictions are less than 1 standard deviation except for BSSA14.

2.6 Summary

We have analyzed numerical simulations of six M7 earthquakes on the Salt Lake City segment of the Wasatch Fault (WF), Utah, to better understand the long-period ground motions that these simulations predict in the adjacent Salt Lake Valley (SLV). We calculated peak spectral accelerations at 2s (SA-2s) and 3s (SA-3s) in an updated Wasatch Front Community Velocity Model (WFCVM-v3d) as well as in a 1D rock model, using the same fault rupture descriptions

as in Roten et al. (2011), in order to separate source and basin effects. The SAs from the 1D model are generally smoother and smaller in amplitude due to higher Vs30 values and the lack of underlying 3D structure. 3D/1D ratios of the SA values depict the 3D basin effects in the SLV, such as focusing, defocusing, and entrapment of waves in the basin, particularly above the deeper parts of the basin. The SA-2s and SA-3s values show a strong correlation [0.6 to 0.8] with two basin depth measurements in the WFCVM, with a smaller (negative) correlation to Vs30 [-0.3 to -0.6]. Based on this result, we developed regression models for the 6-scenario ensemble of ground motions as a function of depth to the isosurfaces of Vs=1.0 km/s and 1.5 km/s in the SLV. The models for the 1.0 km/s isosurface show amplification factors of up to $\sim$2.7 and $\sim$3.7 above the deepest part of the basin for SA-2s and SA-3s, respectively.

We find correlations between the long-period scenario ground motions in the SLV and the underlying fault slip that range from 0.55 to 0.87. The correlations with peak slip rate are somewhat lower, ranging from 0.41 to 0.80. The correlations are larger for the simulations using the 3D basin model, as compared to those obtained from the 1D model, suggesting an interaction between the source characteristics and the basin structure. To assess how well a simple parametric directivity model can explain the long-period ground motion patterns for the individual M7 WF scenarios, we compute directivity factors using the Bayless and Somerville (2013) model. The directivity effects from this parametric model increase the SA-2s and SA-3s values by less than 30% for the scenarios, and increase the similarity between the NGA-West2 GMPEs and simulations in less than half of the cases examined.

As compared to predictions from four NGA-West2 GMPEs, the long-period WF scenario ground motions on soil sites show a gradual increase in bias from $R_{rup} = 0$ to 1-1.5 km and a decrease in bias from R_{rup} $\sim$4 km to $\sim$10 km, with both trends about twice as large in the 3D as in the 1D simulations. The resulting high in the bias plots for R_{rup} $\sim$1-4 km appears to be partly caused by the basin edge effect and/or entrapment of waves in the deeper parts of the basin, combined with scenario specific conditions such as slip distributions not captured by the

GMPEs. However, the presence of the near-fault bias in the 1D simulations (albeit smaller than in the 3D results) suggests that the use of velocity strengthening in the near-surface part of the rupture models also contributes to decreasing the SAs within $\sim$1.5 km of the fault. Tests with a less attenuating Q model than used by Roten et al. (2011) indicates that uncertainties in the Q distribution is likely not contributing to the near fault bias.

Three NGA-West2 GMPEs with explicit hanging wall factors do a reasonably good job of predicting the increased ground motions over the hanging wall for SA-3s. For SA-2s, the simulations show minimal increase over the hanging wall and the GMPEs overpredict the simulations, but the overpredictions are less than one standard deviation.

Acknowledgements

Chapter 2, in full, is a reformatted version of the material as it appears in Final Technical Report for U.S. Geological Survey: Wang, N., D. Roten, K.B. Olsen, and J.C. Pechmann (2017). Rupture direction, hanging wall, basin, and distance effects on ground motions from large normal-faulting earthquakes, Final Technical Report, *U.S. Geological Survey*, Award Nos. G14AP00044 and G14AP00045, 44 pp. 05/19/2017. The dissertation author was the primary investigator and author of this report.

References

Abrahamson, N. and Somerville, P. (1996). "Effects of the hanging wall and footwall on ground motions recorded during the Northridge earthquake". In: *Bulletin of the Seismological Society of America* 86.1B, S93–S99.

Abrahamson, N. and Silva, W. (2008). "Summary of the Abrahamson & Silva NGA ground-motion relations". In: *Earthquake spectra* 24.1, pp. 67–97.

Abrahamson, N. A. (2000). "Effects of rupture directivity on probabilistic seismic hazard analysis". In: *Proceedings of the 6th international conference on seismic zonation*. Vol. 1. Earthquake Engineering Research Institute. Palm Springs, CA, pp. 151–156.

Abrahamson, N. A., Silva, W. J., and Kamai, R. (2014). "Summary of the ASK14 ground motion relation for active crustal regions". In: *Earthquake Spectra* 30.3, pp. 1025–1055.

Ancheta, T. D., Darragh, R. B., Stewart, J. P., Seyhan, E., Silva, W. J., Chiou, B. S., Wooddell, K. E., Graves, R. W., Kottke, A. R., Boore, D. M., Kishida, T, and Donahue, J. (2013). *Peer NGA-West2 database, PEER Report 2013/03*. Report. Pacific Earthquake Engineering Research Center, University of California, Berkeley.

Bayless, J. R. and Somerville, P. (2013). "Bayless and Somerville model, Chapter 2". In: *Final report of the NGA-West2 directivity working group*. Ed. by P. Spudich. Pacific Earthquake Engineering Research Center, University of California, Berkeley.

Boore, D. M., Stewart, J. P., Seyhan, E., and Atkinson, G. M. (2014). "NGA-West2 equations for predicting PGA, PGV, and 5% damped PSA for shallow crustal earthquakes". In: *Earthquake Spectra* 30.3, pp. 1057–1085.

Brocher, T (2006). "Key elements of regional seismic velocity models for ground motion simulations". In: *Proceedings of International Workshop on Long-Period Ground Motion Simulations and Velocity Structures*.

Campbell, K. W. and Bozorgnia, Y. (2008). "NGA ground motion model for the geometric mean horizontal component of PGA, PGV, PGD and 5% damped linear elastic response spectra for periods ranging from 0.01 to 10 s". In: *Earthquake Spectra* 24.1, pp. 139–171.

— (2014). "NGA-West2 ground motion model for the average horizontal components of PGA, PGV, and 5% damped linear acceleration response spectra". In: *Earthquake Spectra* 30.3, pp. 1087–1115.

Chiou, B. S.-J. and Youngs, R. R. (2014). "Update of the Chiou and Youngs NGA model for the average horizontal component of peak ground motion and response spectra". In: *Earthquake Spectra* 30.3, pp. 1117–1153.

Chiou, B.-J. and Youngs, R. R. (2008). “An NGA model for the average horizontal component of peak ground motion and response spectra”. In: *Earthquake spectra* 24.1, pp. 173–215.

Chiou, S.-J., Makdisi, F. I., and Youngs, R. R. (1999a). “Style-of-faulting and Footwall/hanging Wall Effects on Strong Ground Motions”. In: *Seismological Research Letters* 70.216.

— (1999b). *Style-of-faulting and Footwall/hanging Wall Effects on Strong Ground Motions, Final Technical Report*. Tech. rep. US Geological Survey.

Day, S. M., Graves, R., Bielak, J., Dreger, D., Larsen, S., Olsen, K. B., Pitarka, A., and Ramirez-Guzman, L. (2008). “Model for basin effects on long-period response spectra in southern California”. In: *Earthquake Spectra* 24.1, pp. 257–277.

Donahue, J. L. and Abrahamson, N. A. (2014). “Simulation-based hanging wall effects”. In: *Earthquake Spectra* 30.3, pp. 1269–1284.

Kawase, H. (1996). “The cause of the damage belt in Kobe:“The basin-edge effect,” constructive interference of the direct S-wave with the basin-induced diffracted/Rayleigh waves”. In: *Seismological Research Letters* 67.5, pp. 25–34.

O’connell, D. R., Ma, S., and Archuleta, R. J. (2007). “Influence of dip and velocity heterogeneity on reverse-and normal-faulting rupture dynamics and near-fault ground motions”. In: *Bulletin of the Seismological Society of America* 97.6, pp. 1970–1989.

Pitarka, A., Irikura, K., Iwata, T., and Sekiguchi, H. (1998). “Three-dimensional simulation of the near-fault ground motion for the 1995 Hyogo-ken Nanbu (Kobe), Japan, earthquake”. In: *Bulletin of the Seismological Society of America* 88.2, pp. 428–440.

Roten, D, Olsen, K., Pechmann, J., Cruz-Atienza, V., and Magistrale, H (2011). “3D simulations of M 7 earthquakes on the Wasatch fault, Utah, Part I: Long-period (0–1 Hz) ground motion”. In: *Bulletin of the Seismological Society of America* 101.5, pp. 2045–2063.

Roten, D., Fäh, D., Cornou, C., and Giardini, D. (2006). “Two-dimensional resonances in Alpine valleys identified from ambient vibration wavefields”. In: *Geophysical Journal International* 165.3, pp. 889–905.

Somerville, P. G., Smith, N. F., Graves, R. W., and Abrahamson, N. A. (1997). “Modification of empirical strong ground motion attenuation relations to include the amplitude and duration effects of rupture directivity”. In: *Seismological research letters* 68.1, pp. 199–222.

Withers, K. B., Olsen, K. B., and Day, S. M. (2015). “Memory-efficient simulation of frequency-dependent Q”. In: *Bulletin of the Seismological Society of America* 105.6, pp. 3129–3142.

Tables and Figures

Table 2.1: Coefficients for basin amplification factor in Equation (2.3).

Isosurface	b_0	b_1	b_2	c_0	c_1	c_2
$V_s = 1.0\ km/s$	-0.9542	5.647	-23.48	0.1906	-1.781	10.82
$V_s = 1.0\ km/s$	-0.229	0.983	1.214	-0.1846	0.214	0.016

Table 2.2: Average amplification factors from regressions vs. depth to $V_s = 1.0\ km/s$.

Period	Simulation	BSSA14	ASK14	CB14	CY14
2s	0.6920	1.2164	1.0793	1.4010	1.4137
3s	0.6754	1.1270	0.9527	1.4019	1.4236

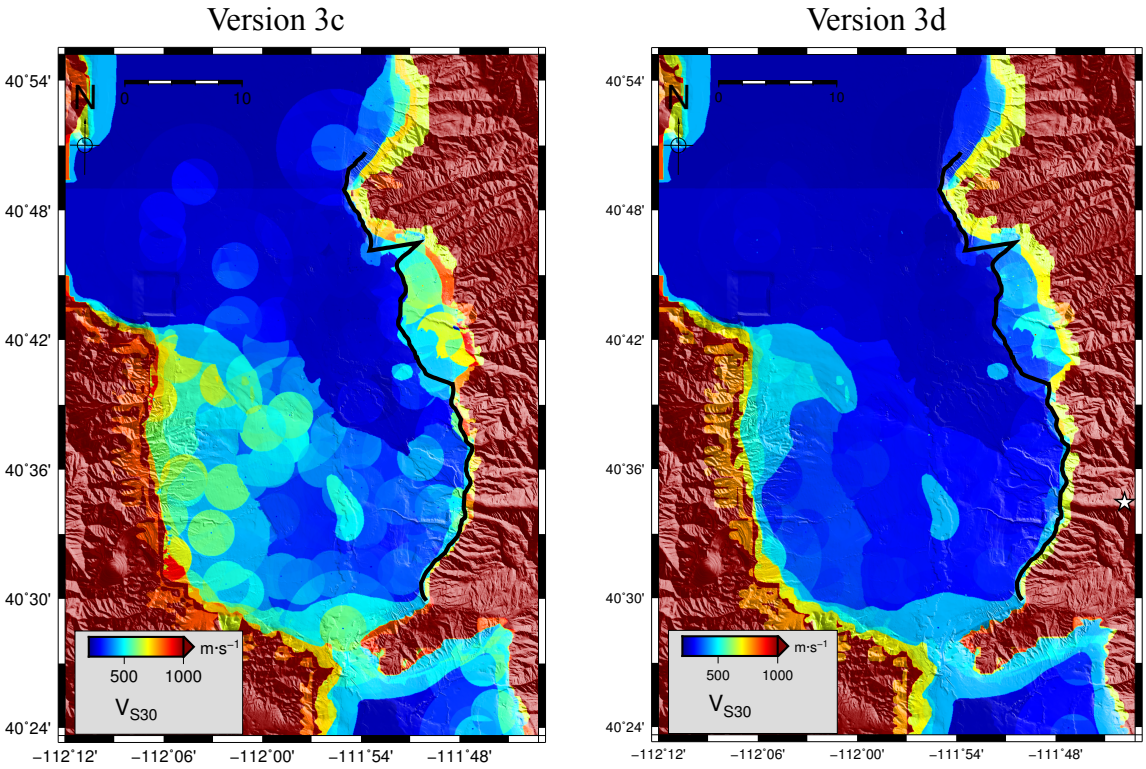

Figure 2.1: Distributions of Vs30 for the WFCVM (left) version 3c and (right) 3d, interpolated from Vs values at zero and 40 m depth. The star shows the location where the 1D rock model is extracted. The black line depicts the WF surface trace.

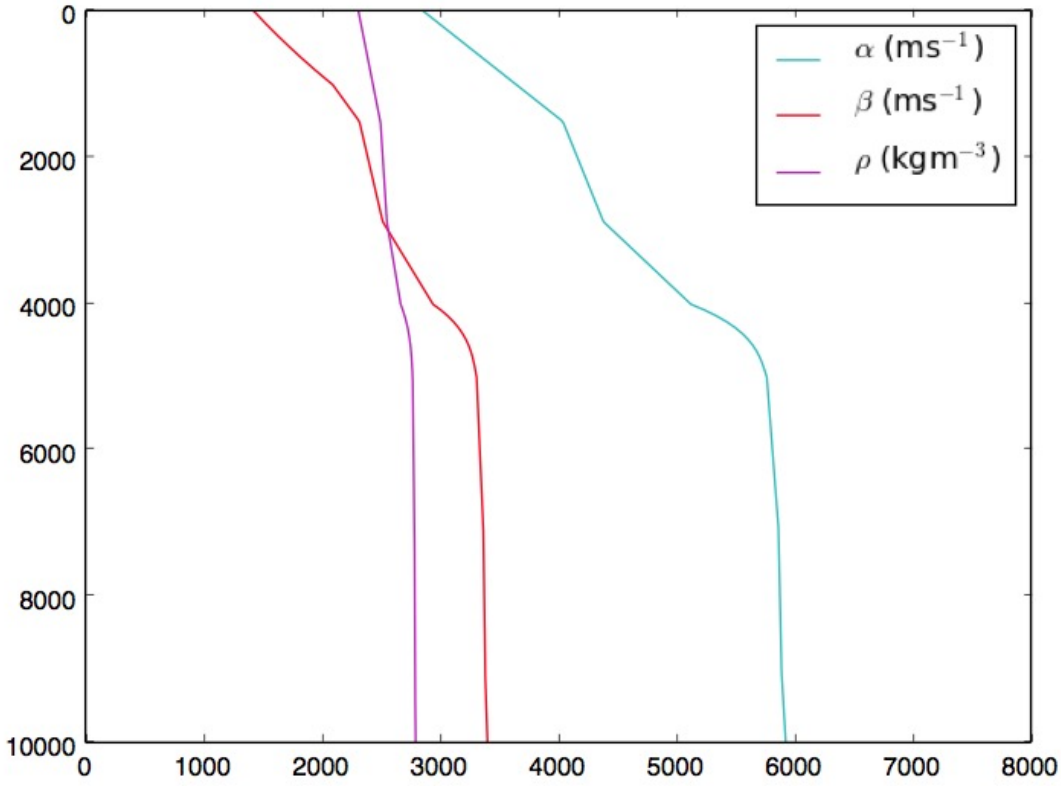

Figure 2.2: 1D rock model used for the 1D SLV simulations. Vp denotes P-wave velocity, Vs S-wave velocity, and ρ density. The Vs30 value for this model is 1444 m/s.

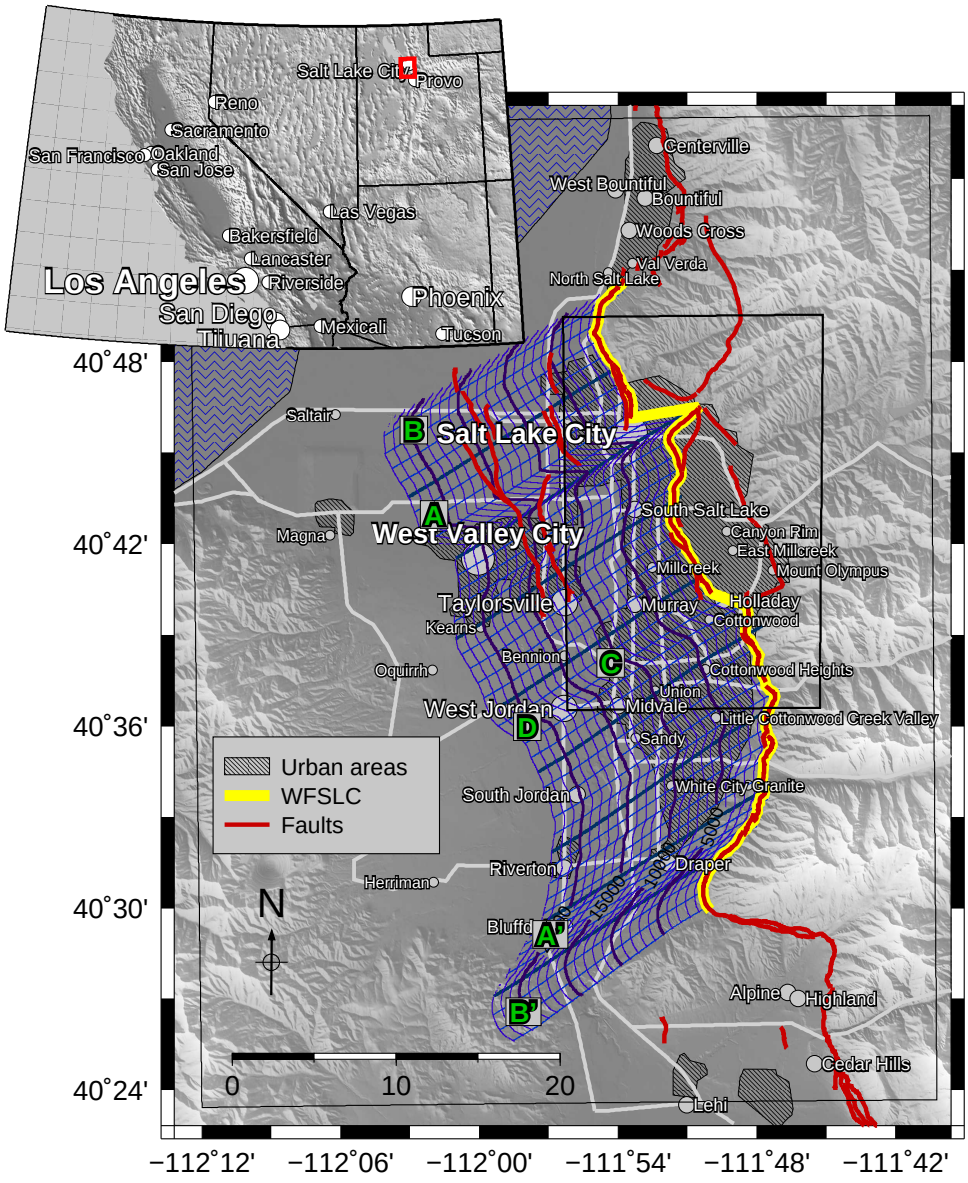

Figure 2.3: Map of the Salt Lake Basin showing known Quaternary surface faulting on the Wasatch fault zone and the surface trace of the WFSLC model. The mesh shows the 3D structure of the WFSLC with along-strike and along-dip distances in 1000 m contours. Letters represent the epicenter locations in the six rupture models. The outer rectangle shows the extent of the computational model used for the simulations (Roten et al., 2011).

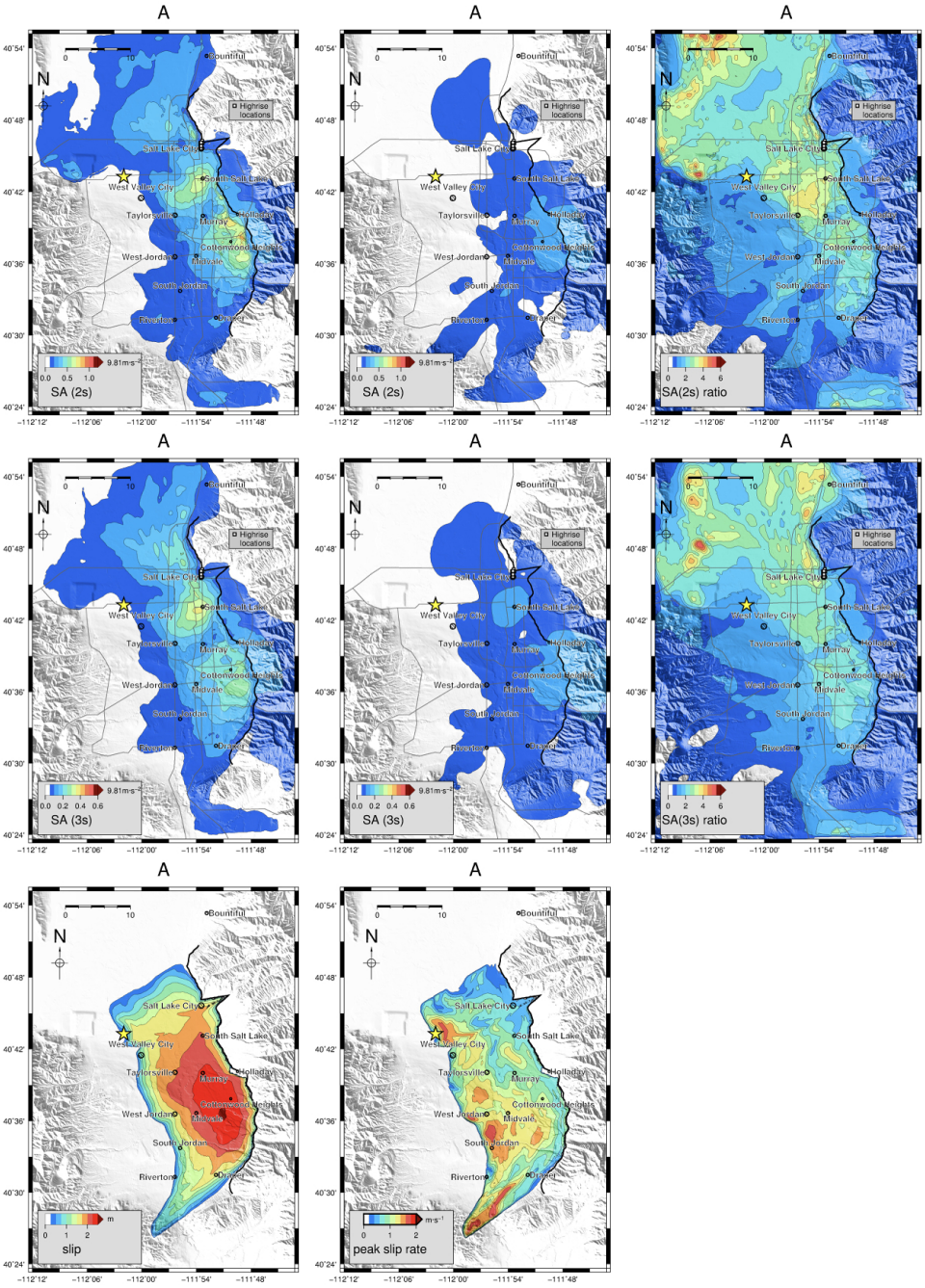

Figure 2.4: Scenario A. (first row, from left to right) SA-2s(3D), SA-2s(1D), SA-2s(3D)/SA-2s(1D) ratio; (second row) SA-3s(3D), SA-3s(1D), SA-3s(3D)/SA-3s(1D) ratio; (third row) slip, peak slip velocity. The star depicts the epicenter, the bold line the WF surface trace.

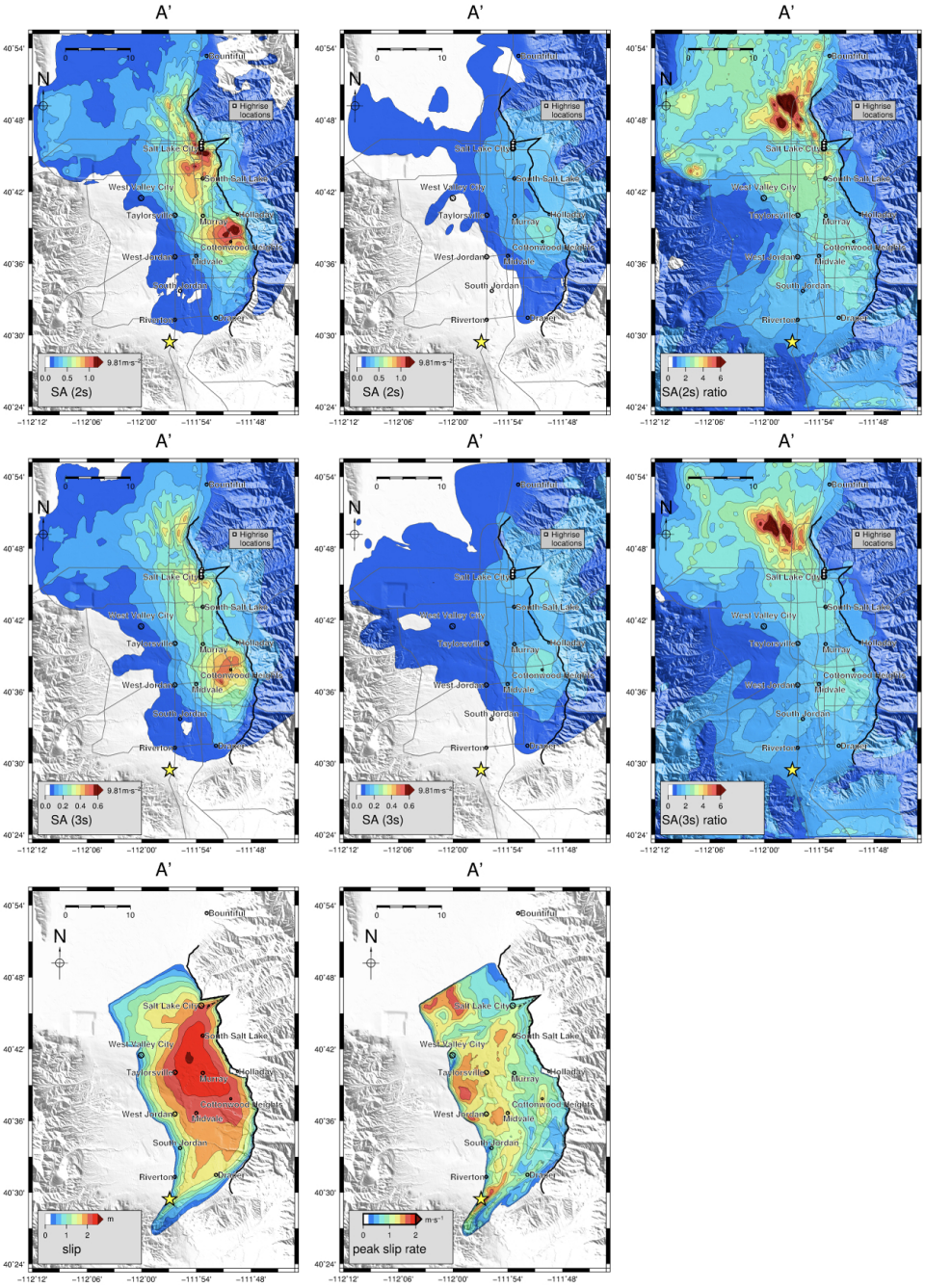

Figure 2.5: Same as Figure 2.4, but for Scenario A'.

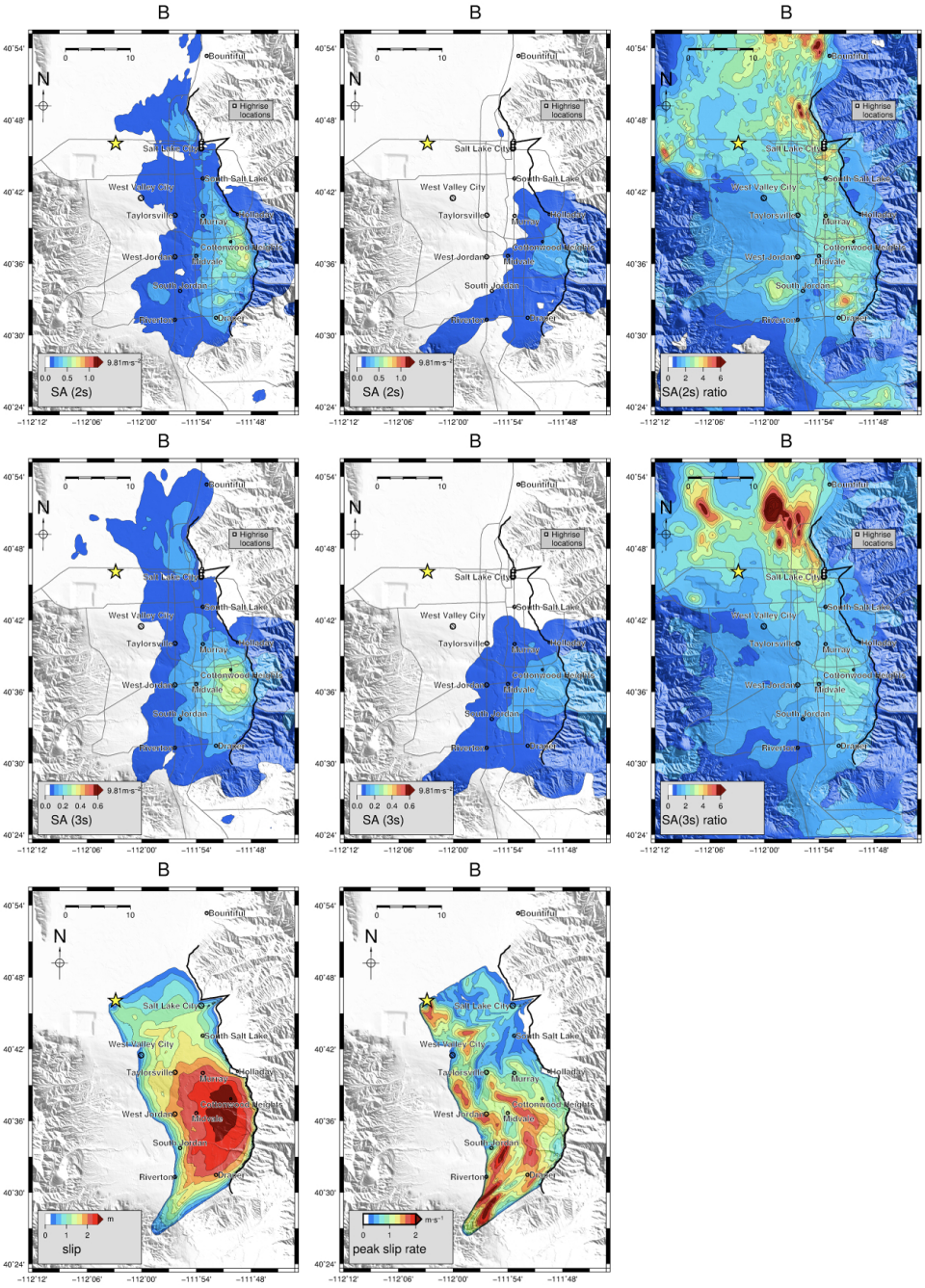

Figure 2.6: Same as Figure 2.4, but for Scenario B.

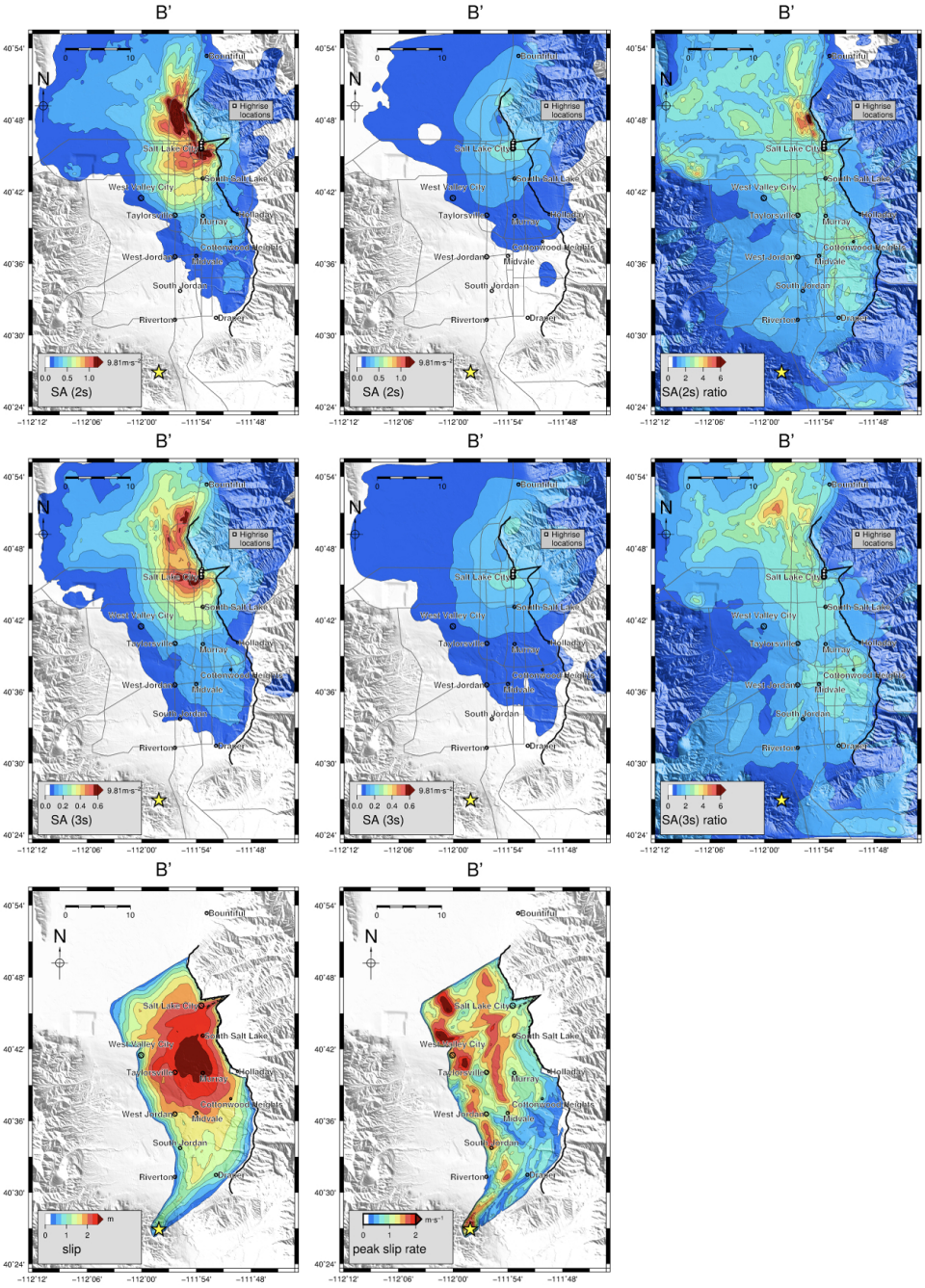

Figure 2.7: Same as Figure 2.4, but for Scenario B'.

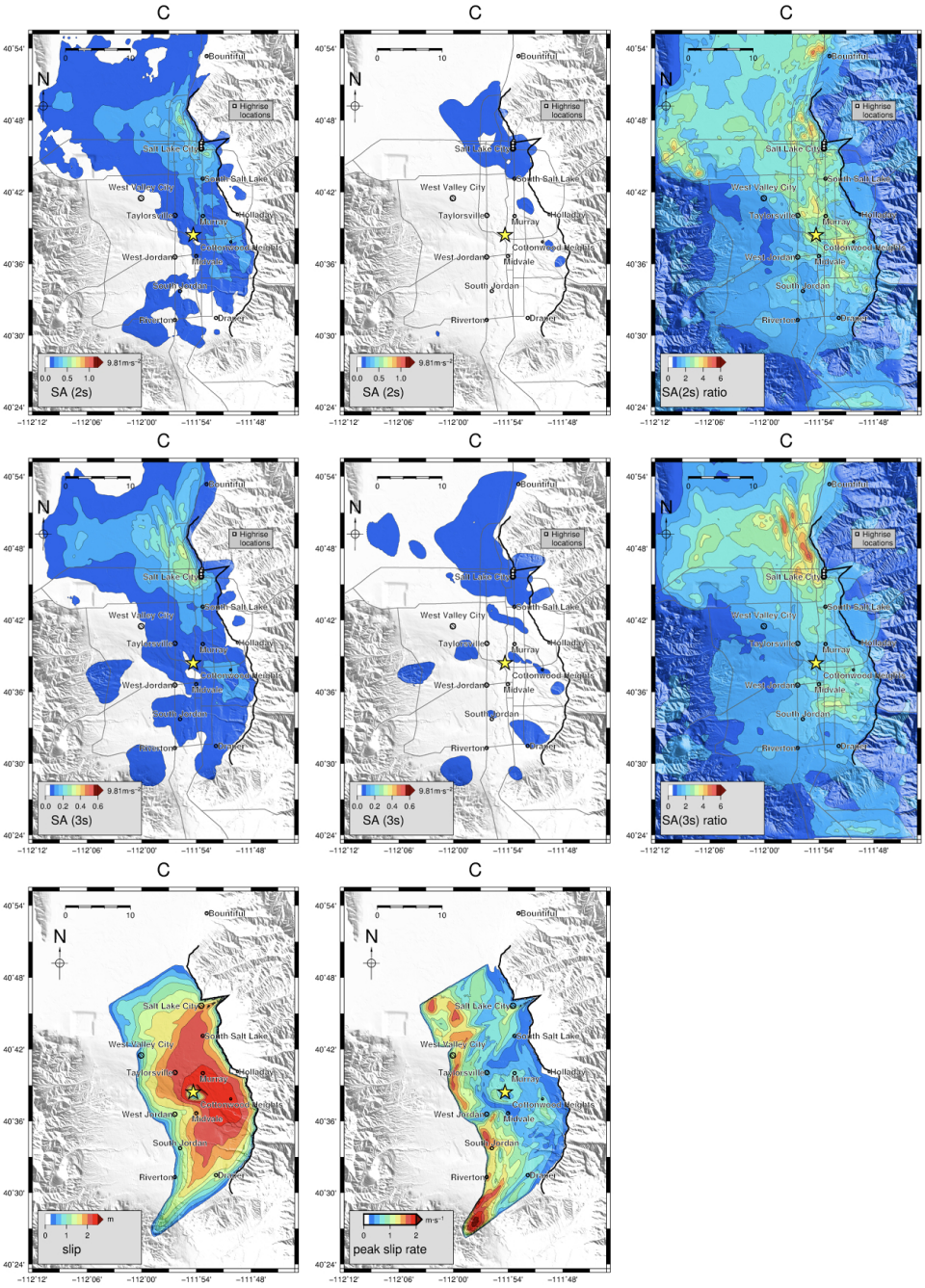

Figure 2.8: Same as Figure 2.4, but for Scenario C.

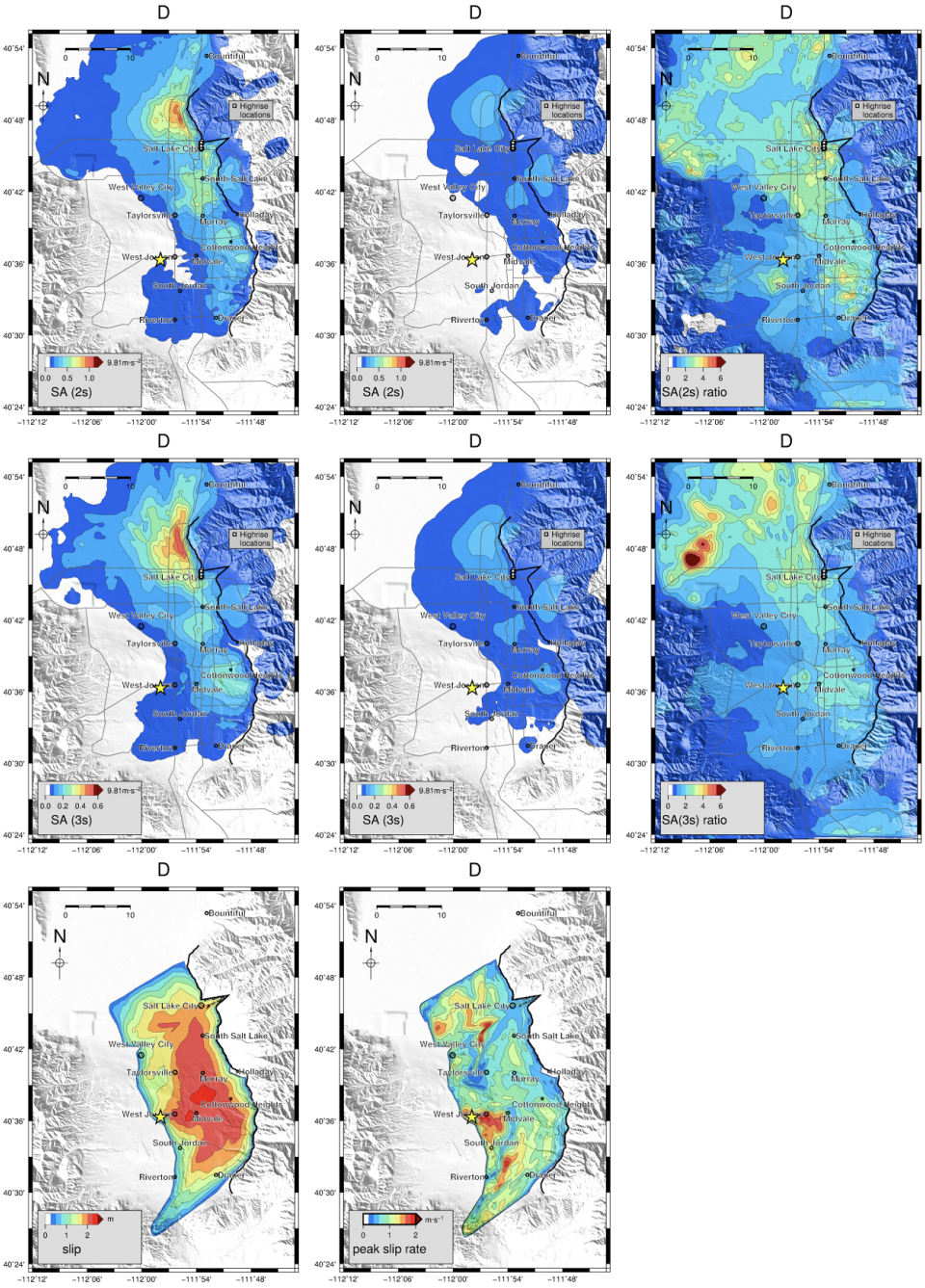

Figure 2.9: Same as Figure 2.4, but for Scenario D.

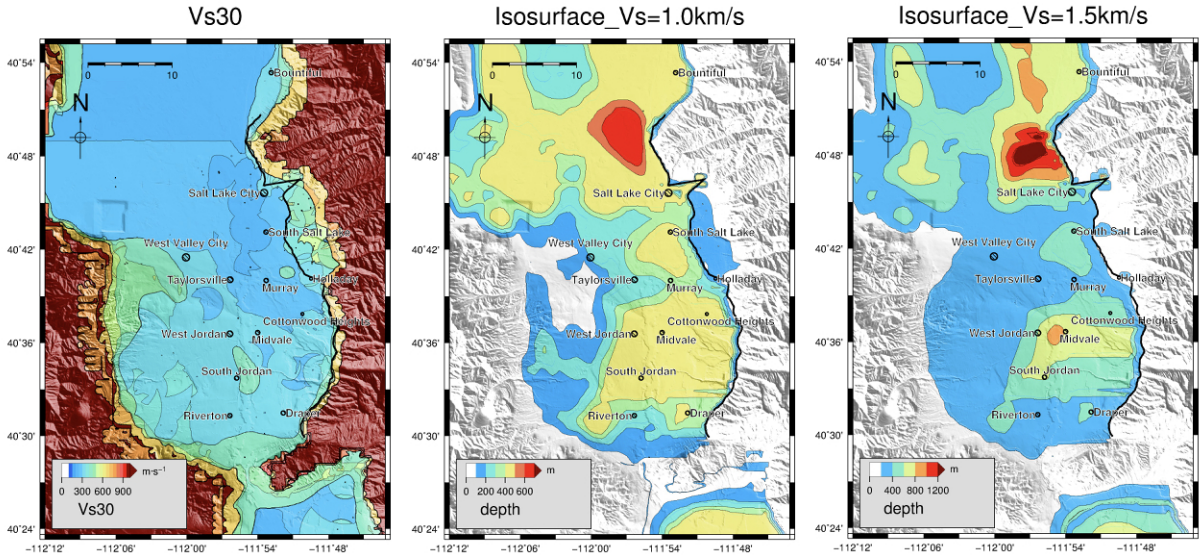

Figure 2.10: Distributions of Vs30 for the WFCVM (left), depth to Vs=1.0 km/s isosurface (middle), and depth to Vs=1.5 km/s isosurface (right). The bold line depicts the WF surface trace.

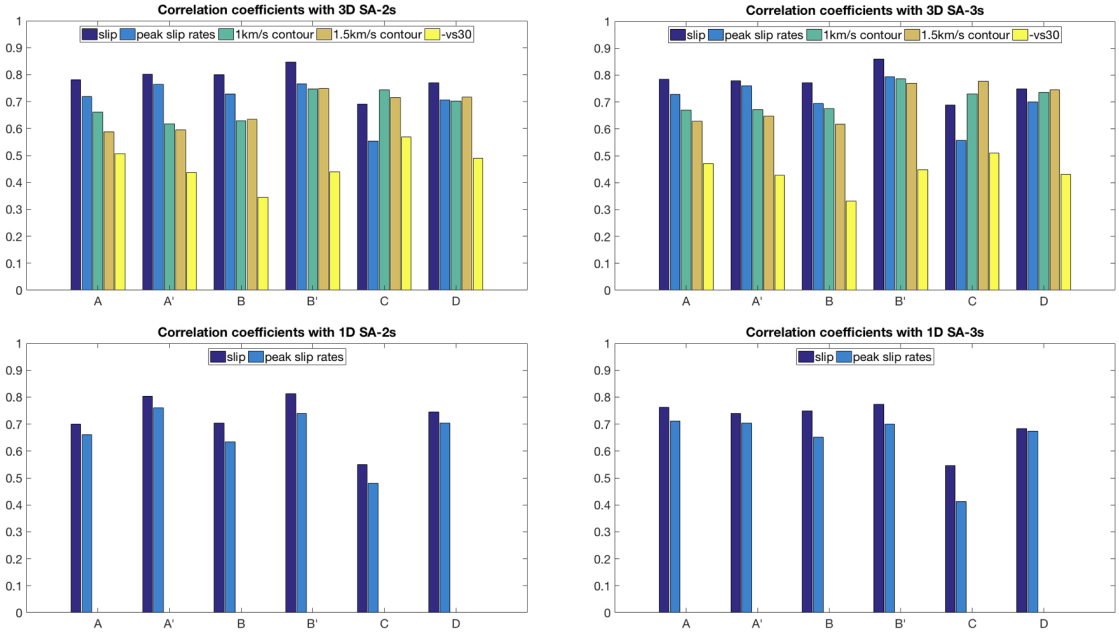

Figure 2.11: Correlation coefficients between the SA-2s (left) and SA-3s (right) values from the six scenarios and the distributions of slip, peak slip rate, depths to Vs=1.5 km/s and 1.0 km/s, and Vs30, for the simulations carried out in the (top) 3D WFCVM model and (bottom) 1D rock model.

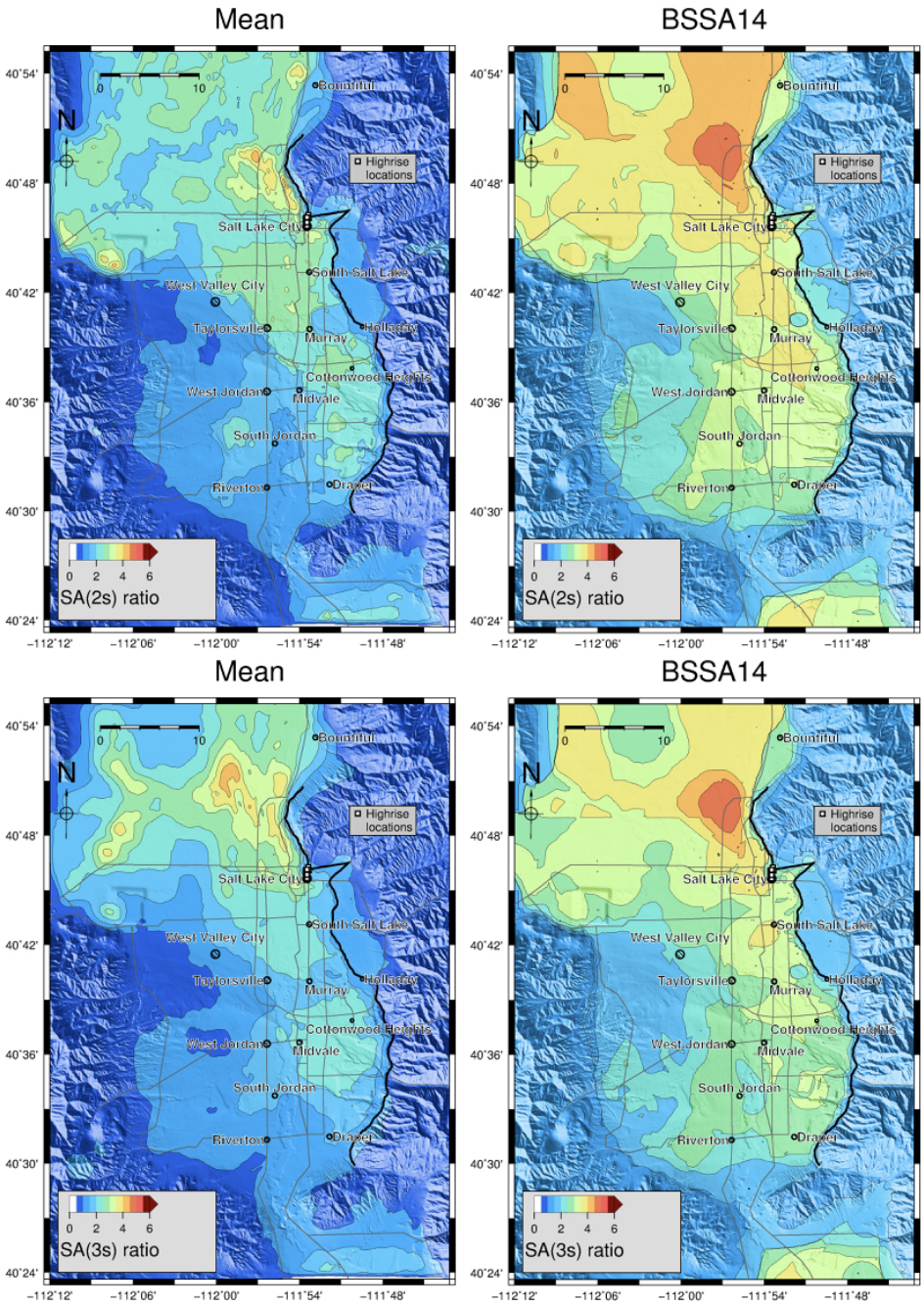

Figure 2.12: Maps of basin amplification for M7.0 Wasatch fault scenarios for (top) SA- 2s and (bottom) SA-3s, from (left) 6-scenario average 3D/1D ratios and (right) the BSSA14 GMPE. The bold line depicts the WF surface trace.

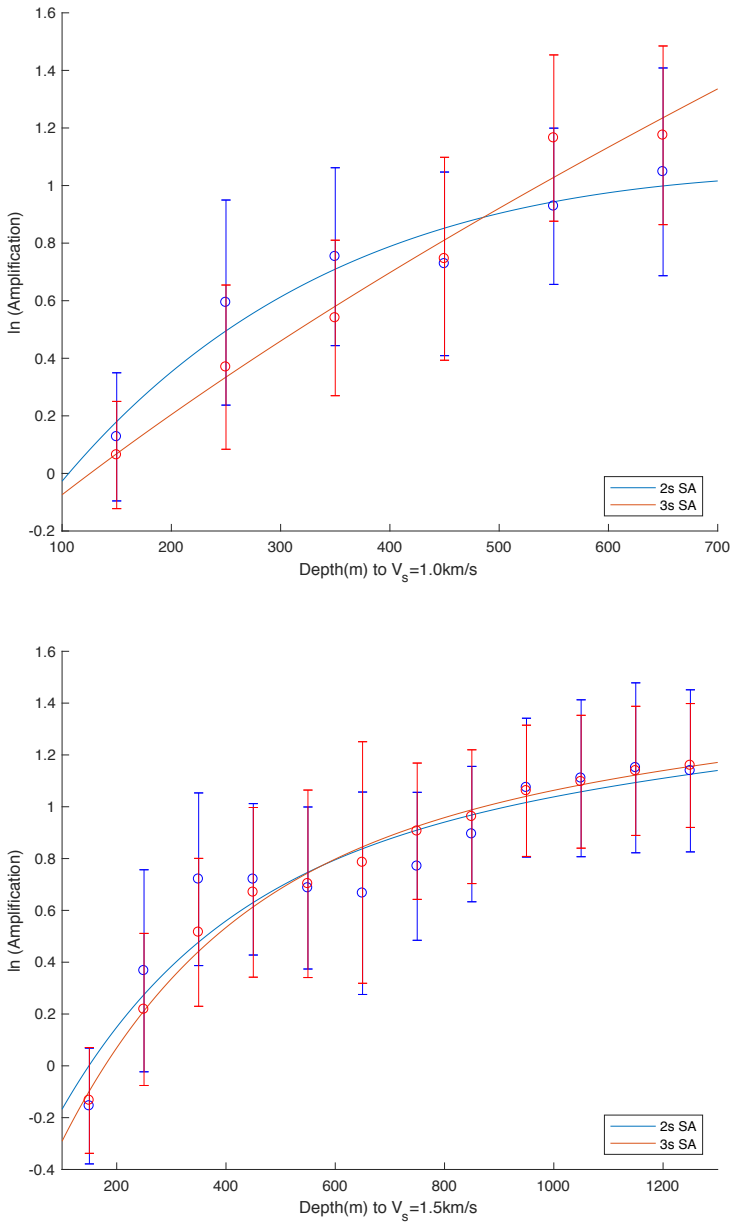

Figure 2.13: Natural log amplification factors as a function of depth to the isosurfaces of (top) Vs=1.0 km/s and (bottom) Vs=1.5 km/s, for SA-2s (blue) and SA-3s (red). The circles depict the means for the depth bins (B), the error bars are the standard deviations, and the curved lines are the regression fits.

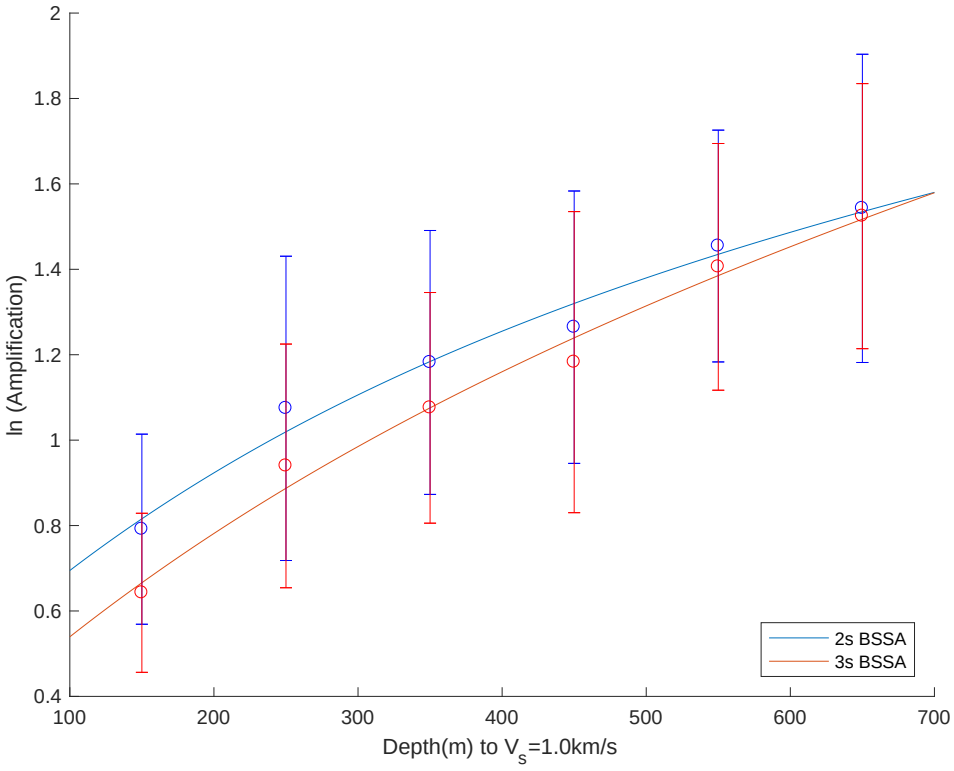

Figure 2.14: Natural log amplification factors as a function of depth to the isosurface of Vs=1.0 km/s, for BSSA14-2s (blue) and BSSA14-3s (red). The circles depict the means for the depth bins (B), the error bars are the standard deviations, and the curved lines are the regression fits.

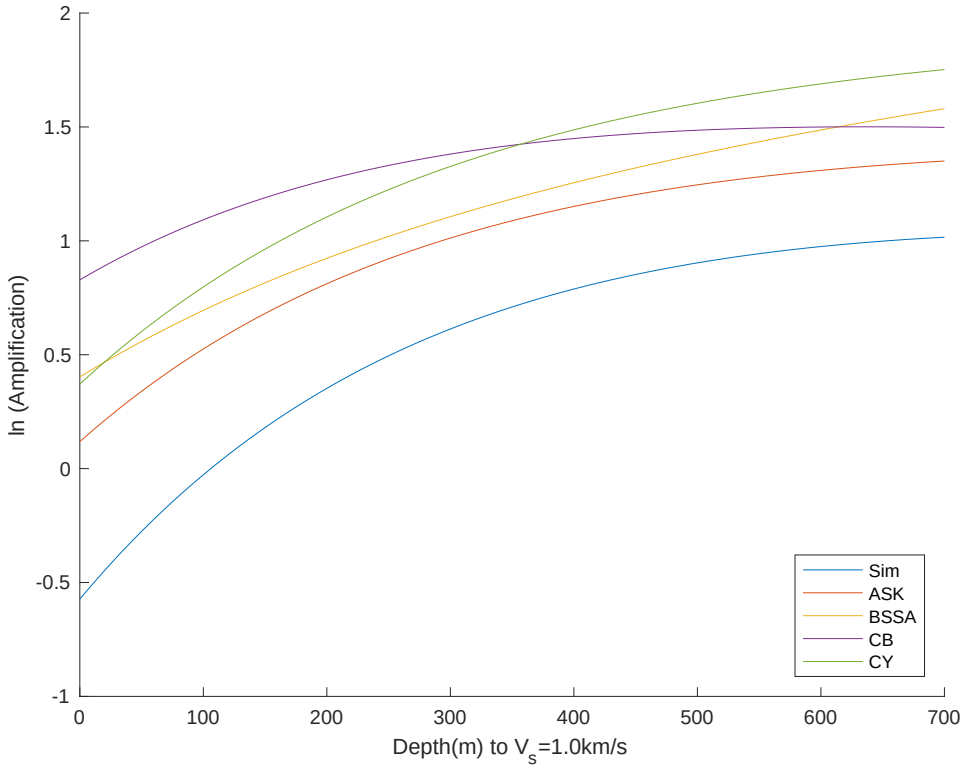

Figure 2.15: Comparison of the basin depth amplification factors regression results for 2s period from the GMPEs (ASK14, BSSA14, CB14, and CY14) to the results of the simulations (Sim).

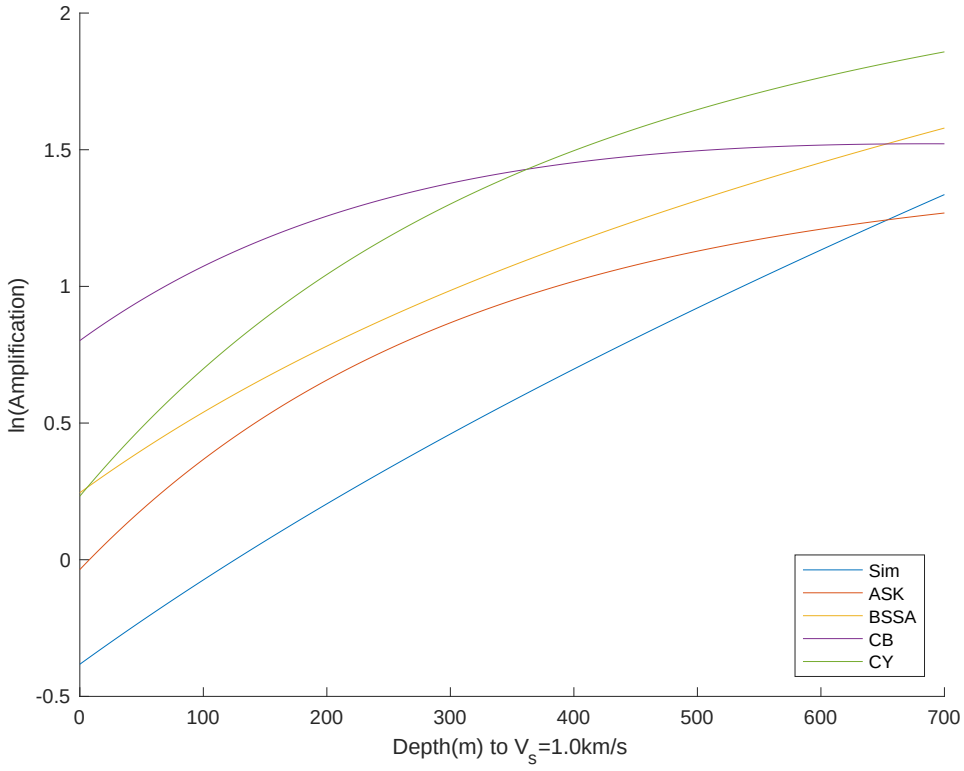

Figure 2.16: Comparison of the basin depth amplification factors regression results for 3s period from the GMPEs (ASK14, BSSA14, CB14, and CY14) to the results of the simulations (Sim).

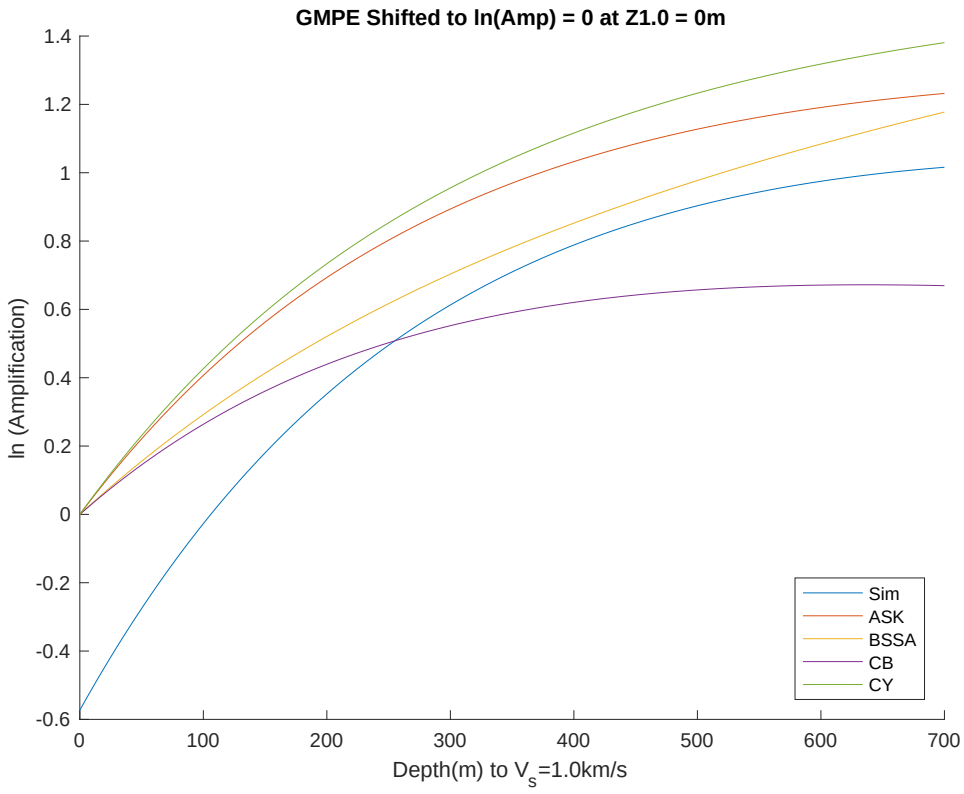

Figure 2.17: Comparison of the regression results for the basin depth amplification factors at a period of 2s from the GMPEs (ASK14, BSSA14, CB14, and CY14) to the results of the simulations (Sim). The GMPEs' regression curves are shifted to ln(Amp)=0 at a depth to the Vs=1.0 km/s isosurface of 0m.

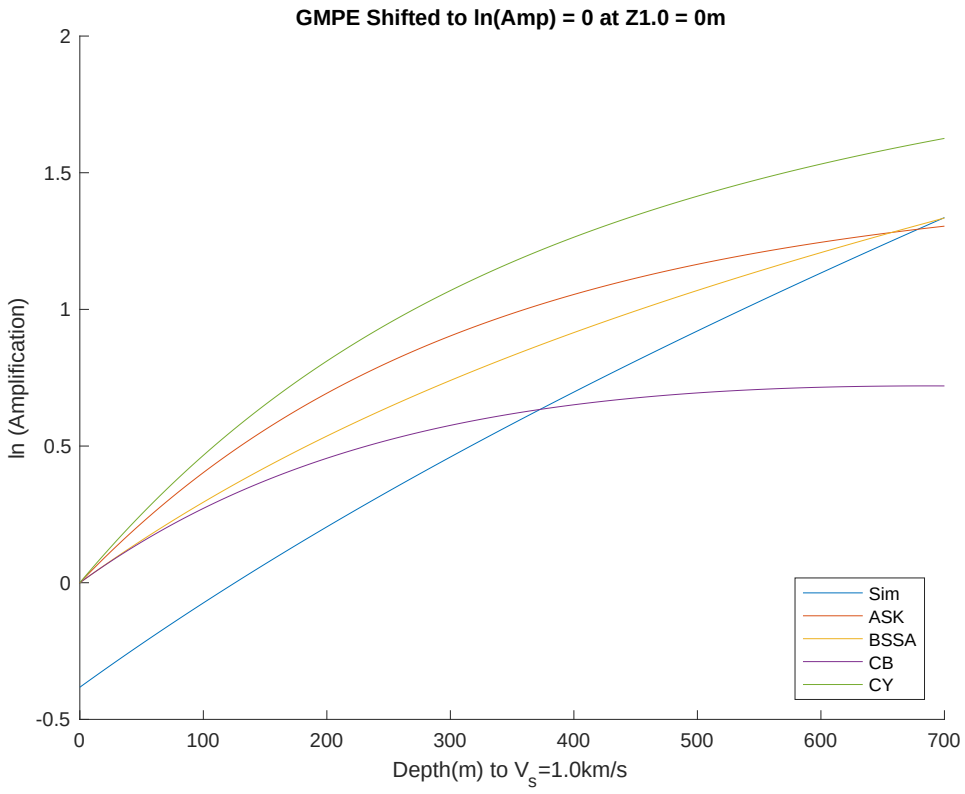

Figure 2.18: Same as Figure 2.17, but for SA-3s.

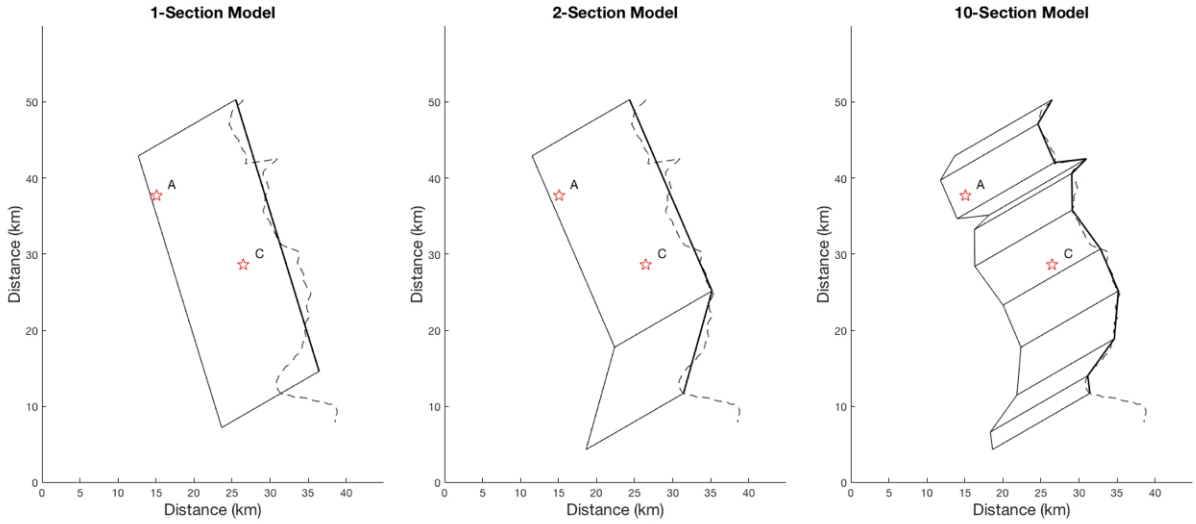

Figure 2.19: Surface projections of (left) 1-section, (middle) 2-section, and (right) 10-section WF approximation models (solid lines: boundaries of the fault segments, with the upper boundary shown in bold) used in the calculation of directivity factors with the Bayless et al. model. Red pentagons depict the epicenters for Scenarios A and C. The dashed line shows the WF fault trace from the simulations.

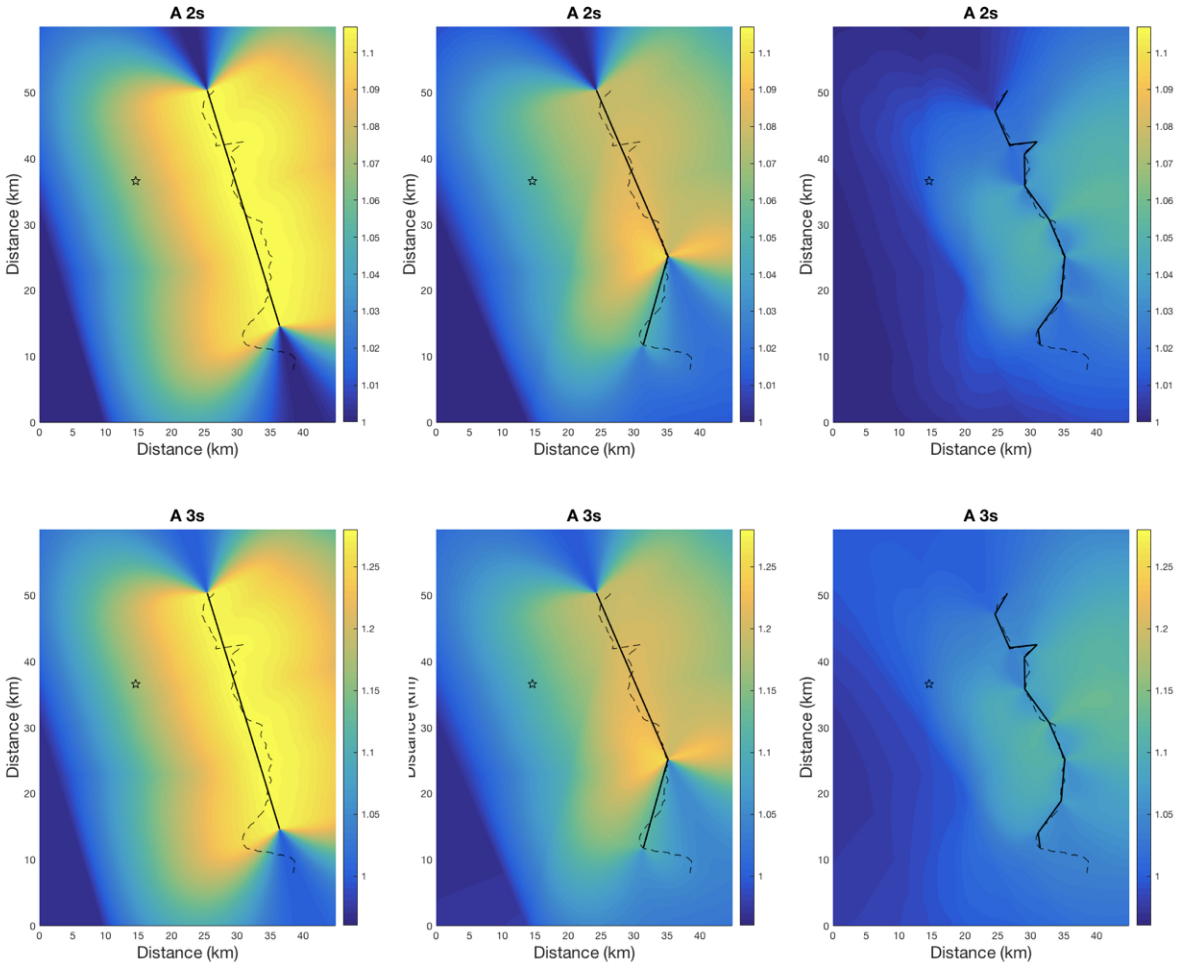

Figure 2.20: Maps of the directivity factors calculated from the (left) 1-section, 2-section (middle), and 10-section (right) WF approximation models (bold lines: segments of surface traces; dashed lines: actual WF fault trace) for scenario A at 2s period (top) and 3s period (bottom). The pentagon depicts the epicenter.

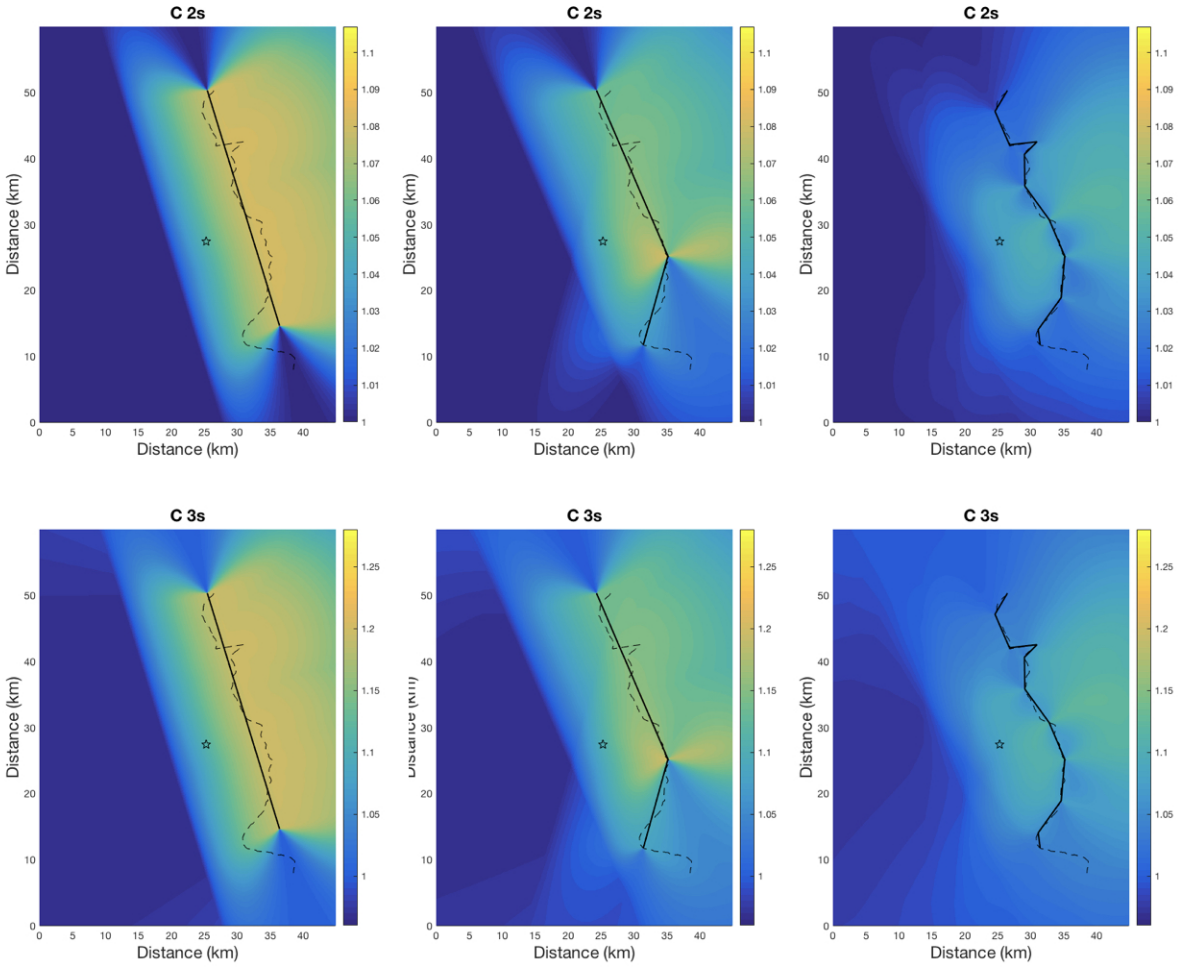

Figure 2.21: Same as Figure 2.20, but for Scenario C.

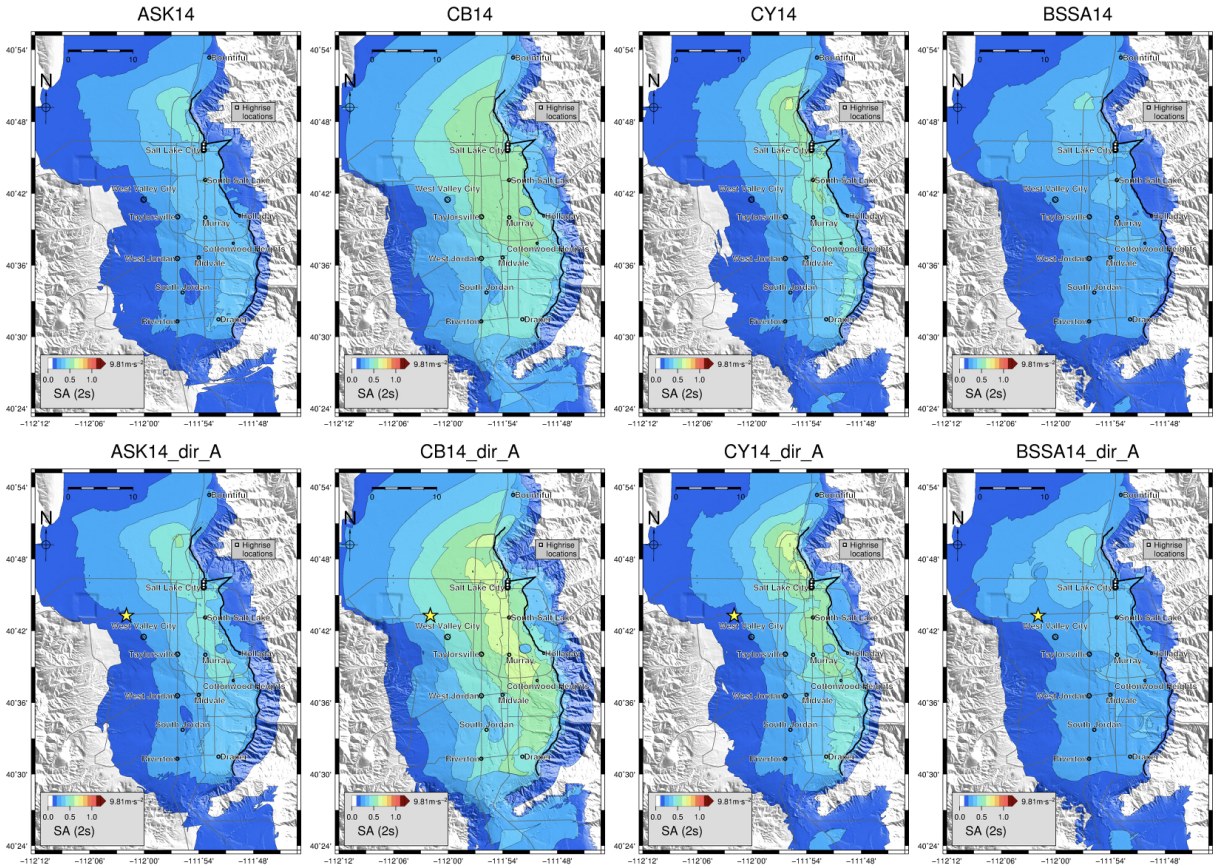

Figure 2.22: SA-2s for Scenario A. (top, from left to right) ASK14, CB14, CY14, and BSSA14 (bottom, from left to right). ASK14_dir, which is ASK14 modified with directivity factors from Bayless and Somerville (2013), CB14_dir, CY14_dir, and BSSA14_dir. All of the GMPE predictions are for the 3D model. The star depicts the epicenter, the bold line the fault surface trace.

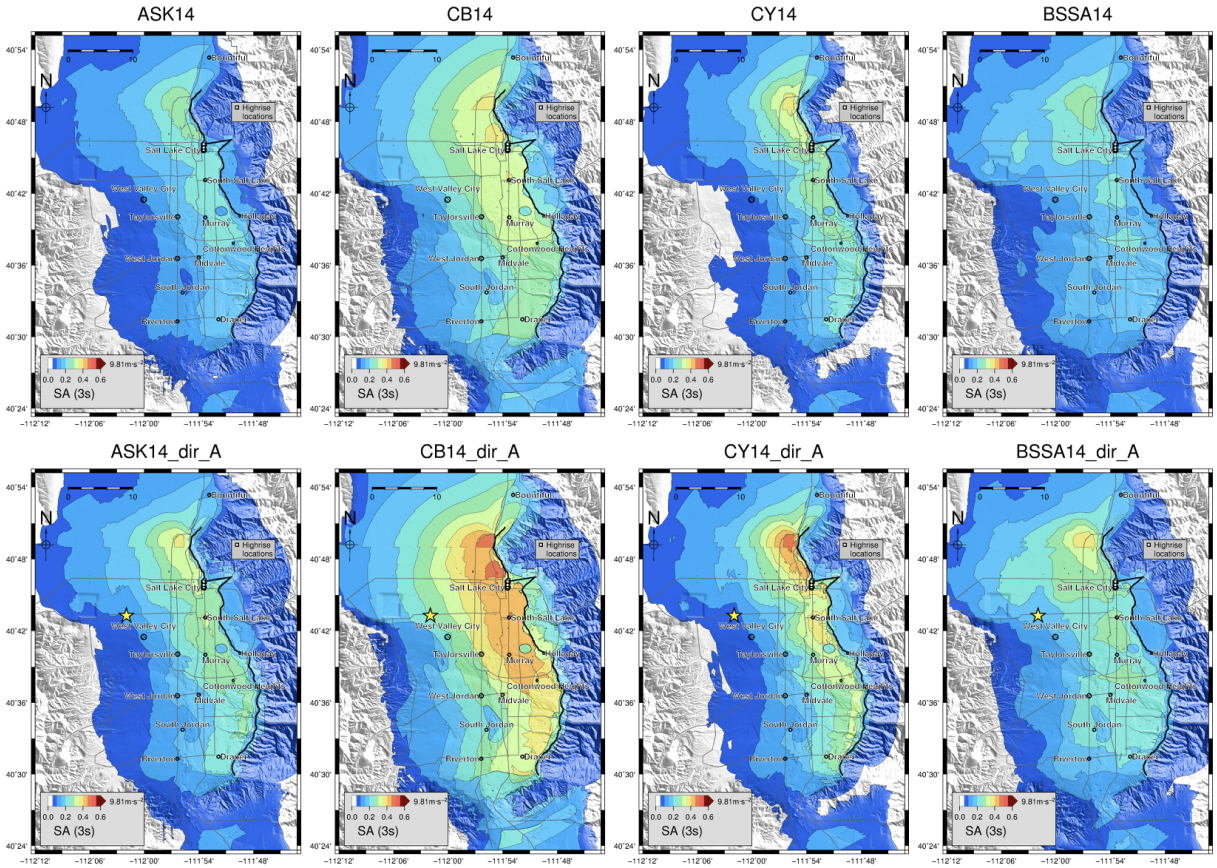

Figure 2.23: Same as Figure 2.22, but for SA-3s.

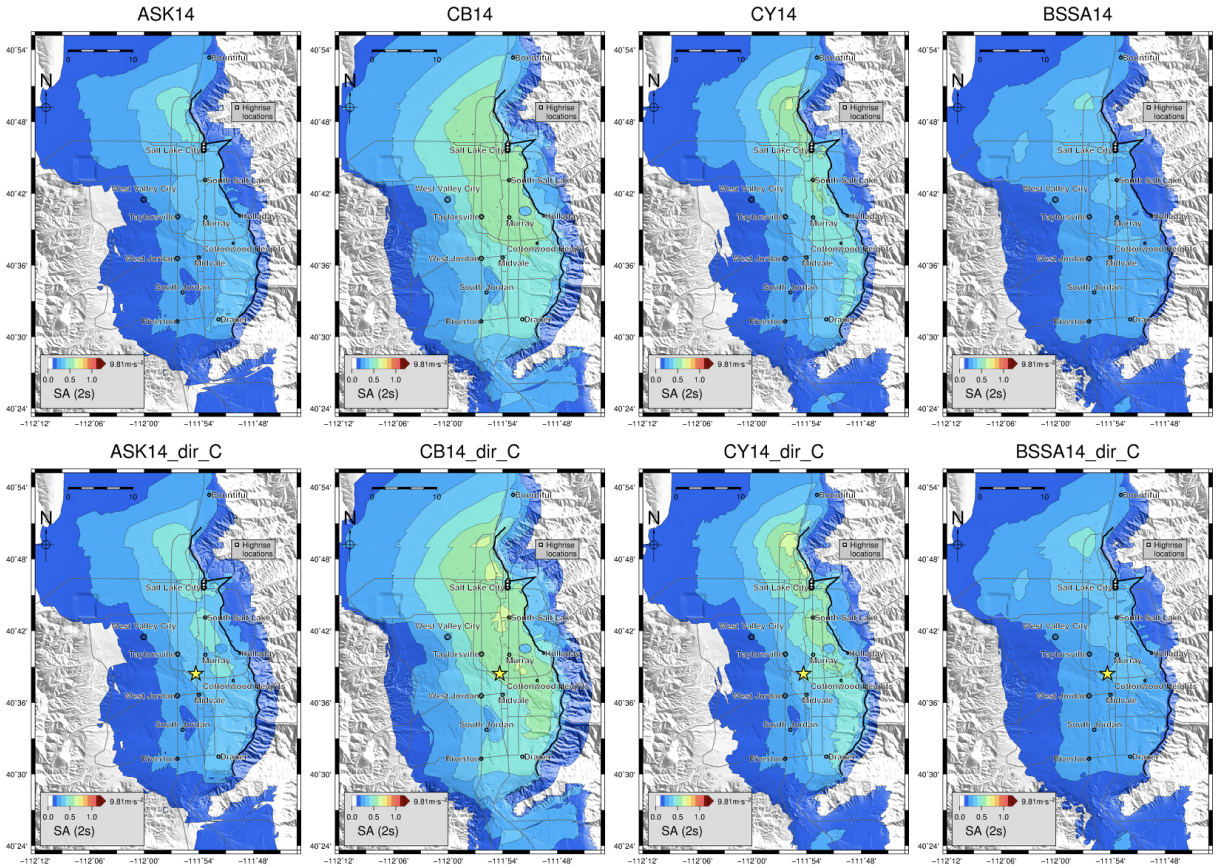

Figure 2.24: Same as Figure 2.22, but for Scenario C.

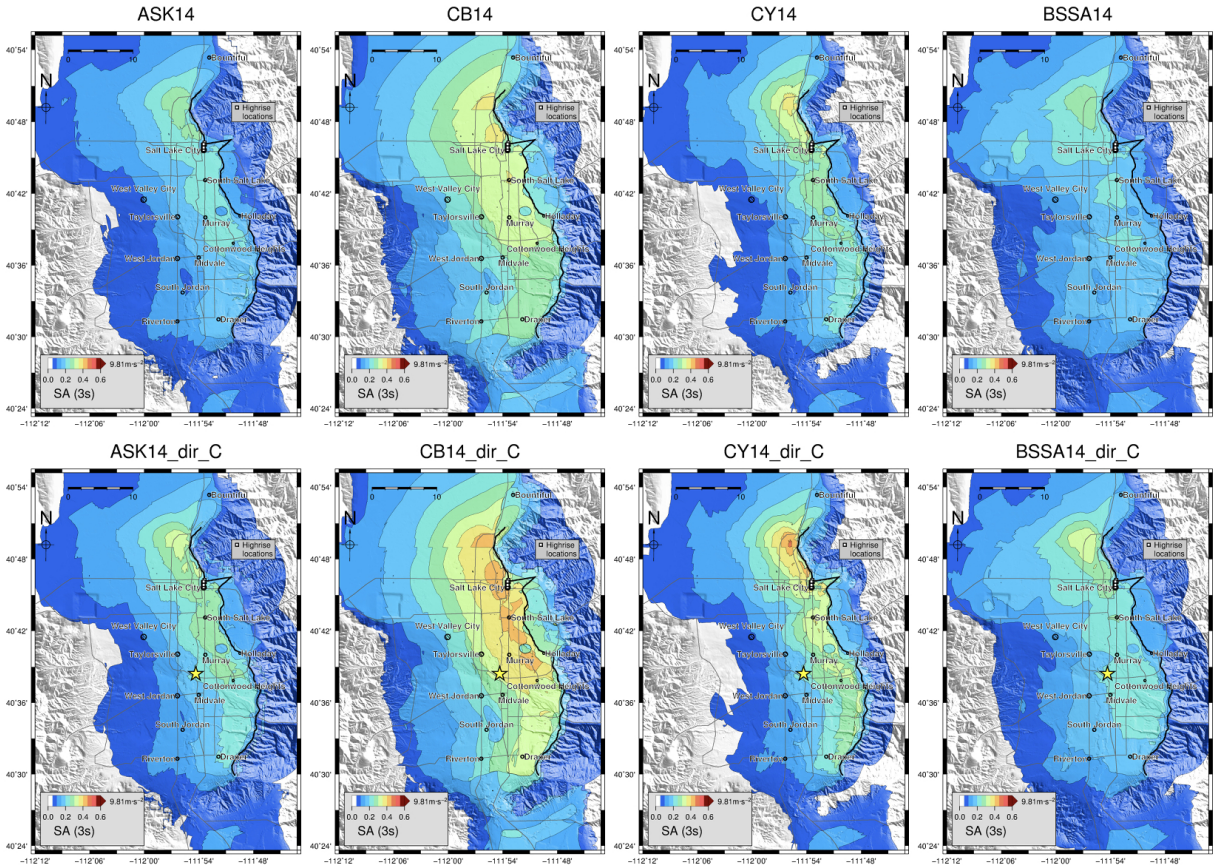

Figure 2.25: Same as Figure 2.23, but for Scenario C.

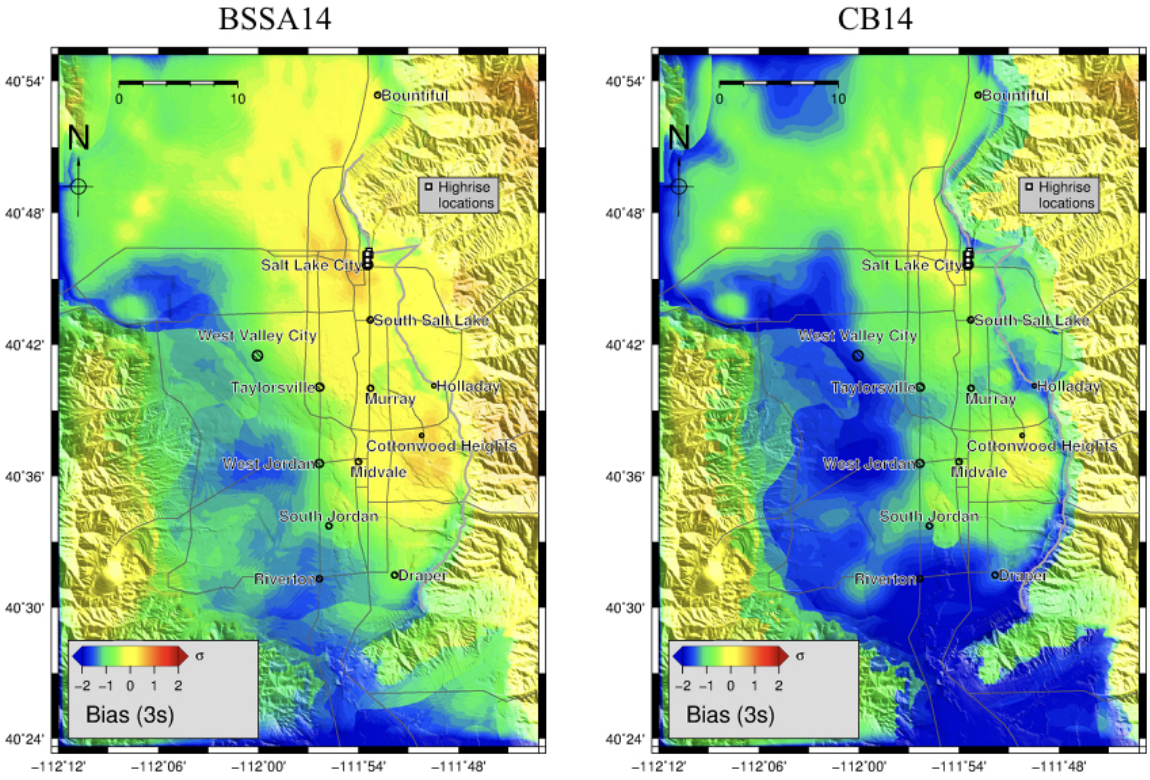

Figure 2.26: Bias between the ensemble of SA-3s(3D) with (left) BSSA14 and (right) CB14.

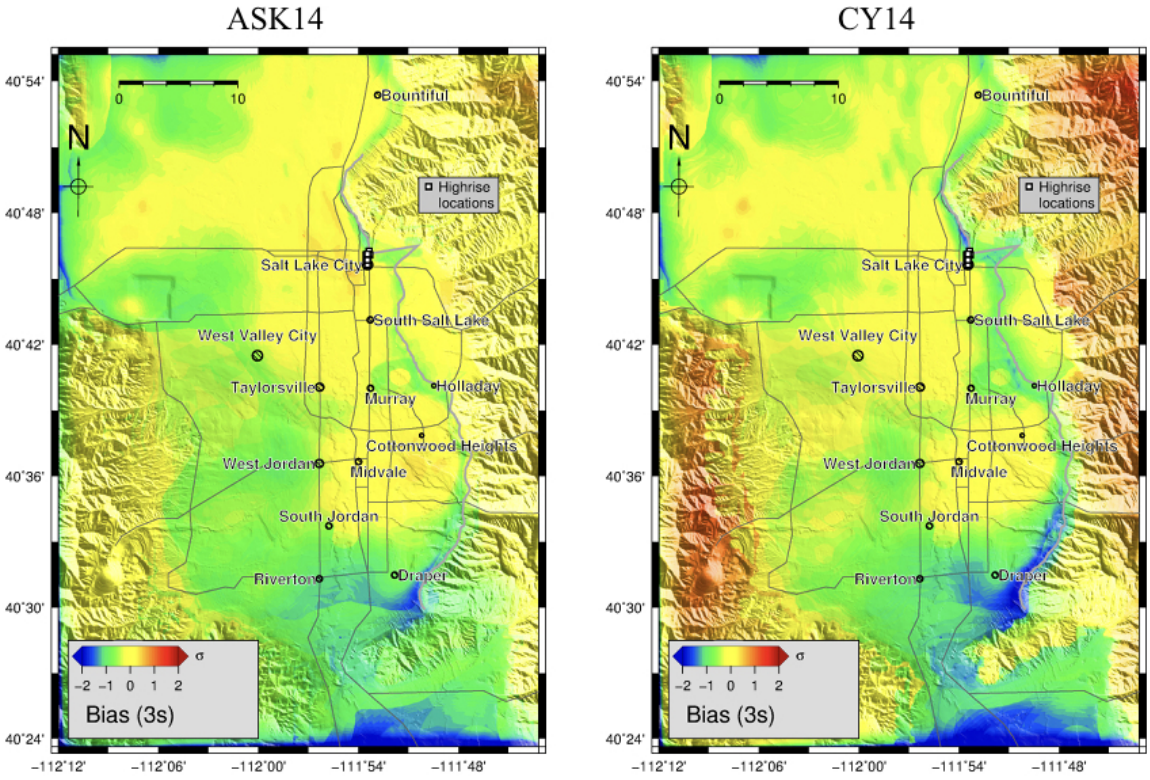

Figure 2.27: Bias between the ensemble of SA-3s(3D) with (left) ASK14 and (right) CY14.

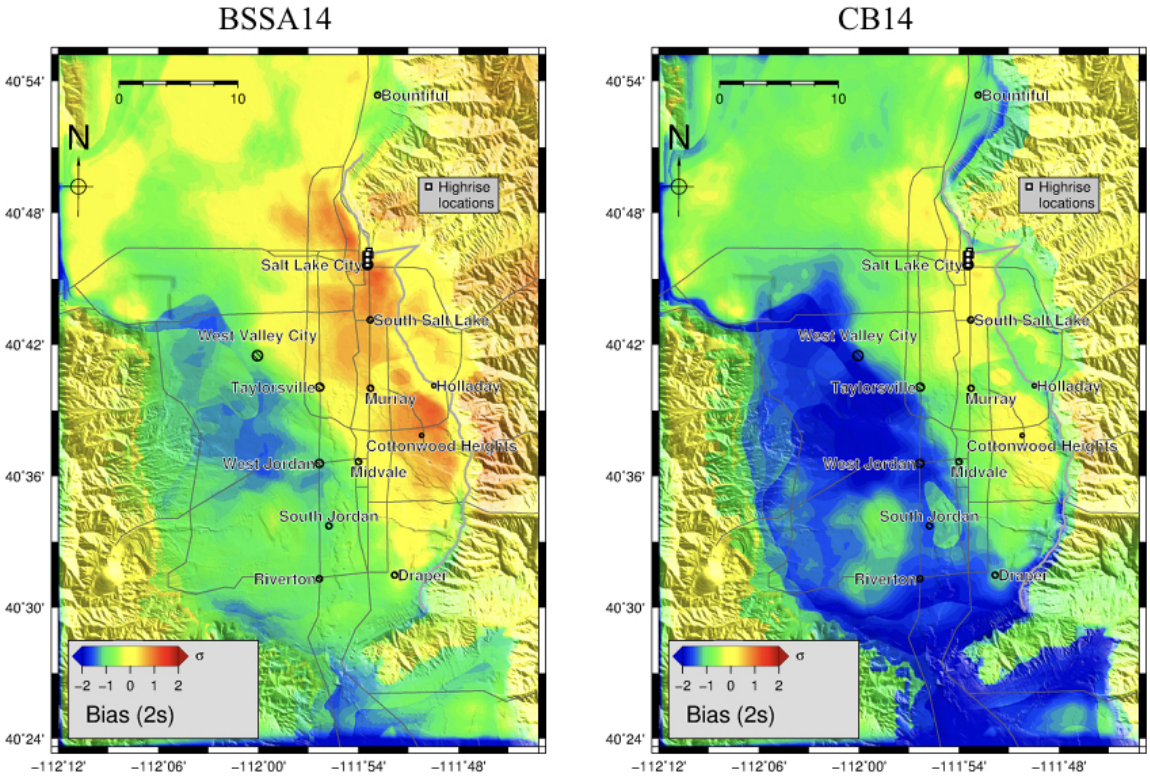

Figure 2.28: Bias between the ensemble of SA-2s(3D) with (left) BSSA14 and (right) CB14.

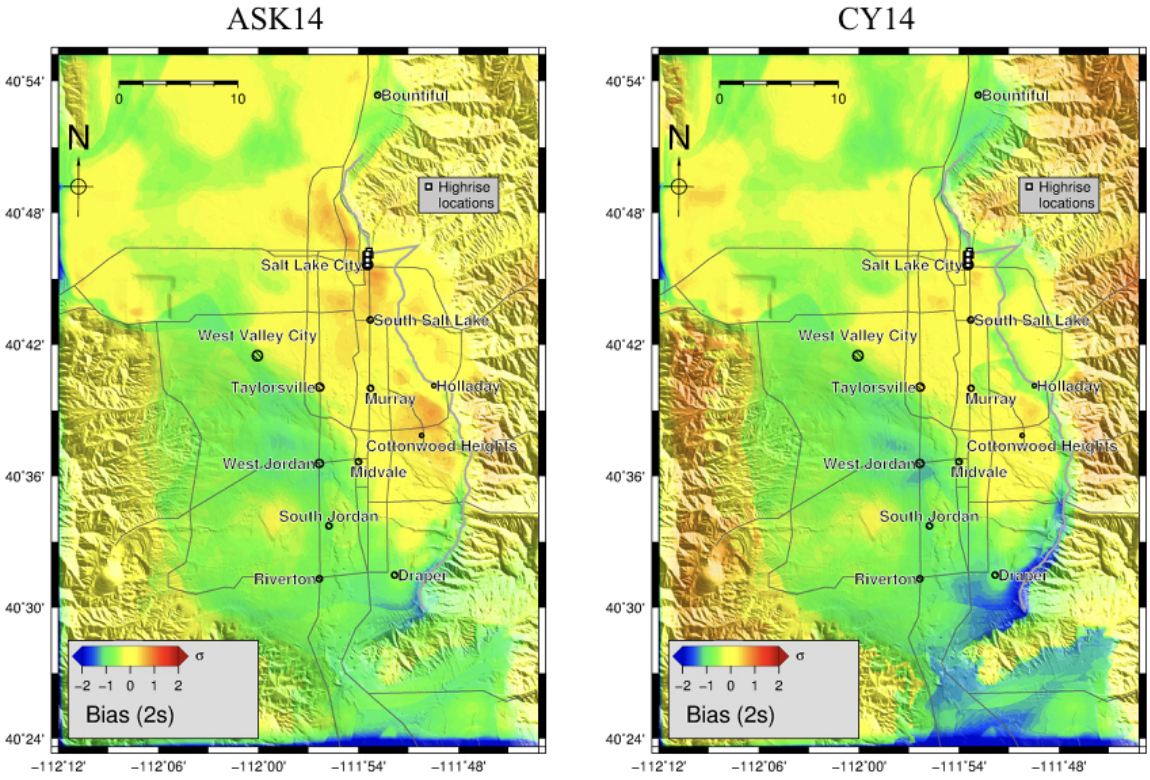

Figure 2.29: Bias between the ensemble of SA-2s(3D) with (left) ASK14 and (right) CY14.

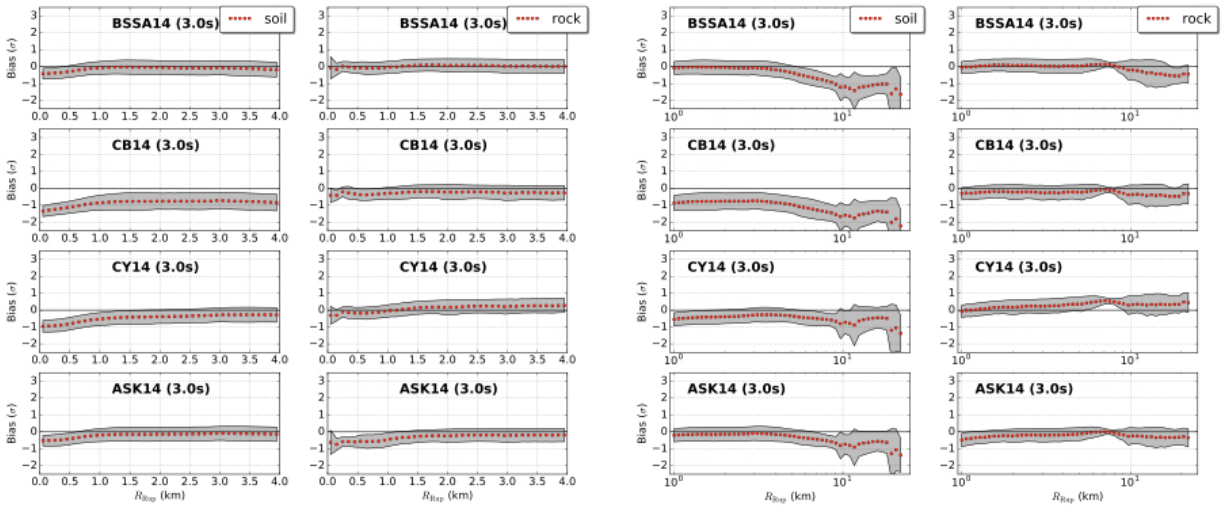

Figure 2.30: Bias between the 6-scenario ensemble of SA-3s(3D) and four leading NGA-West2 GMPEs for soil sites (Vs30 $<$ 750m/s) and rock sites (Vs30 $>$ 750 m/s) as indicated. Note the difference in distance scales between the plots on the left and right sides. The shaded areas show the standard deviations of the residuals.

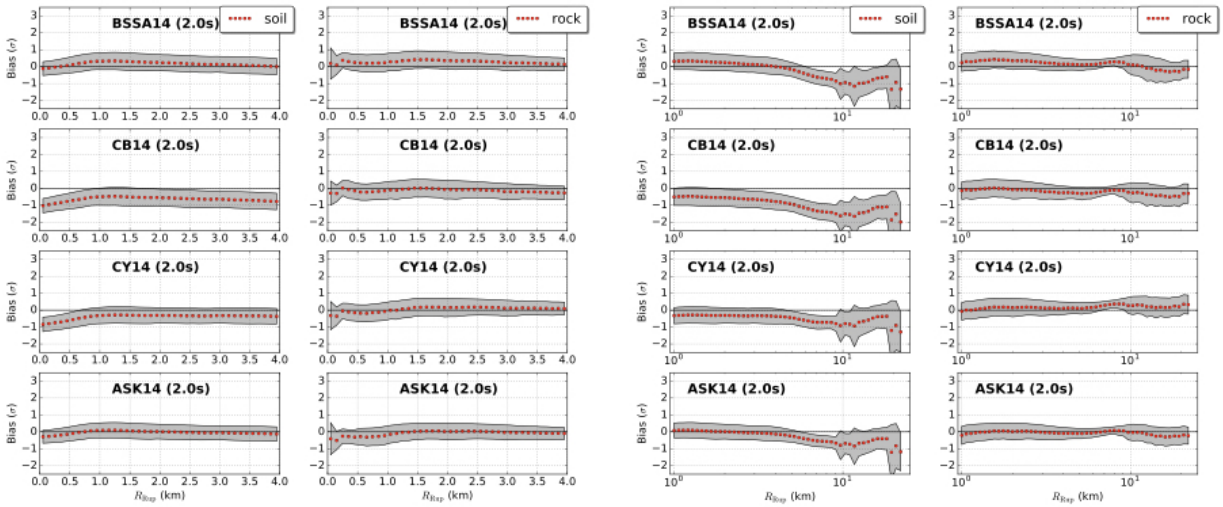

Figure 2.31: Same as Figure 2.30, but for SA-2s.

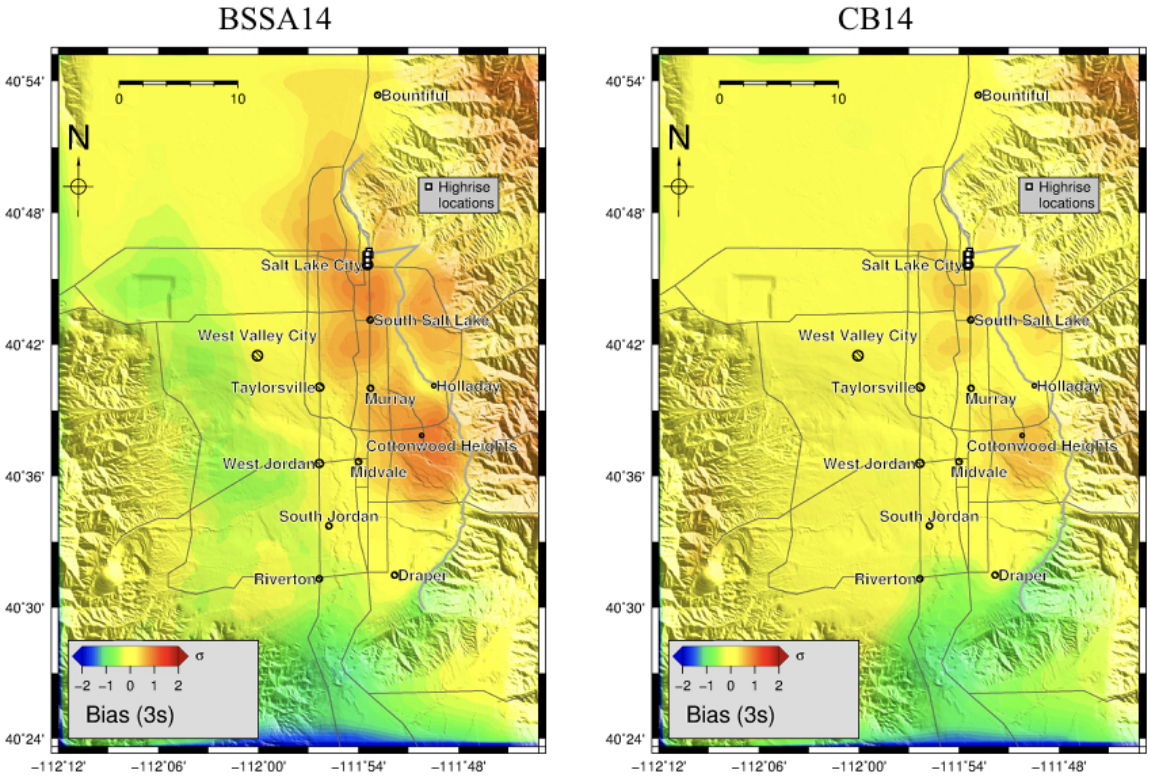

Figure 2.32: Bias between the ensemble of SA-3s(1D) with (left) BSSA14 and (right) CB14.

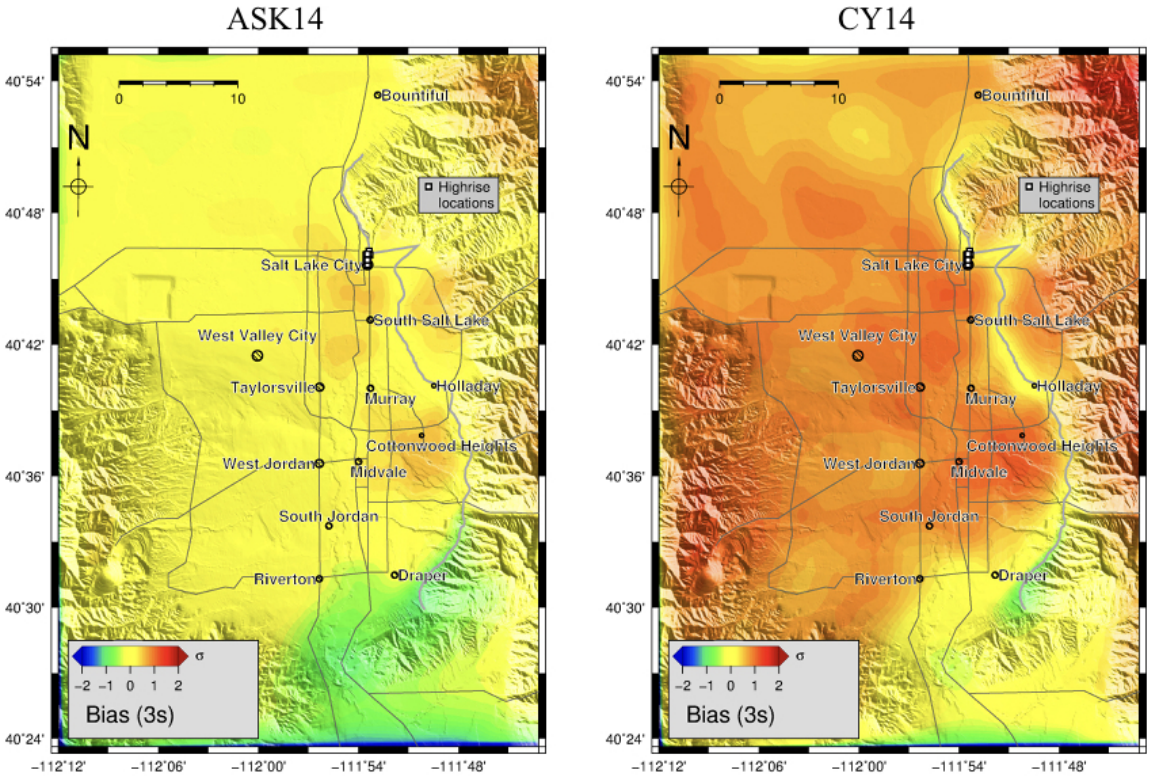

Figure 2.33: Bias between the ensemble of SA-3s(1D) with (left) ASK14 and (right) CY14.

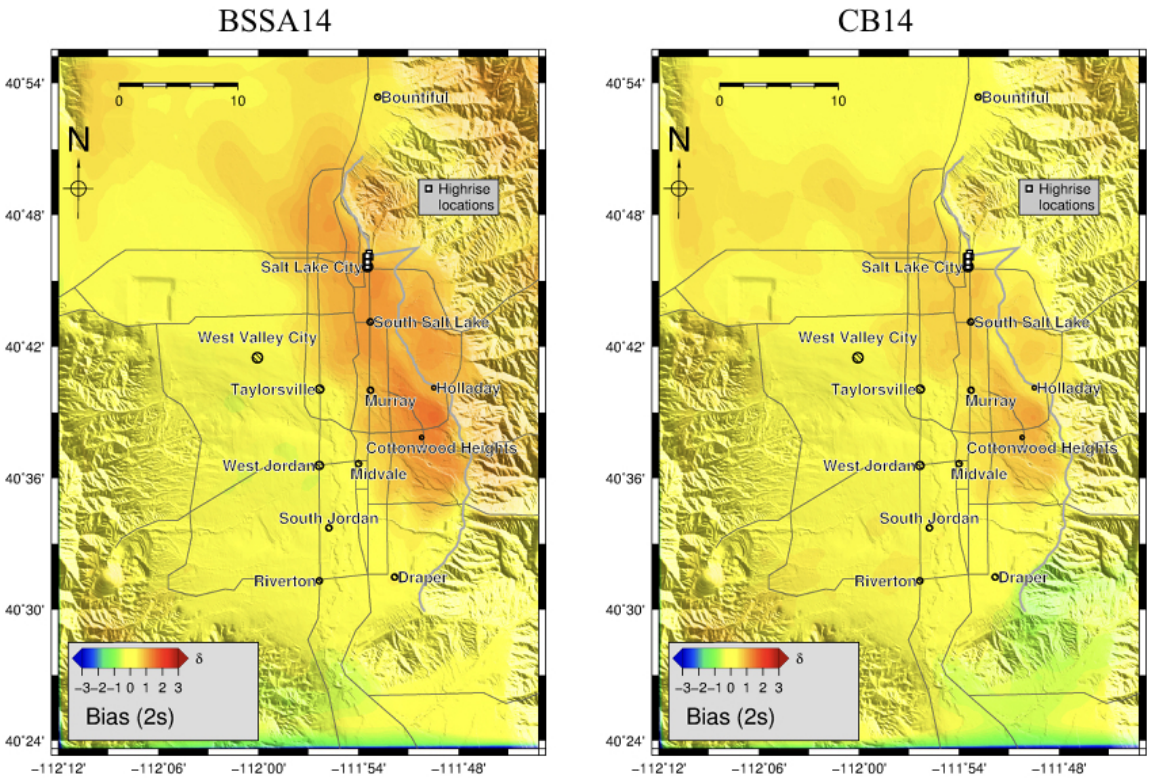

Figure 2.34: Bias between the ensemble of SA-2s(1D) with (left) BSSA14 and (right) CB14.

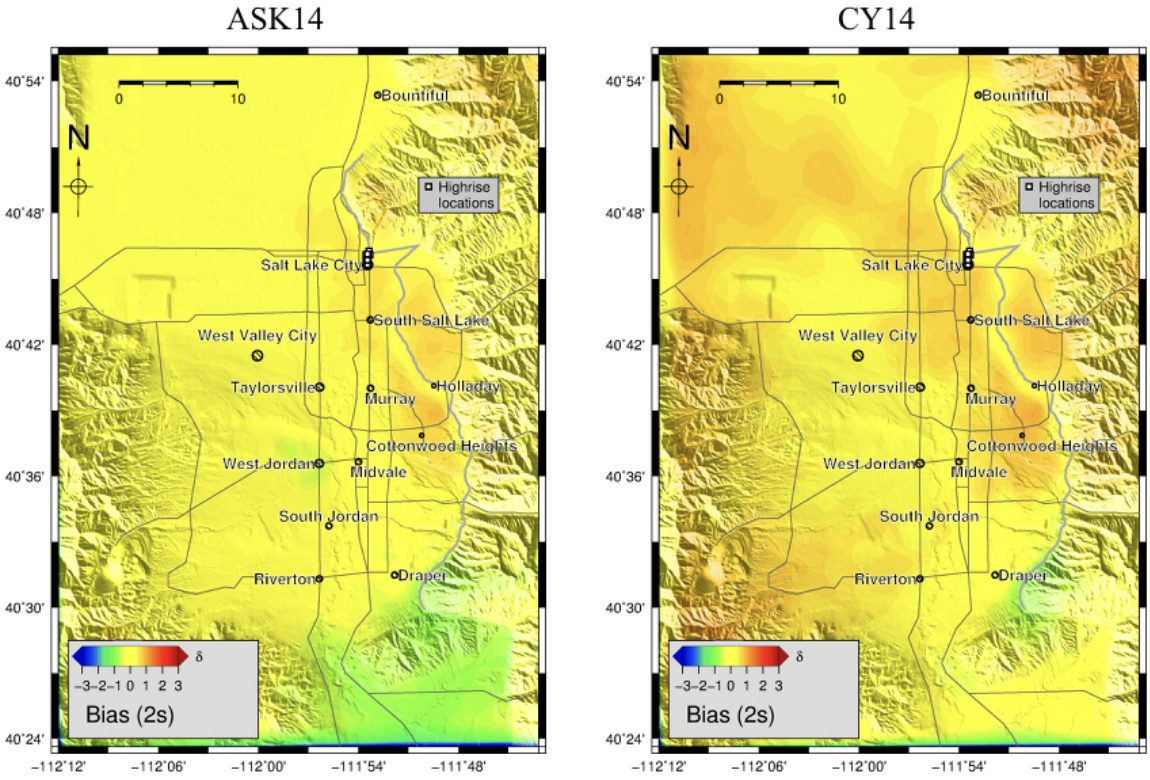

Figure 2.35: Bias between the ensemble of SA-2s(1D) with (left) ASK14 and (right) CY14.

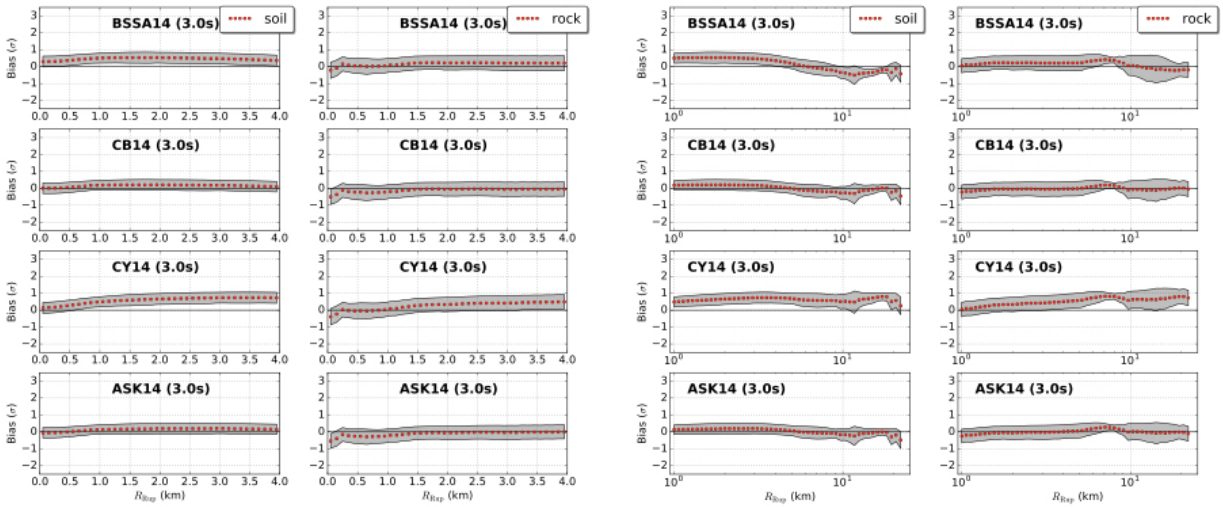

Figure 2.36: Bias between the 6-scenario ensemble of SA-3s(1D) and four leading NGA-West2 GMPEs for soil sites (Vs30 $<$ 750m/s) and rock sites (Vs30 $>$ 750 m/s) in the 3D model, as indicated. Note the difference in distance scales between the plots on the left and right sides. The shaded areas show the standard deviations of the residuals.

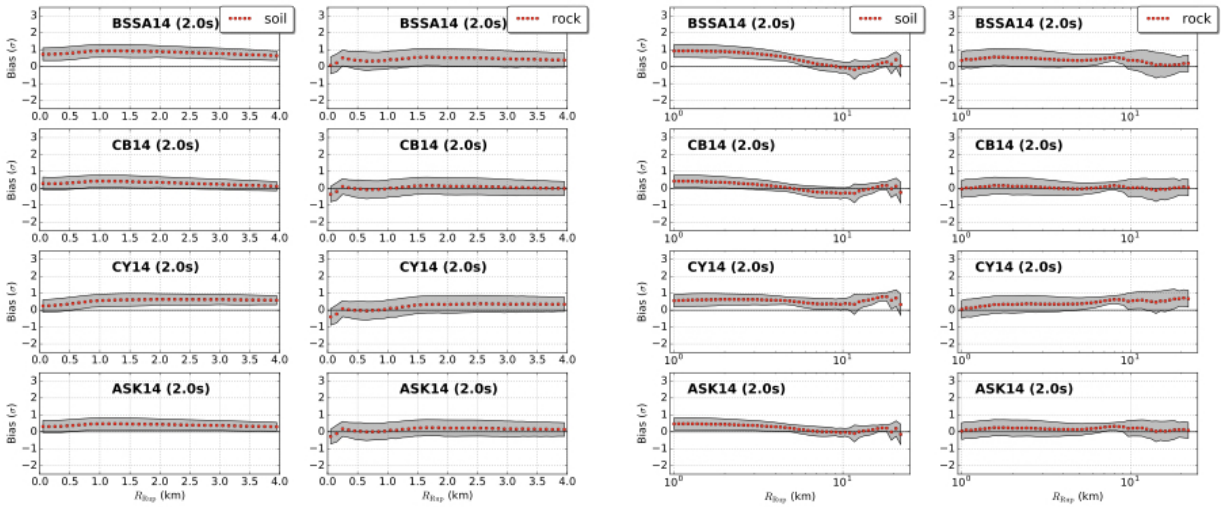

Figure 2.37: Same as Figure 2.36, but for SA-2s.

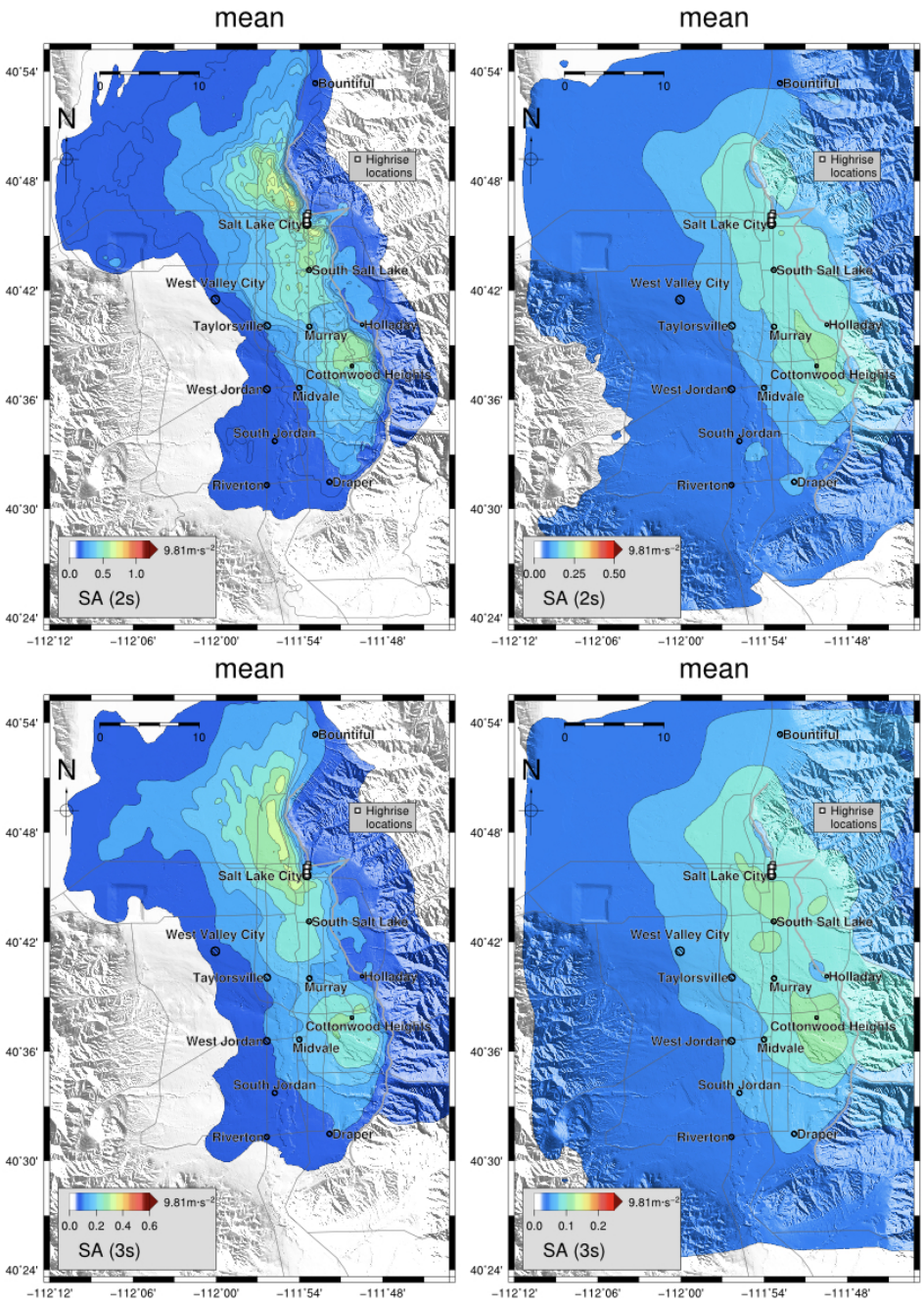

Figure 2.38: Maps of the geometric mean (top) SA-2s and (bottom) SA-3s values for the six scenarios in the (left) 3D WFCVM model and (right) 1D rock model. The bold grey line depicts the fault surface trace.

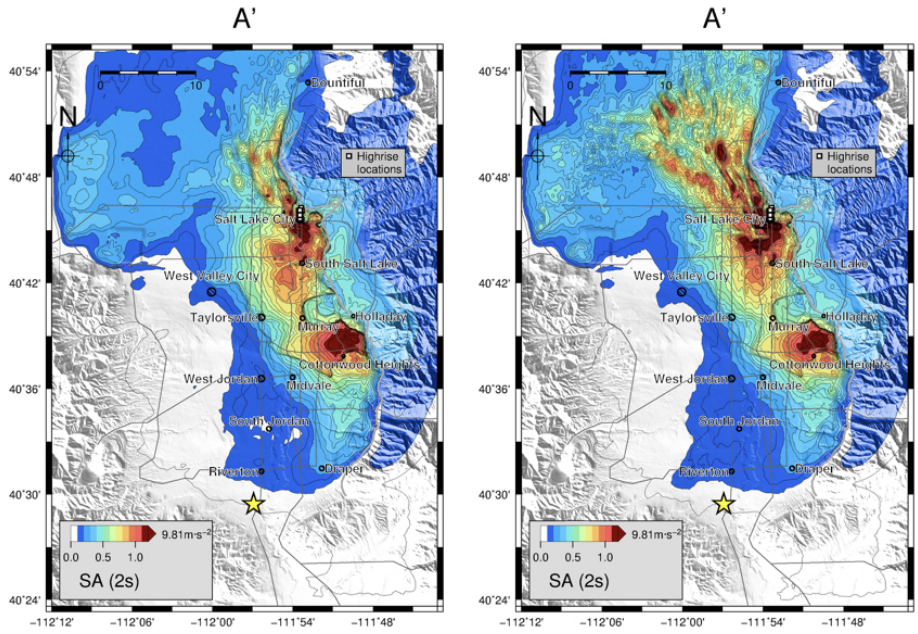

Figure 2.39: Comparison of SA-2s distributions for scenario A', calculated using (left) the Brocher (2006) Q relations as in Roten et al. (2006) and right, Qs=0.1Vs (Vs in km/s) and Qp=2Qs.

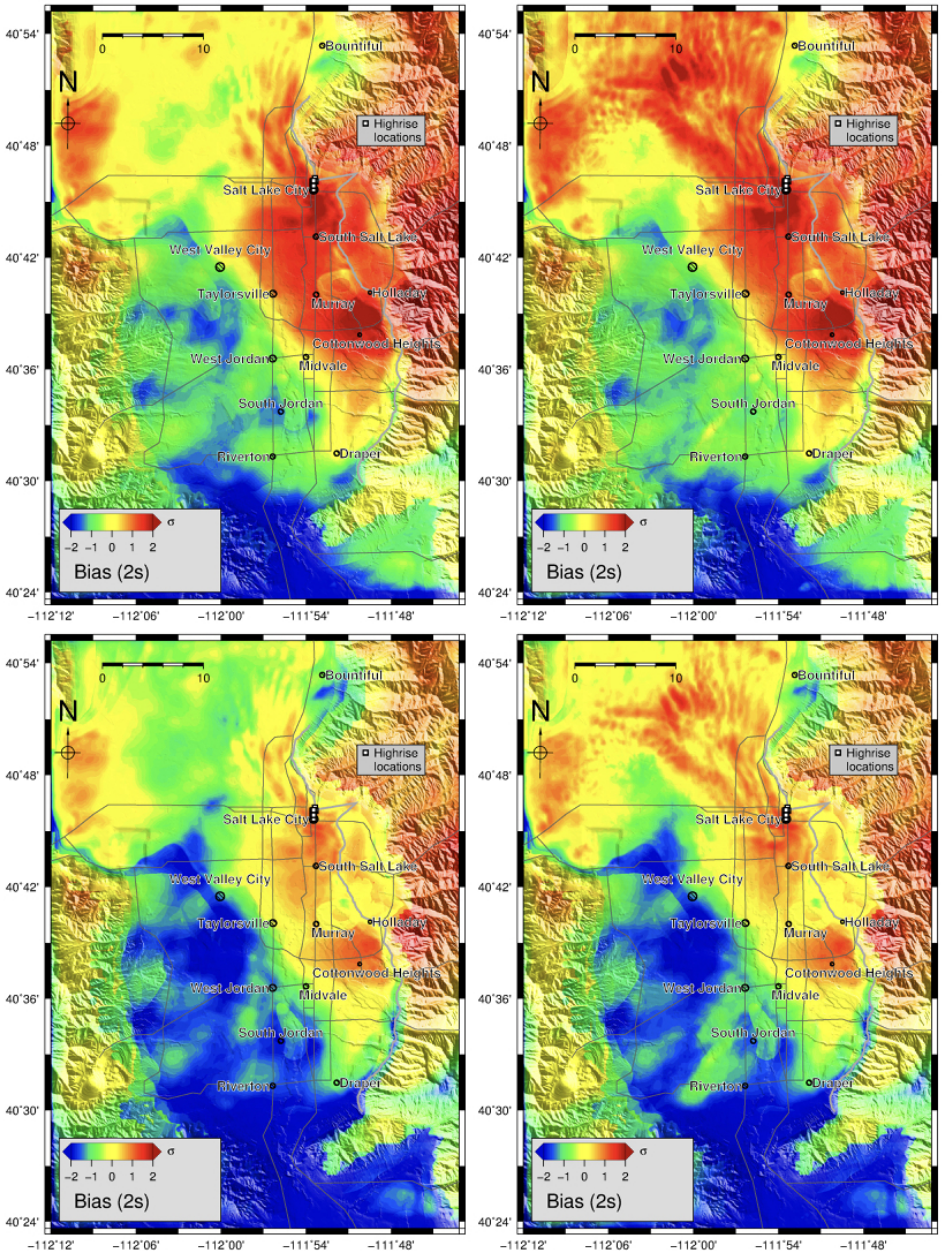

Figure 2.40: Comparison of bias between SA-2s distributions for scenario A' relative to (top) BSSA14 and (bottom) CB14, calculated using (left) the Brocher (2006) Q relations as in Roten et al. (2006) and right, Qs=0.1Vs (Vs in km/s) and Qp=2Qs.

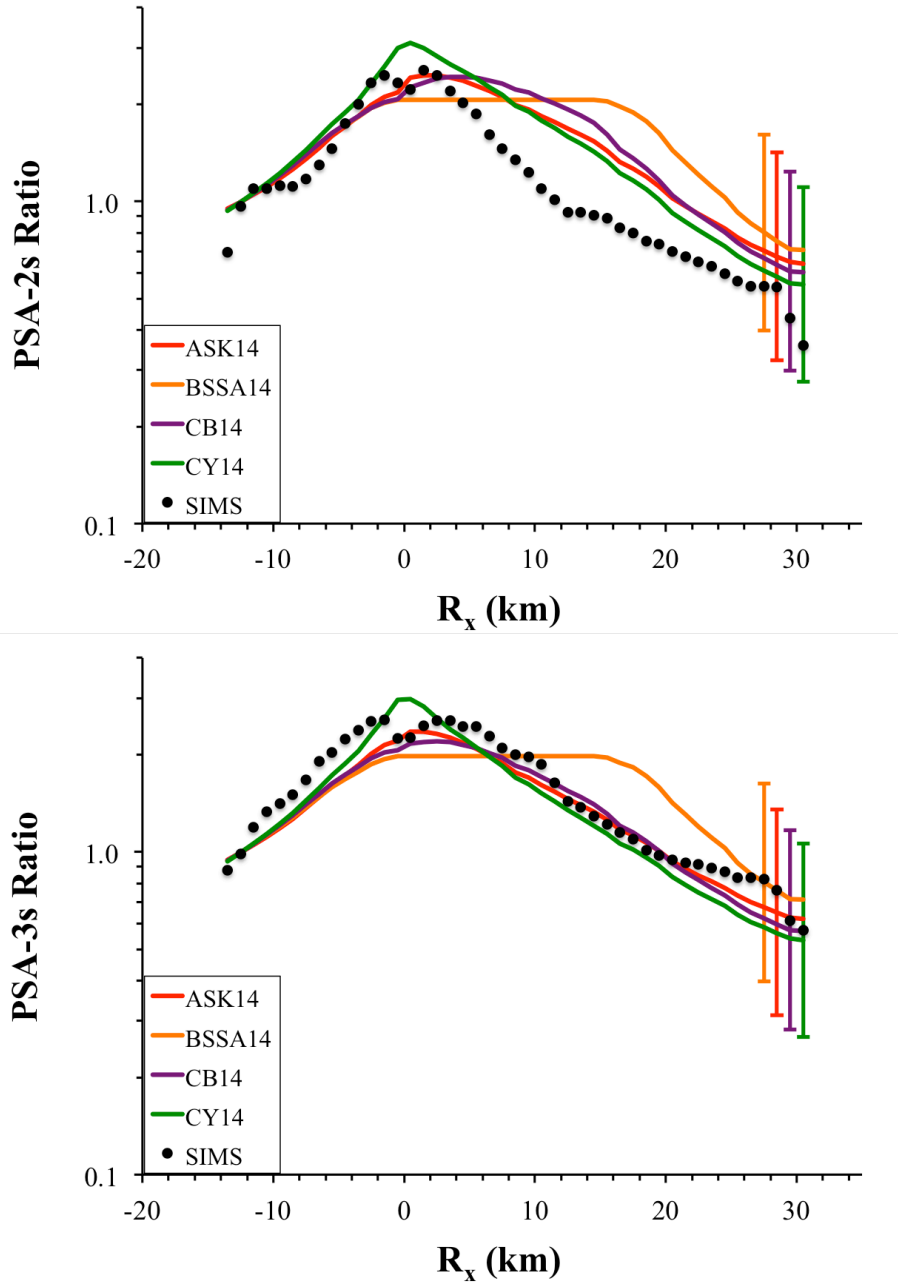

Figure 2.41: Comparison of geometric mean (top) SA-2s and (bottom) SA-3s from the six scenarios (black dots) with GMPE predictions (colored lines with 1 standard deviation error bars) for sites within a 4-km-wide zone trending ENE-WSW across the rupture center. Rx is horizontal distance from the top of the rupture, measured perpendicular to its strike. All SAs are normalized to 1.0 at a site where Rx = -12.2 km. The results plotted are geometric means for 1km Rx bins.

Chapter 3

Signatures of Seismic Waveguides in Los Angeles from Numerical Simulations and Noise Cross Correlations

Waveguides are confined geological units capable of channeling and focusing seismic energy over long distances. In the Los Angeles (LA) area, 3D simulations (e.g., TeraShake, ShakeOut) suggest that the presence of such waveguides caused by the connectivity of the sedimentary basins (Los Angeles (LA) - San Gabriel – Chino – San Bernardino) strongly increases ground motion predictions for large, northwestward ruptures on the southern San Andreas fault (SAF, see Olsen et al., 2006; Olsen et al., 2008; Olsen et al., 2009; Jones et al., 2008; Graves et al., 2011; Day et al., 2012). However, the efficiency of the focusing and therefore the increase in ground motions due to the waveguides depend on the details of the basin structure, which may not be well-resolved in state-of-the-art velocity models for the LA area. Since the effects may have dire consequences on the population in the affected regions, validation of such waveguides is imperative.

In this study, we attempt to validate the presence of two waveguides in the LA region,

as indicated by 3D earthquake simulations, with observed data from earthquakes and ambient noise. Using over 700 temporary (nodal and broadband) and permanent (SCSN) stations as receivers, and 14 stations (located along the SAF) as virtual sources, we calculate and compare all 9 components of the correlation (over ∼40,000 correlations) and Green's function tensor. We compare the numerical and empirical surface-to-surface Green tensors for virtual sources located on the SAF. The regions of large peak motions caused by waveguide focusing in the simulations show generally good agreement with increases in the Green tensor amplitudes, supporting the presence of two separate waveguides in greater LA. Analysis of the cross terms and particle motions confirm that 0.1-0.35 Hz (∼2.5-10s) surface waves play the most important role in the waveguide focusing.

3.1 Introduction

The first large-scale simulations of earthquake wave propagation showed first-order effects of three-dimensional (3D) structural variation on ground motions (e.g., Olsen et al., 1995; Graves et al., 1998). Motivated by these results, and enabled by access to substantial computational resources on parallel supercomputers, 3D structural models were improved and constrained by a variety of geophysical and geotechnical data sources (e.g., gravity measurements, well logs, tomography). For example, Magistrale et al. (1996), Magistrale et al. (1998), Magistrale et al. (2000), Kohler et al. (2003), Süss and Shaw (2003) and Plesch et al. (2007) developed several generations of 3D velocity and density models for the greater Los Angeles area, where a large amount of data from oil exploration was available. Subsequently, these 3D velocity models underwent scrutiny by earthquake modelers comparing their theoretical ground motion predictions to seismic data from historical earthquakes (e.g., Olsen et al., 2003; Day et al., 2008), which along with updates from tomography studies has led to improved accuracy in the models.

The southern San Andreas Fault (SSAF) has produced a history of large (∼M8) earth-

quakes. Most recently, the 1857 (El Cajon) earthquake ruptured 360 km from Parkfield to Wrightwood (Weldon et al., 2004). The two segments of the San Andreas fault south of the 1857 rupture have not produced a major event since 1812, with the southernmost section dormant since about 1690 (Weldon et al., 2004). Considering an average recurrence interval for large earthquakes with surface rupture on these segments of 150-220 years, the SSAF accounts for a major component of the seismic hazard in southern California and northern Mexico.

The uncertainty in ground motion levels expected from a large-magnitude earthquake on the SSAF due to lack of seismic records of such events motivated the large-scale simulation project TeraShake within the Southern California Earthquake Center (SCEC). The TeraShake simulations of M7.7 SSAF scenarios revealed a surprisingly order-of-magnitude larger ground motion levels from the SE-NW ruptures, as compared to NW-SE directions. Olsen et al. (2006) showed that the directional effects on the ground motion was caused by an interconnected series of sedimentary basins (Los Angeles - San Gabriel – Chino – San Bernardino), channeling large-amplitude surface waves into the Los Angeles area. Two branches of waveguide focusing were identified in the simulations - the most efficient branch aligned just south of the San Gabriel Mts with a weaker channel further south along the southern edge of the Chino Basin (see Figure 3.1). This waveguide focusing was later reproduced in the ShakeOut simulations of M7.8 scenarios on the SSAF (Jones et al., 2008; Graves et al., 2008; Olsen et al., 2009).

The efficiency in waveguide focusing depends on the accuracy of the basin structure in the velocity models, where simulations indicate that relatively small perturbations in the connectivity of the sedimentary basins can significantly affect the increase in ground motions from surface wave channeling (Graves, 2013). Thus, despite the large amounts of data constraints in the 3D greater LA basin velocity model, the theoretical predictions of waveguide ground motion amplification are relatively uncertain, and constraints from data is critically needed for their use in seismic hazard analysis.

While no seismic data exist for large historical events on the SSAF, ocean-atmospheric

interactions provide an alternative source of excitation of the solid Earth. Observations of random, low amplitude seismic waves on seismic sensors - seismic "noise" - can provide an estimate of the seismic response of the subsurface, without the need to know the details of the crustal structure. This noise is cross-correlated between seismic sensors over periods of days to months to obtain travel times between (surface) sensors that can be used to generate estimates of the nine components of the Green's functions (impulse response, e.g., Lobkis and Weaver, 2001; Larose et al., 2007; Cupillard and Capdeville, 2010; Prieto et al., 2011; Kwak et al., 2017). A similar procedure can be applied to simulated ground motions, thus facilitating a comparison of theoretical and empirical Green's functions (e.g., Prieto and Beroza, 2008; Denolle et al., 2013; Denolle et al., 2014; Viens et al., 2015).

Until recently, the seismic instrumentation of the region affected by the proposed waveguides was inadequate to provide data for validation of the proposed seismic waveguides in LA. To improve the data constraints a large collaborative effort was initiated, resulting in a large-scale deployment of instruments along 9 profiles in the LA area (see Figure 3.2). In this study, we attempt to validate the presence of the two proposed waveguides in the LA region, as indicated by 3D earthquake simulations, with observed data from ambient noise. Using over 700 temporary (nodal and broadband) and permanent (SCSN) stations as receivers, and 14 stations (located along the SAF) as virtual sources, we calculate all 9 components of the Green's function tensor using over $\sim$40,000 correlations. We then compare the numerical and empirical surface-to-surface Green tensors for virtual sources located on the SAF, to validate the presence of the waveguides found in the simulations.

3.2 Data Collection

The BASIN (Basin Amplification Seismic Investigation) project is part of a multi-institution, multi-year effort. Every member of the BASIN group participated in the experiments:

field, structural, observational and theoretical seismologists teamed up to deploy and recover the instruments. The experiment collected continuous data from 709 3-components (3C) nodes and 23 broadband stations. The nodes recorded for up to 40 days (limitation due to the battery life) while the broadband instruments recorded for 5 months. The deployment was staged in multiple phases: SB4 [February 2017], SG1 and SG2 [February-March 2017]; the broadband stations and SB2, SB3 were deployed in August 2018; SG3, SG4, SB5 were deployed May-June 2018; finally, SB1 was deployed in November 2019 (see Figure 3.2). The size of the total data set, resampled to 40Hz reaches 3TB of data.

3.3 Numerical Simulation of Wave Propagation

The SCEC Community Velocity Model (CVM-S) version 4.26 was used to generate our simulations of Green's tensors. Ground motion simulations using small earthquakes confirm the validity of the CVM-S4.26 (Lee et al., 2014; Lee and Chen, 2016; Taborda et al., 2016; Savran and Olsen, 2019). To compute the Green's functions directly in the velocity structure, we apply a Gaussian force at the source:

$$g = M \frac{1}{\sqrt{2\pi}\sigma} \exp\left(-\frac{(t-4\sigma)^2}{2\sigma^2}\right), \tag{3.1}$$

where $\sigma = 0.5$ is the spread of the Gaussian and determines its bandwidth, and $M = 10^{16}$. The 4σ is present to minimize the amplitude step at time zero. We compute all nine components of the Green's tensor by applying the force in three directions (x: East-West, y: North-South, z: Up-Down). Our simulations cover 200 seconds of wave propagation with a maximum frequency of 1 Hz in the model domain shown in Figure 3.2. We chose the minimum shear wave speed as 500 m/s and discretize the simulation domain with dx = 75 m to resolve the smallest wavelength with 6 grid points using the 4th order staggered-grid finite-difference solution AWP-ODC (Cui et al.,

2013) including topography enabled by curvilinear grids (O'Reilly et al., 2019). The simulations used a 4,464 by 4,224 by 530 mesh, dividing the volume into about 10 billion cubes. Each simulation required approximately 2 hours of wall-time using 144 GPUs on ORNL SUMMIT. Table 3.1 summarizes the simulation parameters used in this study. 14 stations (located along the SAF, see Figure 3.2) were used as sources in our simulations, leading to a total number of 126 simulations. Table 3.2 summarizes the latitudes and longitudes of the source locations.

Figure 3.3 provides a 3D visualization of the isosurface for a shear wave velocity (Vs) of 2 km/s from CVM-S4.26, illustrating the connectivity of the sedimentary basins (Los Angeles - San Gabriel – Chino – San Bernardino, leading to the waveguide focusing in the simulations. A 2D visualization of the sources and nodes on top of the Vs=2 km/s contour is also shown in Figure 3.3.

Examples of simulated wavefield snapshots (bandpass filtered between 0.1-0.35 Hz) using station SVD as the source for the NN component (N-S component of the source, and N-S component of the receiver) are shown in Figure 3.4. These snapshots show strong waveguide focusing within two branches, similar to the findings from simulations of large (M7.7+) earthquake scenarios on the southern San Andreas fault (TeraShake, Olsen et al., 2006; Olsen et al., 2008; ShakeOut, Jones et al., 2008; Graves et al., 2008; Olsen et al., 2009). We note the two branches by "Waveguide Branch 1" and "Waveguide Branch 2" as indicated in Figure 3.4. Our simulations show that the waveguide focusing effects previously observed for large finite-fault ruptures can be reproduced by simple surface point forces. Note that the southern end of nodes SG2 and SB4 are located within Waveguide Branches 1 and 2, respectively, and are also located on top of the deeper parts of the sedimentary LA basin (Figure 3.3). Similar excitation patterns can be observed in simulations with sources located at the eastern and southern parts of the model (CJM, VINE, IPT, ROPE, ROUF, KUZD, SVD, ARNO, LUCI, ALLI, SNO, DEV, see Figures 3.5-3.16). Yet, for the northernmost two sources (TA2, LPC, see Figures 3.17-3.18), smaller amplification is present along the waveguide branches, especially along Waveguide Branch 2. This is also in

agreement with simulations of San Andreas fault scenario earthquakes using adjoint sensitivity analysis of the locations most likely to excite the wave guides (Day et al., 2012). Figures 3.5 - 3.18 show the peak amplitude of the 9 components from simulations using 14 selected sources along the SAF inside the modeling area. For these sources (particularly for the southernmost locations), the waveguide excitation is strongest on the NN component, which is approximately dominated by Love waves at both source and receiver stations.

3.4 Noise-Correlation Calculations

In order to cross-validate against the simulations we focused on computing ambient noise cross-correlations between 8 stations located near the SAF with the network of roughly 250 broadband stations hosted by the Southern California Earthquake Data Center (SCEDC) and temporary deployments in the LA and San Gabriel basins. We leveraged cloud computing and the high-performance computing language Julia to process over 5 TB of raw seismic waveforms recorded between 2017 and 2019 into 20 million ambient noise correlations across all 9 components of the Green's tensor. We did so on Amazon Web Services' EC2 compute platform for less than 100 dollars using just 50 hours of compute time.

For the noise-correlation calculation, we leveraged both broadband records from the SCEDC data center and temporary node deployments in the San Gabriel and Bernardino basins. The temporary nodes were all accelerometers and deployed for 40 day time spans between Spring 2017 and Fall 2019. Before computing the noise correlation functions (NCFs) we apply minimal preprocessing to improve signal coherency and prevent artifacts. For the node deployments, we take one time integral before further preprocessing, in order to enable comparison with the velocity measurements from the broadband data. After integration of the nodes, all traces were downsampled to 40 Hz (the standard for the majority of the broadband records), demeaned, and tapered with a Tukey 5% filter and bandpass filtered using a Butterworth filter with corner

frequencies of 0.05 and 19.9 Hz, just below the Nyquist rate. To improve the NCF signal between the broadband records and nodes, we applied a coherency filter with standard windowing length of 30 samples, and water level of 0.01. We then took the Fourier transforms of these processed signals and computed the NCF in one-hour time intervals. We purposely chose longer hour-length windows to give the signals between the sources and receivers, often spatially distant (up to 100km for the nodes), time to converge. We truncated with a maximum lag of 300 seconds and applied a linear stack to the resultant 24 hour-length correlation windows for each of the 9 tensor components. To generate the Green's functions we took two time derivatives, which is what is used for the plots and calculations.

3.5 Waveguide Signatures in Simulated and Noise-based Green's functions

3.5.1 Amplification Comparison

In the following, we compare the peak amplitude at node stations for components of velocity Green's functions from simulations and ambient noise-correlation. Both simulations and data are bandpass filtered (0.1-0.35 Hz). For the simulations, the Green's functions are directly obtained from the velocity synthetics using the surface point forces along E-W, N-S and U-D; for the data, the velocity Green's functions are obtained via the second derivative of the cross-correlation. In order to compare the relative amplification for simulations and data, peak amplitude values are normalized by 60% of the median values at all node stations for simulations and noise-correlations, respectively. The peak amplitude values for the noise-based Green's functions are smoothed by a unit boxcar filter within each nodeline using a window length of 5 samples (nearby node stations) to minimize effects of station outliers, due to differences in node

sensor deployment condition.

Comparison of the peak amplitude on the NN component of the velocity Green's function for sources SVD, SNO and DEV are shown in Figure 3.19 - 3.21. These 3 stations are located along the stretch of the SSAF found to generate the strongest excitation of the waveguide effects from the adjoint study of Day et al. (2012). The amplification patterns along the nodes generally agree between simulated and noise-based Green's functions. Specifically, we observe amplification in both simulations and noise data for all three sources at (1) the southern ends of SG2, SG1 and SG3 that intersect Waveguide Branch 1 and (2) the southern end of SB4 that intersects with Waveguide Branch 2.

3.5.2 Polarization Analysis

In the following we use polarization analysis of the simulated and ambient noise time series to try to identify the phases propagating in the proposed wave guides. Specifically, we determine the ellipticity of the polarization of the three-component recordings as a criterion to distinguish Love from Rayleigh waves, the former identified by Olsen et al. (2006) to represent the primary phases exciting the wave guides. For example, high ellipticity is indicative of Rayleigh waves, whereas linear motion is more indicative of Love waves. However, this analysis comes with the caveats that incoherent noise and body waves may also produce low ellipticity, and that in a complex basin setting, there may not be clear separation between different modes of surface wave motion (e.g., Brissaud et al., 2020).

The polarization analysis follows the technique proposed by Vidale (1986). We analyse data in windows of duration $\frac{1}{f_{min}}$, where fmin is the minimum frequency of interest ($f_{min} = 0.1$ Hz in this study), and advance the window in steps of $\frac{1}{4f_{min}}$. For each window, we obtain the analytic signal, i.e. envelope and instantaneous phase of the three-component seismograms, using the Hilbert transform. We then determine the eigenvalues and eigenvectors of the covariance matrix

of the three components. The eigenvector of the covariance matrix associated with its largest eigenvalue corresponds to the direction in which the strongest polarization occurs. The relative strength of the imaginary part of this eigenvector indicates whether the signal has more linear or more elliptical character. Following Vidale (1986), we quantify ellipticity as the ratio of its imaginary to real part:

$$P_e = \frac{\sqrt{1 - X_0^2}}{X_0}, \tag{3.2}$$

where X_0 is the real part of the first eigenvector; $P_e = 0$ indicates a linear and $P_e = 1$ a circular motion.

Figures 3.22 - 3.27 show the polarization analysis results at SB4 and SG2 for virtual sources SVD, SNO and DEV. We visualize the results as follows: Ellipticity is represented by purple (low) and green (high) colors. The traces are arranged by geographic distance from the southernmost station of each nodeline. The opacity in the plots is set to peak amplitude in the respective time window, thereby omitting relatively low-amplitude windows. Furthermore, we overlay the time series of peak amplitude in each window as gray lines at three stations at the beginning, center and end of the array. The peak amplitude of the time series on all three components is normalized to the peak amplitude from the corresponding source. Polarization in the three panels corresponds to the East, North, and vertical component from the source.

The results of our polarization analysis provide us with a means to validate the results from the simulations, indicating that ∼4-5 s Love waves and to a minor extent Rayleigh waves are the primary phases exciting the proposed waveguides in Los Angeles by Olsen et al. (2006), Olsen et al. (2008), and Olsen et al. (2009). Thus, a predominance of Love waves is expected to show up as a relatively high-amplitude and low-ellipticity motion. While the simulations as expected show more coherent polarization motion patterns compared with the ambient noise, a remarkable agreement between the two for the low-ellipticity motion (Love waves) at SB4 and

SG2 can be observed for the three sources.

3.6 Discussion and Conclusions

We have compared surface point force synthetics and ambient noise records obtained from a dense deployment in northern Los Angeles to try to validate the presence of two waveguide branches proposed from large-scale simulations of earthquake scenarios on the southern San Andreas fault. Synthetics and cross correlation of virtual source-receiver pairs for data show elevated peak amplitudes in the areas where the presence of the waveguide branches are expected based on earthquake scenarios. Furthermore, the results from polarization analysis is consistent with the findings from the simulations in that Love waves originating near the source represent the dominating seismic phase exciting the waveguide branches, with a smaller contribution from Rayleigh waves. Our results also show that virtual point force sources located on the SAF along and south of the San Bernardino basin effectively excite these waveguides.

While the current ambient noise analysis provides evidence for the existence of the two waveguide branches by increased amplitudes of cross correlations at locations along the nodelines expected from the simulations (e.g. SG2, SB4), further research is still required in future work. For example, there are unexpected data amplitude discrepancies at intersections of different nodelines at nearby sensor locations (see Figures 3.19-3.21). These discrepancies may be caused by (1) seasonal variations of the observed ambient noise in the area, as the various temporary arrays were deployed during different parts of the year (e.g., daily average noise level in winter can be higher than summer, see Hillers et al., 2015); (2) different gain settings between instruments of different nodelines (the nodes between lines belong to different institutions and gain settings were not calibrated); (3) inconsistent deployment conditions, such that some sensors were buried and some were not, as the node sensors are deployed in the urban areas that have complex surface conditions; (4) significant local noise sources, as some nodes were close to busy highways;

such local sources produce increased local noise energy that likely reduced the detected seismic coherency between the nodes and virtual sources.

Although further research needs to be conducted for the noise data, the successful validation of the amplification found in the simulations where the waveguides are expected indicates that the connectivity of the sedimentary basins (Los Angeles - San Gabriel – Chino – San Bernardino) as present in the CVM-S4.26 velocity model is realistic. However, we recommend more detailed analysis of the basin velocity structure in the areas where the largest excitation of the waveguides appear, to further the understanding of the discrepancies between the simulation and data.

Acknowledgements

The authors thank Steven Day for his helpful discussion and suggestions.

Chapter 3, in full, is a reformatted version of a paper currently being prepared: Wang, N., Schmitt, J., Denolle, M., Olsen, K.B., Clements, T., Ermert, L., Clayton, R. (2021). Signatures of Seismic Waveguides in Los Angeles from Numerical Simulations and Noise Cross Correlations. The dissertation author was the primary investigator and author of this paper.

References

Brissaud, Q., Bowden, D. C., and Tsai, V. C. (2020). "Extension of the Basin Rayleigh-Wave Amplification Theory to Include Basin-Edge Effects". In: *Bulletin of the Seismological Society of America* 110.3, pp. 1305–1322.

Cui, Y., Poyraz, E., Olsen, K. B., Zhou, J., Withers, K., Callaghan, S., Larkin, J., Guest, C, Choi, D, Chourasia, A., et al. (2013). "Physics-based seismic hazard analysis on petascale heterogeneous supercomputers". In: *SC'13: Proceedings of the International Conference on High Performance Computing, Networking, Storage and Analysis*. IEEE, pp. 1–12.

Cupillard, P. and Capdeville, Y. (2010). "On the amplitude of surface waves obtained by noise correlation and the capability to recover the attenuation: a numerical approach". In: *Geophysical Journal International* 181.3, pp. 1687–1700.

Day, S. M., Graves, R., Bielak, J., Dreger, D., Larsen, S., Olsen, K. B., Pitarka, A., and Ramirez-Guzman, L. (2008). "Model for basin effects on long-period response spectra in southern California". In: *Earthquake Spectra* 24.1, pp. 257–277.

Day, S. M., Roten, D., and Olsen, K. B. (2012). "Adjoint analysis of the source and path sensitivities of basin-guided waves". In: *Geophysical Journal International* 189.2, pp. 1103–1124.

Denolle, M., Dunham, E., Prieto, G., and Beroza, G. (2013). "Ground motion prediction of realistic earthquake sources using the ambient seismic field". In: *Journal of Geophysical Research: Solid Earth* 118.5, pp. 2102–2118.

— (2014). "Strong ground motion prediction using virtual earthquakes". In: *Science* 343.6169, pp. 399–403.

Graves, R., Jordan, T. H., Callaghan, S., Deelman, E., Field, E., Juve, G., Kesselman, C., Maechling, P., Mehta, G., Milner, K., et al. (2011). "CyberShake: A physics-based seismic hazard model for southern California". In: *Pure and Applied Geophysics* 168.3, pp. 367–381.

Graves, R. W. (Sept. 2013). "Long Period (T¿1 sec) ShakeOut Rupture Simulations in Alternative 3D Seismic Velocity Models". In: Poster Presentation 219 at 2013 SCEC Annual Meeting. Palm, Springs, CA.

Graves, R. W., Aagaard, B. T., Hudnut, K. W., Star, L. M., Stewart, J. P., and Jordan, T. H. (2008). "Broadband simulations for Mw 7.8 southern San Andreas earthquakes: Ground motion sensitivity to rupture speed". In: *Geophysical research letters* 35.22.

Graves, R. W., Pitarka, A., and Somerville, P. G. (1998). "Ground-motion amplification in the Santa Monica area: Effects of shallow basin-edge structure". In: *Bulletin of the Seismological Society of America* 88.5, pp. 1224–1242.

Hillers, G, Ben-Zion, Y, Campillo, M, and Zigone, D (2015). "Seasonal variations of seismic velocities in the San Jacinto fault area observed with ambient seismic noise". In: *Geophysical Journal International* 202.2, pp. 920–932.

Jones, L. M., Bernknopf, R., Cox, D., Goltz, J., Hudnut, K., Mileti, D., Perry, S., Ponti, D., Porter, K., Reichle, M., Seligson, H., Shoaf, K., Treiman, J., and Wein, A. (2008). *The ShakeOut scenario,USGS Open-File Report 2008–1150*. Tech. rep. US Geological Survey.

Kohler, M., Magistrale, H, and Clayton, R. (2003). "Mantle heterogeneities and the SCEC reference three-dimensional seismic velocity model version 3". In: *Bulletin of the Seismological Society of America* 93.2, pp. 757–774.

Kwak, S., Song, S. G., Kim, G., Cho, C. S., and Shin, J. S. (2017). "Investigating the capability to extract impulse response functions from ambient seismic noise using a mine collapse event". In: *Geophysical Research Letters* 44.19, pp. 9653–9662.

Larose, E., Roux, P., and Campillo, M. (2007). "Reconstruction of Rayleigh–Lamb dispersion spectrum based on noise obtained from an air-jet forcing". In: *The Journal of the Acoustical Society of America* 122.6, pp. 3437–3444.

Lee, E.-J. and Chen, P. (2016). "Improved basin structures in Southern California obtained through full-3D seismic waveform tomography (F3DT)". In: *Seismological Research Letters* 87.4, pp. 874–881.

Lee, E.-J., Chen, P., Jordan, T. H., Maechling, P. B., Denolle, M. A., and Beroza, G. C. (2014). "Full-3-D tomography for crustal structure in southern California based on the scattering-integral and the adjoint-wavefield methods". In: *Journal of Geophysical Research: Solid Earth* 119.8, pp. 6421–6451.

Lobkis, O. I. and Weaver, R. L. (2001). "On the emergence of the Green's function in the correlations of a diffuse field". In: *The Journal of the Acoustical Society of America* 110.6, pp. 3011–3017.

Magistrale, H, Graves, R, and Clayton, R (1998). "A standard three-dimensional seismic velocity model for southern California: version 1". In: *Eos Transactions AGU* 79, F605.

Magistrale, H., Day, S., Clayton, R. W., and Graves, R. (2000). "The SCEC southern California reference three-dimensional seismic velocity model version 2". In: *Bulletin of the Seismological Society of America* 90.6B, S65–S76.

Magistrale, H., McLaughlin, K., and Day, S. (1996). "A geology-based 3D velocity model of the Los Angeles basin sediments". In: *Bulletin of the Seismological Society of America* 86.4, pp. 1161–1166.

Olsen, K., Day, S., and Bradley, C. (2003). “Estimation of Q for long-period (¿ 2 sec) waves in the Los Angeles basin”. In: *Bulletin of the Seismological Society of America* 93.2, pp. 627–638.

Olsen, K., Day, S., Dalguer, L., Mayhew, J, Cui, Y, Zhu, J, Cruz-Atienza, V., Roten, D, Maechling, P, Jordan, T., and Chourasia, A (2009). “ShakeOut-D: Ground motion estimates using an ensemble of large earthquakes on the southern San Andreas fault with spontaneous rupture propagation”. In: *Geophysical Research Letters* 36.4.

Olsen, K., Day, S., Minster, J., Cui, Y, Chourasia, A, Okaya, D, Maechling, P, and Jordan, T (2008). “TeraShake2: Spontaneous rupture simulations of M w 7.7 earthquakes on the southern San Andreas fault”. In: *Bulletin of the Seismological Society of America* 98.3, pp. 1162–1185.

Olsen, K., Day, S., Minster, J., Cui, Y., Chourasia, A., Faerman, M., Moore, R., Maechling, P., and Jordan, T. (2006). “Strong shaking in Los Angeles expected from southern San Andreas earthquake”. In: *Geophysical Research Letters* 33.7.

Olsen, K. B., Archuleta, R. J., and Matarese, J. R. (1995). “Three-dimensional simulation of a magnitude 7.75 earthquake on the San Andreas fault”. In: *Science* 270.5242, pp. 1628–1632.

O’Reilly, O., Breuer, A. N., Cui, Y., Goulet, C. A., Olsen, K. B., Roten, D., Thomas-Collignon, G., and Yeh, T. (Aug. 2019). “Simulation of elastic waves in the presence of topography using a curvilinear staggered grid finite difference method”. In: Poster Presentation at 2019 SCEC Annual Meeting. Palm, Springs, CA.

Plesch, A., Shaw, J. H., Benson, C., Bryant, W. A., Carena, S., Cooke, M., Dolan, J., Fuis, G., Gath, E., Grant, L., et al. (2007). “Community fault model (CFM) for southern California”. In: *Bulletin of the Seismological Society of America* 97.6, pp. 1793–1802.

Prieto, G. A. and Beroza, G. C. (2008). “Earthquake ground motion prediction using the ambient seismic field”. In: *Geophysical Research Letters* 35.14.

Prieto, G. A., Denolle, M., Lawrence, J. F., and Beroza, G. C. (2011). “On amplitude information carried by the ambient seismic field”. In: *Comptes Rendus Geoscience* 343.8-9, pp. 600–614.

Savran, W. and Olsen, K. (2019). “Ground motion simulation and validation of the 2008 Chino Hills earthquake in scattering media”. In: *Geophysical Journal International* 219.3, pp. 1836–1850.

Süss, M. P. and Shaw, J. H. (2003). “P wave seismic velocity structure derived from sonic logs and industry reflection data in the Los Angeles basin, California”. In: *Journal of Geophysical Research: Solid Earth* 108.B3.

Taborda, R., Azizzadeh-Roodpish, S., Khoshnevis, N., and Cheng, K. (2016). “Evaluation of the southern California seismic velocity models through simulation of recorded events”. In: *Geophysical Journal International* 205.3, pp. 1342–1364.

Vidale, J. E. (1986). “Complex polarization analysis of particle motion”. In: *Bulletin of the Seismological society of America* 76.5, pp. 1393–1405.

Viens, L., Miyake, H., and Koketsu, K. (2015). “Long-period ground motion simulation of a subduction earthquake using the offshore-onshore ambient seismic field”. In: *Geophysical Research Letters* 42.13, pp. 5282–5289.

Weldon, R., Scharer, K., Fumal, T., and Biasi, G. (2004). “Wrightwood and the earthquake cycle: What a long recurrence record tells us about how faults work”. In: *GSA today* 14.9, pp. 4–10.

Tables and Figures

Table 3.1: Simulation parameters

Domain	
Velocity model	UCVM-S4.26
Length	334800 m
Width	316800 m
Depth	43200 m
Southwest corner	-119.2, 32.7
Spatial resolution	
Maximum frequency	1 Hz
Minimum Vs	500 m/s
Points per minimum wavelength	6
Grid discretization	75 m
Temporal resolution	
Time discretization	0.002 s
Simulation time	200.0 s
Number of timesteps	1000000

Table 3.2: Source station locations

Source	Latitude(°)	Longitude(°)
TA2	34.38203	-117.67822
LPC	34.31478	-117.54642
CJM	34.27117	-117.42448
VINE	34.23744	-117.40344
IPT	34.19701	-117.28498
ROPE	34.18348	-117.31934
ROUF	34.18172	-117.29407
KUZD	34.13530	-117.17528
SVD	34.10647	-117.09822
ARNO	34.10574	-117.11326
LUCI	34.06675	-117.00280
ALLI	34.04877	-116.94848
SNO	34.03515	-116.80778
DEV	33.93597	-116.57794

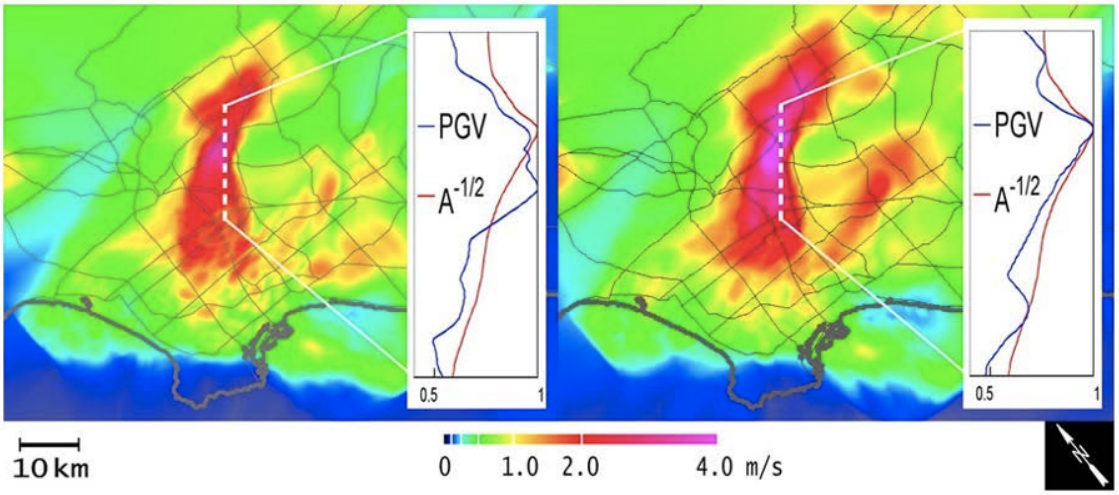

Figure 3.1: Maximum root-mean-square (RMS) peak amplitude for M7.7 SSAF scenarios from SE with two different source descriptions. The curves show the correlation of peak amplitude for (left) SE-NW1 and (right) SE-NW2 scenarios. The curves show the correlation of Peak amplitude (blue) and the reciprocal cross-sectional area (red) of the sediment channel between the Los Angeles and San Gabriel basins, measured as the area of the vertical cross-section striking N50°W that lies inside the 2 km/s S-wave speed isosurface. Both curves are normalized to their respective maxima along the dashed profile. Lines on the maps depict major freeways and the coastline. From Olsen et al. (2006).

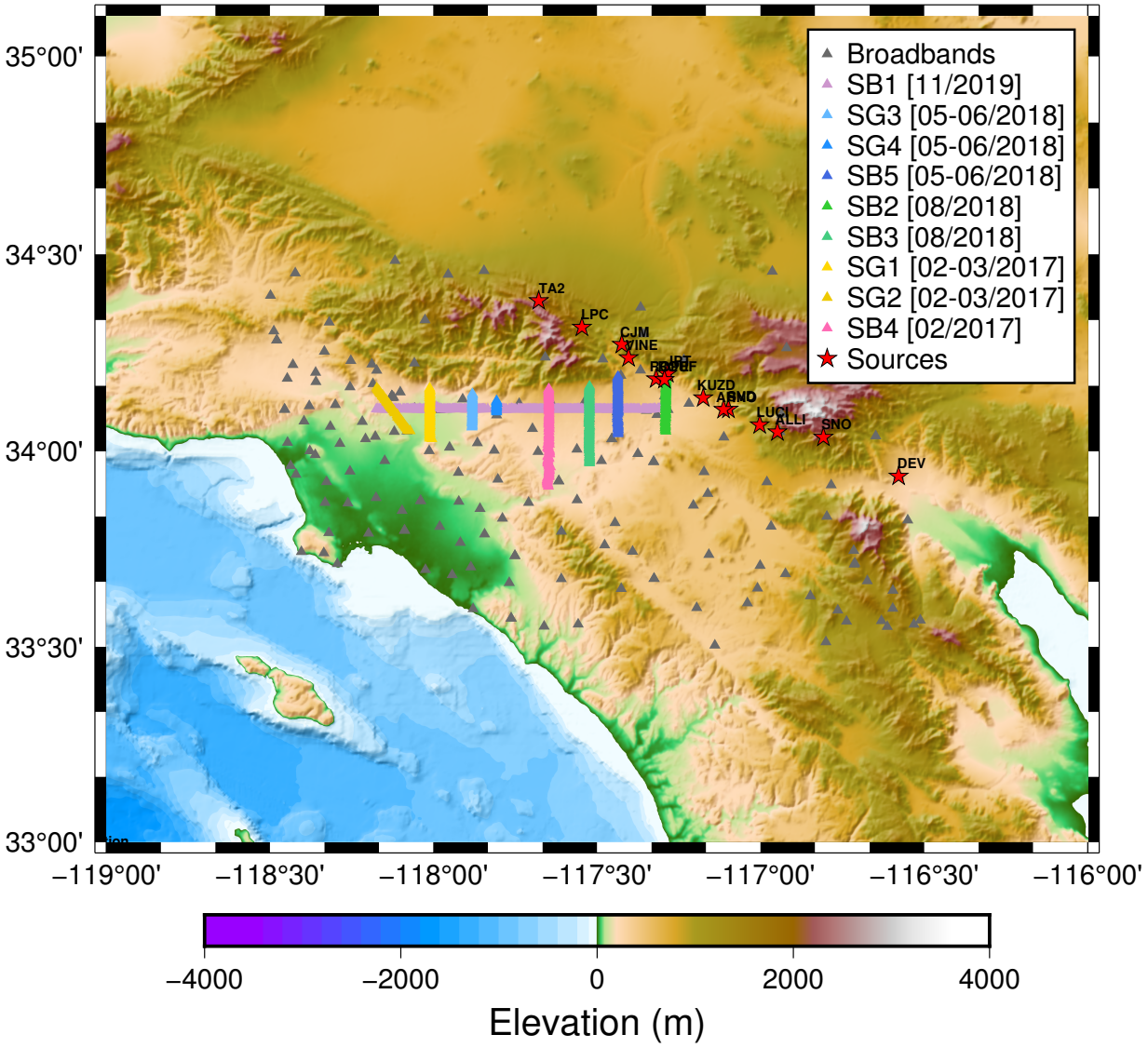

Figure 3.2: Nodal and broadband station locations (triangles), and 14 sources (stars) locations along SAF. Different deployment times for the stations are indicated by different colors of the arrays.

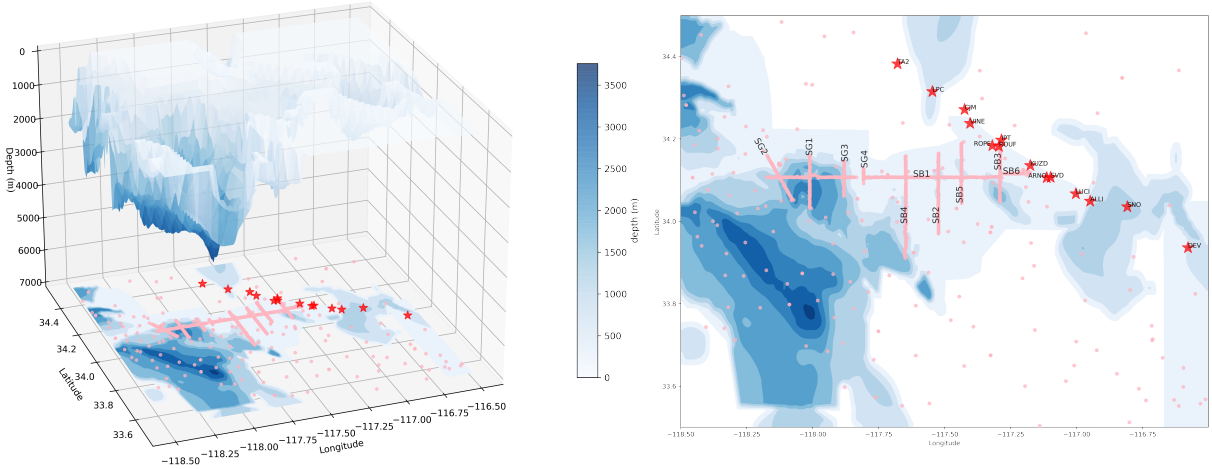

Figure 3.3: 3D (left) and 2D (right) visualization of the Vs=2 km/s isosurface from CVM-S4.26 and the locations of virtual sources (stars) and node stations (dots).

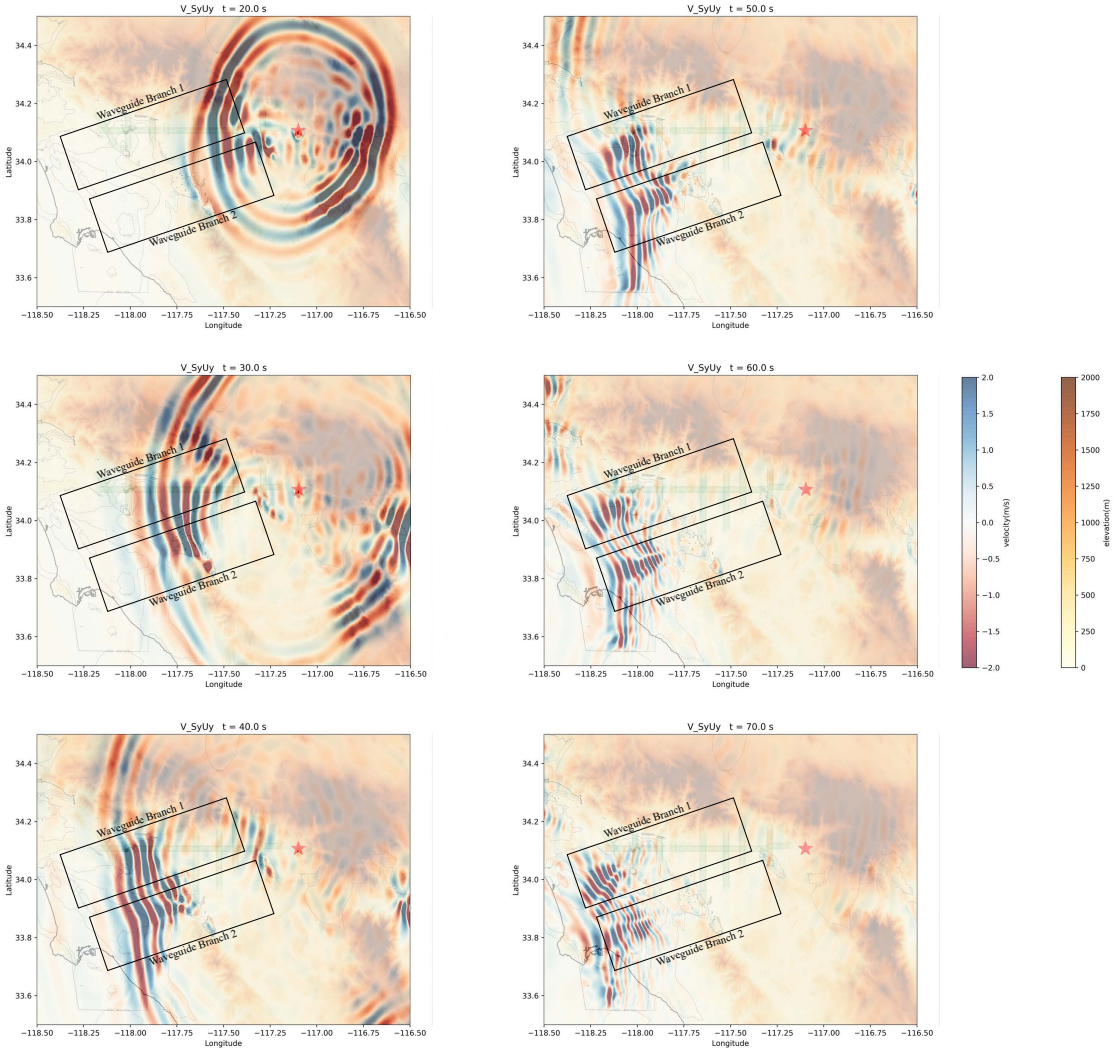

Figure 3.4: Snapshots of the NN component of the Green tensor for a simulation with SVD as source at times of 20s, 30s, 40s, 50s, 60s, and 70s. Proposed regions of waveguide branches 1 and 2 are indicated by black rectangles.

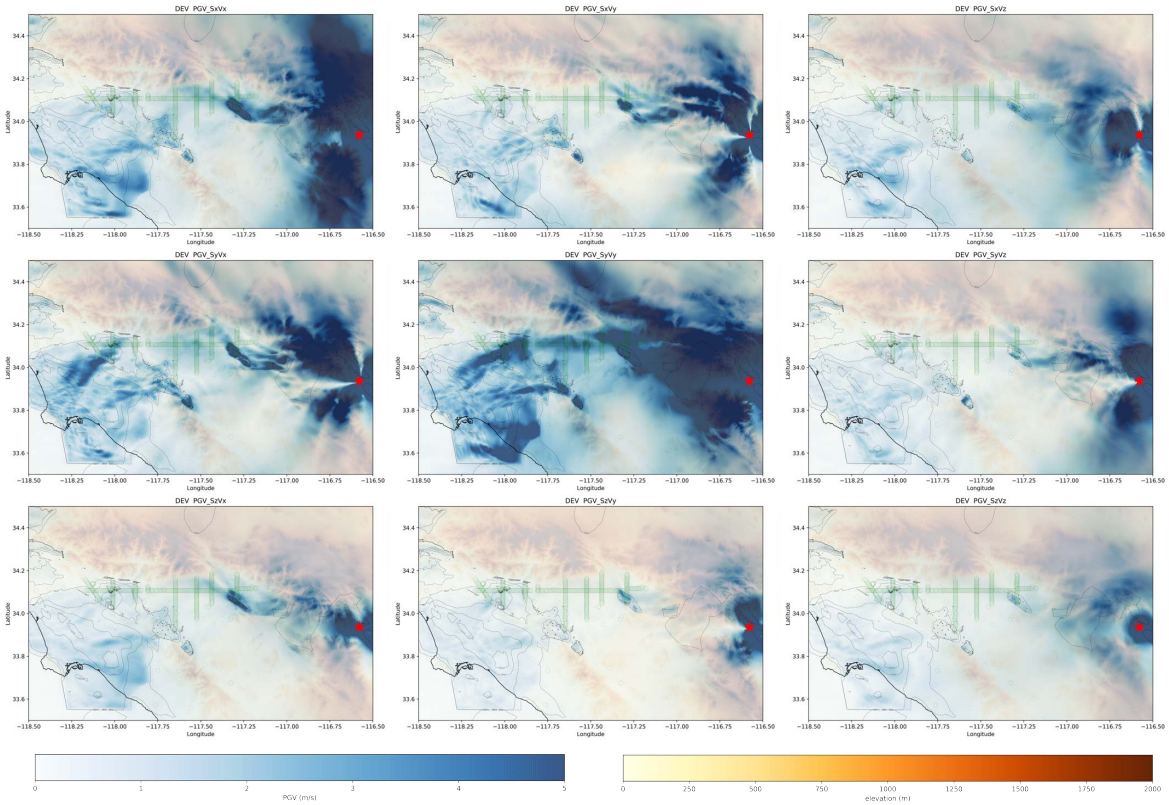

Figure 3.5: Peak amplitude synthetics for the 9 components of the Green's tensor obtained using source DEV (star). The green circles depict the location of the temporary arrays (see Figure 3.3).

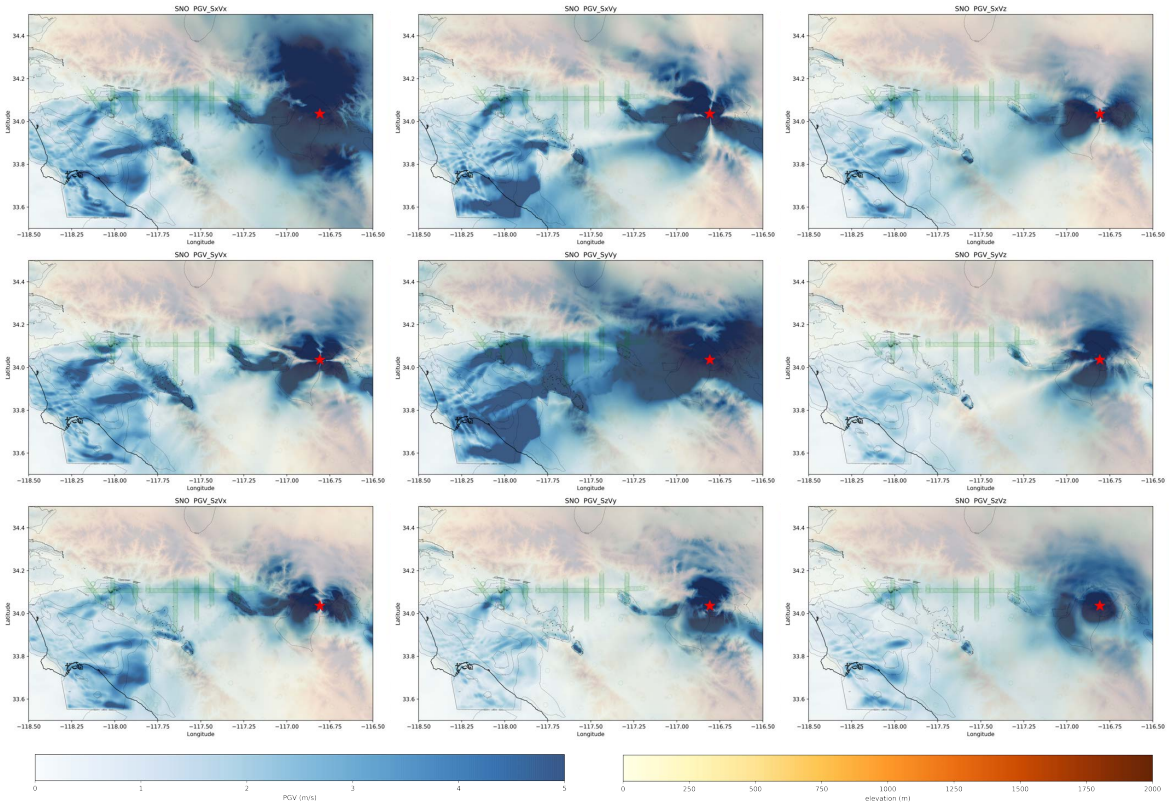

Figure 3.6: Same as Figure 3.5, but for SNO as the source.

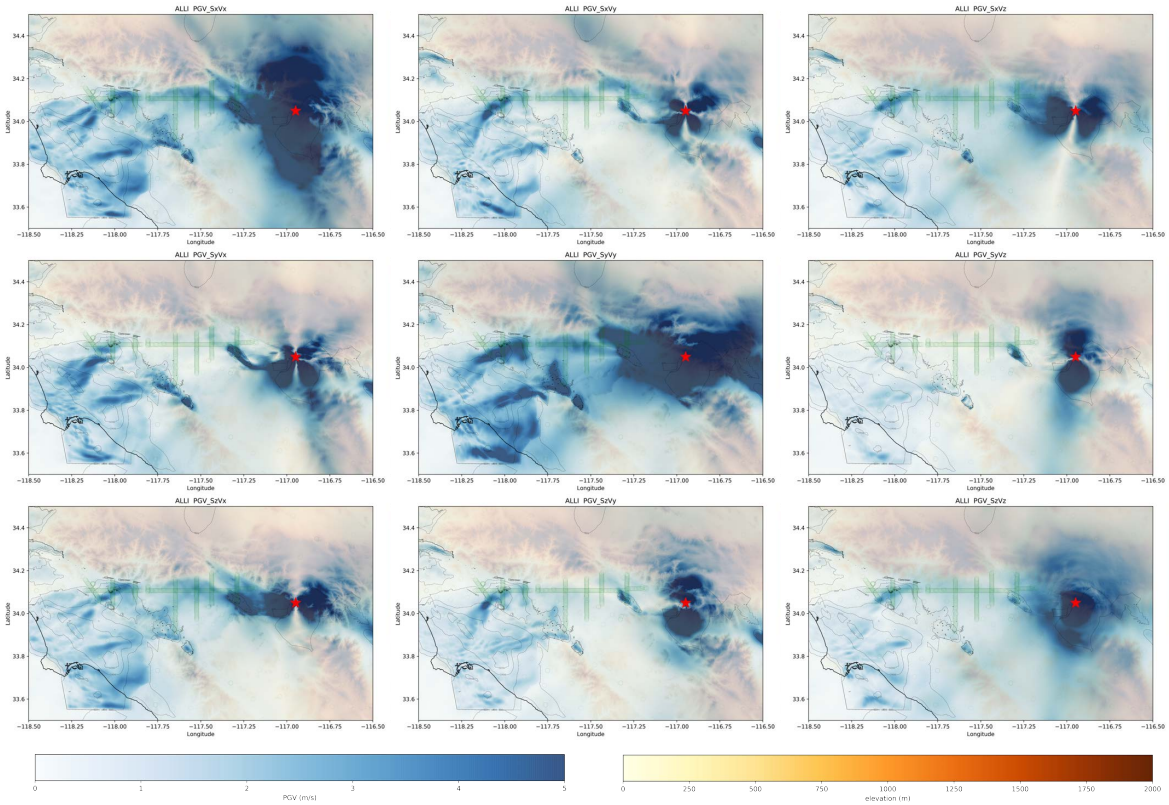

Figure 3.7: Same as Figure 3.5, but for ALLI as the source.

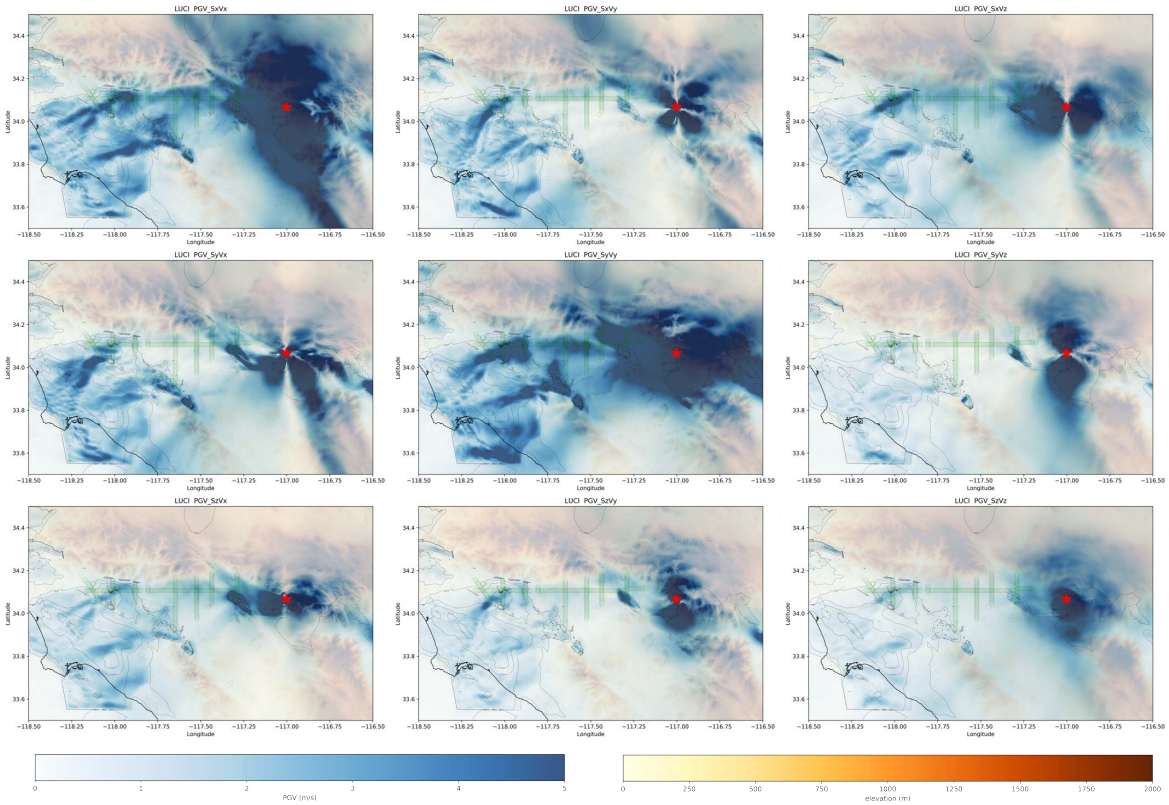

Figure 3.8: Same as Figure 3.5, but for LUCI as the source.

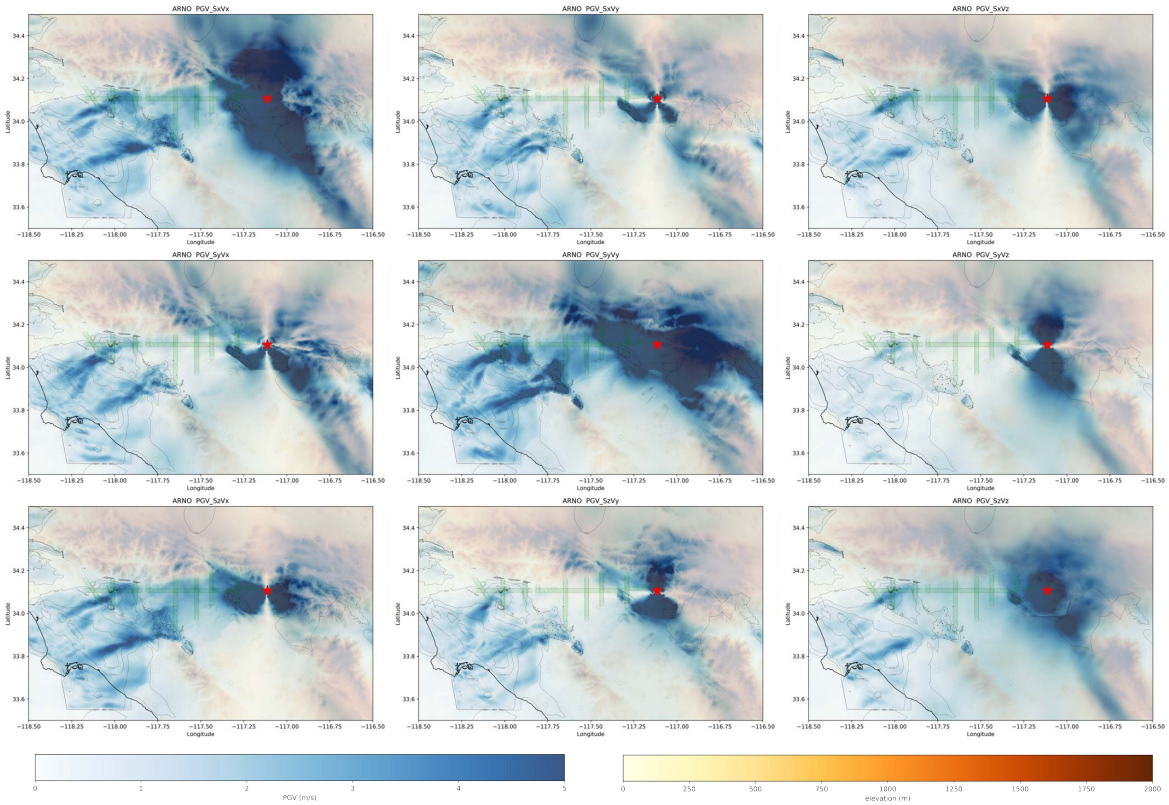

Figure 3.9: Same as Figure 3.5, but for ARNO as the source.

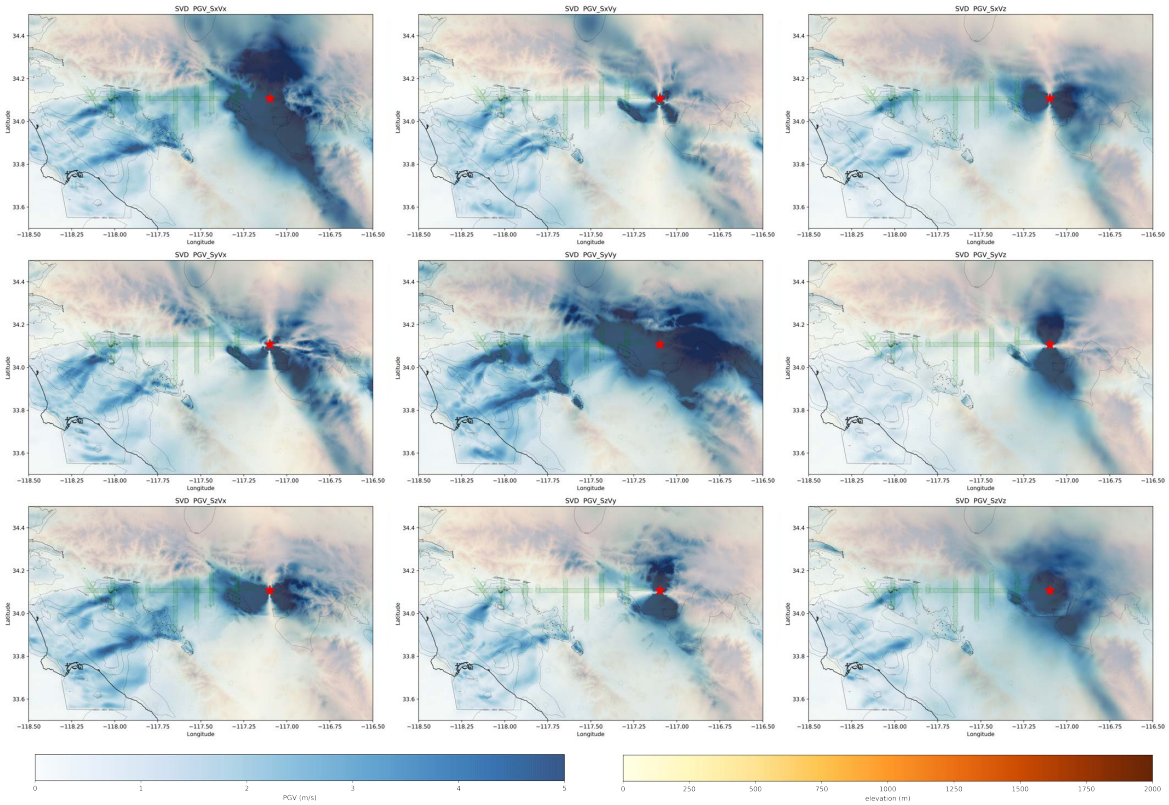

Figure 3.10: Same as Figure 3.5, but for SVD as the source.

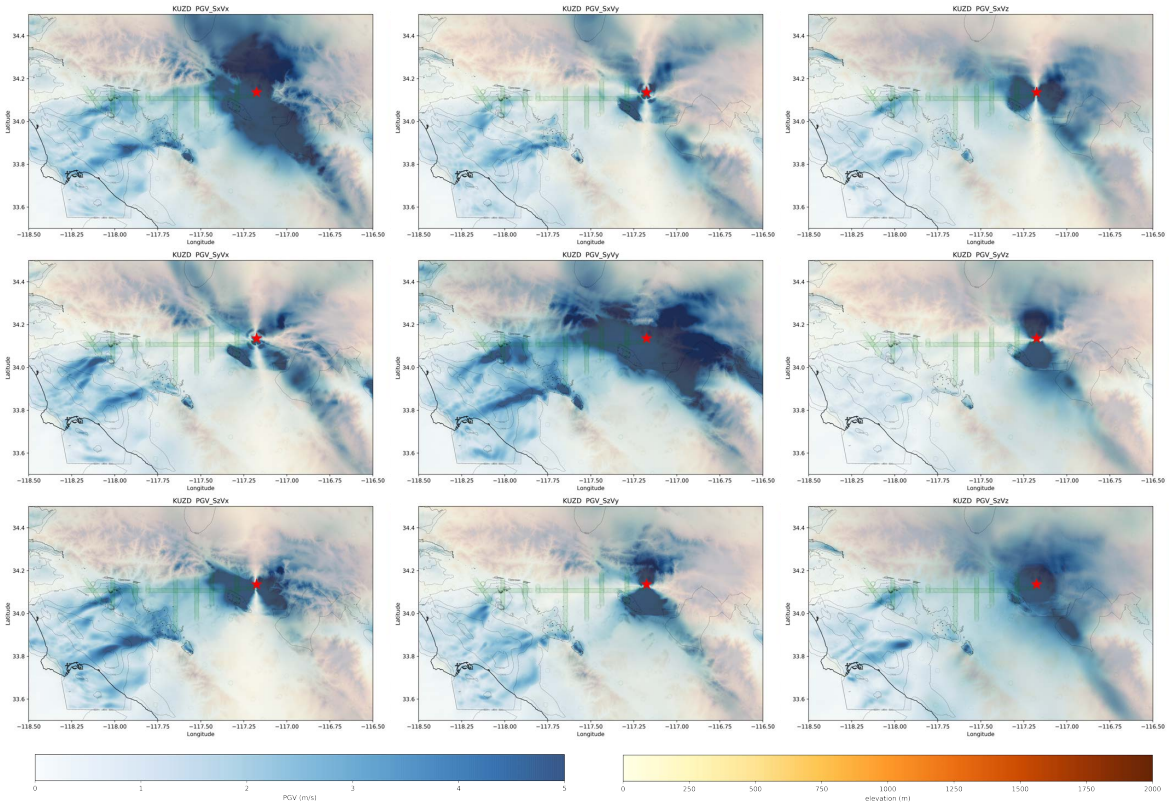

Figure 3.11: Same as Figure 3.5, but for KUZD as the source.

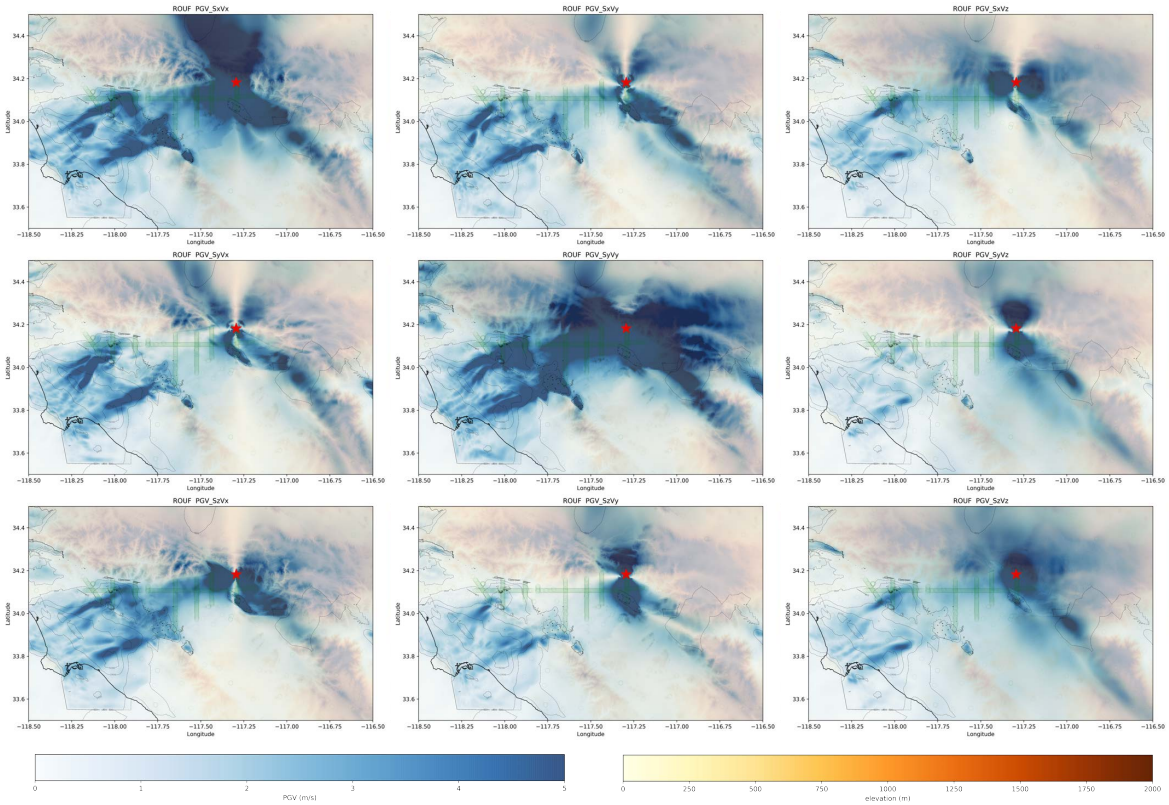

Figure 3.12: Same as Figure 3.5, but for ROUF as the source.

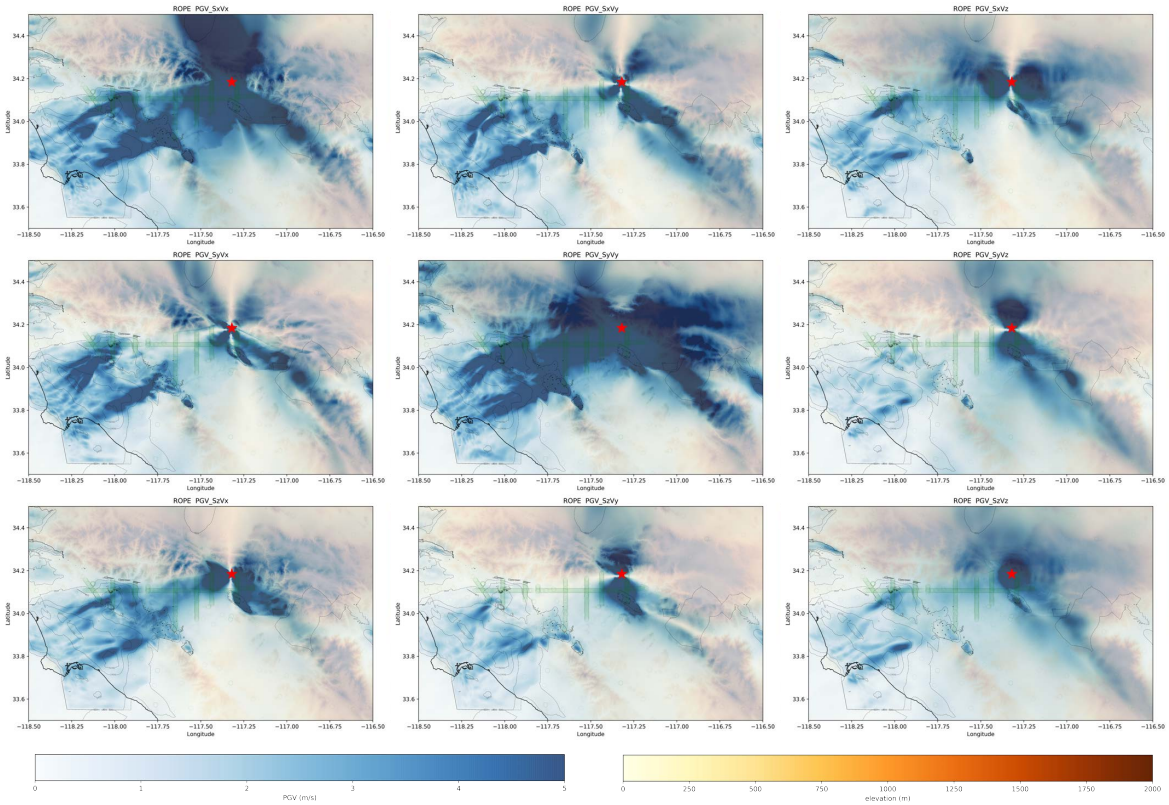

Figure 3.13: Same as Figure 3.5, but for ROPE as the source.

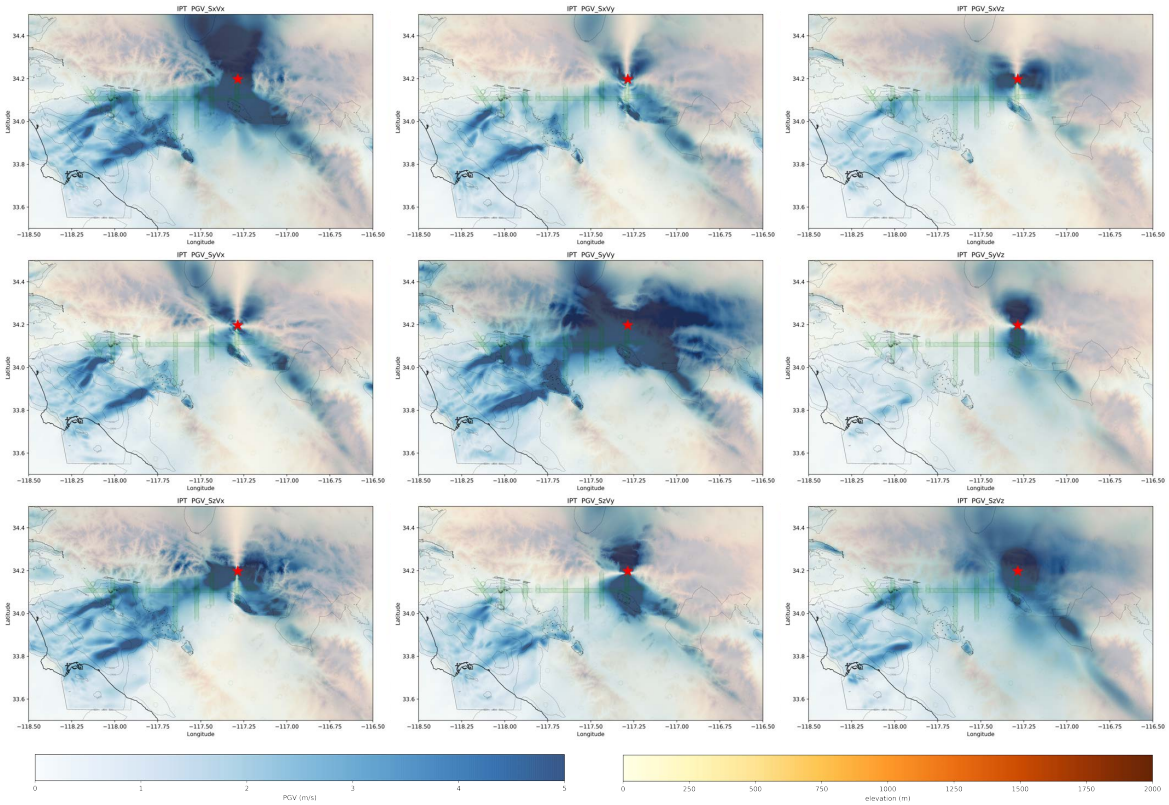

Figure 3.14: Same as Figure 3.5, but for IPT as the source.

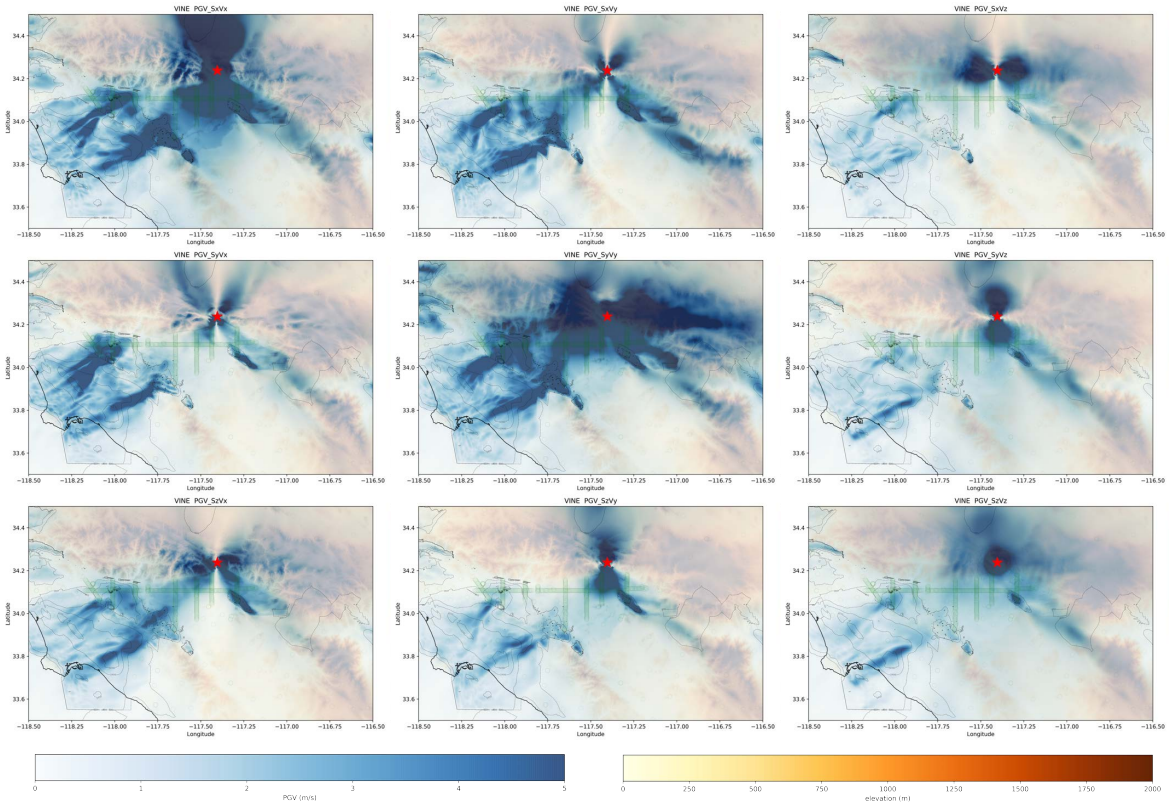

Figure 3.15: Same as Figure 3.5, but for VINE as the source.

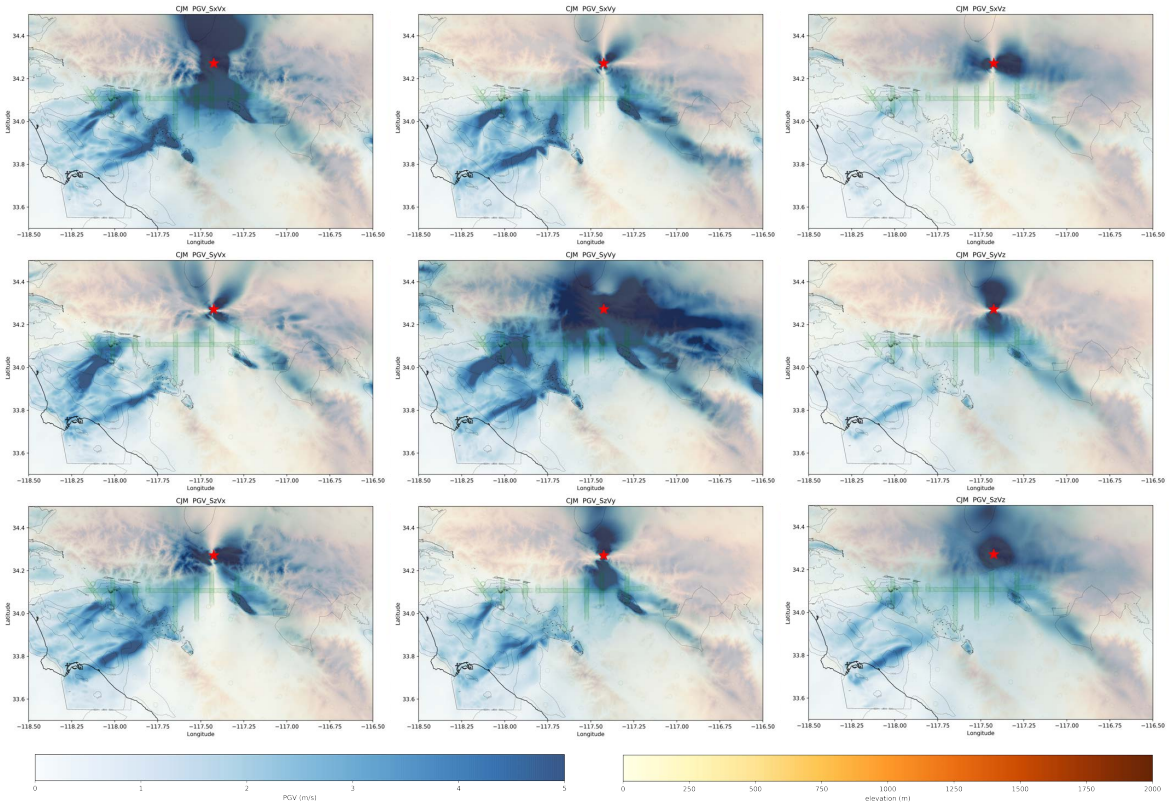

Figure 3.16: Same as Figure 3.5, but for CJM as the source.

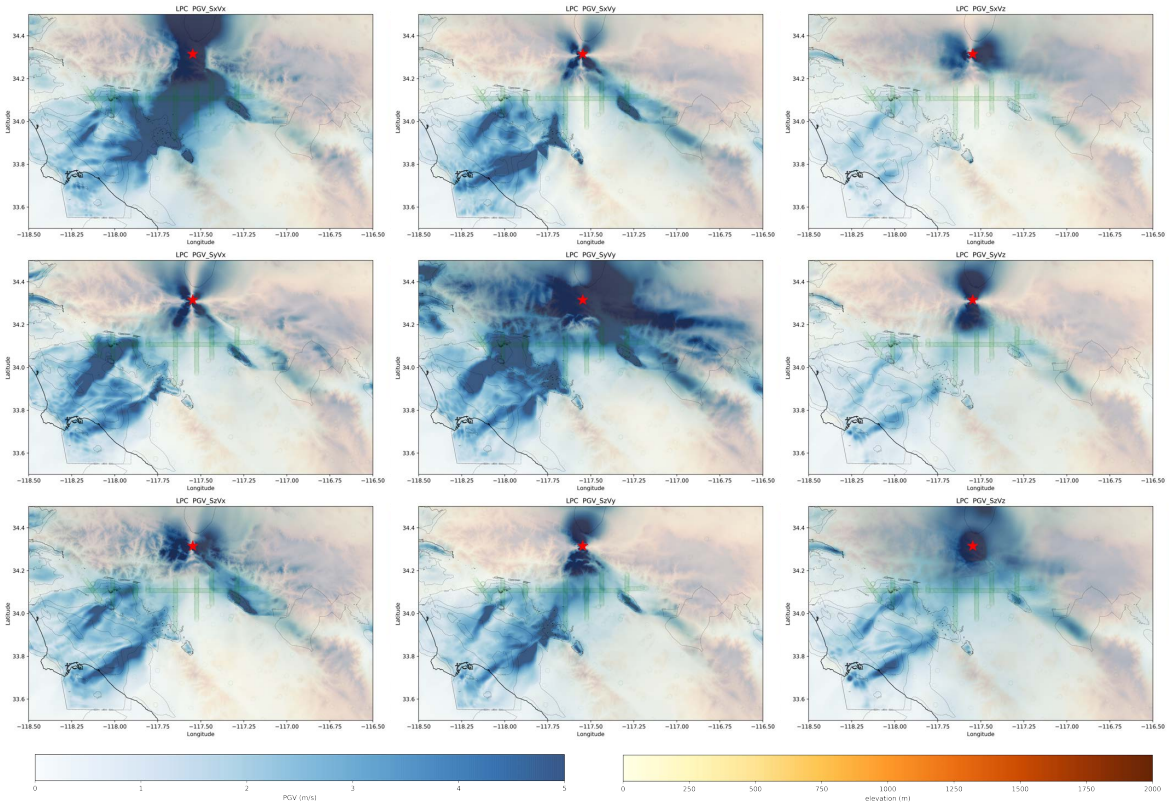

Figure 3.17: Same as Figure 3.5, but for LPC as the source.

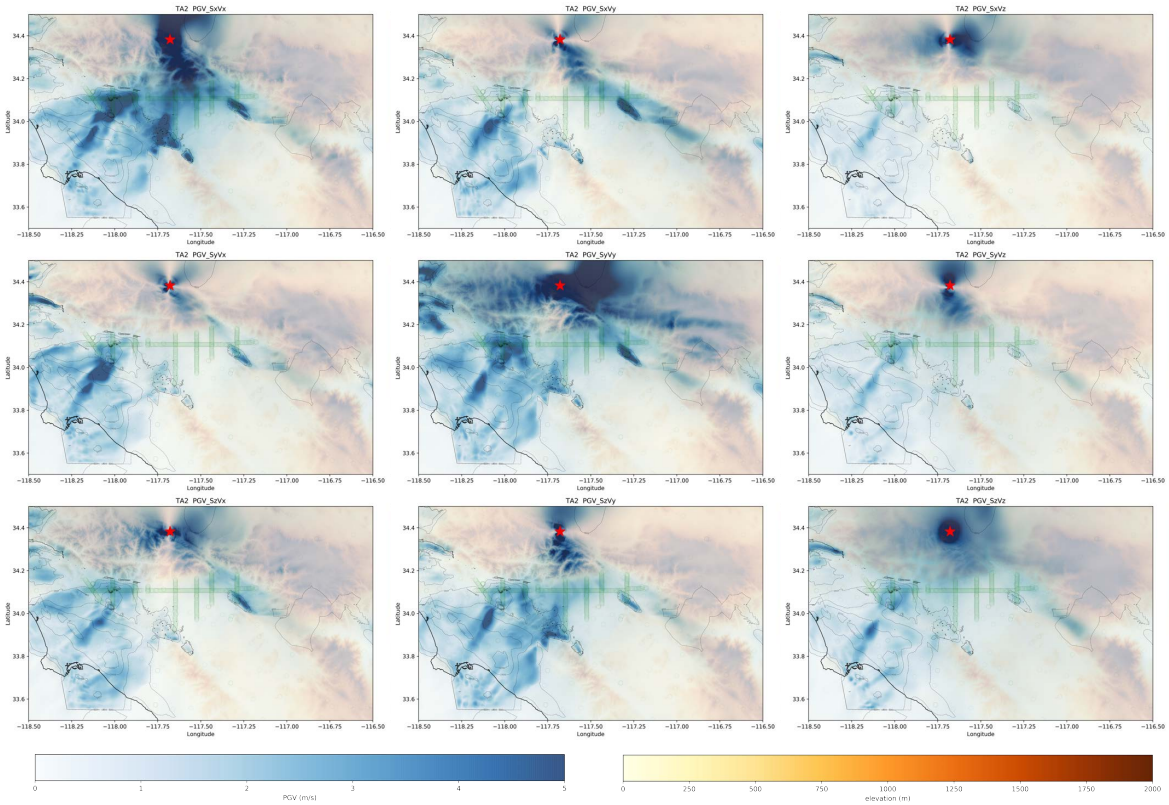

Figure 3.18: Same as Figure 3.5, but for TA2 as the source.

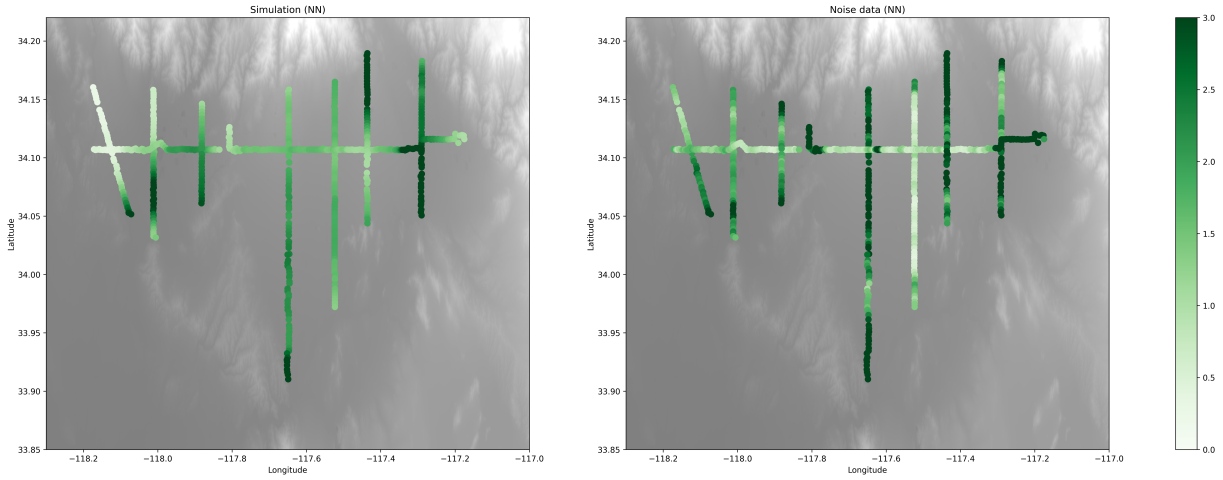

Figure 3.19: Normalized peak amplitude of simulated (left) and noise-based (right) Green's functions (NN component) for source SVD.

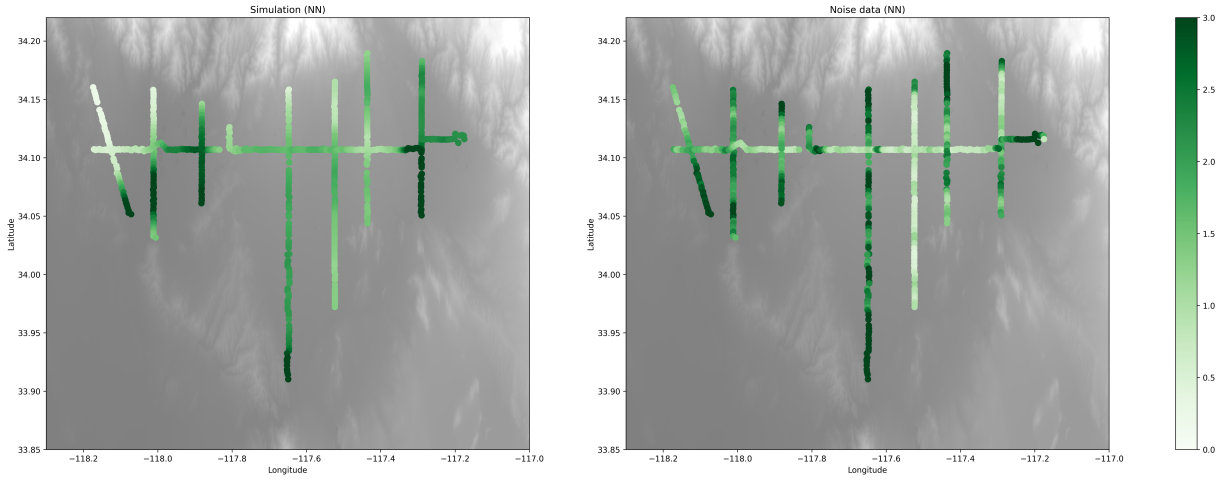

Figure 3.20: Same as Figure 3.19, but for SNO as the source.

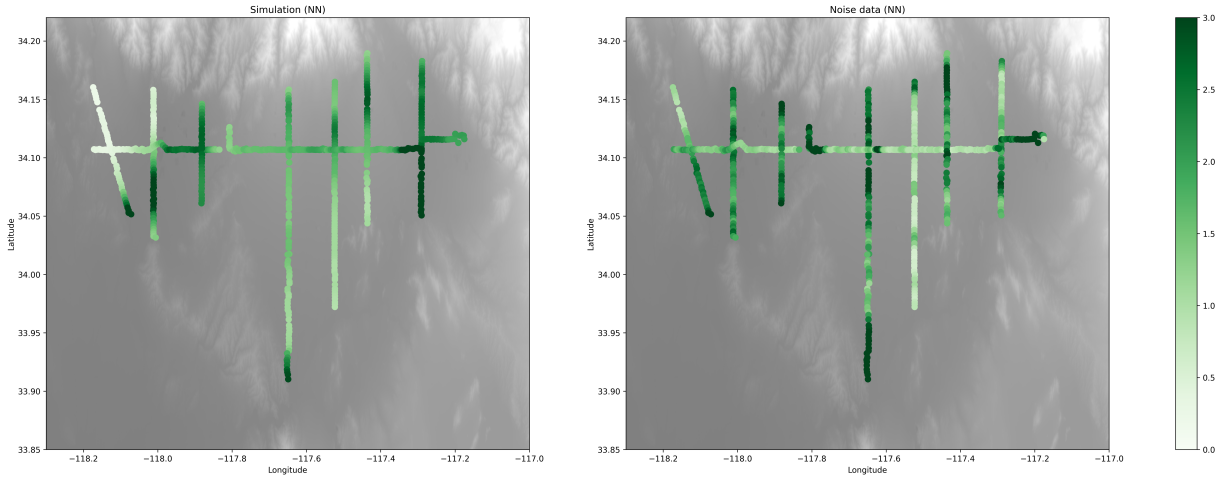

Figure 3.21: Same as Figure 3.19, but for DEV as the source.

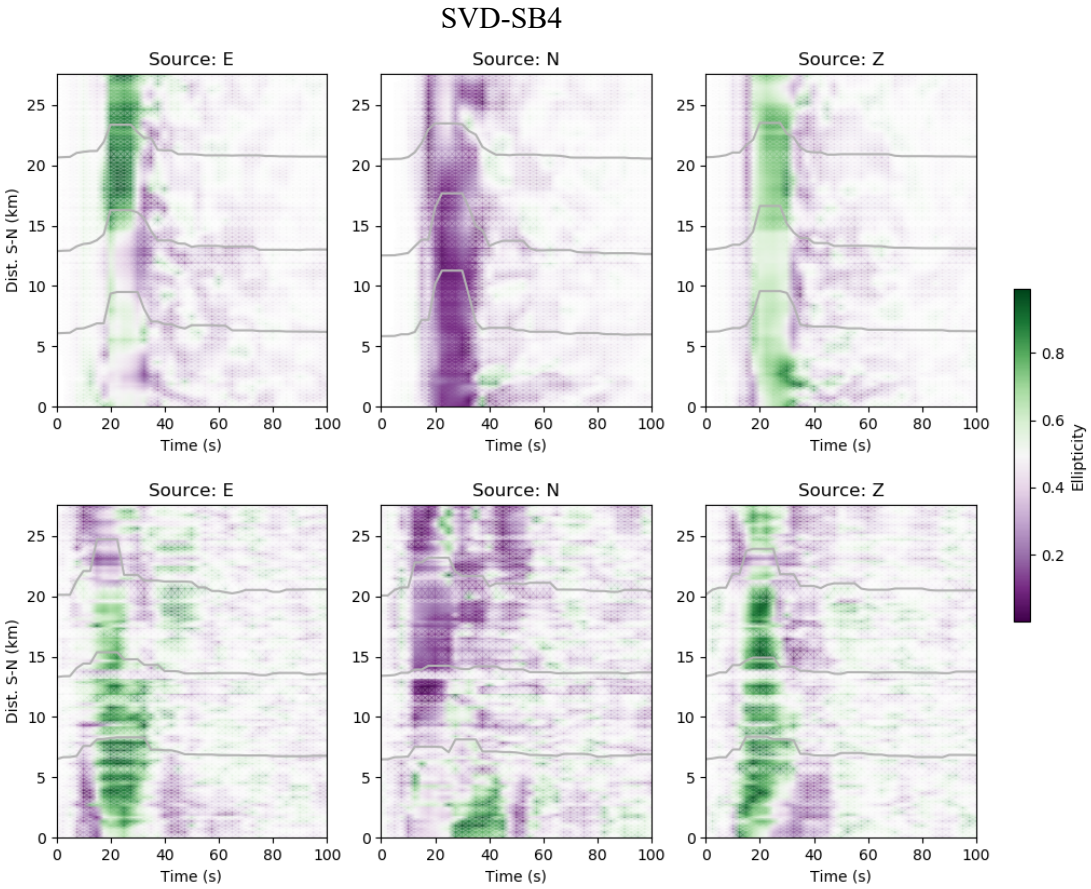

Figure 3.22: Polarization along SB4 (see Figure 3.3) on the East (left), North (middle), and vertical (right) components from simulations (top) and noise-correlations (bottom) for source SVD. Low-ellipticity is represented by purple and high-ellipticity by green. Gray lines show the time series of normalized peak amplitude in each window at three example stations.

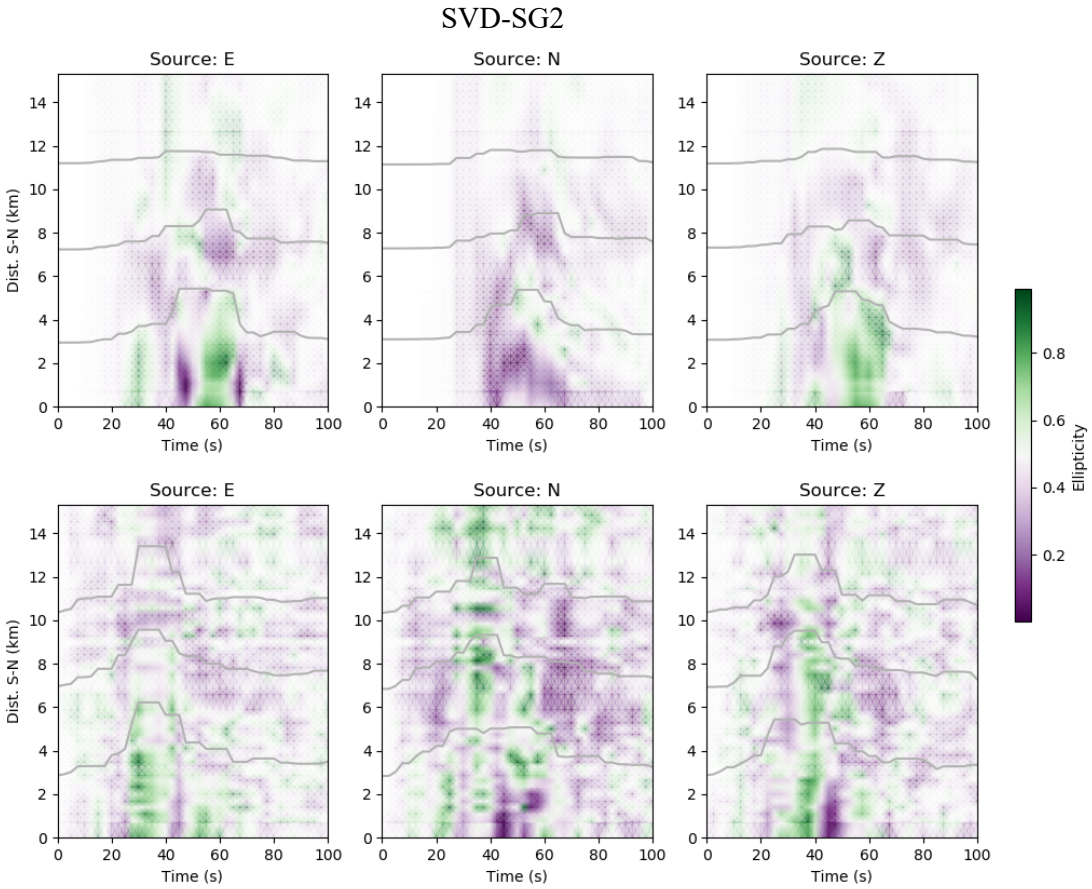

Figure 3.23: Same as Figure 3.22, but along SG2.

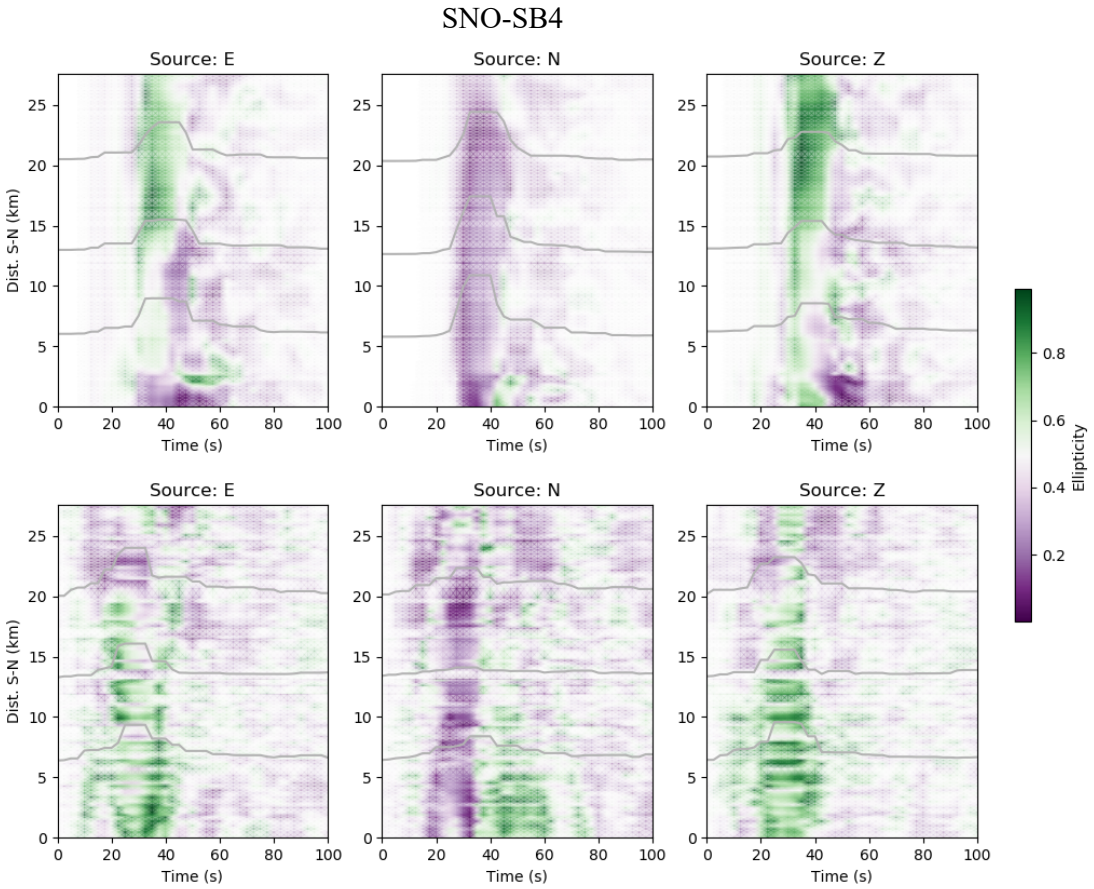

Figure 3.24: Polarization along SB4 (see Figure 3.3) on the East (left), North (middle), and vertical (right) components from simulations (top) and (bottom) noise-correlations for source SNO. Low-ellipticity is represented by purple and high-ellipticity by green. Gray lines show the time series of normalized peak amplitude in each window at three example stations.

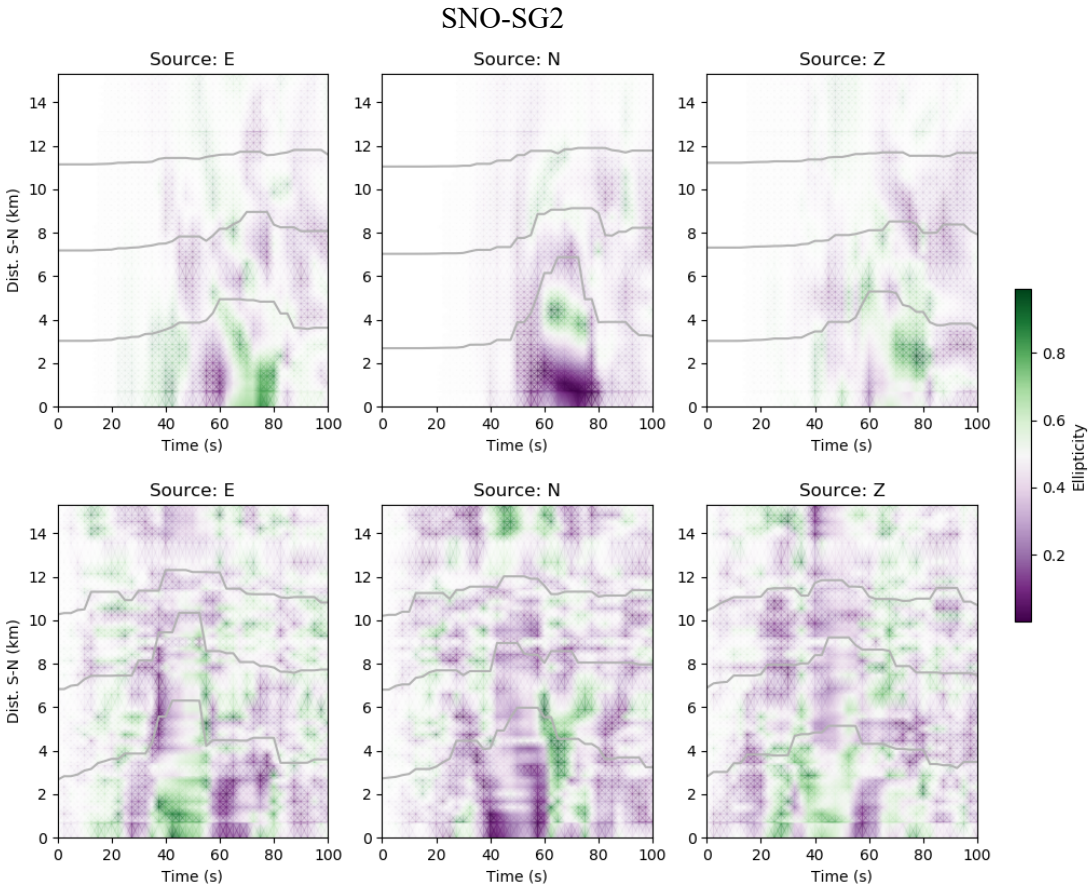

Figure 3.25: Same as Figure 3.24, but along SG2.

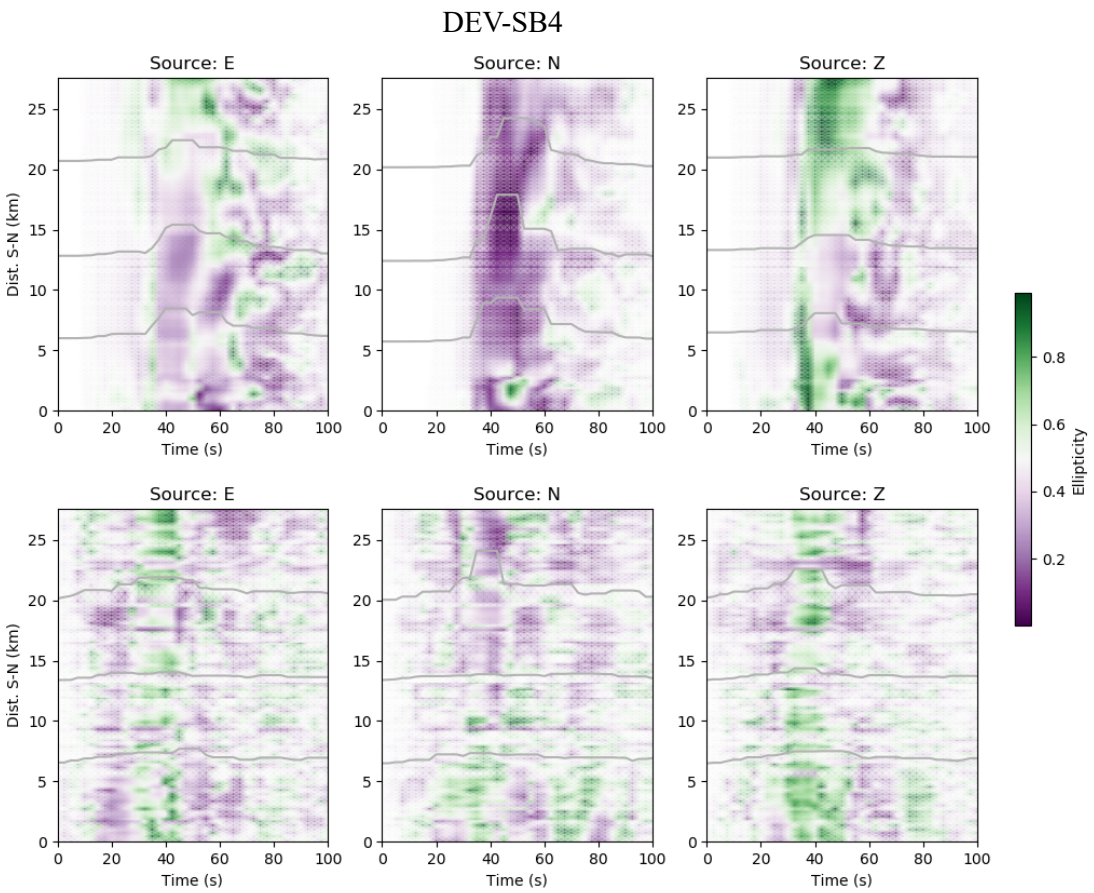

Figure 3.26: Polarization along SB4 (see Figure 3.3) on the East (left), North (middle), and vertical (right) component from simulations (top) and noise-correlations (bottom) for source DEV. Low-ellipticity is represented by purple and high-ellipticity by green. Gray lines show the time series of normalized peak amplitude in each window at three example stations.

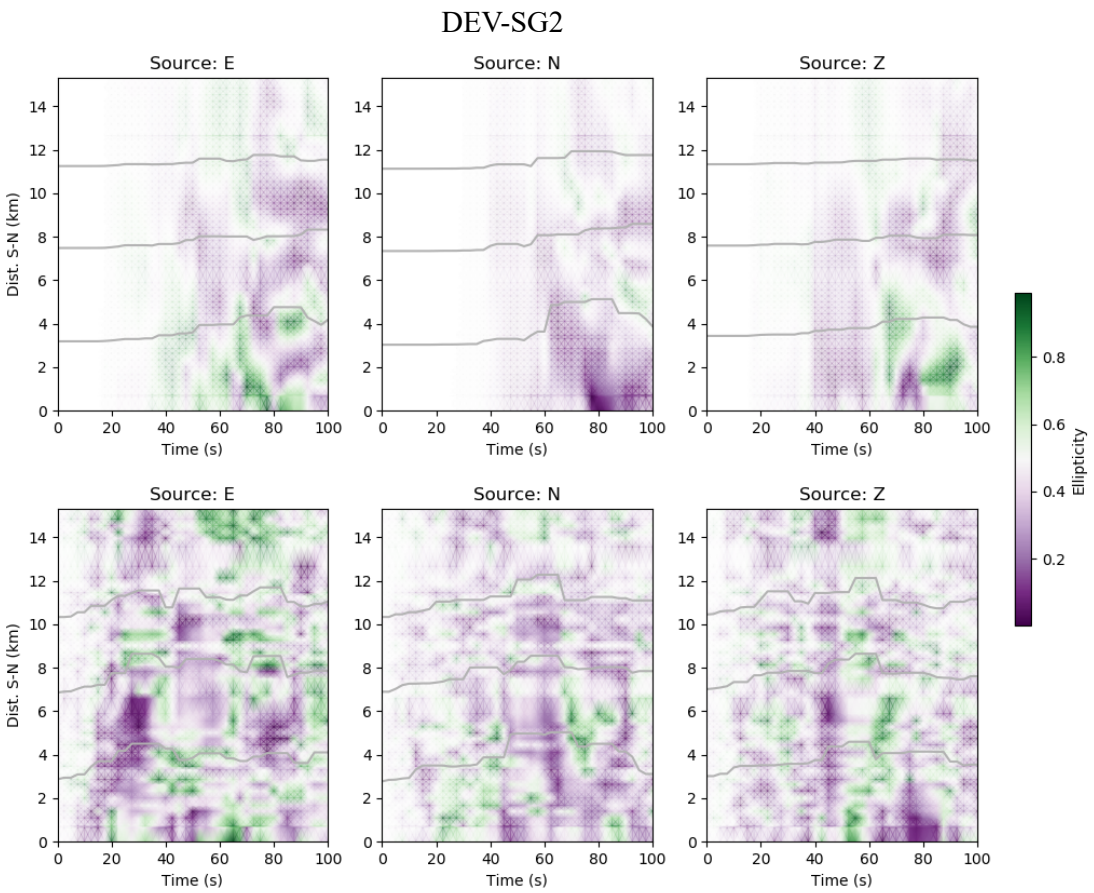

Figure 3.27: Same as Figure 3.26, but along SG2.

Chapter 4

Broadband Ground-Motion Simulation with Inter-Frequency Correlations

Ground motion simulations can be viable alternatives to empirical relations for seismic hazard analysis when data are sparse. Inter-frequency correlation is revealed in recorded seismic data, which has implications for seismic risk (Bayless and Abrahamson, 2018b). However, in many cases, simulated ground motion time series, in particular those originating from stochastic methods, lack inter-frequency correlation. Here, we develop a post-processing method to rectify simulation techniques that otherwise produce synthetic time histories deficient in inter-frequency correlation structure. An empirical correlation matrix is used in our approach to generate correlated random variables which are multiplied in the frequency domain with the Fourier amplitudes of the synthetic ground motion time series. The method is tested using the San Diego State University (SDSU) Broadband Ground-Motion Generation Module, which is a broadband ground motion generator that combines deterministic low-frequency and stochastic high-frequency signals, validated for the median of the spectral acceleration. Using our method, the results for 7 western U.S. earthquakes with magnitude between 5.0 and 7.2 show that empirical inter-frequency correlations are well simulated for a large number of realizations without biasing

the fit of the median of the spectral accelerations to data. The best fit of the inter-frequency correlation to data is obtained assuming that the horizontal components are correlated with a correlation coefficient of about 0.7.

4.1 Introduction

Numerical simulations can provide critical information for seismic hazard analysis at near-fault distances and for large-magnitude earthquakes where strong motion records are sparse. Recent advances in simulation methods due to improved source characterization, accuracy of wave propagation methods, and available computational resources have increased potential benefits for seismic hazard assessment. Ground motions generated by many broadband simulation methods (e.g., Atkinson and Assatourians, 2015; Graves and Pitarka, 2015; Olsen and Takedatsu, 2015; Crempien and Archuleta, 2015) have been used as input for engineering applications. However, while these methods have been tuned to produce median spectral acceleration in good agreement with that from strong motion data, less attention has been paid to their correlation behavior compared with empirical data (Bayless and Abrahamson, 2018b).

Seismic ground motions recorded from earthquakes reveal both inter-frequency and spatial correlation. A number of studies have been done over the past decades for the spatial correlation of response spectra (e.g., Wesson and Perkins, 2001; Kawakami and Mogi, 2003; Boore et al., 2003; Wang and Takada, 2005; Goda and Hong, 2008; Jayaram and Baker, 2009; Esposito and Iervolino, 2011; Sokolov et al., 2012; Sokolov and Wenzel, 2013; Loth and Baker, 2013; Markhvida et al., 2018; Heresi and Miranda, 2019) and inter-frequency correlations of response spectra (e.g., Baker and Cornell, 2006; Baker and Jayaram, 2008; Goda and Atkinson, 2009; Cimellaro, 2013; Akkar et al., 2014; Azarbakht et al., 2014; Abrahamson et al., 2014; Baker and Bradley, 2017), as well as some recent studies for inter-frequency correlations of Fourier spectra (e.g., Wharf, 2016; Stafford, 2017; Bayless and Abrahamson, 2019). In addition, many studies (e.g., Burks and

Baker, 2014; Weatherill et al., 2015; Stafford, 2017; Bayless and Abrahamson, 2018b) have demonstrated how seismic hazard assessment from simulations without such correlation can lead to underprediction of the seismic risk.

Stafford (2017) and Bayless and Abrahamson (2018b) both proposed techniques to incorporate inter-frequency correlations into the Boore (2003) simulation method. The Boore (2003) method generates a windowed Gaussian noise, transformed into the frequency domain and shaped by the deterministic Fourier amplitude spectrum for a scenario. Stafford (2017) used a model that is developed using two as-recorded horizontal components of unsmoothed Fourier Amplitude Spectrum (FAS). Bayless and Abrahamson (2018b) used an inter-frequency model that is developed using a smoothed and orientation-independent Fourier Amplitude Spectrum called Effective Amplitude Spectrum (EAS, as described in the following sections). We choose to apply the model developed using the EAS, applied to each of the two horizontal components, as our simulations are performed separately for each component. In contrast to the two recent studies mentioned above, we optimize the results for the inter-frequency correlation based on assumptions about the correlation of the two horizontal orthogonal components. Specifically, we find that incorporating two correlated FAS components can lead to a more accurate correlation structure in EAS, as described in the following sections.

The aim of this study is to develop a new approach for including inter-frequency correlation in stochastic ground motion simulations, and to demonstrate and validate the approach on an established and validated ground motion simulation tool. We have selected the San Diego State University (SDSU) Broadband Ground-Motion Generation Module (Olsen and Takedatsu, 2015) which is implemented on the Southern California Earthquake Center (SCEC) Broadband Platform (BBP) for this purpose. The SDSU BBP module participated in and passed the SCEC BBP validation exercise (Dreger et al., 2015; Goulet et al., 2015). The focus of this exercise was on validating simulated median pseudo-spectral accelerations for earthquakes in western and eastern US and Japan, as well as Next Generation Attenuation (NGA) Ground Motion Prediction

Equations (GMPEs). The stochastic component of the SDSU method has undergone extensive calibration with respect to pseudo-spectral acceleration (PSA) using GMPEs and strong motion data, aiming at improving the prediction of ground motions. However, the SDSU Module was designed to provide satisfactory fits to data for median ground motions only, lending itself as an appropriate testbed for incorporating inter-frequency correlation.

Pseudo-spectral acceleration (PSA) has traditionally been the preferred metric in earthquake engineering. However, PSA for a given response frequency depends (nonlinearly) on ground motion amplitudes over a range of frequencies. On the other hand, the Fourier Amplitude Spectrum (FAS) is simply obtained by Fourier transform of the time series and can therefore be used more directly in ground-motion simulation of time histories. This extends to inter-frequency correlations as well, as shown by Bayless and Abrahamson (2019) for ground motions from the Pacific Earthquake Engineering Research Center (PEER) Next Generation Attenuation (NGA) West2 database.

This paper starts by reviewing the intensity measure and the empirical covariance matrix for inter-frequency correlations that we used. We then explain and verify our approach to compute the correlation, and demonstrate how the inter-frequency correlation coefficients are applied to the SDSU Module.

4.2 Fourier Amplitude Spectrum (FAS) and Effective Amplitude Spectrum (EAS)

The Fourier Amplitude Spectrum (FAS) is the amplitude spectrum of the Fourier transform of the acceleration time series. The Effective Amplitude Spectrum (EAS), defined by Goulet et al.

(2018) as

$$EAS(f) = \sqrt{\frac{1}{2}[FAS_{HC1}^2(f) + FAS_{HC2}^2(f)]}\,, \tag{4.1}$$

is used as the intensity measure in our study. In Equation 4.1, FAS_{HC1} and FAS_{HC2} are the FAS of the two as-recorded horizontal components of a three component acceleration time series, and f is the frequency in Hertz. The EAS is independent of the recording instrument's orientation. The EAS is smoothed using the $\log_{10}$-scale Konno and Ohmachi (1998) smoothing window selected by Kottke et al. (2018):

$$W(f) = \left(\frac{\sin\left(b \log\left(\frac{f}{f_c}\right)\right)}{b \log\left(\frac{f}{f_c}\right)} \right)^4\,, \tag{4.2}$$

where W is the weight defined at frequency f for a window with center frequency f_c, and $b = \frac{2\pi}{b_w} = 60\pi$ where b_w is the smoothing window bandwidth in $\log_{10}$ units. For more details on the smoothing technique, the reader is referred to Kottke et al. (2018).

4.3 Inter-Frequency Correlations of Within-Event Residual

We follow the notation defined by Atik et al. (2010):

$$y_{es} = \mu_{es} + \delta B_e + \delta W_{es}\,, \tag{4.3}$$

where y_{es} is the natural logarithm of the ground-motion intensity measure observed at station s during earthquake e, and μ_{es} is the mean prediction of the natural logarithm of the intensity measure. δB_e is the between-event residual (or inter-event residual), representing the average shift of the observed ground motion for an individual earthquake e from the population mean prediction. δW_{es} is the within-event residual (or intra-event residual), depicting the misfit between

an individual observation at station s from the earthquake-specific mean prediction. The source effect average (over all azimuths) is described by the between-event residual that reflects the influence of factors such as stress drop and variation of slip in time and space that cannot be captured by the inclusion of magnitude, faulting style, and source depth in the mean prediction. Azimuthal variations in source, path, and site effects are described by the within-event residual that reflects the influence of factors such as crustal heterogeneity, deeper geological structure, and near-surface layering that cannot be captured by a simple distance metric and a site-classification based on the average shear-wave velocity (Atik et al., 2010). These residuals are normally distributed with zero mean and are uncorrelated with each other.

In this study, we focus on within-event variability only. While between-event variability conceptually can be treated in a similar fashion, it would require extensive changes to the target code for our analysis (the SDSU broadband module) as well as current computational procedures on the SCEC BBP. For these reasons, we leave the between-event variability for future work.

We target the EAS within-event residual through epsilon (ε),

$$\varepsilon(f) = \frac{\delta W_{es}(f)}{\phi(f)} = \frac{\ln EAS_{es}(f) - \mu_{\ln EAS_{es}}(f) - \delta B_e}{\varphi(f)} , \tag{4.4}$$

the within-event residual normalized by its standard deviation φ. The value of the within-event residual of EAS depends on frequency f. By the normalization, epsilon is standard normally distributed.

For a given set of observations, the values of ε at neighboring frequencies (f) are probabilistically correlated. If a ground motion intensity measure is stronger than average at a certain frequency, then it tends to also be stronger at nearby frequencies; however, the ε values are weakly correlated if the frequency pair are widely-separated (Bayless and Abrahamson, 2018b). The correlation coefficient of ε at two frequencies f_1 and f_2 can be estimated by the maximum likelihood estimator (Kutner et al., 2004) using the Pearson product-moment correlation coefficient (Fisher,

1958),

$$\rho_{\varepsilon(f_1)\varepsilon(f_2)} = \frac{\sum_{i=1}^{n} \left(\varepsilon_i(f_1) - \bar{\varepsilon}(f_1)\right)\left(\varepsilon_i(f_2) - \bar{\varepsilon}(f_2)\right)}{\sqrt{\sum_{i=1}^{n} \left(\varepsilon_i(f_1) - \bar{\varepsilon}(f_1)\right)^2}\sqrt{\sum_{i=1}^{n} \left(\varepsilon_i(f_2) - \bar{\varepsilon}(f_2)\right)^2}}\,, \tag{4.5}$$

in which n is the number of observations, $\varepsilon_i(f_1)$ and $\varepsilon_i(f_2)$ represent the ith observation of ε at frequencies f_1 and f_2, respectively, $\bar{\varepsilon}(f_1)$ and $\bar{\varepsilon}(f_2)$ are their sample means, and the expectations of $\bar{\varepsilon}(f_1)$ and $\bar{\varepsilon}(f_2)$ are both zero. This correlation is important when simulated time histories are used for seismic risk analysis because variability in the dynamic structural response will be underestimated if the inter-frequency correlation in simulated ground motions is unrealistically low (Bayless and Abrahamson, 2018b).

Bayless and Abrahamson (2019) generated an empirical estimate of ρ for the EAS within-event residual (with the within-event residual partitioned into site-to-site and within-site residuals) using the NGA-West2 database (regression from shallow crustal earthquakes, with M>3) at frequencies from 0.1 Hz to 24 Hz. The epsilon at each frequency, which was determined in the Bayless and Abrahamson (2018a) EAS model regression, was calculated from the individual EAS values and the earthquake-specific smoothed EAS median model for each recorded event at each station. Then, $\rho_{\varepsilon(f_1)\varepsilon(f_2)}$ was calculated for each pair of frequencies, f_1 and f_2. Figure 4.1 shows the empirical correlation coefficients. This empirical estimation for the inter-frequency correlation coefficients of the within-event residual is applied into the implementation method described in the following section.

4.4 The SDSU Broadband Ground-Motion Generation Module (SDSU Module)

The SDSU Module is a hybrid method that merges deterministic low-frequency (LF) synthetics and high-frequency (HF) scatterograms (Olsen and Takedatsu, 2015; Mai et al., 2010; Mena et al., 2010). On the SCEC BBP, the LFs are input through the standard rupture format using a number of source realizations (e.g., 50) from Graves and Pitarka (2015) kinematic source generator module. The HF scatterograms are simulated for each of the three components of ground motion based on the theory for multiple scattering by Zeng et al. (1991) and Zeng et al. (1993), with user-specified site scattering parameters in a 1D velocity structure. The direct P-wave arrival time is found using 3D ray tracing (Hole, 1992), after which the seismic-scattering wave energy appears. A source time function is then convolved with the scatterograms, assuming that the scattering operators and moment release originate throughout the fault but start at the hypocenter (Olsen and Takedatsu, 2015).

The SDSU Module is available to generate input synthetics for structural seismic risk analysis, as one of the ground motion generator modules of the SCEC BBP. However, the current SDSU Module does not incorporate realistic inter-frequency correlations into the simulations, as shown by the resulting inter-frequency correlation coefficients for the Loma Prieta earthquake using the current SDSU Module synthetics compared with the empirical result in Figure 4.2. At frequencies below the merging frequency between deterministic and stochastic signals (typically 1 Hz), the inter-frequency correlations of epsilon show some promise, but the correlation is still much lower than the empirical value. At frequencies above 1 Hz, the inter-frequency correlations of epsilon are significantly lower than the empirical value and drop to almost zero moving away from the reference frequency. In the following we develop and validate a method to implement inter-frequency correlations of epsilon for FAS into the synthetics generated by the SDSU BBP module.

4.5 Inclusion of Inter-frequency Correlation in the Fourier Amplitude Spectrum

The empirical correlation available for this study is developed for the orientation independent EAS, while our simulations generate separate components of ground motion. For that reason, we apply the EAS empirical correlation to the two horizontal components of FAS with assumptions about the relationship of the two components at the same station.

The procedure to generate a new ground motion time series with realistic inter-frequency correlations is as follows:

(1) take the Fourier transform of the two horizontal components of the synthetic ground motion time series. For each component, let the number of frequency points be n, the Fourier amplitude and phase at the ith frequency be $Amp_{mean}(i)$ and $Ph_{mean}(i)$, respectively;

(2) for the two horizontal components 1 and 2, respectively, sample normally distributed vector-valued random variable R_{HC1} and R_{HC2} with zero mean, constant standard deviation, σ, and size n. R_{HC1} and R_{HC2} can be independent or correlated with a correlation coefficient ρ_R. An illustration of R_{HC1} and R_{HC2} is shown in Figure 4.4(a). Correlated R_{HC1} and R_{HC2} (R^c_{HC1} and R^c_{HC2}) can be generated by:

(a) express covariance matrix C of the two components:

$$C = \begin{bmatrix} 1 & \rho_R \\ \rho_R & 1 \end{bmatrix} ; \tag{4.6}$$

(b) apply the Cholesky decomposition of covariance matrix C and

obtain a 2 by 2 upper triangular matrix U as:

$$C = U^T U \ ; \tag{4.7}$$

(c) right multiply matrix $[R_{HC1}\ ,\ R_{HC1}]$ by U and obtain two correlated random variables R^c_{HC1} and R^c_{HC2} with correlation coefficient ρ_R:

$$[R^c_{HC1}\ ,\ R^c_{HC2}] = [R_{HC1}\ ,\ R_{HC2}]\,U\ , \tag{4.8}$$

where $[R^c_{HC1}\ ,\ R^c_{HC2}]$ and $[R_{HC1}\ ,\ R_{HC2}]$ are n by 2 matrices with R^c_{HC1} or R_{HC1} as the first columns and R^c_{HC2} or R_{HC2} as the second columns, respectively. The upper triangular matrix is used here because the correlation is between the two columns of the matrix $\left[R^c_{HC1}\ ,\ R^c_{HC2}\right]$. An illustration of R^c_{HC1} and R^c_{HC2} is shown in Figure 4.4(b).

The following steps are the same for R_{HC1} and R_{HC2} (or R^c_{HC1} and R^c_{HC2}), so the 'HC1' and 'HC2' subscripts (or superscript 'c') are dropped for notational brevity and R refers to either of the two random variables.

(3) express the empirical correlation $\rho_{\varepsilon(f_1)\varepsilon(f_2)}$ from Equation 4.5 in matrix form Σ (n by n, real, symmetric, and positive definite), and apply the Cholesky decomposition of Σ as

$$\Sigma = LL^T\ , \tag{4.9}$$

where L is a n by n lower triangular matrix (Seydel, 2017);

(4) left multiply random variable R in (3) (within the corresponding frequency range 0.1-24 Hz) by L as

$$S = LR\ , \tag{4.10}$$

to generate a normal random variable S with zero mean and covariance equal to $\sigma^2 LL^T = \sigma^2\Sigma$ (Seber and Lee, 2012). The lower triangular matrix is used here because the correlation is between the rows of R. An illustration of S^c_{HC1} and S^c_{HC2} is shown in Figure 4.4(c). Note that, here, for the corresponding frequency points outside the 0.1-24Hz range, S=R;

(5) multiply the exponential of S with Amp_{mean} to compute the Fourier amplitude of the new ground motion synthetics, Amp_{new}, as

$$Amp_{new}(i) = Amp_{mean}(i)\exp S_i \; ; \tag{4.11}$$

(6) calculate the new ground-motion time series by applying the inverse Fourier transform to the amplitude spectrum obtained in (5) and phase spectrum from (1).

The method can be applied as the last step to simulate the ground-motion using the SDSU SCEC BBP module. It maintains the mean of the natural logarithm of the Fourier amplitude for the updated ground-motion synthetics, since the mean of S_i in step (5) equals 0. Taking the natural logarithm of the equation in step (5) we get

$$\ln Amp_{new}(i) = \ln Amp_{mean}(i) + S_i \; . \tag{4.12}$$

We tested our method by calculating the within-event residual for simulations of the Loma Prieta earthquake using the SDSU broadband module (Olsen and Takedatsu, 2015) on the SCEC BBP. We generate 50 source realizations for the Loma Prieta earthquake using the kinematic source generator module by Graves and Pitarka (2015). These 50 source realizations have variations in hypocenter locations and slip distributions that are represented by the between-event residual. Here, we refer to each of the 50 source realizations as a separate event. For each event, we generate 10 simulations with imposed within-event inter-frequency correlation at all

the stations. The 10 simulations differ by the random variables (R_{HC1} and R_{HC2}) in Step (2). The mean of the 10 simulations and their within-event residual are computed for each event, respectively. The within-event residual at all stations and all the 50 events are then pooled together at the corresponding frequencies. Note that, at each station and each frequency f, the epsilon of within-event residual $\varepsilon(f)$ has a size of 500 (50 events by 10 simulations). A total of 40 stations are used for the Loma Prieta earthquake in our simulations, so that the population of the epsilon of the within-event residual $\varepsilon(f)$ at each frequency f is 20,000 (500 by 40 stations).

This method generates correlated synthetic time series that are very similar to the original results from the current SDSU BBP Module. Figures 4.5 and 4.6 show one component of synthetic time histories (velocity and acceleration) and FAS, respectively, at station 8001-CLS (see Figure 4.3 for location) for the Loma Prieta earthquake before and after implementing the inter-frequency correlations. A suite of 10 simulated EAS sequences for one of the 50 events at station 8001-CLS for the Loma Prieta earthquake with inter-frequency correlation of the within-event residual implemented using this method is shown in Figure 4.7. Suites of 10 simulated EAS sequences for the rest of the 50 events at station 8001-CLS for the Loma Prieta earthquake are provided in Figure S4.1. Figure 4.8(a) shows that the resulting inter-frequency correlation coefficients obtained by our method (using independent R_{HC1} and R_{HC2} in Step (2)) for the Loma Prieta earthquake compare very well with the empirical result, as intended. Figure 4.9 compares the bias (natural log misfit between the median observed and predicted PSA) for the uncorrelated and correlated SDSU synthetics. It is clear that the addition of correlation to the synthetic time histories results in insignificant changes in the bias. In other words, the method can be used as a post-processing step to incorporate correlation into an already established and validated ground motion generator, without biasing the median spectral accelerations.

A small bias remains between the empirical values and the inter-frequency correlation coefficients obtained by our method using independent R_{HC1} and R_{HC2} (Figure 4.8(a)). This bias can be minimized using correlated R_{HC1} and R_{HC2} in Step (2). Baker and Jayaram (2008) show

that epsilon of response spectral accelerations for orthogonal components of ground motions are correlated, with correlation coefficients slightly dependent on period (0.7 - 0.9 for periods from 0.01 s to 10 s). This result indicates that the different components of EAS ground motion (e.g., the two horizontal components) are also correlated. Since EAS is the square root of the mean power of the two horizontal components of FAS (FAS_{HC1}, FAS_{HC2}), implementation of correlated random variables R_{HC1} and R_{HC2} into FAS_{HC1} and FAS_{HC2} can indeed further improve the correlations in EAS. We generate R_{HC1} and R_{HC2} with correlation coefficient ρ_R equal to 0.7 at all frequencies in Step (2) and compute the resulting inter-frequency correlations in EAS (see Figure 4.8(b)). Note that the fit to the empirical value is further improved as compared with the inter-frequency correlations in EAS using independent random variables for the two horizontal components. The value of the correlation coefficient here is chosen to provide an optimal fit in the final inter-frequency correlation results and similar to those described in Baker and Jayaram (2008). The resulting inter-frequency correlation coefficients using other values of correlation coefficient between R_{HC1} and R_{HC2} are provided in Figures S4.2 – S4.4, available in the electronic supplement of this article. These results suggest that a correlation analysis between the FAS values of two orthogonal components may further improve the results.

Figures for the resulting inter-frequency correlation coefficients from the other six western U.S. earthquakes are provided in Figures S4.5 – S4.10, available in the electronic supplement of this article.

4.6 Discussion

We have developed and tested our method to include inter-frequency correlation using the SCEC SDSU BBP code. However, the approach can easily be implemented in other simulation methods. The SDSU SCEC BBP Module V1.6.2 has almost no correlation in the simulated result, so the empirical correlation matrix was applied directly on the broadband time histories with the

desired results. If the method is applied to synthetic time histories that already include a level of inter-frequency correlation different from that for empirical data, the correlation matrix Σ in step (3) can be adjusted accordingly. In addition, the empirical correlation coefficients used in this study are rather general without statistically significant magnitude, distance, site parameter, or regional dependencies (Bayless and Abrahamson, 2019). However, studies on the empirical correlations are on-going, and more parameter-specific results (e.g., for source and region) are likely to be obtained in the future. Including such updates into our method will be straightforward due to its flexible nature.

In our approach, the inter-frequency correlations are only implemented into the amplitude spectrum where we modify the Fourier amplitude while using the original phase spectrum (as is also the case for the correlation analysis of other methods, e.g., Stafford, 2017; Bayless and Abrahamson, 2018b). This is equivalent to applying a zero-phase filter to the uncorrelated synthetics to produce the correlated synthetics. We also tested the use of a causal minimum-phase filter and obtained insignificant differences from the zero-phase filter in our application.

It is worth noting the similarity on how S_i (step (5) of our method) and the within-event residual affect the inter-frequency correlations. The value of the standard deviation σ in Step (2) should be chosen such that it is consistent with the standard deviation of the original FAS. σ can also be implemented as frequency dependent if needed. For the SDSU SCEC BBP module, the same equations and scaling are used for simulating each component of the ground motions, thus σ is chosen to be the same for each component. However, other simulation methodologies may warrant different treatment of σ.

Figure 4.10 shows the resulting inter-frequency correlation coefficients in response spectral accelerations obtained by our method for the Loma Prieta earthquake. The comparison shows a good level of agreement between our simulated result and the within-event correlation model regressed by Baker and Jayaram (2008). This result shows that implementing inter-frequency correlations developed for FAS can also improve the correlation in spectral accelerations.

This method can be further enhanced to incorporate (frequency-dependent) spatial correlations into the simulations by extending the correlated random variables in Step (2) to two-dimensions, in order to facilitate even more realistic seismic risk analysis. This effort, along with correlation analysis of the FAS components, is part of an ongoing project.

4.7 Conclusions

We present a post-processing method to introduce inter-frequency correlations into seismic synthetic time histories, mimicking that seen in recorded ground motions, in order to allow more realistic seismic risk analysis. After implementing the correlation into the current SDSU SCEC BBP Module we show that the method generates correlated synthetic time series with inter-frequency correlation that match that of empirical data very well. We show that incorporating the inter-frequency correlation developed for the Fourier amplitudes also significantly improves the correlations in response spectral accelerations. Introducing the inter-frequency correlation affects the median spectral accelerations insignificantly, and therefore retains the goodness-of-fit.

Data and Resources

Analyses and graphics production were performed using the numeric computing environment MATLAB (www.mathworks.com, last accessed May 2019). The empirical correlation coefficients table was provided by Jeff Bayless and Norman Abrahamson. Simulations in this article are performed using the Southern California Earthquake Center (SCEC) Broadband Platform (BBP) code. Figures showing examples of simulated effective amplitude spectrum (EAS), interfrequency correlation implemented in broadband synthetics for the Northridge, Landers, Chino Hills, North Palm Springs, Chino Hills, and Whittier events, and dependency of the results on the correlation between the two horizontal components are provided in the supplemental

material of this article.

Acknowledgements

This research was supported by the Southern California Earthquake Center (SCEC; Contribution Number 9932). SCEC is funded by National Science Foundation (NSF) Cooperative Agreement EAR-1600087 and U.S. Geological Survey (USGS) Cooperative Agreement G17AC00047. The authors are grateful to Jeff Bayless, two anonymous reviewers, Associate Editor Hiroshi Kawase, and Editor-in-Chief Thomas Pratt for useful review comments and suggestions that helped improve the article.

Chapter 4, in full, is a reformatted version of the material as it appears in Bulletin of the Seismological Society of America: Wang, N., Takedatsu, R., Olsen, K.B., and Day, S.M. (2019). Broadband ground-motion simulation with interfrequency correlations. *Bulletin of the Seismological Society of America*, 109(6), 2437-2446. The dissertation author was the primary investigator and author of this paper.

References

Abrahamson, N. A., Silva, W. J., and Kamai, R. (2014). "Summary of the ASK14 ground motion relation for active crustal regions". In: *Earthquake Spectra* 30.3, pp. 1025–1055.

Akkar, S., Sandıkkaya, M. A., and Ay, B. Ö. (2014). "Compatible ground-motion prediction equations for damping scaling factors and vertical-to-horizontal spectral amplitude ratios for the broader Europe region". In: *Bulletin of Earthquake Engineering* 12.1, pp. 517–547.

Atik, L. A., Abrahamson, N., Bommer, J. J., Scherbaum, F., Cotton, F., and Kuehn, N. (2010). "The variability of ground-motion prediction models and its components". In: *Seismological Research Letters* 81.5, pp. 794–801.

Atkinson, G. M. and Assatourians, K. (2015). "Implementation and validation of EXSIM (a stochastic finite-fault ground-motion simulation algorithm) on the SCEC broadband platform". In: *Seismological Research Letters* 86.1, pp. 48–60.

Azarbakht, A, Mousavi, M, Nourizadeh, M, and Shahri, M (2014). "Dependence of correlations between spectral accelerations at multiple periods on magnitude and distance". In: *Earthquake engineering & structural dynamics* 43.8, pp. 1193–1204.

Baker, J. W. and Bradley, B. A. (2017). "Intensity measure correlations observed in the NGA-West2 database, and dependence of correlations on rupture and site parameters". In: *Earthquake Spectra* 33.1, pp. 145–156.

Baker, J. W. and Cornell, C. A. (2006). "Spectral shape, epsilon and record selection". In: *Earthquake Engineering & Structural Dynamics* 35.9, pp. 1077–1095.

Baker, J. W. and Jayaram, N. (2008). "Correlation of spectral acceleration values from NGA ground motion models". In: *Earthquake Spectra* 24.1, pp. 299–317.

Bayless, J. and Abrahamson, N. A. (2018a). *An empirical model for Fourier amplitude spectra using the NGA-West2 database, PEER Report 2018/07*. Report. Pacific Earthquake Engineering Research Center, University of California, Berkeley.

— (2018b). "Evaluation of the Interperiod Correlation of Ground-Motion SimulationsEvaluation of the Interperiod Correlation of Ground-Motion Simulations". In: *Bulletin of the Seismological Society of America* 108.6, pp. 3413–3430.

— (2019). "An Empirical Model for the Interfrequency Correlation of Epsilon for Fourier Amplitude Spectra". In: *Bulletin of the Seismological Society of America* 109.3, pp. 1058–1070.

Boore, D. M. (2003). "Simulation of ground motion using the stochastic method". In: *Pure and applied geophysics* 160.3, pp. 635–676.

Boore, D. M., Gibbs, J. F., Joyner, W. B., Tinsley, J. C., and Ponti, D. J. (2003). "Estimated ground motion from the 1994 Northridge, California, earthquake at the site of the Interstate 10 and La Cienega Boulevard bridge collapse, West Los Angeles, California". In: *Bulletin of the Seismological Society of America* 93.6, pp. 2737–2751.

Burks, L. S. and Baker, J. W. (2014). "Validation of ground-motion simulations through simple proxies for the response of engineered systemsvalidation of ground-motion simulations through simple proxies for the response of engineered systems". In: *Bulletin of the Seismological Society of America* 104.4, pp. 1930–1946.

Cimellaro, G. P. (2013). "Correlation in spectral accelerations for earthquakes in Europe". In: *Earthquake Engineering & Structural Dynamics* 42.4, pp. 623–633.

Crempien, J. G. and Archuleta, R. J. (2015). "UCSB method for simulation of broadband ground motion from kinematic earthquake sources". In: *Seismological Research Letters* 86.1, pp. 61–67.

Dreger, D. S., Beroza, G. C., Day, S. M., Goulet, C. A., Jordan, T. H., Spudich, P. A., and Stewart, J. P. (2015). "Validation of the SCEC broadband platform v14. 3 simulation methods using pseudospectral acceleration data". In: *Seismological Research Letters* 86.1, pp. 39–47.

Esposito, S. and Iervolino, I. (2011). "PGA and PGV spatial correlation models based on European multievent datasets". In: *Bulletin of the Seismological Society of America* 101.5, pp. 2532–2541.

Fisher, R. A. (1958). *Statistical methods for research workers*. Vol. 13. Edinburgh, United Kingdom: Hafner.

Goda, K. and Atkinson, G. M. (2009). "Probabilistic characterization of spatially correlated response spectra for earthquakes in Japan". In: *Bulletin of the Seismological Society of America* 99.5, pp. 3003–3020.

Goda, K. and Hong, H.-P. (2008). "Spatial correlation of peak ground motions and response spectra". In: *Bulletin of the Seismological Society of America* 98.1, pp. 354–365.

Goulet, C., Abrahamson, N., Somerville, P., and Wooddell, K. (2015). "The SCEC Broadband Platform validation exercise for pseudo-spectral acceleration: Methodology for code validation in the context of seismic hazard analyses". In: *Seismol. Res. Lett* 86.1, pp. 17–26.

Goulet, C., Kottke, A, Boore, D., Bozorgnia, Y, Hollenback, J, Kishida, T, Der Kiureghian, A, Ktenidou, O., Kuehn, N., Rathje, E., Thompson, E., and Wang, X. (May 2018). "Effective amplitude spectrum (EAS) as a metric for ground motion modeling using Fourier amplitudes". In: *2018 Seismology of the Americas Meeting*. Miami, Florida: Seismology of the Americas Meeting.

Graves, R. and Pitarka, A. (2015). "Refinements to the Graves and Pitarka (2010) broadband ground-motion simulation method". In: *Seismological Research Letters* 86.1, pp. 75–80.

Heresi, P. and Miranda, E. (2019). "Uncertainty in intraevent spatial correlation of elastic pseudo-acceleration spectral ordinates". In: *Bulletin of Earthquake Engineering* 17.3, pp. 1099–1115.

Hole, J. (1992). "Nonlinear high-resolution three-dimensional seismic travel time tomography". In: *Journal of Geophysical Research: Solid Earth* 97.B5, pp. 6553–6562.

Jayaram, N. and Baker, J. W. (2009). "Correlation model for spatially distributed ground-motion intensities". In: *Earthquake Engineering & Structural Dynamics* 38.15, pp. 1687–1708.

Kawakami, H. and Mogi, H. (2003). "Analyzing spatial intraevent variability of peak ground accelerations as a function of separation distance". In: *Bulletin of the Seismological Society of America* 93.3, pp. 1079–1090.

Konno, K. and Ohmachi, T. (1998). "Ground-motion characteristics estimated from spectral ratio between horizontal and vertical components of microtremor". In: *Bulletin of the Seismological Society of America* 88.1, pp. 228–241.

Kottke, A, Rathje, E, Boore, D., Thompson, E, Hollenback, J, Kuehn, N, Goulet, C., Abrahamson, N., Bozorgnia, Y, and Der Kiureghian, A (2018). *Selection of random vibration procedures for the NGA east project, PEER Report No. 2018/05*. Report. Pacific Earthquake Engineering Research Center, University of California, Berkeley.

Kutner, M., Nachtsheim, C., and Neter, J (2004). *Applied linear regression models,Fourth Ed*. New York, New York: McGraw-Hill/Irwin.

Loth, C. and Baker, J. W. (2013). "A spatial cross-correlation model of spectral accelerations at multiple periods". In: *Earthquake Engineering & Structural Dynamics* 42.3, pp. 397–417.

Mai, P. M., Imperatori, W., and Olsen, K. B. (2010). "Hybrid broadband ground-motion simulations: Combining long-period deterministic synthetics with high-frequency multiple S-to-S backscattering". In: *Bulletin of the Seismological Society of America* 100.5A, pp. 2124–2142.

Markhvida, M., Ceferino, L., and Baker, J. W. (2018). "Modeling spatially correlated spectral accelerations at multiple periods using principal component analysis and geostatistics". In: *Earthquake Engineering & Structural Dynamics* 47.5, pp. 1107–1123.

Mena, B., Mai, P. M., Olsen, K. B., Purvance, M. D., and Brune, J. N. (2010). "Hybrid broadband ground-motion simulation using scattering Green's functions: Application to large-magnitude events". In: *Bulletin of the Seismological Society of America* 100.5A, pp. 2143–2162.

Olsen, K. and Takedatsu, R. (2015). “The SDSU broadband ground-motion generation module BBtoolbox version 1.5”. In: *Seismological Research Letters* 86.1, pp. 81–88.

Seber, G. A. and Lee, A. J. (2012). *Linear regression analysis*. Vol. 329. Hoboken, New Jersey: John Wiley and Sons.

Seydel, R. U. (2017). “Generating random numbers with specified distributions”. In: *Tools for Computational Finance*. London, United Kingdom: Springer.

Sokolov, V. and Wenzel, F. (2013). “Further analysis of the influence of site conditions and earthquake magnitude on ground-motion within-earthquake correlation: analysis of PGA and PGV data from the K-NET and the KiK-net (Japan) networks”. In: *Bulletin of Earthquake Engineering* 11.6, pp. 1909–1926.

Sokolov, V., Wenzel, F., Wen, K.-L., and Jean, W.-Y. (2012). “On the influence of site conditions and earthquake magnitude on ground-motion within-earthquake correlation: analysis of PGA data from TSMIP (Taiwan) network”. In: *Bulletin of Earthquake Engineering* 10.5, pp. 1401–1429.

Stafford, P. J. (2017). “Interfrequency Correlations among Fourier Spectral Ordinates and Implications for Stochastic Ground-Motion SimulationInterfrequency Correlations among Fourier Spectral Ordinates and Implications”. In: *Bulletin of the Seismological Society of America* 107.6, pp. 2774–2791.

Wang, M. and Takada, T. (2005). “Macrospatial correlation model of seismic ground motions”. In: *Earthquake spectra* 21.4, pp. 1137–1156.

Weatherill, G., Silva, V, Crowley, H, and Bazzurro, P (2015). “Exploring the impact of spatial correlations and uncertainties for portfolio analysis in probabilistic seismic loss estimation”. In: *Bulletin of Earthquake Engineering* 13.4, pp. 957–981.

Wesson, R. L. and Perkins, D. M. (2001). “Spatial correlation of probabilistic earthquake ground motion and loss”. In: *Bulletin of the Seismological Society of America* 91.6, pp. 1498–1515.

Wharf, C. (2016). “Discrete multivariate representation of Fourier spectral ordinates, M.Sc. Thesis”. MA thesis. Department of Civil and Environmental Engineering, London, United Kingdom: Imperial College London.

Zeng, Y., Aki, K., and Teng, T.-L. (1993). “Mapping of the high-frequency source radiation for the Loma Prieta earthquake, California”. In: *Journal of Geophysical Research: Solid Earth* 98.B7, pp. 11981–11993.

Zeng, Y., Su, F., and Aki, K. (1991). “Scattering wave energy propagation in a random isotropic scattering medium: 1. Theory”. In: *Journal of Geophysical Research: Solid Earth* 96.B1, pp. 607–619.

Tables and Figures

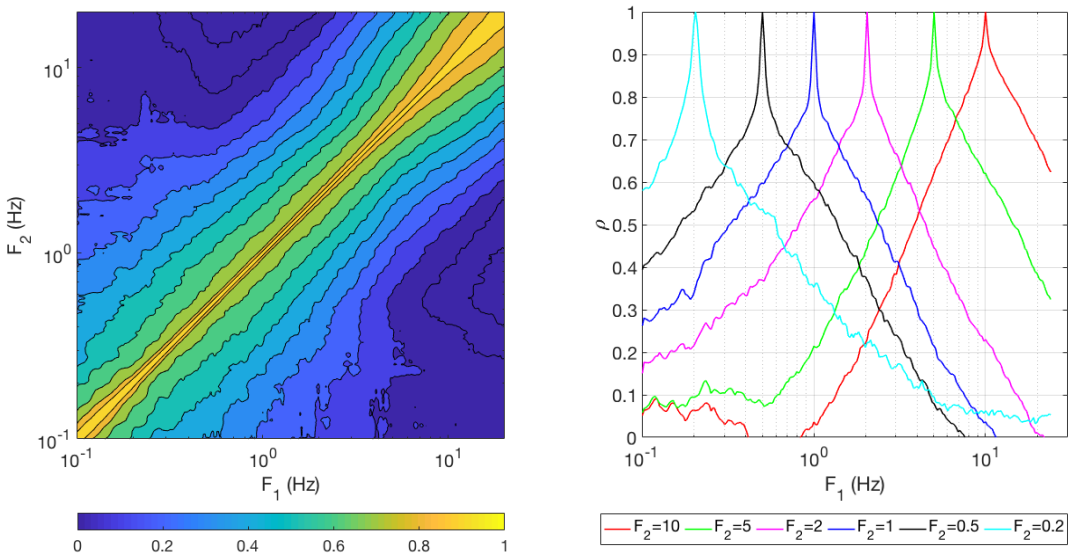

Figure 4.1: (left) Empirical within-event residual inter-frequency correlation coefficients contour plot and (right) cross-section versus frequency at conditioning frequencies 0.2 Hz, 0.5 Hz, 1 Hz, 2 Hz, 5 Hz, and 10 Hz. Modified from Bayless and Abrahamson (2019).

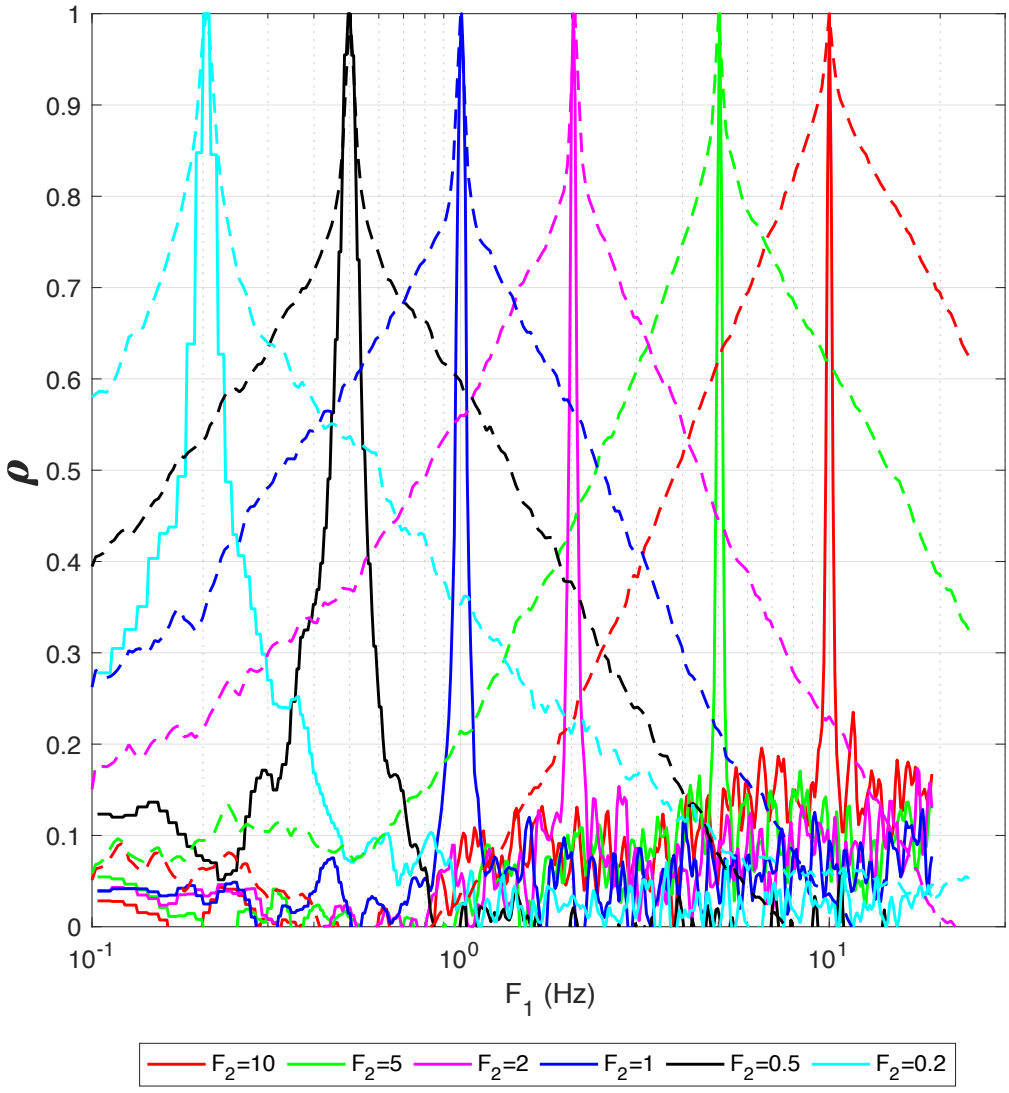

Figure 4.2: The inter-frequency correlation coefficients of epsilon at reference frequencies 0.2 Hz, 0.5 Hz, 1 Hz, 2 Hz, 5 Hz and 10 Hz from the current SDSU Module using 50 source realizations of the Loma Prieta earthquake (solid lines), compared to the empirical correlation coefficients (Bayless and Abrahamson (2019); dashed lines).

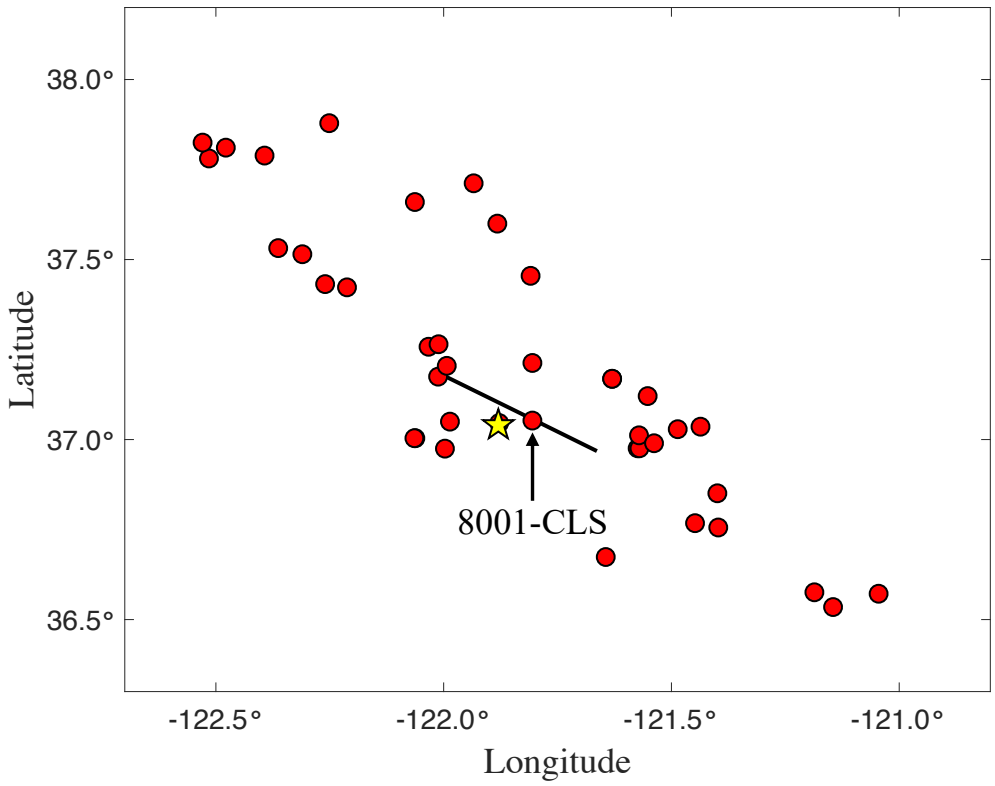

Figure 4.3: Location map for the Loma Prieta earthquake. The star depicts the epicenter, the bold line the fault trace, and the red dots show the stations. Station 8001-CLS, where we compare time histories, is highlighted. Figure modified from SCEC BBP output.

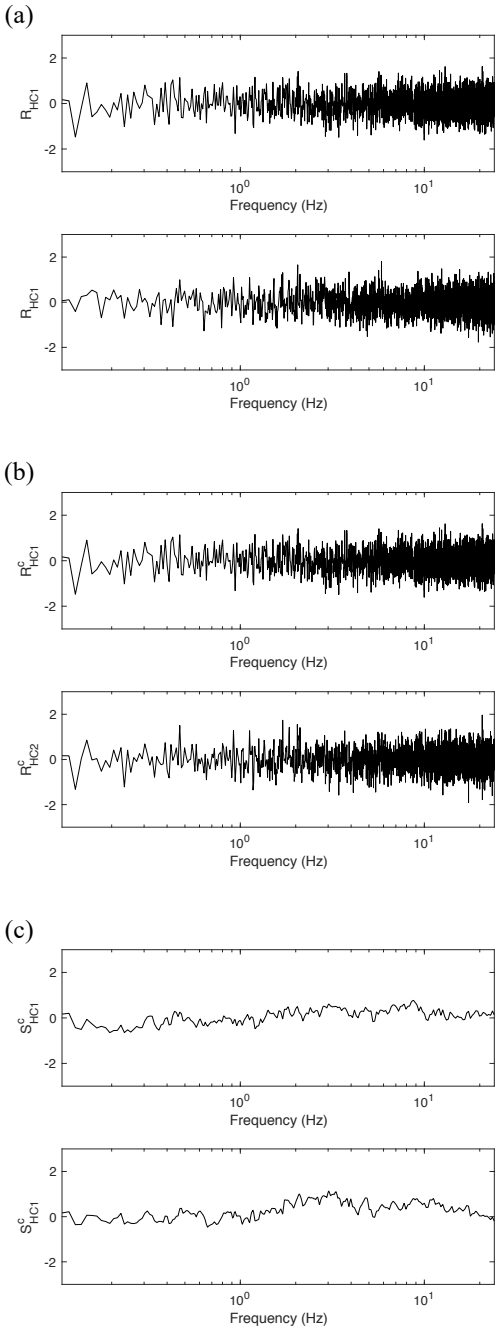

Figure 4.4: Illustration of steps (2) through (4) showing two independent normally distributed vector-valued random variables, corresponding to frequencies from 0.1Hz to 24Hz for the two horizontal FAS components in terms of (a) R_{HC1} and R_{HC2} (b) R^c_{HC1} and R^c_{HC2}, and (c) S^c_{HC1} and S^c_{HC2}.

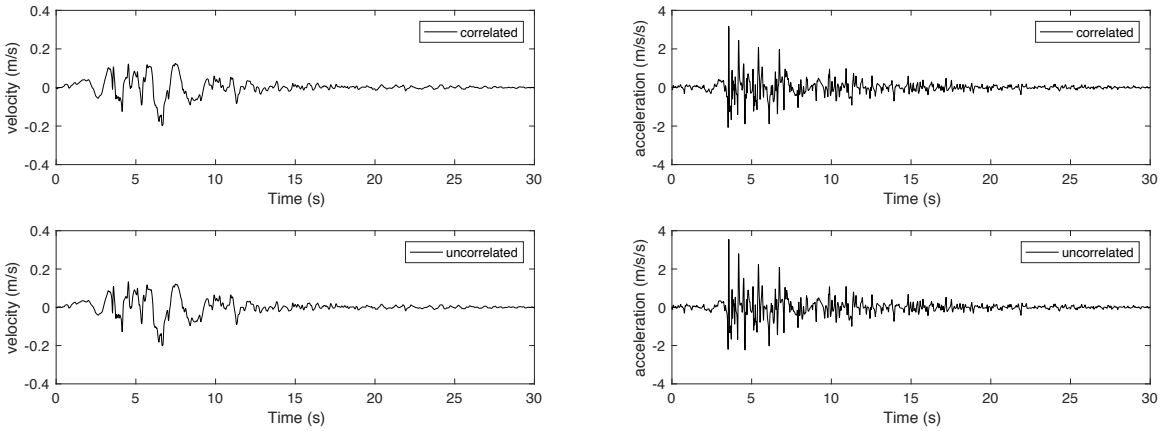

Figure 4.5: Examples of the north-south component of velocities (left) and accelerations (right) at station 8001-CLS for the Loma Prieta earthquake after (top) and before (bottom) implementing the inter-frequency correlations.

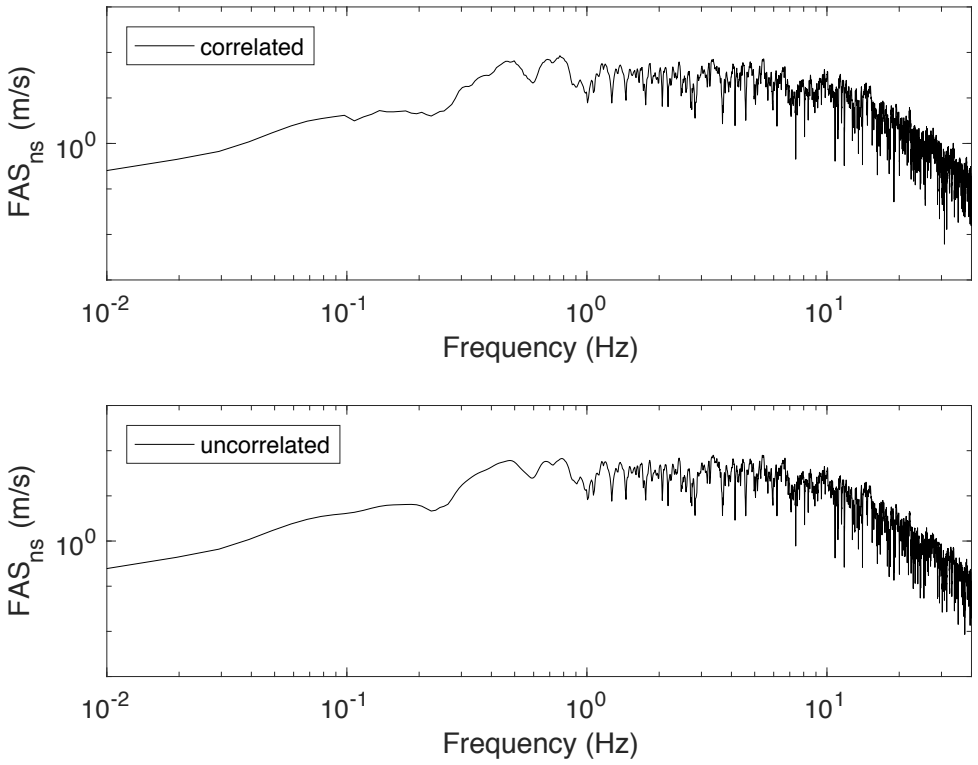

Figure 4.6: Examples of the north-south component of FAS for one simulation at station 8001-CLS for the Loma Prieta earthquake (top) after and (bottom) before implementing the inter-frequency correlations.

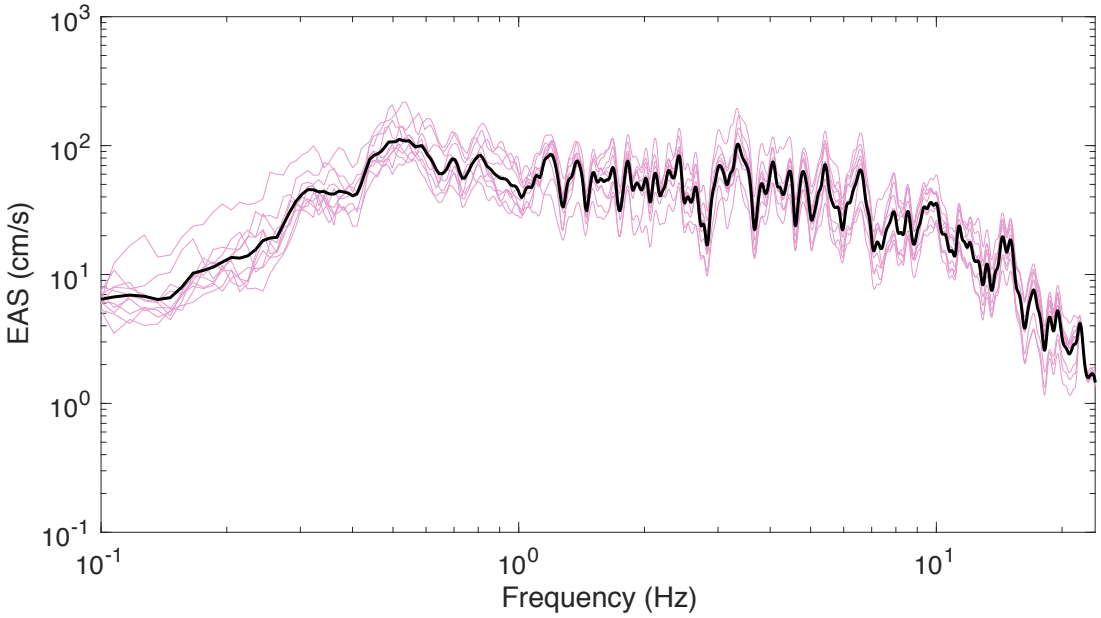

Figure 4.7: A suite of 10 simulated EAS (thin pink lines) with inter-frequency correlation of the within-event residual implemented and their mean (bold black line) for one of the 50 events at station 8001-CLS for the Loma Prieta earthquake. Suites of 10 simulated EAS for the rest of the 50 events at station 8001-CLS for the Loma Prieta earthquake are provided in Figure S4.1.

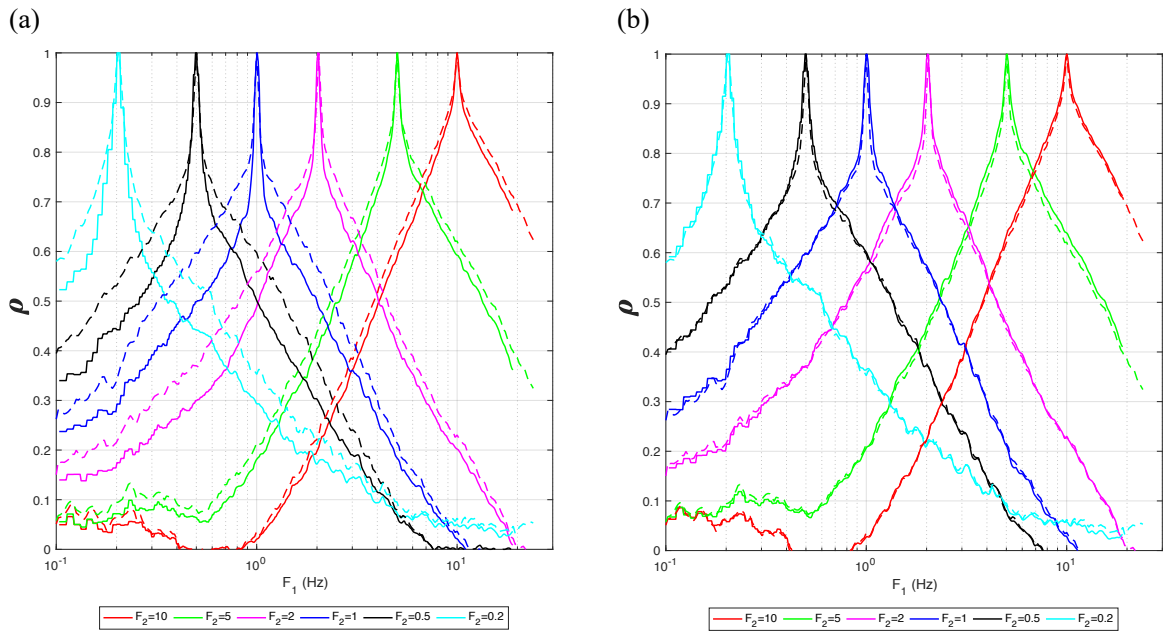

Figure 4.8: The inter-frequency correlation coefficients of epsilon at reference frequencies 0.2 Hz, 0.5 Hz, 1 Hz, 2 Hz, 5 Hz and 10 Hz from the empirical correlation coefficients (Bayless and Abrahamson (2019); dashed lines) and the SDSU SCEC BBP Module (solid lines) after applying our method for two horizontal components using (a) independent random variables and (b) correlated random variables with a correlation coefficient of 0.7 for the Loma Prieta earthquake.

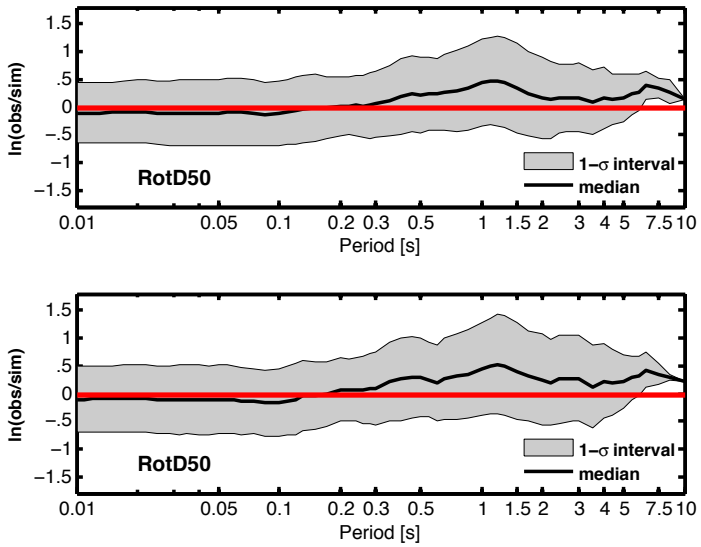

Figure 4.9: The logarithm misfit between the median observation of 50 source realizations and the median prediction for the current (top) and improved (bottom) SDSU synthetics for the Loma Prieta earthquake.

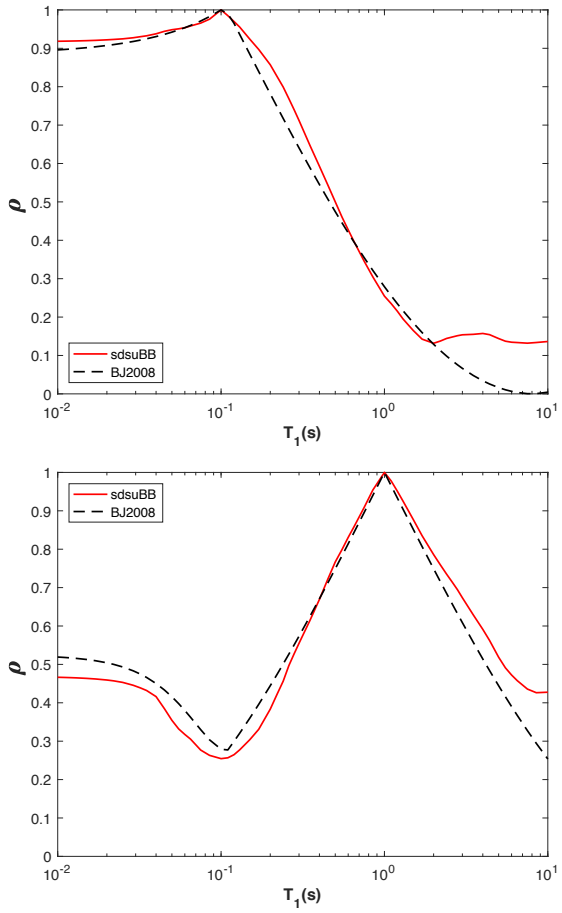

Figure 4.10: Comparison of the inter-frequency spectral acceleration correlation coefficients of epsilon at reference periods 0.1 s (top) and 1 s (bottom) from the Baker and Jayaram (2008) model (dashed black lines) and the SDSU SCEC BBP Module after applying our method (solid red lines) for the Loma Prieta earthquake with 50 simulations.

Supplementary Materials

Figures showing examples of simulated EAS, inter-frequency correlation implemented in broadband synthetics for the Northridge, Landers, Chino Hills, North Palm Springs, Chino Hills, and Whittier earthquakes, and dependency of the results on the correlation between the two horizontal components.

Suite of 10 simulated EAS for each of the 50 events at station 8001-CLS for the Loma Prieta earthquake with inter-frequency correlation of the within-event residual implemented are shown in Figure S4.1.

Correlation between the two horizontal components

Baker and Jayaram (2008) show that epsilon of spectral accelerations for orthogonal components of ground motions are correlated, with correlation coefficients between 0.7 to 0.9, and slightly dependent on period from 0.01s to 10s. This result indicates that the two horizontal components of EAS ground motion may also be correlated. We generate R_{HC1} and R_{HC2} with correlation coefficient of 0.7 (Figure S4.2), 0.8 (Figure S4.3) and 0.9 (Figure S4.4) at all frequencies and compute the resulting inter-frequency correlations in EAS, respectively. The value 0.7 of the correlation coefficient is found to give the best fit in the final inter-frequency correlation results and similar to those described in Baker and Jayaram (2008).

Inter-frequency correlation implemented into the other six western U.S. earthquakes

In addition to the M6.9 1989 Loma Prieta earthquake, we have also implemented inter-frequency correlation into six other SCEC validation earthquakes in California: M7.2 1992 Landers; M6.7 1994 Northridge; M6.1 1986 North Palm Springs; M5.9 1987 Whittier; M5.4 2008 Chino Hills; and M5.5 2007 Alum Rock. The final inter-frequency correlation coefficients of epsilon for the six earthquakes using 50 source realizations compared with the empirical

correlation coefficients calculated by Bayless and Abrahamson (2018b) are shown in Figure S4.5 – S4.10. The results for all the 7 western U.S. earthquakes with magnitude between 5.0 and 7.2 show that empirical inter-frequency correlations are well predicted.

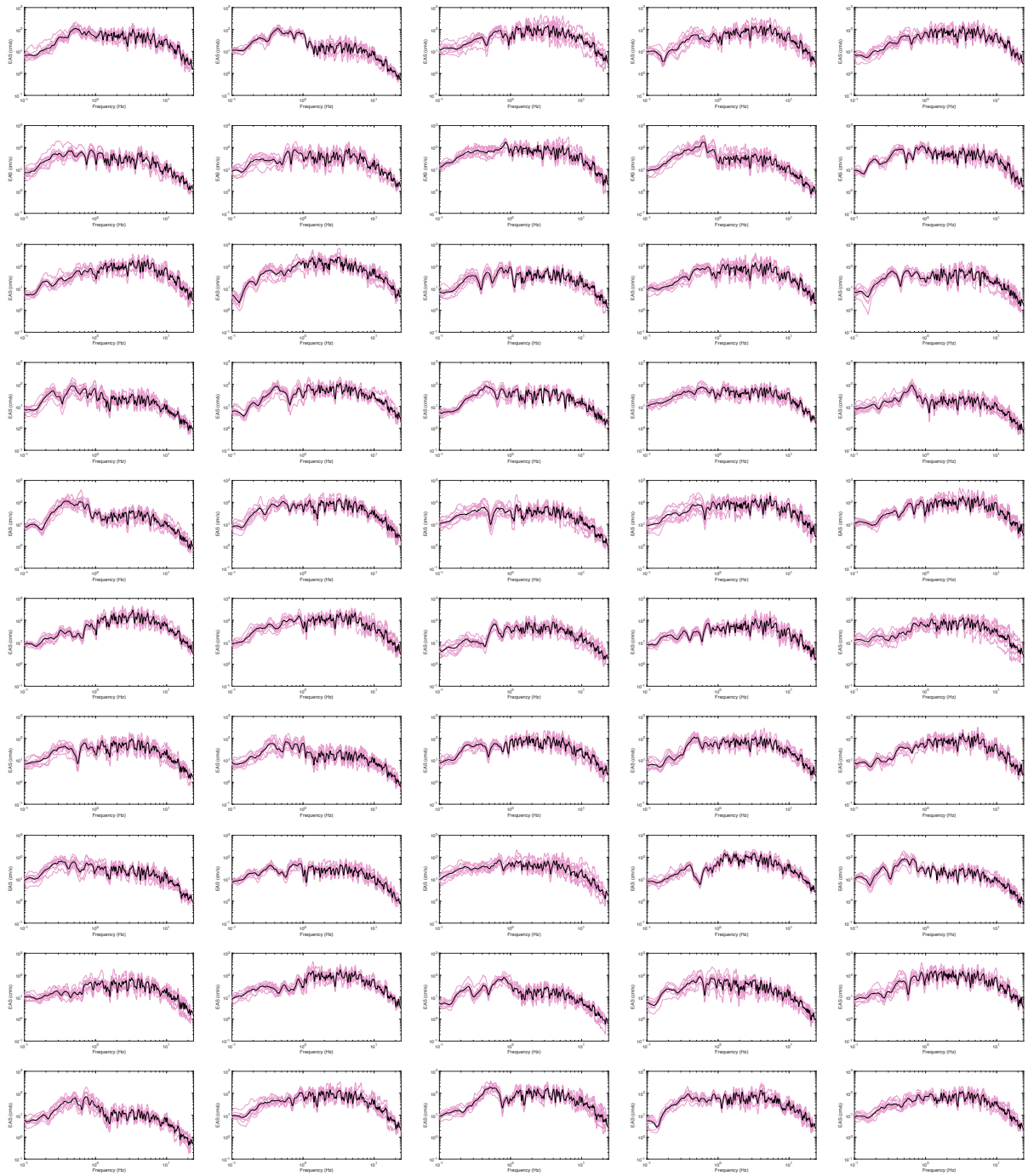

Figure S4.1: Suite of 10 simulated EAS (thin pink lines) with inter-frequency correlation of the within-event residual implemented and their mean (bold black line) for each of the 50 events (source realizations) at station 8001-CLS for the Loma Prieta earthquake.

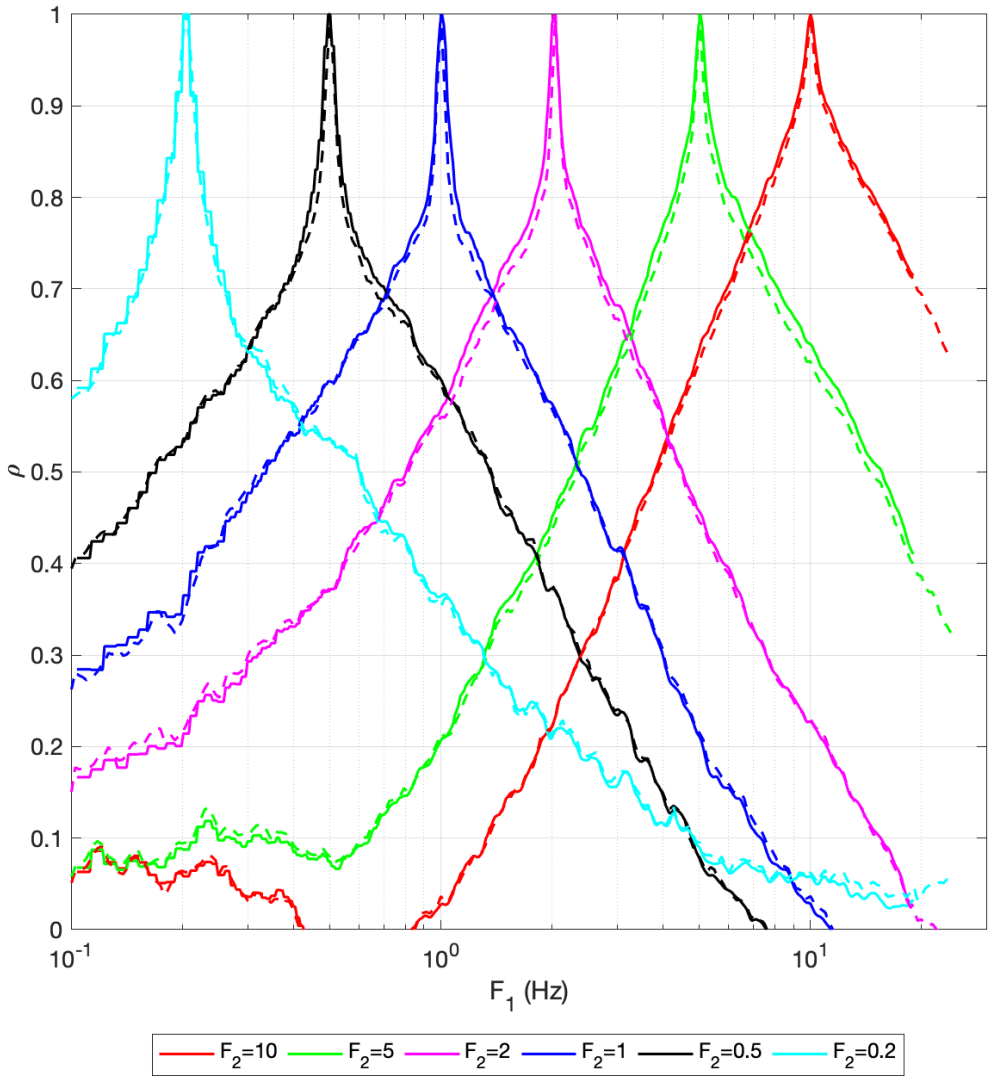

Figure S4.2: The inter-frequency correlation coefficients of epsilon at reference frequencies 0.2 Hz, 0.5 Hz, 1 Hz, 2 Hz, 5 Hz and 10 Hz from the empirical correlation coefficients (dashed lines) and the SDSU SCEC BBP Module after applying our method using correlated random variables with a correlation coefficient of 0.7 at two horizontal components (solid lines) for the Loma Prieta earthquake.

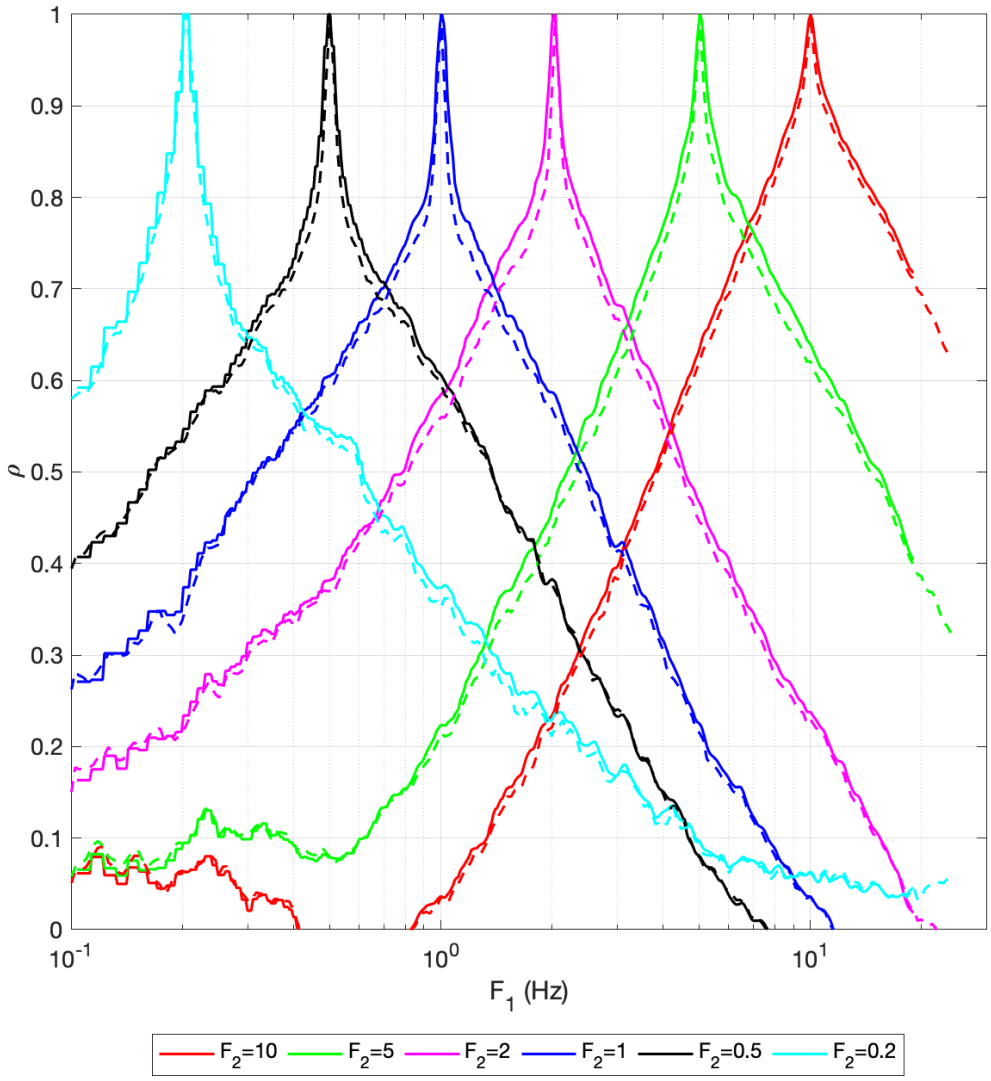

Figure S4.3: Same as Figure S4.2, but for a correlation coefficient of 0.8.

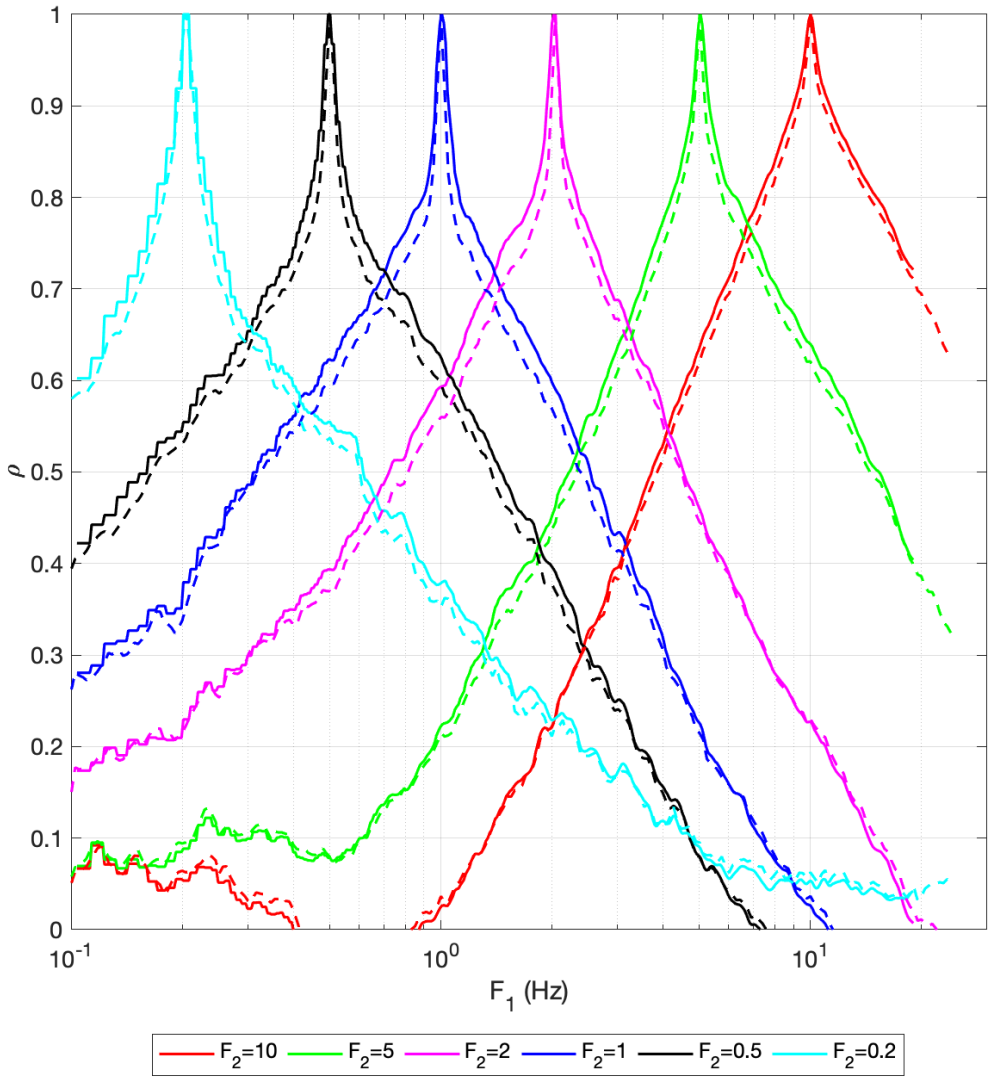

Figure S4.4: Same as Figure S4.2, but for a correlation coefficient of 0.9.

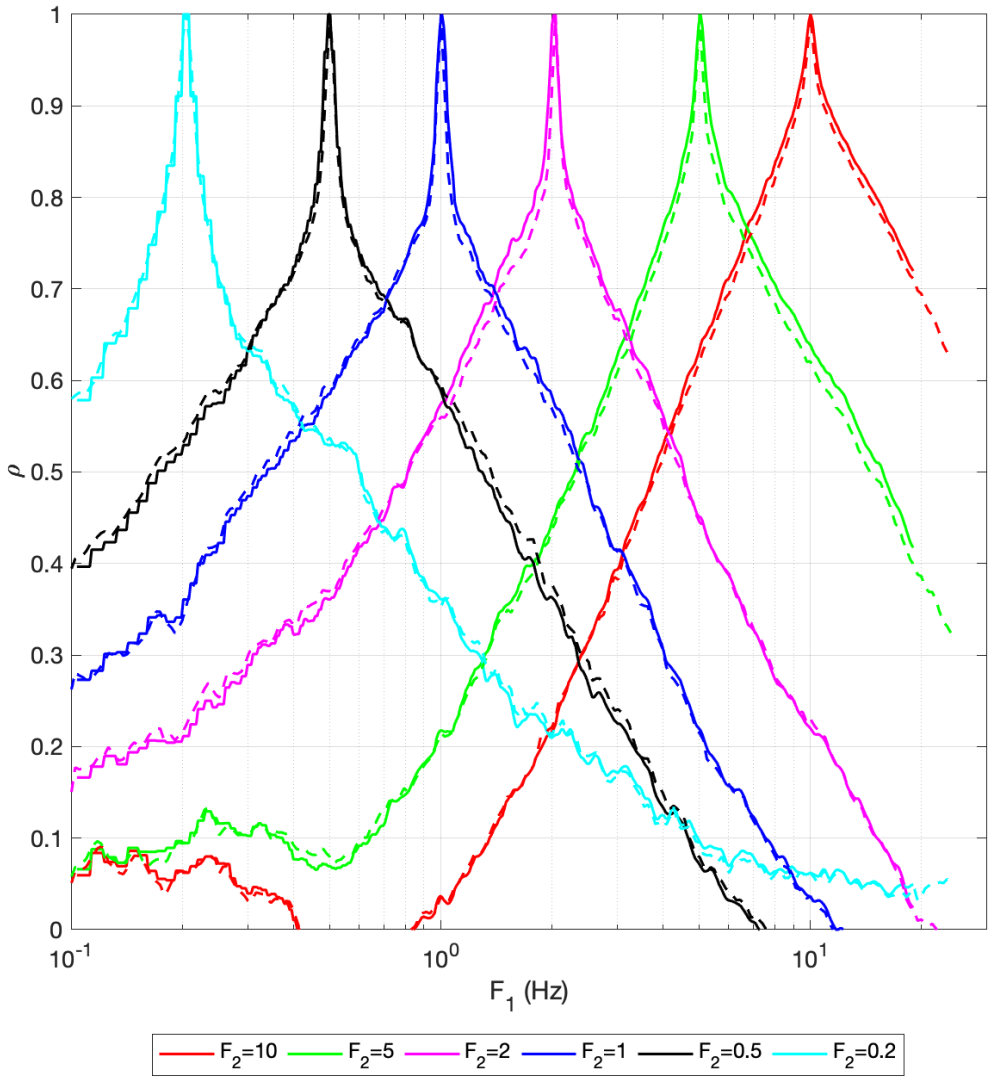

Figure S4.5: The inter-frequency correlation coefficients of epsilon at reference frequencies 0.2 Hz, 0.5 Hz, 1 Hz, 2 Hz, 5 Hz and 10 Hz from the empirical correlation coefficients (dashed lines) and the SDSU SCEC BBP Module after applying our method using correlated random variables with a correlation coefficient of 0.7 for the two horizontal components (solid lines) for the Landers earthquake.

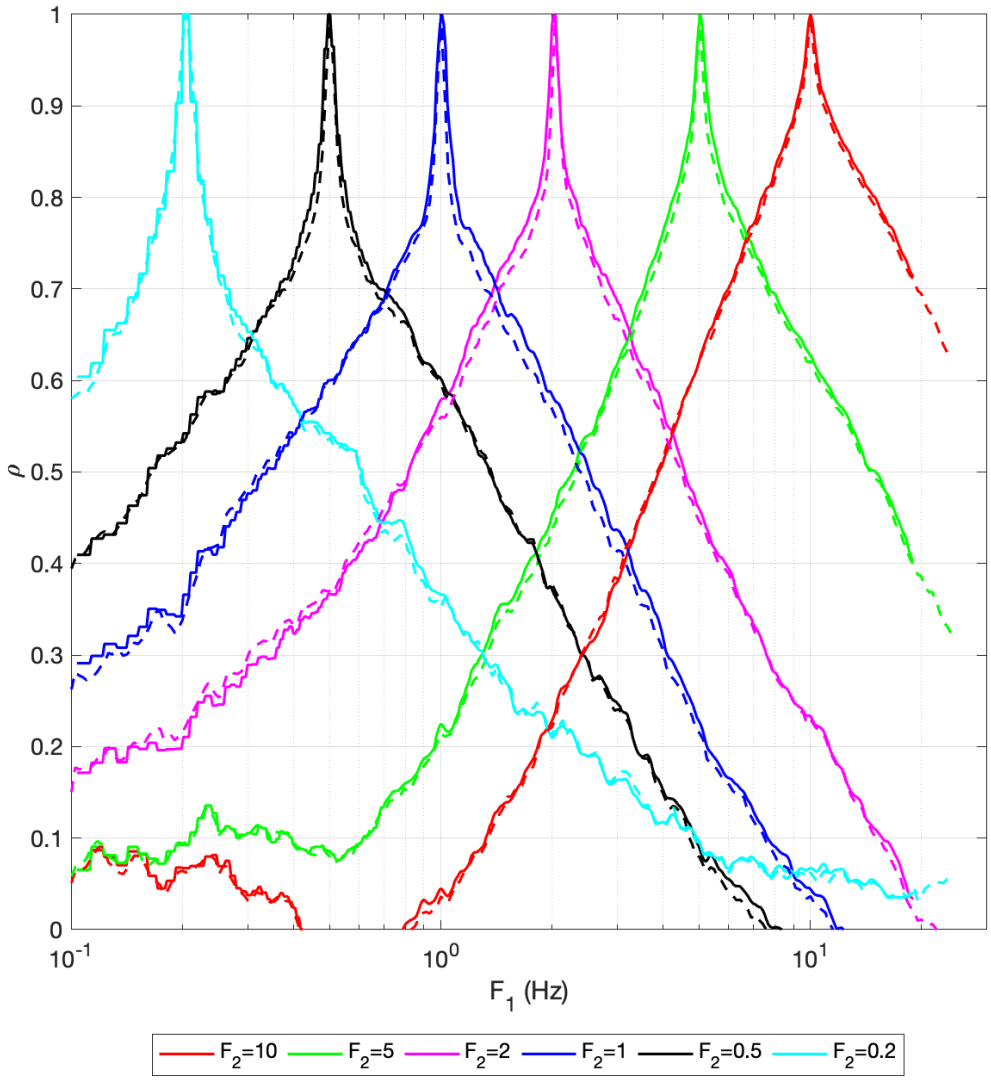

Figure S4.6: Same as Figure S4.5, but for the Northridge earthquake.

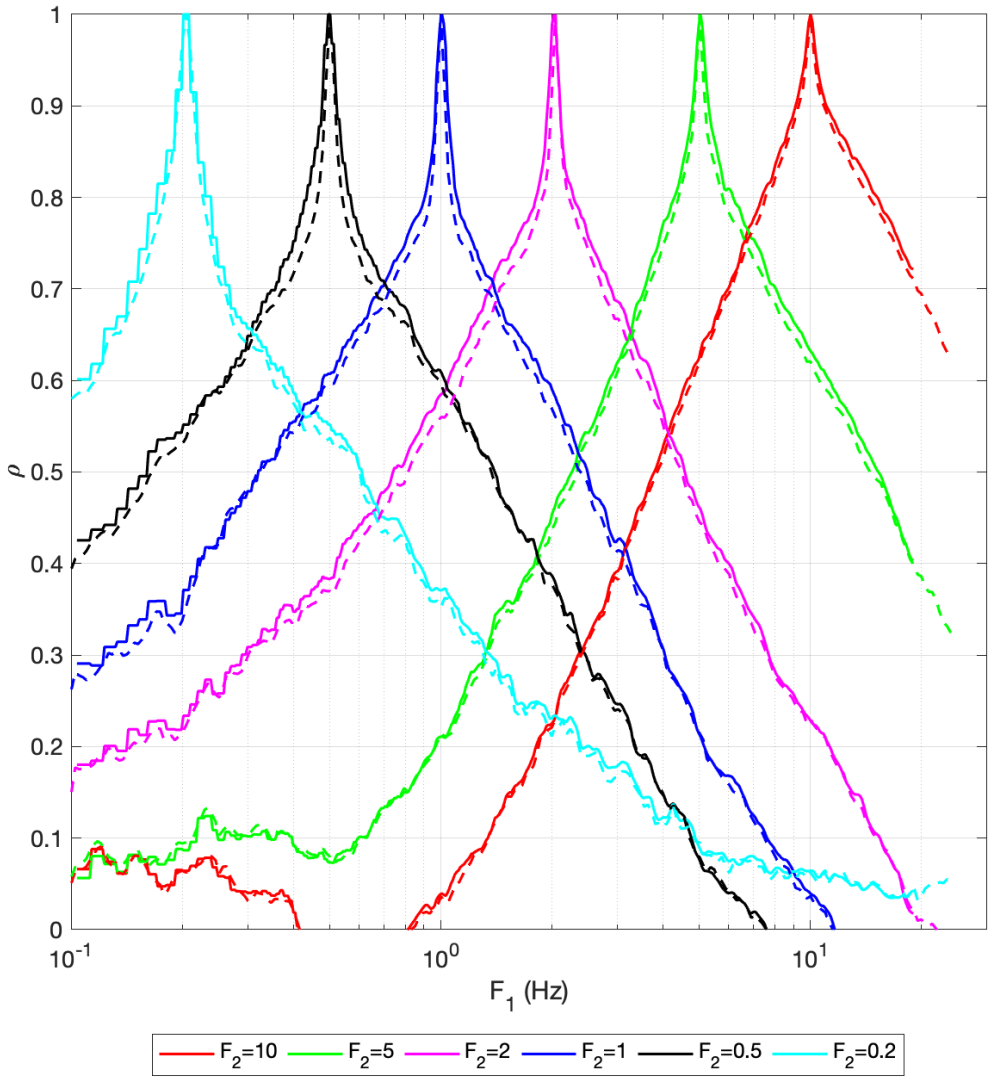

Figure S4.7: Same as Figure S4.5, but for the North Palm Springs earthquake.

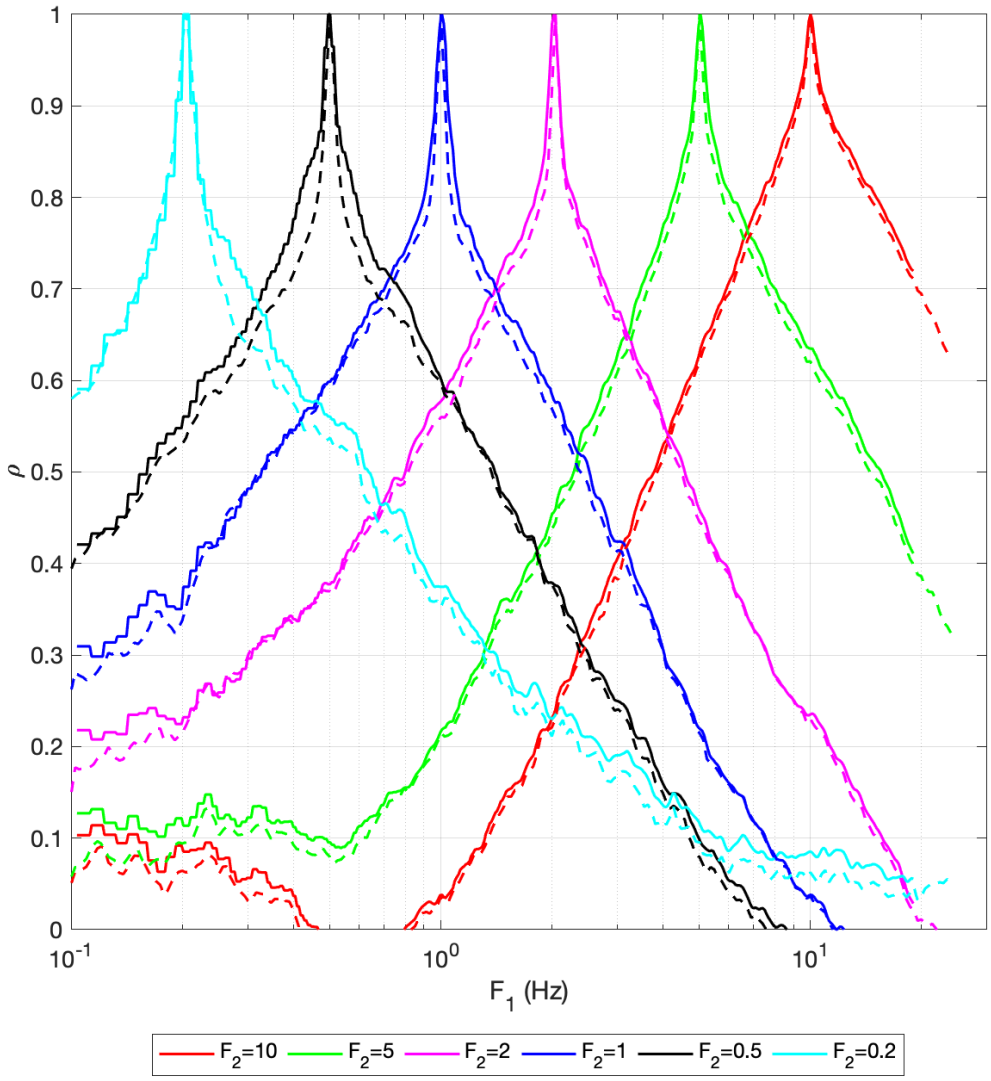

Figure S4.8: Same as Figure S4.5, but for the Whittier earthquake.

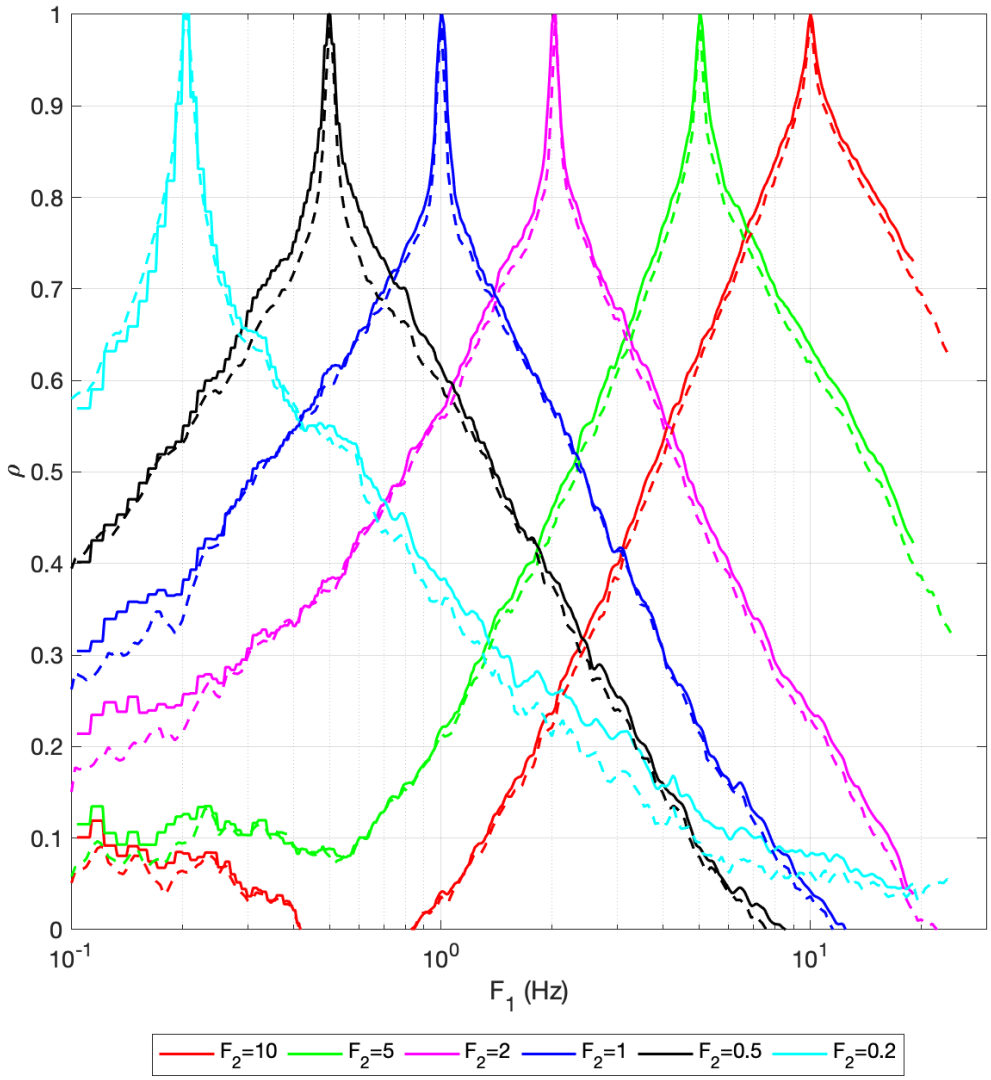

Figure S4.9: Same as Figure S4.5, but for the Chino Hills earthquake.

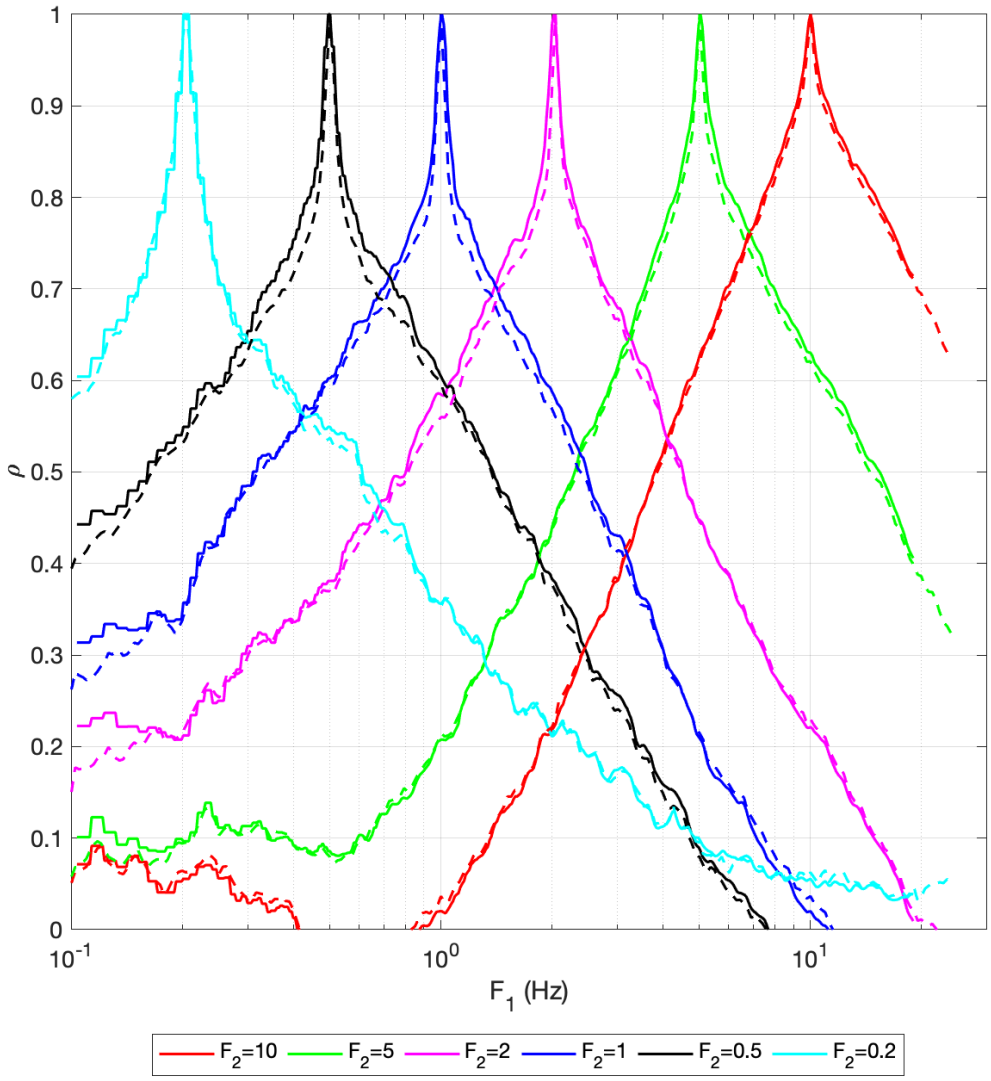

Figure S4.10: Same as Figure S4.5, but for the Alum Rock earthquake.

Chapter 5

A Frequency-Dependent Ground-Motion Spatial Correlation Model of Within-Event Residuals for Fourier Amplitude Spectra

Ground motion time series recorded at stations separated by up to about 50 km show a frequency-dependent spatial coherency structure, and the corresponding ground motion intensity measures are found to be correlated. As omitting this correlation can result in underestimation of seismic losses in risk analysis, it is critical to quantify the spatial correlation structure for ground motion Fourier spectra estimated at different sites during a single event within a region. Toward this goal, we have developed an empirical frequency-dependent spatial correlation model for the within-event residuals of effective Fourier amplitude spectra from the Pacific Earthquake Engineering Research Center (PEER) Next Generation Attenuation (NGA) West2 database. The correlation model shows slower decrease of the spatial correlation with distance at lower frequencies compared with higher frequencies, in agreement with the underlying ground motion data, and no significant dependence on the magnitude of the earthquakes is observed. We use this empirical model to incorporate frequency-dependent spatial correlation into a hybrid deterministic-

stochastic broadband ground motion generation module, which successfully generates synthetic time series for seven western US earthquakes with frequency-dependent spatial correlation that closely mimics that of the empirical model. Furthermore, the method also significantly improves the correlation for spectral accelerations, cumulative absolute velocities, and Arias intensities, compared with that derived from the original broadband module.

5.1 Introduction

Ground motion time series recorded from earthquakes reveal a spatial coherency structure at stations separated by up to a few tens of kilometers, causing intensity measures such as peak ground velocities, peak ground accelerations, and peak spectral accelerations (i.e. response spectra) to be correlated (e.g., Abrahamson et al., 1991; Bolt et al., 1982; Bycroft, 1980; Der Kiureghian, 1996; Hao et al., 1989; Harichandran and Vanmarcke, 1986). A number of studies have been carried out over the past decades addressing the spatial correlation of ground motions (e.g., Boore et al., 2003; Esposito and Iervolino, 2011; Goda and Hong, 2008; Heresi and Miranda, 2019; Jayaram and Baker, 2009; Kawakami and Mogi, 2003; Loth and Baker, 2013; Markhvida et al., 2018; Sokolov et al., 2012; Wang and Takada, 2005; Wesson and Perkins, 2001). In general, these previous studies have investigated correlations between spectral accelerations for a range of periods, using earthquake records from different locations.

Seismic loss estimation in a region with exposed infrastructure is used by earthquake insurance companies to estimate expected damage in future catastrophes. The accuracy of the insured loss estimates in a region is critically dependent on the spatial correlation between the ground motion intensities at different sites during a single event, which can be significant at distances up to 50km (e.g., Abrahamson et al., 1991; Bolt et al., 1982; Bycroft, 1980; Der Kiureghian, 1996; Hao et al., 1989; Harichandran and Vanmarcke, 1986). Strong motion data naturally include such correlation, but is often available in insufficient amounts for loss analysis,

in particular for large events and close to the causative fault. Instead, numerical simulations can provide key information for seismic hazard analysis. Seismic hazard assessment has benefited from recent advances in simulation methods due to improved source characterization, accuracy of numerical methods, and availability of powerful computational resources. However, while ground motion simulations produced from complex 3D rupture and crustal models may include realistic spatial correlation structure (e.g., Withers et al., 2019), those obtained by more simplified deterministic simulations (e.g. 1D) and, in particular, by stochastic approaches (e.g., Atkinson et al., 2009; Beresnev and Atkinson, 1997; Boore, 2003; Boore, 2009; Motazedian and Atkinson, 2005), oftentimes do not. For example, many broadband simulation methods (e.g., Atkinson and Assatourians, 2015; Crempien and Archuleta, 2015; Graves and Pitarka, 2015; Olsen and Takedatsu, 2015), which have been tuned to produce good agreement with median spectral acceleration from strong motion data, have received less attention to their spatial correlation behavior. The importance of including spatial correlation in ground motion simulations has been illustrated by many studies (e.g., Jayaram and Baker, 2010; Miller and Baker, 2015) for loss estimates, clearly showing that simulations without spatial correlation can result in an underestimation of seismic risk.

Pseudo-spectral acceleration (PSA) has traditionally been the preferred metric in earthquake engineering, and many studies have proposed spatial correlation models for PSA. However, each PSA ordinate depends (nonlinearly) on ground motion amplitudes over a range of frequencies, and therefore a correlation model for PSA does not provide a direct means to impose the correlation structure on numerically simulated time histories (or on other ground-motion metrics derived therefrom). On the contrary, the Fourier amplitude spectrum (FAS) provides a straightforward means to incorporate an empirical correlation model into simulated ground motion time histories, through frequency-domain multiplication, but its empirical estimation is complicated by the fact that its value depends upon recording-instrument orientation. The effective amplitude spectrum (EAS), defined in the next section, avoids this complication, and

bears a simple relationship to the FAS. Therefore, the aim of this study is to (1) develop a new, empirical frequency-dependent spatial correlation model of EAS and (2) describe and demonstrate its implementation into numerically simulated ground motion. In that implementation, the empirical EAS correlation model is used to generate separate but correlated FAS adjustments to the two horizontal components at a given site. Specifically, we use the findings for inter-frequency correlation by Wang et al. (2019) to generate correlated horizontal-component FAS residuals with correlation coefficient 0.7.

5.2 Within-Event Residual of the EAS

FAS, the amplitude spectrum of Fourier transform of the acceleration time series, depends on the recording instrument's orientation. Such dependency may cause an undesirable bias in applications of the calculated FAS values. On the contrary, the EAS defined by Goulet et al. (2018) as follows:

$$EAS(f) = \sqrt{\frac{1}{2}[FAS_{HC1}^2(f) + FAS_{HC2}^2(f)]}\,, \tag{5.1}$$

is rotation independent, and will therefore be used as the intensity measure for our empirical model development. As discussed later, we then use the EAS correlation model, with the method of Wang et al. (2019), to generate FAS adjustments to simulated time histories. In Equation 5.1, FAS_{HC1} and FAS_{HC2} are the FAS of two orthogonal as-recorded horizontal components acceleration time series, and f is the frequency in Hertz. The EAS is smoothed by the $\log_{10}$-scale Konno and Ohmachi (1998) smoothing window (e.g. Kottke et al., 2018):

$$W(f) = \left(\frac{\sin\left(b \log\left(\frac{f}{f_c}\right)\right)}{b \log\left(\frac{f}{f_c}\right)} \right)^4 . \tag{5.2}$$

Here, W is a weight at frequency f designed for a window with center frequency f_c, and $b = \frac{2\pi}{b_w} = 60\pi$, where b_w is the smoothing window bandwidth in $\log_{10}$ units (see Kottke et al. (2018) for more details on the smoothing technique). Note that the smoothing of the EAS can have a direct impact on the correlation. A comparison of the models of Stafford (2017) and Bayless and Abrahamson (2019) indicates that it is possible that smoothing contributes to larger inter-frequency correlations. PEER NGA-East ((PEER), 2015) selected the Konno and Ohmachi (1998) type of smoothing window which leads to minimal bias on the amplitudes of the smoothed EAS compared to the unsmoothed EAS. The parameter b (188.5 in our study) was selected such that the random vibration theory (RVT) calibration properties after the smoothing were minimally affected (Kottke et al., 2018). Using the smoothed EAS with the same b, we maintain consistency with the PEER database as well as with other PEER projects, including the NGA-East empirical FAS models (Goulet et al., 2018) and the Bayless and Abrahamson (2018b) EAS model.

Following the notation by Atik et al. (2010) we define y_{es} as the natural logarithm of the ground-motion intensity measure observed at station s during earthquake e:

$$y_{es} = \mu_{es} + \delta B_e + \delta W_{es} \ , \tag{5.3}$$

where μ_{es} is the mean prediction of the natural logarithm of the intensity measure, δB_e is the between-event (or inter-event) residual representing the average shift of the observed ground motion for an individual earthquake e from the population mean prediction, and δW_{es} is the within-event residual (or intra-event residual), depicting the misfit between an individual observation at station s from the earthquake-specific mean prediction. The between-event residual includes average source effects (over all azimuths) such as stress drop and spatial and temporal variation of fault slip that are not captured by magnitude, faulting style, and source depth in the mean prediction. The within-event residual comprises azimuthal variations in source, path, and site effects that reflect the influence of factors such as crustal heterogeneity, deeper geological

structure, and near-surface layering that cannot be captured by a simple distance metric and a site-classification based on the average shear-wave velocity (Atik et al., 2010). These residuals are normally distributed with zero mean and are uncorrelated with each other. Following these definitions, the normalized EAS within-event residual, ε, at station s during earthquake e is calculated as a function of frequency f as:

$$\varepsilon(f) = \frac{\delta W_{es}(f)}{\phi(f)} = \frac{\ln EAS_{es}(f) - \mu_{\ln EAS_{es}}(f) - \delta B_e}{\varphi(f)}\,, \tag{5.4}$$

where φ is the standard deviation of δW_{es}, and ε is standard normally distributed.

5.3 Semivariogram Analysis

A semivariogram (γ) characterizes the strength of statistical dissimilarity as a function of distance and is often used to describe spatially distributed random variables in geostatistics (see Appendix A for a summary of semivariograms). Under the stationary and isotropic assumptions, the semivariograms are independent of the locations and offset direction of the site pair but depend on the distance between the sites. The empirical semivariogram matrix for ε at each frequency pair $(f_i,\ f_j)$ can be summarized by an isotropic semivariogram matrix (Γ) as a function of separation distance *h*:

$$\Gamma(h) = \gamma_{f_i,f_j}(h) = \begin{bmatrix} \gamma_{f_1,f_1}(h) & \cdots & \gamma_{f_1,f_n}(h) \\ \vdots & \ddots & \vdots \\ \gamma_{f_n,f_1}(h) & \cdots & \gamma_{f_n,f_n}(h) \end{bmatrix} \tag{5.5}$$

where matrix element γ_{f_i,f_j} is as defined, in terms of ε, by Equation 5.25. Similarly, the empirical

isotropic covariance matrix (C) can be written as a function of separation distance h as:

$$C(h) = c_{f_i,f_j}(h) = \begin{bmatrix} c_{f_1,f_1}(h) & \cdots & c_{f_1,f_n}(h) \\ \vdots & \ddots & \vdots \\ c_{f_n,f_1}(h) & \cdots & c_{f_n,f_n}(h) \end{bmatrix} , \tag{5.6}$$

and we have

$$C(h) = C(0) - \Gamma(h) \ . \tag{5.7}$$

5.4 Empirical Frequency-Dependent Spatial Correlation Model of Within-Event Residuals

5.4.1 Data Sources

In this study, the frequency-dependent spatial correlation model is developed from EAS values for recorded ground motions in the PEER NGA West2 database (Ancheta et al., 2014). The NGA-West2 database includes shallow crustal earthquakes with M>3 in active tectonic regions (dominated by California and Nevada earthquakes). The normalized within-event EAS residual, ε, was determined from the Bayless and Abrahamson (2018b) ground motion model. This model was calculated from the individual EAS values and the earthquake-specific smoothed EAS median value at each station for each recorded event. The within-event residuals used in this study are obtained from Bayless and Abrahamson (2018b). For more details on the ground-motion database and data selection criteria, see Bayless and Abrahamson (2018b) and Abrahamson et al. (2014).

Semivariograms γ_{f_i,f_j} of ε were calculated for each pair of frequencies, f_i and f_j (at frequency points 0.1-1 Hz with a spacing of 0.1 Hz, and 1-23 Hz with a spacing of 1 Hz) and as a

function of h from 0 to 120 km with a bin size equal to 2 km. Figure 5.1 shows an example of the semivariogram produced for the frequency pair $f_1 = f_2 = 1$ Hz computed from the data.

5.4.2 Linear Model of Coregionalization

Previous studies (e.g., Wang and Takada, 2005) have observed an exponential decay of the ground motion spatial correlation, suggesting that the semivariogram can be well fit using an exponential model. For this reason, we assume a functional form of the semivariogram with the general behavior:

$$\gamma(h) = S\left[1 - \exp\left(-\frac{3h}{R}\right)\right] , \tag{5.8}$$

where S is the sill that represents the asymptotic value of $gamma\,(h)$ as h goes to infinity, and R is the range that represents the distance at which the value of $\gamma(h)$ equals 95% of the sill. In the multivariate case (as in Equation 5.25), this general behavior would imply a semivariogram at a given frequency pair f_i and f_j of the form:

$$\gamma_{ij}\,(h) = S_{ij}\left[1 - \exp\left(-\frac{3h}{R_{ij}}\right)\right] . \tag{5.9}$$

However, it has been shown that (for within-event residuals of spectral accelerations) R_{ij} varies at different frequencies such that lower frequencies tend to have larger ranges than do higher frequencies (Loth and Baker, 2013). To better represent these frequency dependencies, we followed an approach similar to that of Loth and Baker (2013), using a nested semivariogram model (a linear combination of single semivariogram models):

$$\gamma_{ij}\,(h) = P_{ij}^{1}\left(1 - \exp\left(-\frac{3h}{R_1}\right)\right) + P_{ij}^{2}\left(1 - \exp\left(-\frac{3h}{R_2}\right)\right) + P_{ij}^{3} . \tag{5.10}$$

Combining all elements γ_{ij}, we obtain the linear model of coregionalization:

$$\Gamma(h) = \mathbf{P^1}\left(1-\exp\left(-\frac{3h}{R_1}\right)\right)+\mathbf{P^2}\left(1-\exp\left(-\frac{3h}{R_2}\right)\right)+\mathbf{P^3}\,, \tag{5.11}$$

where $\mathbf{P^1}$ and $\mathbf{P^2}$ are coregionalization matrices corresponding to the short-range and long-range models, respectively. Note that the third term, the coregionalization matrix $\mathbf{P^3}$ in Equation 5.11 corresponds to the nugget effect,

$$\gamma(h) = \begin{cases} 0, & if\ h = 0 \\ S, & if\ h > 0 \end{cases}, \tag{5.12}$$

which can be used to represent discontinuity of the semivariogram at separation distances larger than zero. Ranges $R_1 = 10$ km and $R_2 = 100$ km provide a reasonable fit to the data and are adopted in our model. The coregionalization matrices, $\mathbf{P^1}$, $\mathbf{P^2}$ and $\mathbf{P^3}$, which are symmetric and semipositive definite, are estimated from the empirical semivariogram data by the procedure given in the next section.

5.4.3 Empirical Frequency-Dependent Spatial Correlation Model for Covariance

We use the Goulard-Voltz algorithm (Goulard and Voltz, 1992) to develop our frequency-dependent spatial correlation model for covariance. The iterative algorithm, commonly used to fit a linear model of coregionalization with semipositive definite coregionalization matrices, uses a least square fitting technique to find the coregionalization matrices that minimize the weighted sum of squares:

$$WSS = \sum_{k=1}^{K} \omega_k \parallel \hat{\Gamma}(h_k) - \Gamma(h_k) \parallel^2 = \sum_{k=1}^{K} \omega_k \sum_{i,j=1}^{N} \left[\hat{\gamma}_{ij}(h_k) - \gamma_{ij}(h_k)\right]^2\,, \tag{5.13}$$

where $\hat{\Gamma}(h_k)$ and $\hat{\gamma}_{ij}(h_k)$ represent the semivariogram values computed from the model, and $\Gamma(h_k)$ or $\gamma_{ij}(h_k)$ represent the semivariogram values computed from the empirical data at h_k, the center of the kth bin. ω_k is a positive weight at h_k, which is defined as $\omega_k = \frac{1}{h_k}$ in this study.

Let us denote $\left(1-\exp\left(-\frac{3h}{R_1}\right)\right)$ by $g^1(h)$, $\left(1-exp\left(-\frac{3h}{R_2}\right)\right)$ by $g^2(h)$ and 1 by $g^3(h)$. Equation 5.11 can then be written as:

$$\Gamma(h) = \sum_{l=1}^{L} \mathbf{P^l} g^l(h)\ ,\ \ L = 3. \tag{5.14}$$

The Goulard-Voltz algorithm is now executed using the following steps:

(1) Initialize the coregionalization matrices $\mathbf{P^l}$, $l = 1,2,3$ in this study.

(2) Iterate from (a) to (c):

(a) Compute WSS with the current coregionalization matrices.

(b) For each l:

(b1) Compute the new coregionalization matrix $\widetilde{\mathbf{P}}^{\mathbf{l}}$ as:

$$\widetilde{\mathbf{P}}^{\mathbf{l}} = \frac{\sum_{k=1}^{K} \omega_k g^l(h_k)[\hat{\Gamma}(h_k) - \sum_u^L = 1, u \neq l \mathbf{P^u} g^u(h_k)]}{\sum_{k=1}^{K} \omega [g^l(h_k)]^2} \tag{5.15}$$

(b2) Decompose $\widetilde{\mathbf{P}}^{\mathbf{l}}$ as $\widetilde{\mathbf{P}}^{\mathbf{l}} = \mathbf{Q_l}\Lambda_\mathbf{l}\mathbf{Q_l^T}$ where $\mathbf{Q_l}\mathbf{Q_l^T}$ is an identity matrix and $\Lambda_\mathbf{l}$ is a diagonal matrix.

(b3) Change all the negative diagonal elements of $\Lambda_\mathbf{l}$ to zero to obtain $\Lambda_\mathbf{l}^+$ (this step is applied for ensuring semipositive definiteness of each coregionalization matrix).

(b4) Update $\widetilde{\mathbf{P}}^{\mathbf{l}}$ as a semipositive definite matrix $\widetilde{\mathbf{P}}^{\mathbf{l}} = \mathbf{Q_l}\Lambda_\mathbf{l}^+\mathbf{Q_l^T}$.

(c) Compute WSS with the updated coregionalization matrices and loop over (a) to (c) until the difference of the WSS value from (a) and (c) is smaller than a positive

prespecified value.

The empirical semivariogram and the estimated multivariate semivariogram model are shown in Figure 5.2 for example frequency pairs. Noting that

$$C(0) = \lim_{h \to +\infty} \Gamma(h) = \mathbf{P^1} + \mathbf{P^2} + \mathbf{P^3} \ , \tag{5.16}$$

the correlation matrix in Equation 5.6 can be derived from Equation 5.7 as:

$$C(h) = \mathbf{P^1} \exp\left(-\frac{3h}{R_1}\right) + \mathbf{P^2} \exp\left(-\frac{3h}{R_2}\right) + \mathbf{P^3} I_{\{h=0\}} \ , \tag{5.17}$$

where

$$I_{h=0} = \begin{cases} 1, & if\ h = 0 \\ 0, & if\ h \neq 0 \end{cases} \tag{5.18}$$

is the indicator function.

The resulting coregionalization matrices with each element corresponding to a pair of 32 frequency points 0.1-1 Hz with a spacing of 0.1 Hz and 1-23 Hz with a spacing of 1 Hz are provided in Tables S5.1-S5.3 in the supplemental material of this article. Note that the coregionalization matrices after computation from the Goulard-Voltz algorithm are normalized as:

$$\frac{P_{ij}^l}{\sqrt{P_{ii}^1 + P_{ii}^2 + P_{ii}^3} + \sqrt{P_{jj}^1 + P_{jj}^2 + P_{jj}^3}} \ . \tag{5.19}$$

The correlation coefficient model is shown in Figure 5.3 for example frequency pairs. Figure 5.4 shows the separation distances where the correlation coefficient of frequency pairs with two identical frequencies drop to 0.5. It can be seen that, as expected, the correlation at lower frequencies (< 0.4 Hz) persists to larger separation distances, as compared to higher

frequencies. This is expected, as lower-frequency signals are less affected by smaller-scale crustal features (e.g., topographic relief, velocity perturbations) that tend to control the variation of more high-frequency motion. The small increase (about 2 km) in the separation distances at frequencies larger than 4 Hz in Figure 5.4 is discussed in the Discussion section.

Note that when $h = 0$ in Equation 5.17, the correlation model becomes $C(0) = \mathbf{P^1} + \mathbf{P^2} + \mathbf{P^3}$, which represents the inter-frequency correlation at a single site. Hence, the presented frequency-dependent spatial correlation model also includes the inter-frequency correlation simultaneously. A comparison of the regressed within-event inter-frequency correlation model with the empirical within-event inter-frequency correlation from Bayless and Abrahamson (2019) is shown in Figure 5.5. The presented model compares well with the empirical inter-frequency correlation, especially at higher correlation values.

5.5 Inclusion of Frequency-Dependent Spatial Correlation into Ground Motion Simulation

We demonstrate and validate our spatial correlation approach on the San Diego State University Broadband Ground Motion Generation Module (hereafter the "SDSU Module") (Olsen and Takedatsu, 2015; Mai et al., 2010; Mena et al., 2010). The SDSU Module is a hybrid method merging deterministic low-frequency (LF) synthetics and high-frequency (HF) stochastic contributions designated as scatterograms. The SDSU Module is implemented on the Southern California Earthquake Center (SCEC) Broadband Platform (BBP), using a number of source realizations (e.g., 50) from the Graves and Pitarka (2015) kinematic source generator to generate the LFs. The HF scatterograms are simulated for each component of ground motion based on the multiple scattering theory by Zeng et al. (1991) and Zeng et al. (1993). The seismic-scattering wave energy appears after the direct P-wave arrival time, calculated using 3D ray tracing (Hole,

1992). The scatterograms are then convolved with an appropriately magnitude-scaled source time function, assuming that the scattering operators and moment release originate throughout the fault, starting at the hypocenter (Olsen and Takedatsu, 2015).

The SDSU Module passed the SCEC BBP validation exercise (Dreger et al., 2015; Goulet et al., 2015), which assessed ground motion simulations on the basis of their median pseudo-spectral acceleration (PSA) predictions for a specified set of earthquakes in western and eastern US and Japan, as well as on their degree of agreement with median estimates from the NGA Ground Motion Prediction Equations (GMPEs). Thus, the method has undergone thorough calibration for PSA using GMPEs and strong motion data. However, this validation exercise did not extend to validation of prediction variability measures, and the current SDSU Module (i.e., current as of the above-referenced validation exercise) does not generate time history sets with significant spatial correlation. For example, Figure 5.6 (top) shows the resulting spatial correlation coefficients for the Loma Prieta earthquake using the current SDSU Module synthetics compared with the correlation model presented here (Equation 5.17). It is clear that the spatial correlation coefficients of ε are significantly lower than the empirical model value for station separation distances larger than 1 km. In the following, we implement a post-processing procedure for introducing spatial correlation in SDSU Module synthetic time histories, and show that the results match our specified empirical EAS correlation model.

Our implementation approach for the frequency-dependent spatial correlation is an extension of that developed by Wang et al. (2019) for incorporating inter-frequency correlation. The spatial correlation model in Equation 5.17 is developed for the within-event residual of the orientation-independent EAS, while the SDSU Module simulations generate separate components of ground motion. For this reason, we apply the EAS frequency-dependent spatial correlation model to the FAS of each of the two horizontal components generated by the method. The resulting synthetic time histories are then found to include correlations in agreement with the EAS correlation model, provided the FAS adjustments made to the two individual horizontal

components at each station are suitably correlated. We use a correlation coefficient of 0.7 for the two FAS component adjustments at the same station, a value recommended by Wang et al. (2019) from their study on inter-frequency correlation. The procedure is described in detail in Appendix B.

We illustrate our method using 50 source realizations for the Loma Prieta earthquake obtained by the kinematic source generator module by Graves and Pitarka (2015). These 50 source realizations have variations in hypocenter locations and slip distributions that are represented by the between-event residual. Here, we refer to each of the 50 source realizations as a separate event. For each event, we generate 10 simulations with imposed within-event frequency-dependent spatial correlation at all the stations. The 10 simulations differ by the random variables (R_{HC1} and R_{HC2}) in Step (2) in Appendix B. The mean of the 10 simulations and their within-event residuals are computed for each event, respectively. The within-event residual of all the 50 events are then pooled together at the corresponding frequencies and stations. Note that, at each station and each frequency, the sampled ε of within-event residual has a length of 500 (50 events by 10 simulations). A total of 40 stations are used for the Loma Prieta earthquake in our simulations.

Figure 5.6 (bottom) shows the spatial correlation coefficients of EAS from 50 source realizations of the Loma Prieta earthquake generated from the SDSU Module with the implementation of our spatial correlation method, at example frequency pairs. In contrast to the low interstation correlation obtained from the current version of the module, the correlation implementation step results in correlation of the synthetics that very closely follows the empirical model, with significant correlation persisting to distances of ∼50 km. Figure 5.7 shows the inter-frequency correlation coefficients of EAS from 50 source realizations of the Loma Prieta earthquake generated from the SDSU Module with the implementation of our frequency-dependent spatial correlation model, at 5 reference frequencies. This verifies that the presented frequency-dependent spatial correlation model can address both the spatial correlation and the inter-frequency correlation simultaneously.

Figure 5.8 shows one example component of synthetic time histories of acceleration and FAS at a station (8001-CLS) for the Loma Prieta earthquake before and after implementing the proposed spatial correlation model. The "uncorrelated" case here in Figure 5.8 is computed when the off-diagonal correlation terms of the correlation matrixes (Step (5) in Appendix B) are being set to zero. The comparison shows that the resulting correlation has subtle effects on the time domain. Similar comparisons at other 39 stations are provided in Figure S5.1, available in the supplemental material of this article. Note that the FAS correlation adjustment, which is done with an assumption of zero phase adjustment (as is also the case for the inter-frequency correlation analysis, e.g., Stafford, 2017; Bayless and Abrahamson, 2018a; Wang et al., 2019), does not lead to any visibly anomalous behavior in the time domain, such as non-causality. For this reason, we did not embrace the additional complexity of doing the FAS adjustments in the form of a causal filter. The resulting spatial correlation coefficients from six other western U.S. earthquakes considered in the SCEC broadband validation exercise (the 1992 M7.2 1992 Landers, the 1994 M6.7 Northridge, the 1986 M6.1 North Palm Springs, the 1987 M5.9 Whittier, the 2008 M5.4 Chino Hills, and the 2007 M5.5 Alum Rock earthquakes) are provided in Figures S5.2 - S5.7, available in the supplemental material of this article.

5.6 Comparison to Other Correlation Models

Loth and Baker (2013) regressed a within-event spatial correlation model for spectral accelerations based on recordings of 8 earthquakes from the PEER NGA database. The assumptions of stationarity and isotropy are present in both the presented model and the Loth and Baker (2013) model. While the regression model in Equation 5.11 has the same format as the regression model function of Loth and Baker (2013) model, the range parameters R_1 and R_2 are chosen differently than in the Loth and Baker PSA model, to better fit to the empirical correlation of EAS. Figure 5.9 shows the resulting cross-correlation coefficients of response spectral accelerations for the Loma

Prieta earthquake synthetics after applying the EAS spatial correlation implementation method, indicating that incorporating the empirical spatial correlation into the EAS of ground motion simulations can also lead to an improvement of the spatial correlation in spectral accelerations. The comparison shows that the Loth and Baker (2013) model's correlation coefficients decay slightly faster than the simulated correlation coefficients. These differences are likely caused by a combination of the following factors. (1) The Loth and Baker (2013) model is regressed for spectral accelerations using a smaller database with 2080 recordings from 8 earthquakes while the present model is regressed from a much larger database with 13,346 recordings from 232 earthquakes. (2) The values of the modeled covariance matrices of Loth and Baker (2013) are obtained by averaging all the fitted coregionalization matrices over various earthquakes while the presented model fits the covariance matrices once after pooling the residuals from all the earthquakes together. (3) The smoothing technique applied in the EAS dataset, which may have increased the correlation, as described previously. One other possible cause of these differences is that the simulations use the actual median as the referencing median to compute the within-event residuals instead of the median ground motion models of PSA used by Loth and Baker (2013). A direct comparison of the two models is provided in Figure S5.8, available in the supplemental material of this article.

Stafford (2017) developed inter-frequency correlation models for FAS. A comparison of the presented within-event inter-frequency correlation model ($h = 0$ in Equation 5.17) with Stafford's (2017) within-event inter-frequency correlation model is shown in Figure 5.10. The within-event inter-frequency correlation of Stafford (2017) shown here is computed as the combination of their between-site and within-site correlation components. Stafford's (2017) correlation model shows lower correlation and faster decay at higher reference frequency than the model developed in this study and the Bayless and Abrahamson (2019) empirical correlation. These differences are likely caused by a combination of the following factors. (1) The different ground motion component used. The use of both as-recorded FAS horizontal components in Stafford

(2017) is a key difference from this study which uses an orientation-independent horizontal component, EAS. (2) The different database and median ground motion model used. Stafford (2017) used a subset of the PEER NGA West1 database to develop the correlation model and used a FAS ground motion model adapted from Yenier and Atkinson (2015) to compute the residual. (3) The different smoothing technique applied. Stafford (2017) used unsmoothed FAS and this study uses smoothed EAS. By averaging the EAS in frequency windows, it is possible that the smoothing could increase the correlation between adjacent frequencies. In this study, the smoothed EAS is chosen to maintain consistency with prior studies, as mentioned before.

5.7 Discussion

In this study, we regressed the spatial correlation model at 32 frequency points from 0.1 to 23 Hz, which sufficed to illustrate the efficacy of the implementation of the method. However, if the spatial correlation is needed at additional frequency pairs, a straightforward two-dimensional interpolation of the coregionalization matrices $\mathbf{P^1}$, $\mathbf{P^2}$ and $\mathbf{P^3}$ can be applied.

We observe no meaningful event-size dependence of the spatial correlation of earthquake ground motion for the magnitude range in our analysis, as shown by Figure 5.11, where results are binned by magnitude. Some apparent variation of the spatial correlation with magnitude for smaller sample partitions from the full database is due to unbalanced sampling of earthquake magnitude at a particular distance or frequency. This is consistent with the empirical model of inter-frequency correlation for the EAS residual by Bayless and Abrahamson (2019) that also showed no statistically significant magnitude dependence.

As shown in Figure 5.4, the correlation at lower frequencies (< 0.4 Hz) persists to larger separation distances, as compared to higher frequencies, which is expected. Moreover, a small increase of the separation distances at frequencies larger than 4 Hz (meaning that the correlation decreases more slowly with distance at higher frequencies) is observed in Figure 5.4. We also

observed such trend at periods smaller than 0.2s (i.e. frequencies larger than 5 Hz) in the Loth and Baker (2013) model (for spectral accelerations) which is based on recordings of 8 earthquakes with magnitudes between 6 and 7.6 from the PEER NGA database as shown in Figure S5.9. We find that the increase in our EAS correlation model at frequencies larger than 4 Hz is mostly dominated by the data from earthquakes with magnitudes between 6 to 7, while the trend is not obvious for other magnitudes (M3-6 and M7-8), as shown in Figure S5.10. This result warrants further investigation of the data screening procedure or the median ground motion models (used as reference to calculate the residuals). In any case, the trend is relatively small (separation distances increased by $\sim$2 km from 4 Hz to 23 Hz when the correlation coefficient equals 0.5), and further decreases as the correlation coefficient increases until no noticeable increase is observed when the correlation coefficient equals 0.7, as shown in Figure S5.11. Thus, the trend does not affect our overall result that the empirical correlation at lower frequencies persists to larger separation distances. Figures S5.9 - 5.11 are available in the supplemental material of this article.

In our analysis, we use a linear coregionalization model to generate our spatial correlation model because of its efficiency using the Goulard-Voltz algorithm, its applicability to a broad frequency range, and its simplicity in the implementation approach. However, other models or regression methods such as the Markov-type screening hypothesis model (Goda and Hong, 2008) and the principal components semivariogram model (Markhvida et al., 2018) may also provide adequate implementation support for the frequency-dependent spatial correlation model.

We have applied the spatial correlation technique to the SDSU Module, which (otherwise) produces broadband synthetic time series with little spatial correlation for either low-frequency deterministic or high-frequency stochastic components. For this reason, the empirical spatial correlation matrices were applied directly to the broadband synthetics as a post-processing procedure. If the method is applied to synthetic time histories from other ground motion generation methods (such as the ones using 3D rupture and crustal models) that already include a certain level of inherent spatial correlation, the procedure should be adjusted to avoid possible double

counting. An example of such adjustment is to generate spatially correlated residuals in the process such that the SRSS (square root of the sum of the squares), which consists of the residuals' spatial covariance as well as the inherent spatial covariance, becomes the desired total value that matches the empirical spatial correlation model developed in this study.

The fact that the SDSU Module correlation implementation allows the correlated synthetics to essentially replicate the empirical correlation for PSA suggests that one could now use the correlated SDSU Module synthetics (with the present EAS correlation model implemented) to generate any other ground motion metrics with a valid "empirical" correlation, such as Arias intensity and Cumulative Absolute Velocity. Figure 5.12, as an example, shows the improved spatial cross-correlation coefficients of cumulative absolute velocity and Arias intensity (combining two orthogonal horizontal components using the arithmetic mean, Travasarou et al. (2003)) for the Loma Prieta earthquake synthetics after applying the spatial correlation implementation method. This also suggests that the correlated SDSU Module synthetics may provide a means for deriving correlation models for other ground motion metrics. However, further study addressing the spatial variation in the duration of ground motion might be needed to justify such a procedure.

Bayless and Abrahamson (2018b) used a mixed-effect regression in their EAS data set (as used in our analysis). This regression should include a mean bias term in Equation 5.3 (e.g., Lee et al., 2020; Afshari and Stewart, 2016). Omission of this mean bias term could cause the within-event (and the between-event) residuals to be altered and lead to a net increase in the estimated spatial correlations. However, we checked that the overall mean bias is negligible in our analysis, justifying leaving out the bias term.

5.8 Conclusions

We have developed a frequency-dependent spatial correlation model of ε (the normalized within-event residual) of EAS from the PEER NGA-West2 database, in order to mimic the spatial

correlation of observed ground motion data between stations, critical for applications such as seismic risk analysis. The spatial correlation coefficients at lower frequencies decrease more slowly with distance than those at higher frequencies, with no significant dependence on the magnitude of the earthquakes observed. The empirical spatial correlation model of ε is regressed for a linear coregionalization model of semivariograms using the Goulard-Voltz algorithm. We implement the frequency-dependent spatial correlation into ground motion simulations via the SDSU Module on the SCEC BBP. Our method makes use of a two-dimensional Gaussian random variable that has a correlation matrix corresponding to the developed spatial cross-correlation model. The EAS correlation calculated from sets of spatially distributed, two-component synthetic seismograms using our method closely match the empirical EAS correlation model, and the correlation in spectral accelerations from these seismograms is also significantly improved. Because the correlated synthetics successfully replicate empirically derived correlations of spectral acceleration, we suggest that the correlated synthetics from our model could also provide an efficient means for deriving spatially correlated models for other ground motion metrics.

5.9 Appendix A

A semivariogram characterizes the strength of statistical dissimilarity as a function of distance and is often used to describe spatially distributed random variables in geostatistics. The semivariogram is defined as:

$$\gamma(s_x, s_y) = \frac{1}{2} \mathrm{E}\left[\left(Z(s_x) - Z(s_y)\right)^2 \right] , \tag{5.20}$$

where E[ ] denotes the expectation, $Z(s_x)$ and $Z(s_y)$ are random variables at site location s_x and s_y, respectively, and $\gamma(s_x, s_y)$ is the value of the semivariogram for $Z(s_x)$ and $Z(s_y)$. The covariance

of two random variables $Z(s_x)$ and $Z(s_y)$ is defined as:

$$c(s_x, s_y) = cov(s_x, s_y) = \mathrm{E}\left[\left(Z(s_x) - \mathrm{E}[Z(s_x)]\right)\left(Z(s_y) - \mathrm{E}[Z(s_y)]\right)\right] \ . \tag{5.21}$$

When empirically estimating the semivariogram or covariance of ground motion observations, the stationary and isotropic assumptions usually need to be established due to the absence of enough data to constrain the additional parameters resulting from a non-stationary and non-isotropic model. Under the stationary and isotropic assumptions, the semivariogram and covariance are independent of the locations and offset direction of the site pair but depend on the distance between the sites. Denoting the separation distance as h, we can write the semivariogram as:

$$\gamma(h) = \frac{1}{2}\,\mathrm{E}\left[\ \left(Z(s_x) - Z(s_{x+h})\right)^2\right] \tag{5.22}$$

and the covariance as:

$$c(h) = \mathrm{E}\left[\left(Z(s_x) - \mathrm{E}[Z(s_x)]\right)\left(Z(s_{x+h}) - \mathrm{E}[Z(s_{x+h})]\right)\right] \ . \tag{5.23}$$

Here, note that $\mathrm{E}[Z(s_x)] = \mathrm{E}[Z(s_{x+h})]$ under the assumption of stationarity, are constant at all sites. The relationship between $\gamma(h)$ and $c(h)$ is given by

$$c(h) = c(0) - \gamma(h) \ . \tag{5.24}$$

For a given set of ground motion observations, the values of ε at nearby stations are correlated and the similarity decreases as the separation distance increases. It can also be shown that ε at neighboring frequencies (f) are probabilistically correlated and are weakly correlated if the frequency pair are widely-separated (Bayless and Abrahamson, 2018a). To calculate the semivariogram of ε at multiple frequency pairs, a multivariate semivariogram is used in this study. Denoting $Z_i = \varepsilon(f_i)$ and $Z_j = \varepsilon(f_j)$, we can write the multivariate semivariogram for frequency

pair $\left(f_i,\ f_j\right)$ as:

$$\gamma_{ij}(h) = \frac{1}{2} E\left[\left(Z_i(s_x) - Z_i(s_{x+h})\right)\left(Z_j(s_x) - Z_j(s_{x+h})\right)\right] , \tag{5.25}$$

where $Z_i(s_x)$ represents the ε at station s_x at frequency f_i. γ_{ij} can then be estimated using:

$$\gamma_{ij}(h) = \frac{1}{2N_{ij,h}} \sum_{k=1}^{N_{ij,h}} \left[\left(Z_i\left(s_{k,x}\right) - Z_i\left(s_{k,x+h}\right)\right)\left(Z_j\left(s_{k,x}\right) - Z_j\left(s_{k,x+h}\right)\right)\right] , \tag{5.26}$$

where $N_{ij,h}$ represents the total number of observations of ε at the frequency pair $\left(f_i,\ f_j\right)$ with a separation distance h.

5.10 Appendix B

Here, we describe the implementation approach of our frequency-dependent spatial correlation into the SDSU Module. The current implementation is focused on only two horizontal components; however, this approach generalizes to the vertical component (once the vertical component correlation is defined). The steps are as follows:

(1) Take the Fourier transform of the two horizontal components of the synthetic ground motion time series at all stations, and let the station number be m. For each component, let the number of frequency points be n, the Fourier amplitude and phase at the ith frequency be $Amp_{mean}(i)$ and $Ph_{mean}(i)$, respectively;

(2) For the two horizontal components 1 and 2, sample normally distributed vector-valued random variables R_{HC1} and R_{HC2}, respectively, with zero mean, constant standard deviation, σ (0.5 for the Loma Prieta event, which is consistent with the original BBP value), and size n at all stations. R^c_{HC1} and R^c_{HC2} are correlated with a correlation

coefficient $\rho_R = 0.7$ (Wang et al., 2019), and can be generated by the following steps:

(a) express covariance matrix C of the two components:

$$\gamma_{ij}(h) = \frac{1}{2N_{ij,h}} C = \begin{bmatrix} 1 & \rho_R \\ \rho_R & 1 \end{bmatrix} = \begin{bmatrix} 1 & 0.7 \\ 0.7 & 1 \end{bmatrix} ; \qquad (5.27)$$

(b) apply the Cholesky decomposition of covariance matrix C and obtain a 2-by-2 upper triangular matrix U as:

$$\gamma_{ij}(h) = \frac{1}{2N_{ij,h}} C = U^T U ; \qquad (5.28)$$

(c) right multiply matrix $[R_{HC1} , R_{HC2}]$ by U so that the resulting two new random variables R^c_{HC1} and R^c_{HC2} have correlation coefficient ρ_R equal to 0.7:

$$[R^c_{HC1} , R^c_{HC2}] = [R_{HC1} , R_{HC2}] U , \qquad (5.29)$$

where $[R^c_{HC1} , R^c_{HC2}]$ and $[R_{HC1} , R_{HC2}]$ are n-by-2 matrices with R^c_{HC1} or R_{HC1} as the first columns and R^c_{HC2} or R_{HC2} as the second columns, respectively. Only the upper triangular matrix featuring the correlation between the two columns of the matrix $\left[R^c_{HC1} , R^c_{HC2}\right]$ is used here (Wang et al., 2019).

(3) Repeat step (2) three times to generate three sets of independent standard normal random variables $\left[R^{1c}_{HC1} , R^{1c}_{HC2}\right]$, $\left[R^{2c}_{HC1} , R^{2c}_{HC2}\right]$, $\left[R^{3c}_{HC1} , R^{3c}_{HC2}\right]$. For each component, obtain three independent sets of n-by-m random variables Rs^1_{HC1}, Rs^2_{HC1} or Rs^3_{HC1} by combining the vector R^{1c}_{HC1}, R^{2c}_{HC1} or R^{3c}_{HC1} for the first component at all the stations. Similarly, obtain Rs^1_{HC2}, Rs^2_{HC2} and Rs^3_{HC2} for the second component.

The following steps are then the same for the two components, so the 'HC1' and 'HC2' subscripts are dropped for notational brevity and Rs^1, Rs^2, Rs^3 refer to either of the two components of the three n by m random variables, if not specified.

(4) Calculate m by m matrices $\mathbf{D^1}$ and $\mathbf{D^2}$ with each element representing the cross-correlation at different station pairs (S_x, S_y), that correspond to the coregionalization model factors $\exp\left(-\frac{3h}{R_1}\right)$ and $\exp\left(-\frac{3h}{R_2}\right)$ in model $C(h)$:

$$D^l_{xy} = \exp\left(-\frac{3h_{xy}}{R_l}\right),\ l = 1,2\ ; \tag{5.30}$$

(5) Apply the Cholesky decomposition to $\mathbf{P^1}$, $\mathbf{P^2}$, $\mathbf{P^3}$ to get lower triangular matrices $\mathbf{K^1}$, $\mathbf{K^2}$, $\mathbf{K^3}$, and to $\mathbf{D^1}$, $\mathbf{D^2}$ to get upper triangular matrices $\mathbf{L^1}$, $\mathbf{L^2}$:

$$\mathbf{P^1} = \mathbf{K^1}\left(\mathbf{K^1}\right)^T, \mathbf{P^2} = \mathbf{K^2}\left(\mathbf{K^2}\right)^T,\ \mathbf{P^3} = \mathbf{K^3}\left(\mathbf{K^3}\right)^T\ , \tag{5.31}$$

and

$$\mathbf{D^1} = \left(\mathbf{L^1}\right)^T \mathbf{L^1},\ \ \mathbf{D^2} = \left(\mathbf{L^2}\right)^T \mathbf{L^2}.\ . \tag{5.32}$$

(6) Compute

$$S = S^1 + S^2 + S^3 = \mathbf{K^1} Rs^1 \mathbf{L^1} + \mathbf{K^2} Rs^2 \mathbf{L^2} + \mathbf{K^3} Rs^3\ , \tag{5.33}$$

such that S is a matrix of random variables with rows corresponding to different frequencies and columns corresponding to different stations, and S following the correlation model $C(h)$. Note that, here, for the corresponding frequency points outside the 0.1-23 Hz range, $S = (Rs^1 + Rs^2 + Rs^3)/3$;

(7) For all the stations, take the exponential of the corresponding column of S (S^{col}), and multiply $\exp(S^{col})$ with the station's Amp_{mean} to compute the Fourier amplitude of

the new ground motion synthetics, Amp_{new}, as

$$Amp_{new}(i) = Amp_{mean}(i) \exp S_i^{col} \; ; \tag{5.34}$$

(8) Calculate the new ground-motion time series by applying the inverse Fourier transform to the amplitude spectrum obtained in (5) and phase spectrum from (1).

Data and Resources

Analyses and graphics production were performed using the numeric computing environment MATLAB (www.mathworks.com, last accessed March 2020). All data are from the Pacific Earthquake Engineering Research Center (PEER) Next Generation Attenuation (NGA) West2 database (Ancheta et al., 2014). Simulations in this paper are performed on the SCEC BBP.

Acknowledgements

The authors thank Jeff Bayless for providing the EAS dataset used in the analysis. They also thank Jeff Bayless and Samuel Shen for their advice and comments during this research project, and are grateful to Brendon Bradley, one anonymous reviewer, the Associate Editor, and the Editor-in-Chief for useful review comments and suggestions that helped improve the article.

The author(s) disclosed receipt of the following financial support for the research, authorship, and/or publication of this article: This research was supported by the Southern California Earthquake Center (SCEC; Contribution Number 10911). SCEC is funded by the National Science Foundation (NSF) Cooperative Agreement EAR-1600087 and the U.S. Geological Survey (USGS) Cooperative Agreement G17AC00047.

Chapter 5, in full, is a reformatted version of the material as it appears in Earthquake

Spectra: Wang, N., Olsen, K.B., Day S.M. (2021). A frequency-dependent ground-motion spatial correlation model of within-event residuals for Fourier amplitude spectra. *Earthquake Spectra*. The dissertation author was the primary investigator and author of this paper.

References

Abrahamson, N., Schneider, J. F., and Stepp, J. C. (1991). "Spatial coherency of shear waves from the Lotung, Taiwan large-scale seismic test". In: *Structural Safety* 10.1-3, pp. 145–162.

Abrahamson, N. A., Silva, W. J., and Kamai, R. (2014). "Summary of the ASK14 ground motion relation for active crustal regions". In: *Earthquake Spectra* 30.3, pp. 1025–1055.

Afshari, K. and Stewart, J. P. (2016). "Physically parameterized prediction equations for significant duration in active crustal regions". In: *Earthquake Spectra* 32.4, pp. 2057–2081.

Ancheta, T. D., Darragh, R. B., Stewart, J. P., Seyhan, E., Silva, W. J., Chiou, B. S.-J., Wooddell, K. E., Graves, R. W., Kottke, A. R., Boore, D. M., et al. (2014). "NGA-West2 database". In: *Earthquake Spectra* 30.3, pp. 989–1005.

Atik, L. A., Abrahamson, N., Bommer, J. J., Scherbaum, F., Cotton, F., and Kuehn, N. (2010). "The variability of ground-motion prediction models and its components". In: *Seismological Research Letters* 81.5, pp. 794–801.

Atkinson, G. M. and Assatourians, K. (2015). "Implementation and validation of EXSIM (a stochastic finite-fault ground-motion simulation algorithm) on the SCEC broadband platform". In: *Seismological Research Letters* 86.1, pp. 48–60.

Atkinson, G. M., Assatourians, K., Boore, D. M., Campbell, K., and Motazedian, D. (2009). "A guide to differences between stochastic point-source and stochastic finite-fault simulations". In: *Bulletin of the Seismological Society of America* 99.6, pp. 3192–3201.

Bayless, J. and Abrahamson, N. A. (2018a). *An empirical model for Fourier amplitude spectra using the NGA-West2 database, PEER Report 2018/07*. Report. Pacific Earthquake Engineering Research Center, University of California, Berkeley.

— (2018b). "Evaluation of the Interperiod Correlation of Ground-Motion SimulationsEvaluation of the Interperiod Correlation of Ground-Motion Simulations". In: *Bulletin of the Seismological Society of America* 108.6, pp. 3413–3430.

— (2019). "An Empirical Model for the Interfrequency Correlation of Epsilon for Fourier Amplitude Spectra". In: *Bulletin of the Seismological Society of America* 109.3, pp. 1058–1070.

Beresnev, I. A. and Atkinson, G. M. (1997). "Modeling finite-fault radiation from the ω n spectrum". In: *Bulletin of the Seismological Society of America* 87.1, pp. 67–84.

Bolt, B. A., Loh, C., Penzien, J, Tsai, Y., and Yeh, Y. (1982). *Preliminary report on the SMART 1 strong motion array in Taiwan, Report UCB/EERC-82/13*. Report. University of California, Earthquake Engineering Research Center.

Boore, D. M. (2003). “Simulation of ground motion using the stochastic method”. In: *Pure and applied geophysics* 160.3, pp. 635–676.

— (2009). “Comparing stochastic point-source and finite-source ground-motion simulations: SMSIM and EXSIM”. In: *Bulletin of the Seismological Society of America* 99.6, pp. 3202–3216.

Boore, D. M., Gibbs, J. F., Joyner, W. B., Tinsley, J. C., and Ponti, D. J. (2003). “Estimated ground motion from the 1994 Northridge, California, earthquake at the site of the Interstate 10 and La Cienega Boulevard bridge collapse, West Los Angeles, California”. In: *Bulletin of the Seismological Society of America* 93.6, pp. 2737–2751.

Bycroft, G. N. (Aug. 1980). *El Centro, California, differential ground motion array, Report 80-919*. Tech. rep. US Geological Survey.

Crempien, J. G. and Archuleta, R. J. (2015). “UCSB method for simulation of broadband ground motion from kinematic earthquake sources”. In: *Seismological Research Letters* 86.1, pp. 61–67.

Der Kiureghian, A (1996). “A coherency model for spatially varying ground motions”. In: *Earthquake engineering & structural dynamics* 25.1, pp. 99–111.

Dreger, D. S., Beroza, G. C., Day, S. M., Goulet, C. A., Jordan, T. H., Spudich, P. A., and Stewart, J. P. (2015). “Validation of the SCEC broadband platform v14. 3 simulation methods using pseudospectral acceleration data”. In: *Seismological Research Letters* 86.1, pp. 39–47.

Esposito, S. and Iervolino, I. (2011). “PGA and PGV spatial correlation models based on European multievent datasets”. In: *Bulletin of the Seismological Society of America* 101.5, pp. 2532–2541.

Goda, K. and Hong, H.-P. (2008). “Spatial correlation of peak ground motions and response spectra”. In: *Bulletin of the Seismological Society of America* 98.1, pp. 354–365.

Goulard, M. and Voltz, M. (1992). “Linear coregionalization model: tools for estimation and choice of cross-variogram matrix”. In: *Mathematical Geology* 24.3, pp. 269–286.

Goulet, C., Abrahamson, N., Somerville, P., and Wooddell, K. (2015). “The SCEC Broadband Platform validation exercise for pseudo-spectral acceleration: Methodology for code validation in the context of seismic hazard analyses”. In: *Seismol. Res. Lett* 86.1, pp. 17–26.

Goulet, C., Kottke, A, Boore, D., Bozorgnia, Y, Hollenback, J, Kishida, T, Der Kiureghian, A, Ktenidou, O., Kuehn, N., Rathje, E., Thompson, E., and Wang, X. (May 2018). “Effective amplitude spectrum (EAS) as a metric for ground motion modeling using Fourier amplitudes”. In: *2018 Seismology of the Americas Meeting*. Miami, Florida: Seismology of the Americas Meeting.

Graves, R. and Pitarka, A. (2015). "Refinements to the Graves and Pitarka (2010) broadband ground-motion simulation method". In: *Seismological Research Letters* 86.1, pp. 75–80.

Hao, H, Oliveira, C., and Penzien, J (1989). "Multiple-station ground motion processing and simulation based on SMART-1 array data". In: *Nuclear Engineering and Design* 111.3, pp. 293–310.

Harichandran, R. S. and Vanmarcke, E. H. (1986). "Stochastic variation of earthquake ground motion in space and time". In: *Journal of engineering mechanics* 112.2, pp. 154–174.

Heresi, P. and Miranda, E. (2019). "Uncertainty in intraevent spatial correlation of elastic pseudo-acceleration spectral ordinates". In: *Bulletin of Earthquake Engineering* 17.3, pp. 1099–1115.

Hole, J. (1992). "Nonlinear high-resolution three-dimensional seismic travel time tomography". In: *Journal of Geophysical Research: Solid Earth* 97.B5, pp. 6553–6562.

Jayaram, N. and Baker, J. W. (2009). "Correlation model for spatially distributed ground-motion intensities". In: *Earthquake Engineering & Structural Dynamics* 38.15, pp. 1687–1708.

— (2010). "Efficient sampling and data reduction techniques for probabilistic seismic lifeline risk assessment". In: *Earthquake Engineering & Structural Dynamics* 39.10, pp. 1109–1131.

Kawakami, H. and Mogi, H. (2003). "Analyzing spatial intraevent variability of peak ground accelerations as a function of separation distance". In: *Bulletin of the Seismological Society of America* 93.3, pp. 1079–1090.

Konno, K. and Ohmachi, T. (1998). "Ground-motion characteristics estimated from spectral ratio between horizontal and vertical components of microtremor". In: *Bulletin of the Seismological Society of America* 88.1, pp. 228–241.

Kottke, A, Rathje, E, Boore, D., Thompson, E, Hollenback, J, Kuehn, N, Goulet, C., Abrahamson, N., Bozorgnia, Y, and Der Kiureghian, A (2018). *Selection of random vibration procedures for the NGA east project, PEER Report No. 2018/05*. Report. Pacific Earthquake Engineering Research Center, University of California, Berkeley.

Lee, R. L., Bradley, B. A., Stafford, P. J., Graves, R. W., and Rodriguez-Marek, A. (2020). "Hybrid broadband ground motion simulation validation of small magnitude earthquakes in Canterbury, New Zealand". In: *Earthquake Spectra* 36.2, pp. 673–699.

Loth, C. and Baker, J. W. (2013). "A spatial cross-correlation model of spectral accelerations at multiple periods". In: *Earthquake Engineering & Structural Dynamics* 42.3, pp. 397–417.

Mai, P. M., Imperatori, W., and Olsen, K. B. (2010). "Hybrid broadband ground-motion simulations: Combining long-period deterministic synthetics with high-frequency multiple

S-to-S backscattering". In: *Bulletin of the Seismological Society of America* 100.5A, pp. 2124–2142.

Markhvida, M., Ceferino, L., and Baker, J. W. (2018). "Modeling spatially correlated spectral accelerations at multiple periods using principal component analysis and geostatistics". In: *Earthquake Engineering & Structural Dynamics* 47.5, pp. 1107–1123.

Mena, B., Mai, P. M., Olsen, K. B., Purvance, M. D., and Brune, J. N. (2010). "Hybrid broadband ground-motion simulation using scattering Green's functions: Application to large-magnitude events". In: *Bulletin of the Seismological Society of America* 100.5A, pp. 2143–2162.

Miller, M and Baker, J (2015). "Ground-motion intensity and damage map selection for probabilistic infrastructure network risk assessment using optimization". In: *Earthquake Engineering & Structural Dynamics* 44.7, pp. 1139–1156.

Motazedian, D. and Atkinson, G. M. (2005). "Stochastic finite-fault modeling based on a dynamic corner frequency". In: *Bulletin of the Seismological Society of America* 95.3, pp. 995–1010.

Olsen, K. and Takedatsu, R. (2015). "The SDSU broadband ground-motion generation module BBtoolbox version 1.5". In: *Seismological Research Letters* 86.1, pp. 81–88.

(PEER), P. E. E. R. C. (2015). *NGA-East: Median ground-motion models for the Central and Eastern North America region, PEER Report 2015/04*. Report. Pacific Earthquake Engineering Research Center, University of California, Berkeley.

Sokolov, V., Wenzel, F., Wen, K.-L., and Jean, W.-Y. (2012). "On the influence of site conditions and earthquake magnitude on ground-motion within-earthquake correlation: analysis of PGA data from TSMIP (Taiwan) network". In: *Bulletin of Earthquake Engineering* 10.5, pp. 1401–1429.

Stafford, P. J. (2017). "Interfrequency Correlations among Fourier Spectral Ordinates and Implications for Stochastic Ground-Motion SimulationInterfrequency Correlations among Fourier Spectral Ordinates and Implications". In: *Bulletin of the Seismological Society of America* 107.6, pp. 2774–2791.

Travasarou, T., Bray, J. D., and Abrahamson, N. A. (2003). "Empirical attenuation relationship for Arias intensity". In: *Earthquake engineering & structural dynamics* 32.7, pp. 1133–1155.

Wang, M. and Takada, T. (2005). "Macrospatial correlation model of seismic ground motions". In: *Earthquake spectra* 21.4, pp. 1137–1156.

Wang, N., Takedatsu, R., Olsen, K. B., and Day, S. M. (2019). "Broadband ground-motion simulation with interfrequency correlations". In: *Bulletin of the Seismological Society of America* 109.6, pp. 2437–2446.

Wesson, R. L. and Perkins, D. M. (2001). “Spatial correlation of probabilistic earthquake ground motion and loss”. In: *Bulletin of the Seismological Society of America* 91.6, pp. 1498–1515.

Withers, K. B., Olsen, K. B., Shi, Z., and Day, S. M. (2019). “Validation of Deterministic Broadband Ground Motion and Variability from Dynamic Rupture Simulations of Buried Thrust EarthquakesValidation of Deterministic Broadband Ground Motion and Variability”. In: *Bulletin of the Seismological Society of America* 109.1, pp. 212–228.

Yenier, E. and Atkinson, G. M. (2015). “An equivalent point-source model for stochastic simulation of earthquake ground motions in California”. In: *Bulletin of the Seismological Society of America* 105.3, pp. 1435–1455.

Zeng, Y., Aki, K., and Teng, T.-L. (1993). “Mapping of the high-frequency source radiation for the Loma Prieta earthquake, California”. In: *Journal of Geophysical Research: Solid Earth* 98.B7, pp. 11981–11993.

Zeng, Y., Su, F., and Aki, K. (1991). “Scattering wave energy propagation in a random isotropic scattering medium: 1. Theory”. In: *Journal of Geophysical Research: Solid Earth* 96.B1, pp. 607–619.

Tables and Figures

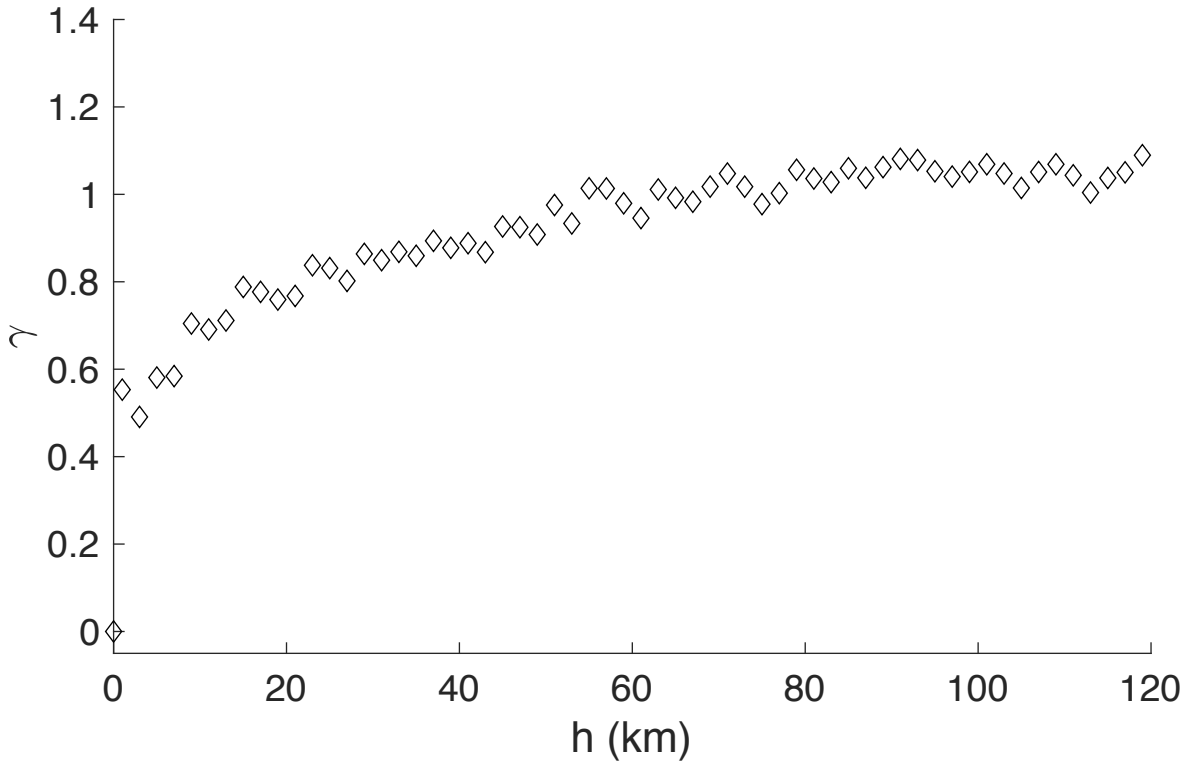

Figure 5.1: Semivariogram as a function of h at the frequency pair $f_1 = f_2 = 1$ Hz computed from the dataset.

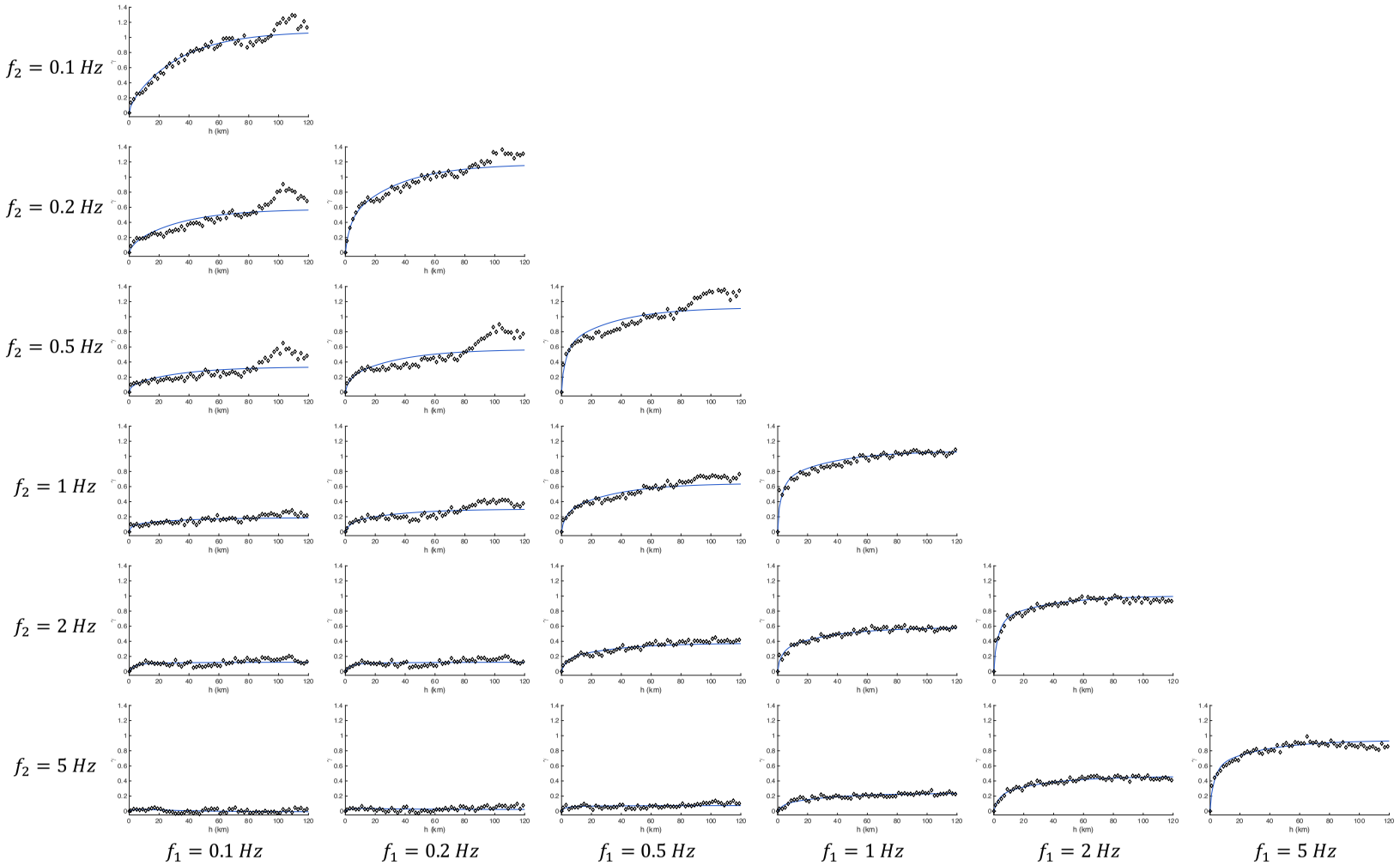

Figure 5.2: Empirical semivariograms (diamonds) and the fitted multivariate semivariogram model (solid lines) at frequency pairs for 0.1, 0.2, 0.5, 1, 2 and 5 Hz.

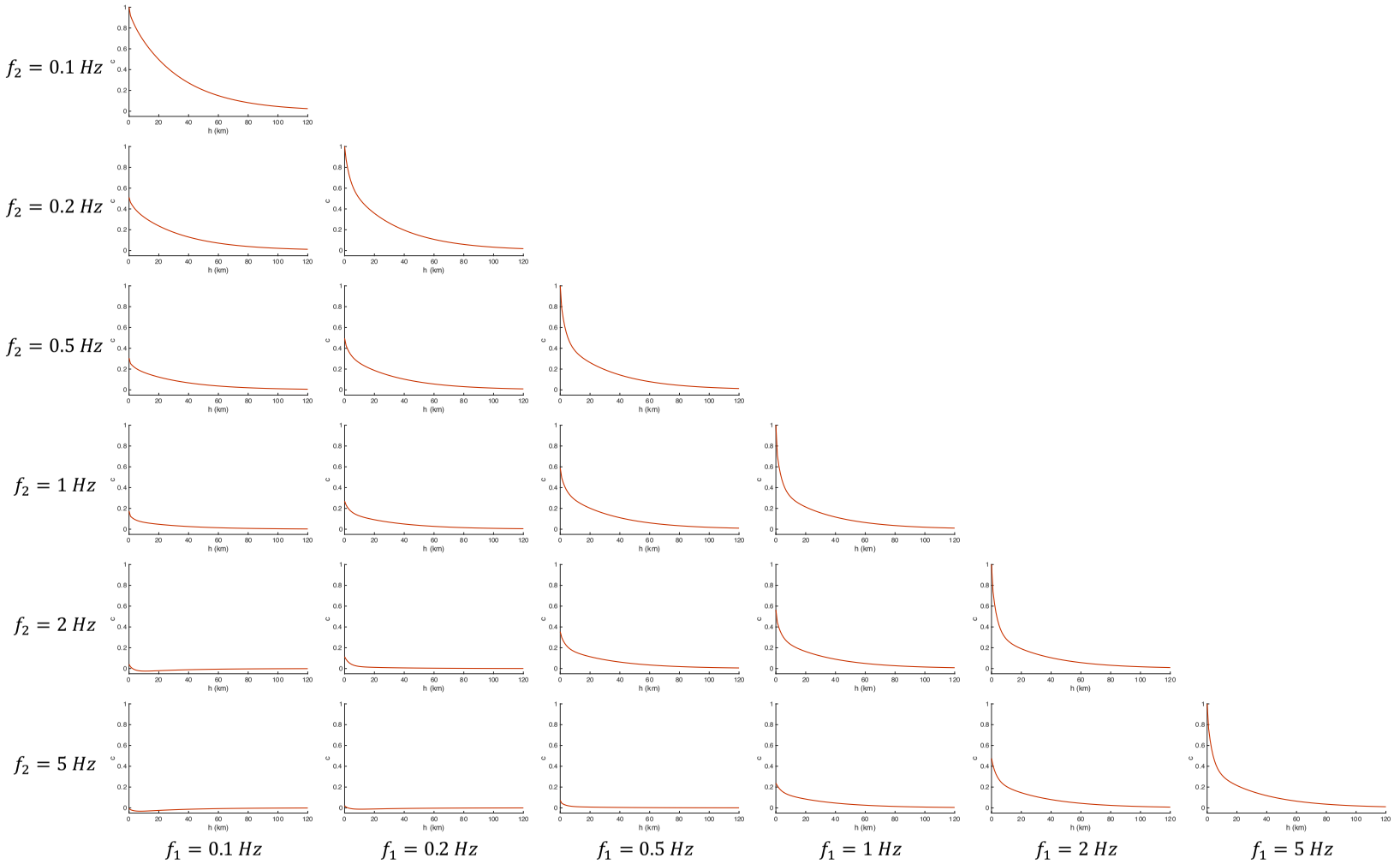

Figure 5.3: The resulting correlation coefficient model at frequency pairs for 0.1, 0.2, 0.5, 1, 2 and 5 Hz.

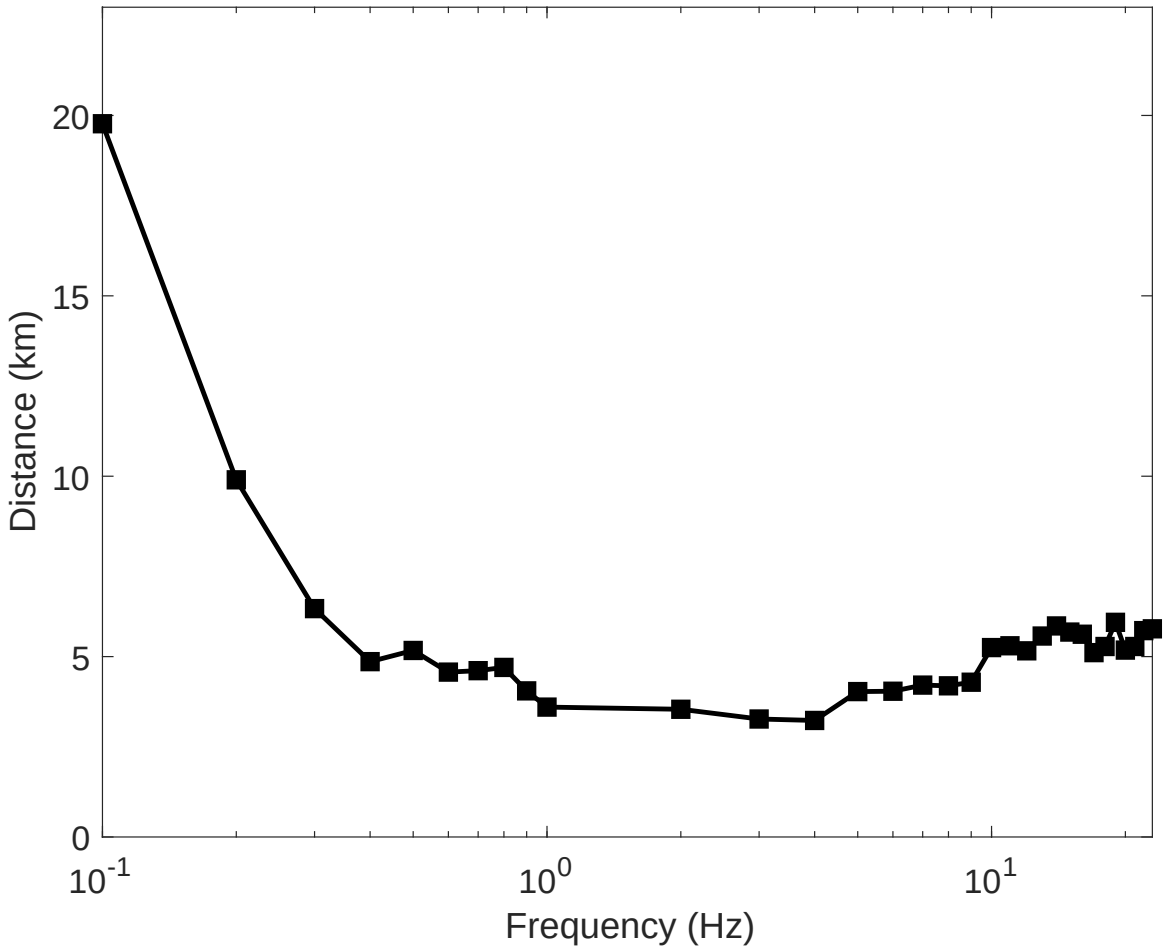

Figure 5.4: Separation distances where the correlation coefficient drops to 0.5 using pairs of two identical frequencies.

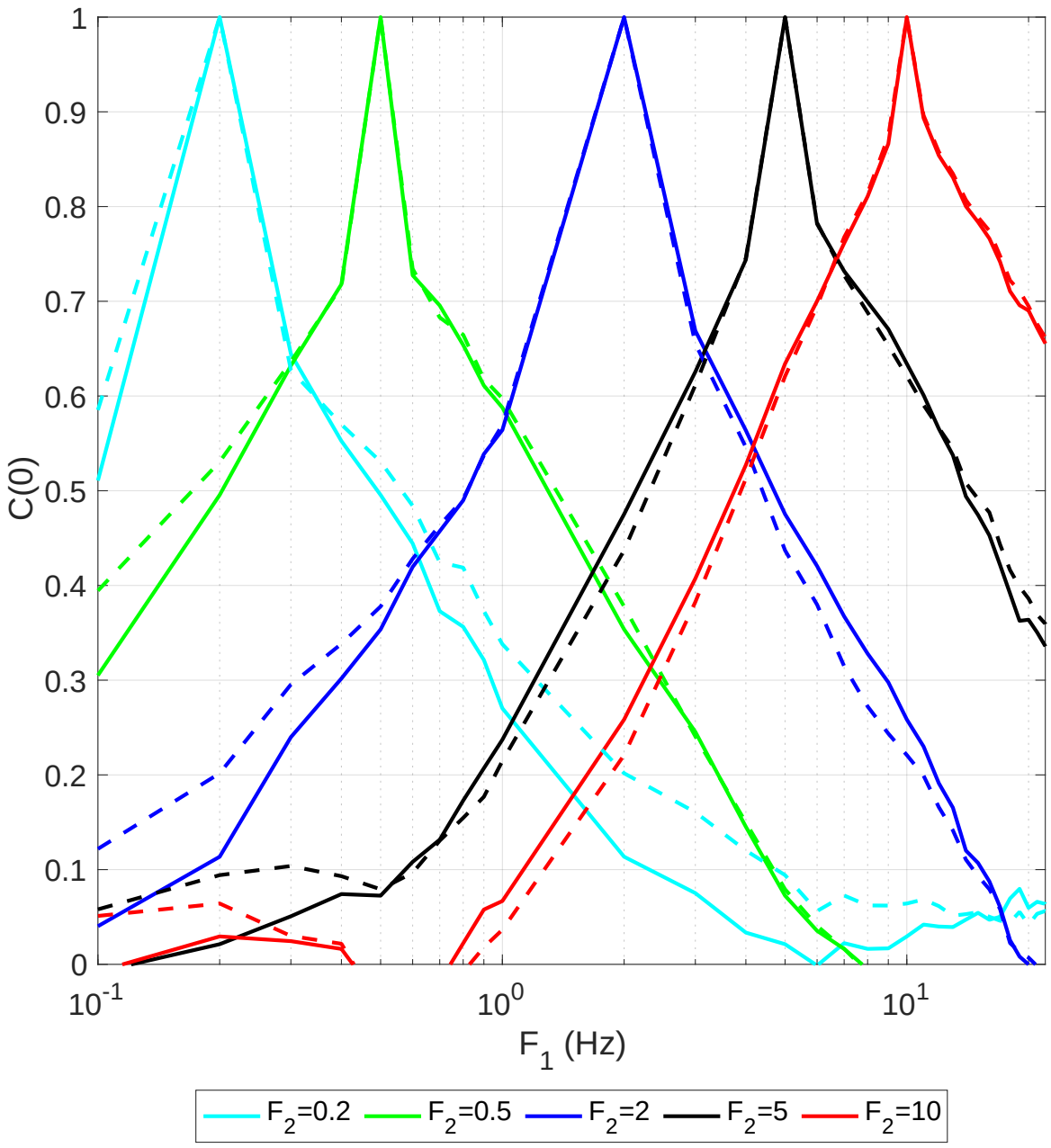

Figure 5.5: Comparison of the within-event inter-frequency correlation model after setting $h = 0$ in Equation 5.17 (solid lines) and the Bayless and Abrahamson (2019) empirical within-event inter-frequency correlation coefficients (dashed lines), at reference frequencies 0.2 Hz, 0.5 Hz, 2 Hz, 5 Hz, and 10 Hz.

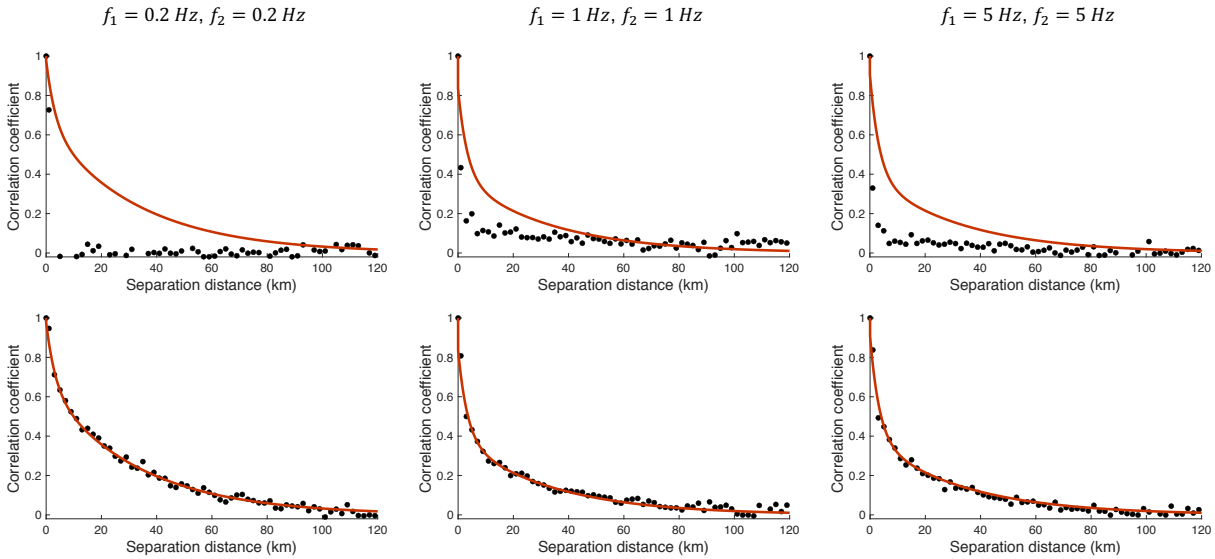

Figure 5.6: Comparison of the spatial correlation coefficients of ε for EAS at the reference frequency pairs $f_1 = f_2 = 0.2$ Hz (left), $f_1 = f_2 = 1$ Hz (middle) and $f_1 = f_2 = 5$ Hz (right) from the proposed model (red lines) and the SDSU Module before (top) and after (bottom) applying our method (dots) for the Loma Prieta earthquake with 50 source realizations.

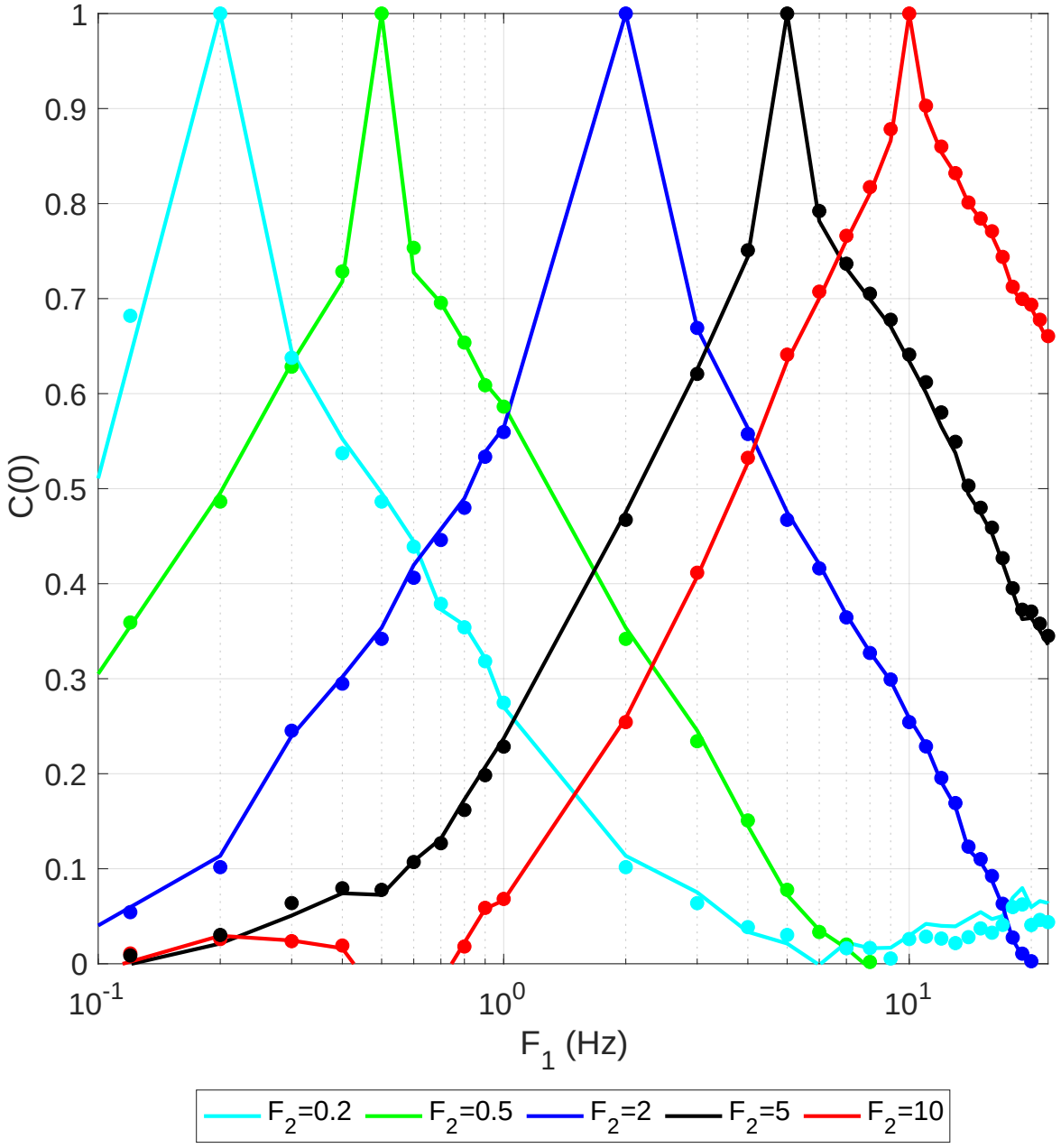

Figure 5.7: Comparison of the inter-frequency correlation resulting from the presented model setting $h = 0$ in Equation 5.17 (solid lines) and the correlation coefficients of ε for EAS from the SDSU Module after applying our method to the Loma Prieta earthquake with 50 source realizations (dots) at reference frequencies 0.2 Hz, 0.5 Hz, 2 Hz, 5 Hz, and 10 Hz.

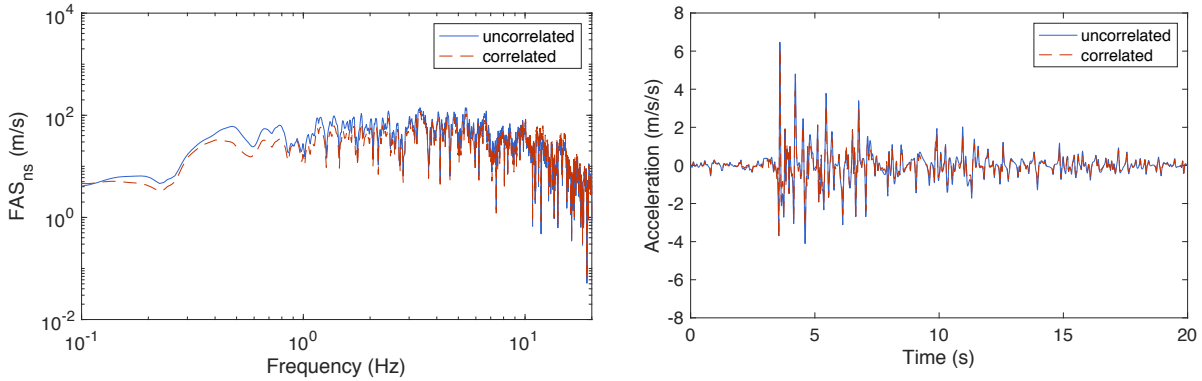

Figure 5.8: Examples of the north-south component of FAS (left) and acceleration time histories (right) for one simulation of the Loma Prieta earthquake at station 8001-CLS after (red dashed line) and before (blue solid line) applying our method to implement the proposed spatial correlation model.

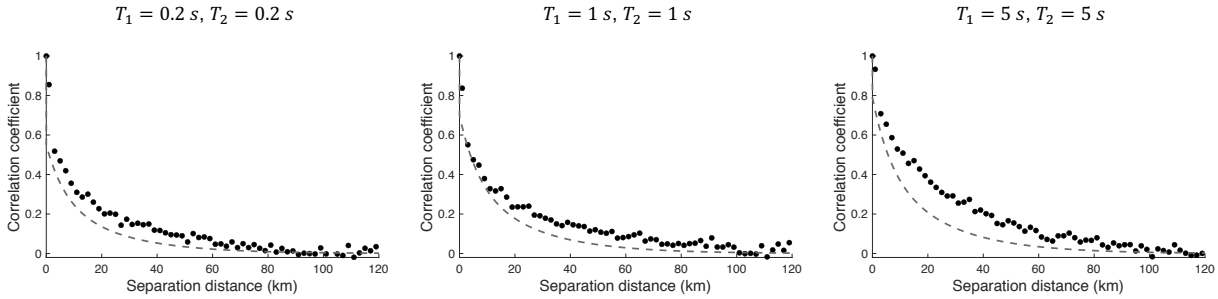

Figure 5.9: Comparison of the spatial correlation coefficients of ε for the spectral accelerations at reference period pairs (left) $T_1 = T_2 = 0.2$ s, (middle) $T_1 = T_2 = 1$ s, and (right) $T_1 = T_2 = 5$ s from the Loth and Baker (2013) model (dashed lines) and the SDSU Module after applying our method (dots) to the Loma Prieta earthquake synthetic seismograms with 50 source realizations.

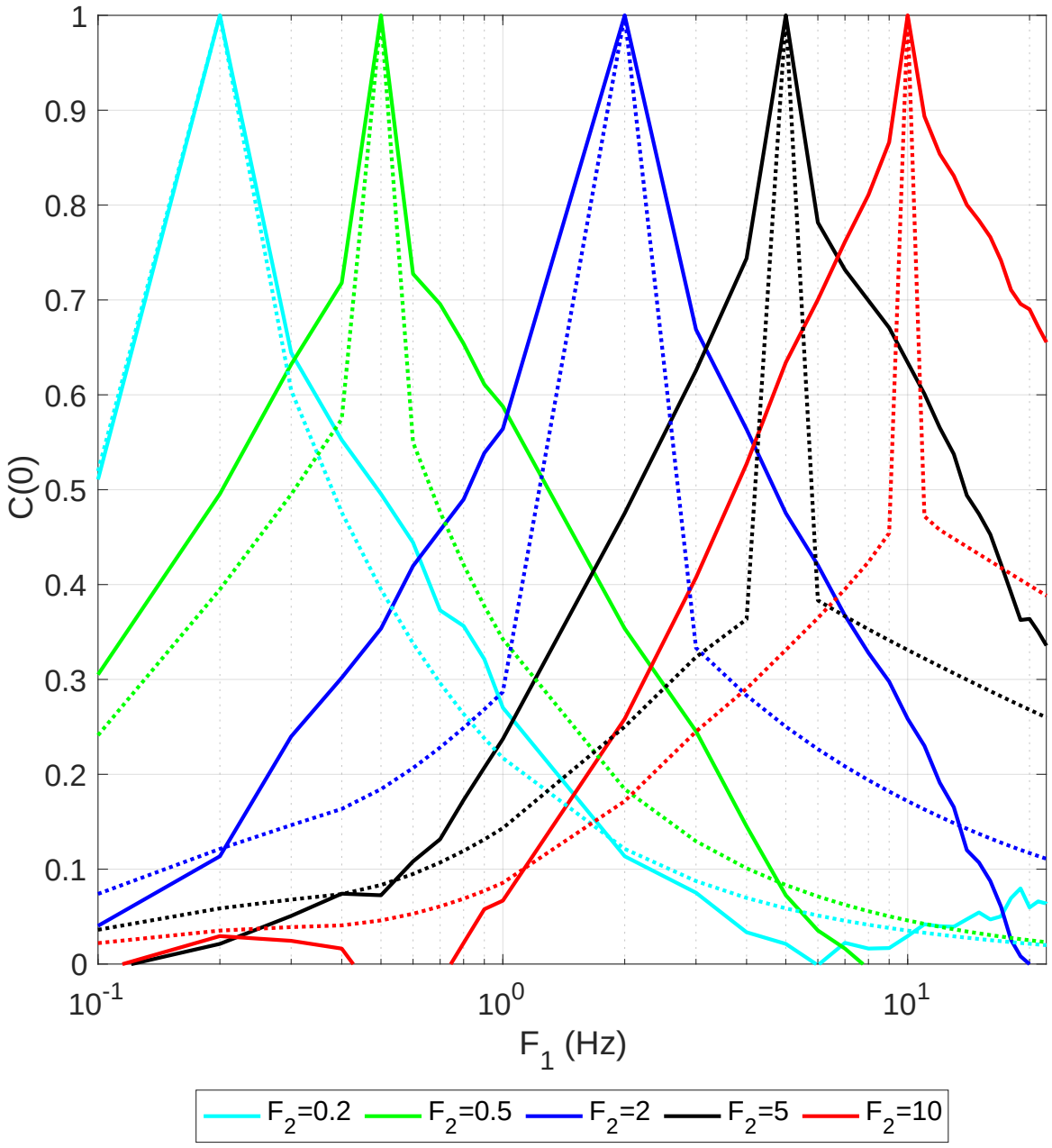

Figure 5.10: Comparison of the within-event inter-frequency correlation model after setting $h = 0$ in Equation 5.17 (solid lines) and Stafford (2017) within-event inter-frequency correlation model (dotted lines), at reference frequencies 0.2 Hz, 0.5 Hz, 2 Hz, 5 Hz, and 10 Hz.

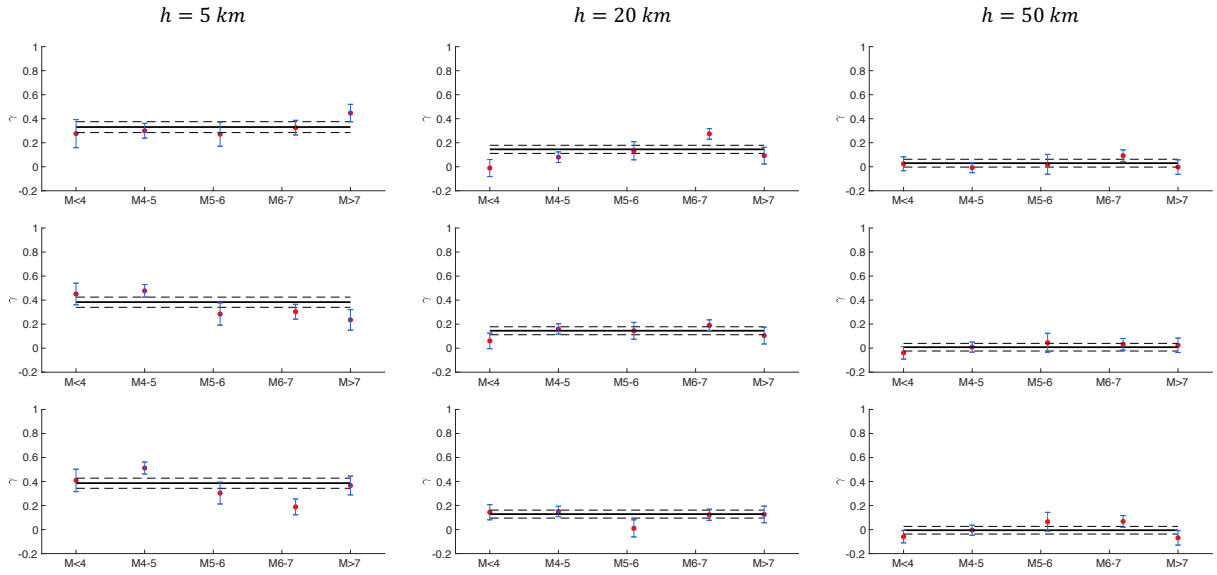

Figure 5.11: Empirical semivariograms for the full (solid lines) and partial (dots) datasets binned by magnitude (M<4, 4≤M<5, 5≤M<6, 6≤M<7, M≥7) at the frequency pairs (top row) $f_1 = f_2 = 1$ Hz, (middle row) $f_1 = f_2 = 2$ Hz, and (bottom row) $f_1 = f_2 = 5$ Hz computed at separation distances (left column) 5 km, (center column) 20 km and (right column) 50 km. Dashed lines and vertical bars represent 99% confidence intervals of the semivariograms for the full and partial datasets, respectively.

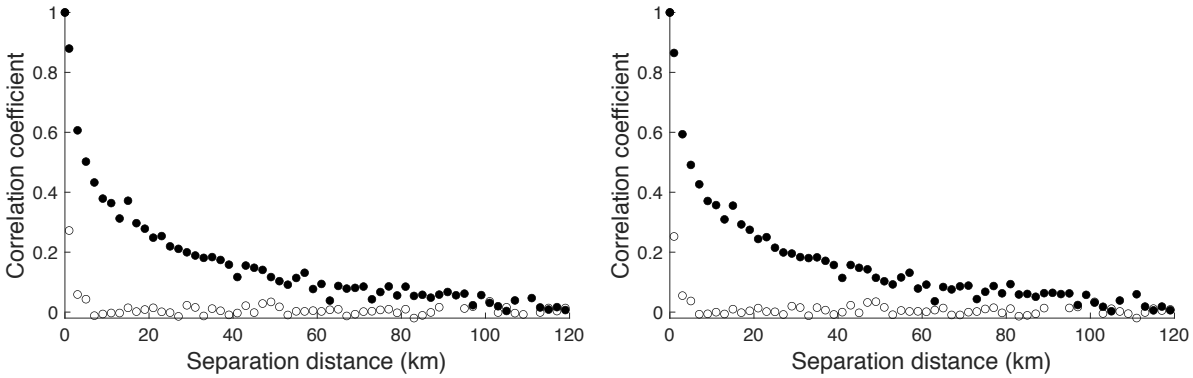

Figure 5.12: Spatial correlation coefficients of ε for the cumulative absolute velocity (left) and Arias intensity (right) from the SDSU Module before (hollow dots) and after (solid dots) applying our method to the Loma Prieta earthquake synthetic seismograms with 50 source realizations.

Supplementary Materials

Implementation examples at all the stations

Figure S5.1 shows the example components of synthetic time histories of acceleration and FAS at all the other stations for the Loma Prieta earthquake before and after implementing the proposed spatial correlation model. The "uncorrelated" case here in Figure S5.1 is computed when the off-diagonal correlation terms of the correlation matrixes (Step (5) in Appendix B) are being set to zero. The comparison shows that the resulting correlation has subtle effects on the time domain.

Spatial correlation implemented into the six western U.S. earthquakes

We use the M6.9 1989 Loma Prieta earthquake as a demonstration of the performance of our spatial correlation method in the manuscript. In addition, we have implemented spatial correlation into six other SCEC validation earthquakes in California, namely the 1992 M7.2 1992 Landers, the 1994 M6.7 Northridge, the 1986 M6.1 North Palm Springs, the 1987 M5.9 Whittier, the 2008 M5.4 Chino Hills, and the 2007 M5.5 Alum Rock earthquakes. The final correlation coefficients of epsilon compared with the proposed model for the six earthquakes using 50 source realizations are shown in Figures S5.2 – S5.7. The results for all the 7 western U.S. earthquakes, with magnitudes between 5.0 and 7.2, show that the spatial correlations are well predicted by our method.

EAS spatial correlation model comparison with Loth and Baker (2013) PSA model

A comparison between our EAS within-event spatial correlation model and the model for PSA by Loth and Baker (2013) is shown in Figure S5.8. The higher the frequency (shorter period), the larger the difference between the two models. This is because that the shorter period PSA values are influenced by a wider frequency range, but the EAS is calculated from the Fourier

transform at each frequency independently.

Empirical spatial correlation model analysis

Our analysis revealed that the EAS spatial correlation tends to decrease more slowly with distance at frequencies larger than about 4 Hz. The separation distance increases by $\sim$2 km from 4 Hz to 23 Hz when the correlation coefficient equals 0.5 for pairs of two identical frequencies (see Figure 5.4 and Discussion Section). We note that a similar trend is present in the Loth and Baker (2013) model for spectral accelerations, which is based on recordings of 8 earthquakes with magnitudes from 6 to 7.6 from the PEER NGA database (see Figure S5.9). Figure S5.10 shows that this trend is dominated by the data from earthquakes with magnitudes between 6 to 7, with smaller contributions from other magnitude bins (M3-6 and M7-8). The trend decreases as the threshold correlation coefficient increases, as shown in Figure S5.11, with no noticeable increase with separation distance observed when the correlation coefficient equals 0.7. While not affecting our spatial correlation technique, future work should attempt to understand the reason for this finding.

Table S5.1: Coregionalization matrix $\mathbf{P}^1$

f (Hz)	0.1	0.2	0.3	0.4	0.5	0.6	0.7	0.8	0.9	1.0	2.0	3.0	4.0	5.0	6.0	7.0	8.0	9.0	10.0	11.0	12.0	13.0	14.0	15.0	16.0	17.0	18.0	19.0	20.0	21.0	22.0	23.0
0.1	0.056	0.061	0.076	0.054	0.048	0.059	0.063	0.054	0.027	0.055	0.073	0.064	0.071	0.035	0.026	0.013	0.013	0.015	-0.001	0.000	-0.007	-0.011	-0.013	-0.021	-0.029	-0.045	-0.058	-0.070	-0.075	-0.077	-0.076	-0.071
0.2	0.061	0.328	0.152	0.154	0.129	0.135	0.113	0.117	0.092	0.096	0.092	0.061	0.077	0.036	0.014	-0.005	-0.007	-0.014	-0.013	-0.015	-0.030	-0.036	-0.041	-0.054	-0.065	-0.074	-0.093	-0.099	-0.099	-0.099	-0.101	-0.084
0.3	0.076	0.152	0.434	0.209	0.174	0.197	0.171	0.158	0.145	0.146	0.132	0.093	0.099	0.048	0.047	0.007	-0.004	0.005	-0.005	-0.007	-0.013	-0.023	-0.027	-0.040	-0.059	-0.052	-0.068	-0.074	-0.075	-0.067	-0.078	-0.075
0.4	0.054	0.154	0.209	0.459	0.219	0.221	0.194	0.169	0.174	0.169	0.141	0.094	0.102	0.058	0.061	0.016	0.011	0.024	0.027	0.025	0.008	-0.004	-0.014	-0.021	-0.038	-0.033	-0.044	-0.047	-0.056	-0.039	-0.062	-0.053
0.5	0.048	0.129	0.174	0.219	0.434	0.242	0.207	0.181	0.184	0.186	0.132	0.072	0.078	0.042	0.043	0.023	0.019	0.025	0.024	0.032	0.013	0.009	0.003	-0.014	-0.028	-0.034	-0.046	-0.050	-0.052	-0.045	-0.064	-0.060
0.6	0.059	0.135	0.197	0.221	0.242	0.485	0.275	0.238	0.234	0.227	0.149	0.094	0.083	0.031	0.029	0.018	0.005	0.017	0.006	0.022	0.013	0.005	-0.001	-0.013	-0.026	-0.035	-0.041	-0.050	-0.054	-0.040	-0.052	-0.040
0.7	0.063	0.113	0.171	0.194	0.207	0.275	0.465	0.263	0.251	0.241	0.161	0.111	0.098	0.061	0.060	0.040	0.028	0.037	0.024	0.030	0.023	0.014	0.019	0.011	-0.006	-0.019	-0.027	-0.032	-0.036	-0.021	-0.031	-0.029
0.8	0.054	0.117	0.158	0.169	0.181	0.238	0.263	0.425	0.275	0.258	0.164	0.101	0.096	0.054	0.044	0.032	0.013	0.029	0.021	0.033	0.028	0.013	0.017	0.004	-0.006	-0.023	-0.028	-0.029	-0.027	-0.017	-0.025	-0.017
0.9	0.027	0.092	0.145	0.174	0.184	0.234	0.251	0.275	0.470	0.283	0.201	0.145	0.115	0.065	0.059	0.039	0.022	0.041	0.037	0.042	0.036	0.019	0.015	0.006	-0.009	-0.026	-0.031	-0.033	-0.030	-0.013	-0.026	-0.018
1.0	0.055	0.096	0.146	0.169	0.186	0.227	0.241	0.258	0.283	0.449	0.210	0.154	0.126	0.085	0.063	0.051	0.035	0.036	0.038	0.033	0.036	0.019	0.022	0.013	0.001	-0.021	-0.032	-0.028	-0.028	-0.014	-0.018	-0.003
2.0	0.073	0.092	0.132	0.141	0.132	0.149	0.161	0.164	0.201	0.210	0.550	0.328	0.268	0.204	0.181	0.157	0.145	0.148	0.138	0.138	0.135	0.120	0.114	0.111	0.096	0.090	0.074	0.070	0.084	0.083	0.091	0.093
3.0	0.064	0.061	0.093	0.094	0.072	0.094	0.111	0.101	0.145	0.154	0.328	0.565	0.356	0.296	0.272	0.238	0.221	0.217	0.189	0.183	0.179	0.163	0.151	0.144	0.136	0.146	0.123	0.115	0.124	0.124	0.117	0.120
4.0	0.071	0.077	0.099	0.102	0.078	0.083	0.098	0.096	0.115	0.126	0.268	0.356	0.520	0.359	0.324	0.291	0.256	0.252	0.217	0.207	0.199	0.184	0.171	0.173	0.163	0.174	0.150	0.136	0.142	0.139	0.137	0.132
5.0	0.035	0.036	0.048	0.058	0.042	0.031	0.061	0.054	0.065	0.085	0.204	0.296	0.359	0.518	0.367	0.339	0.306	0.291	0.254	0.241	0.229	0.218	0.202	0.195	0.194	0.208	0.192	0.178	0.189	0.181	0.170	0.170
6.0	0.026	0.014	0.047	0.061	0.043	0.029	0.060	0.044	0.059	0.063	0.181	0.272	0.324	0.367	0.492	0.370	0.337	0.318	0.272	0.256	0.253	0.239	0.225	0.219	0.215	0.227	0.209	0.196	0.209	0.201	0.185	0.186
7.0	0.013	-0.005	0.007	0.016	0.023	0.018	0.040	0.032	0.039	0.051	0.157	0.238	0.291	0.339	0.370	0.493	0.391	0.373	0.326	0.307	0.284	0.258	0.249	0.241	0.236	0.251	0.233	0.217	0.230	0.223	0.209	0.210
8.0	0.013	-0.007	-0.004	0.011	0.019	0.005	0.028	0.013	0.022	0.035	0.145	0.221	0.256	0.306	0.337	0.391	0.486	0.401	0.348	0.327	0.300	0.273	0.263	0.256	0.245	0.269	0.245	0.227	0.242	0.232	0.219	0.217
9.0	0.015	-0.014	0.005	0.024	0.025	0.017	0.037	0.029	0.041	0.036	0.148	0.217	0.252	0.291	0.318	0.373	0.401	0.485	0.373	0.347	0.314	0.295	0.290	0.277	0.266	0.287	0.265	0.246	0.255	0.239	0.224	0.222
10.0	-0.001	-0.013	-0.005	0.027	0.024	0.006	0.024	0.021	0.037	0.038	0.138	0.189	0.217	0.254	0.272	0.326	0.348	0.373	0.412	0.347	0.312	0.289	0.273	0.267	0.257	0.276	0.259	0.241	0.245	0.233	0.216	0.205
11.0	0.000	-0.015	-0.007	0.025	0.032	0.022	0.030	0.033	0.042	0.033	0.138	0.183	0.207	0.241	0.256	0.307	0.327	0.347	0.347	0.409	0.336	0.309	0.294	0.288	0.279	0.297	0.273	0.259	0.258	0.240	0.220	0.217
12.0	-0.007	-0.030	-0.013	0.008	0.013	0.013	0.023	0.028	0.036	0.036	0.135	0.179	0.199	0.229	0.253	0.284	0.300	0.314	0.312	0.336	0.385	0.327	0.308	0.299	0.291	0.313	0.285	0.269	0.267	0.253	0.232	0.227
13.0	-0.011	-0.036	-0.023	-0.004	0.009	0.005	0.014	0.013	0.019	0.019	0.120	0.163	0.184	0.218	0.239	0.258	0.273	0.295	0.289	0.309	0.327	0.373	0.319	0.306	0.305	0.323	0.302	0.285	0.280	0.271	0.246	0.247
14.0	-0.013	-0.041	-0.027	-0.014	0.003	-0.001	0.019	0.017	0.015	0.022	0.114	0.151	0.171	0.202	0.225	0.249	0.263	0.290	0.273	0.294	0.308	0.319	0.364	0.328	0.317	0.336	0.315	0.292	0.293	0.282	0.257	0.251
15.0	-0.021	-0.054	-0.040	-0.021	-0.014	-0.013	0.011	0.004	0.006	0.013	0.111	0.144	0.173	0.195	0.219	0.241	0.256	0.277	0.267	0.288	0.299	0.306	0.328	0.378	0.345	0.352	0.328	0.311	0.311	0.296	0.274	0.270
16.0	-0.029	-0.065	-0.059	-0.038	-0.028	-0.026	-0.006	-0.006	-0.009	0.001	0.096	0.136	0.163	0.194	0.215	0.236	0.245	0.266	0.257	0.279	0.291	0.305	0.317	0.345	0.386	0.376	0.350	0.331	0.329	0.316	0.291	0.287
17.0	-0.045	-0.074	-0.052	-0.033	-0.034	-0.035	-0.019	-0.023	-0.026	-0.021	0.090	0.146	0.174	0.208	0.227	0.251	0.269	0.287	0.276	0.297	0.313	0.323	0.336	0.352	0.376	0.435	0.386	0.363	0.362	0.351	0.325	0.318
18.0	-0.058	-0.093	-0.068	-0.044	-0.046	-0.041	-0.027	-0.028	-0.031	-0.032	0.074	0.123	0.150	0.192	0.209	0.233	0.245	0.265	0.259	0.273	0.285	0.302	0.315	0.328	0.350	0.386	0.418	0.382	0.375	0.359	0.335	0.330
19.0	-0.070	-0.099	-0.074	-0.047	-0.050	-0.050	-0.032	-0.029	-0.033	-0.028	0.070	0.115	0.136	0.178	0.196	0.217	0.227	0.246	0.241	0.259	0.269	0.285	0.292	0.311	0.331	0.363	0.382	0.400	0.381	0.356	0.337	0.329
20.0	-0.075	-0.099	-0.075	-0.056	-0.052	-0.054	-0.036	-0.027	-0.030	-0.028	0.084	0.124	0.142	0.189	0.209	0.230	0.242	0.255	0.245	0.258	0.267	0.280	0.293	0.311	0.329	0.362	0.375	0.381	0.423	0.382	0.356	0.350
21.0	-0.077	-0.099	-0.067	-0.039	-0.045	-0.040	-0.021	-0.017	-0.013	-0.014	0.083	0.124	0.139	0.181	0.201	0.223	0.232	0.239	0.233	0.240	0.253	0.271	0.282	0.296	0.316	0.351	0.359	0.356	0.382	0.404	0.372	0.363
22.0	-0.076	-0.101	-0.078	-0.062	-0.064	-0.052	-0.031	-0.025	-0.026	-0.018	0.091	0.117	0.137	0.170	0.185	0.209	0.219	0.224	0.216	0.220	0.232	0.246	0.257	0.274	0.291	0.325	0.335	0.337	0.356	0.372	0.383	0.366
23.0	-0.071	-0.084	-0.075	-0.053	-0.060	-0.040	-0.029	-0.017	-0.018	-0.003	0.093	0.120	0.132	0.170	0.186	0.210	0.217	0.222	0.205	0.217	0.227	0.247	0.251	0.270	0.287	0.318	0.330	0.329	0.350	0.363	0.366	0.396

Table S5.2: Coregionalization matrix $\mathbf{P^2}$

f (Hz)	0.1	0.2	0.3	0.4	0.5	0.6	0.7	0.8	0.9	1.0	2.0	3.0	4.0	5.0	6.0	7.0	8.0	9.0	10.0	11.0	12.0	13.0	14.0	15.0	16.0	17.0	18.0	19.0	20.0	21.0	22.0	23.0
0.1	0.904	0.431	0.285	0.272	0.224	0.235	0.166	0.166	0.157	0.086	-0.038	-0.016	-0.075	-0.045	-0.052	-0.026	-0.027	-0.029	-0.009	0.004	-0.007	0.006	0.027	0.043	0.056	0.084	0.103	0.112	0.087	0.083	0.070	0.048
0.2	0.431	0.650	0.472	0.369	0.340	0.298	0.243	0.229	0.213	0.166	0.020	0.006	-0.054	-0.020	-0.016	0.017	0.020	0.028	0.044	0.059	0.067	0.070	0.082	0.106	0.110	0.124	0.167	0.181	0.158	0.169	0.166	0.141
0.3	0.285	0.472	0.526	0.455	0.425	0.361	0.349	0.330	0.302	0.273	0.098	0.060	-0.018	-0.009	-0.018	0.023	0.019	0.016	0.031	0.048	0.046	0.045	0.048	0.067	0.073	0.077	0.110	0.119	0.087	0.089	0.097	0.086
0.4	0.272	0.369	0.455	0.455	0.440	0.393	0.389	0.381	0.339	0.317	0.141	0.093	0.008	-0.002	-0.028	0.004	-0.007	-0.025	-0.011	-0.006	-0.009	-0.009	-0.012	0.000	0.006	0.003	0.024	0.023	0.003	-0.006	0.010	0.008
0.5	0.224	0.340	0.425	0.440	0.477	0.437	0.440	0.429	0.390	0.367	0.207	0.142	0.042	0.014	-0.021	-0.014	-0.029	-0.056	-0.057	-0.062	-0.073	-0.081	-0.093	-0.088	-0.081	-0.089	-0.075	-0.079	-0.097	-0.108	-0.103	-0.105
0.6	0.235	0.298	0.361	0.393	0.437	0.432	0.419	0.422	0.388	0.367	0.243	0.186	0.093	0.065	0.027	0.026	0.008	-0.024	-0.027	-0.039	-0.058	-0.064	-0.083	-0.078	-0.075	-0.085	-0.080	-0.087	-0.102	-0.115	-0.114	-0.119
0.7	0.166	0.243	0.349	0.389	0.440	0.419	0.440	0.433	0.399	0.381	0.259	0.193	0.100	0.061	0.021	0.020	0.004	-0.028	-0.029	-0.042	-0.061	-0.068	-0.088	-0.088	-0.083	-0.095	-0.095	-0.102	-0.117	-0.135	-0.134	-0.135
0.8	0.166	0.229	0.330	0.381	0.429	0.422	0.433	0.456	0.415	0.396	0.285	0.228	0.139	0.107	0.068	0.066	0.050	0.013	0.016	-0.002	-0.022	-0.027	-0.052	-0.053	-0.051	-0.067	-0.071	-0.081	-0.094	-0.114	-0.109	-0.110
0.9	0.157	0.213	0.302	0.339	0.390	0.388	0.399	0.415	0.407	0.382	0.295	0.244	0.165	0.146	0.109	0.105	0.089	0.053	0.050	0.034	0.008	0.000	-0.025	-0.025	-0.026	-0.041	-0.044	-0.056	-0.072	-0.090	-0.088	-0.095
1.0	0.086	0.166	0.273	0.317	0.367	0.367	0.381	0.396	0.382	0.387	0.297	0.246	0.177	0.154	0.116	0.112	0.097	0.062	0.055	0.040	0.015	0.005	-0.024	-0.025	-0.026	-0.044	-0.047	-0.063	-0.075	-0.092	-0.090	-0.096
2.0	-0.038	0.020	0.098	0.141	0.207	0.243	0.259	0.285	0.295	0.297	0.344	0.307	0.269	0.265	0.234	0.209	0.188	0.156	0.135	0.111	0.078	0.062	0.023	0.019	0.008	-0.015	-0.031	-0.050	-0.059	-0.074	-0.085	-0.096
3.0	-0.016	0.006	0.060	0.093	0.142	0.186	0.193	0.228	0.244	0.246	0.307	0.318	0.294	0.301	0.279	0.261	0.244	0.217	0.206	0.184	0.155	0.143	0.109	0.103	0.089	0.065	0.047	0.028	0.021	0.008	-0.002	-0.016
4.0	-0.075	-0.054	-0.018	0.008	0.042	0.093	0.100	0.139	0.165	0.177	0.269	0.294	0.333	0.336	0.325	0.309	0.299	0.279	0.278	0.255	0.230	0.219	0.186	0.177	0.162	0.136	0.119	0.100	0.094	0.084	0.074	0.065
5.0	-0.045	-0.020	-0.009	-0.002	0.014	0.065	0.061	0.107	0.146	0.154	0.265	0.301	0.336	0.390	0.373	0.365	0.357	0.343	0.342	0.325	0.298	0.288	0.258	0.255	0.235	0.210	0.197	0.178	0.170	0.162	0.153	0.138
6.0	-0.052	-0.016	-0.018	-0.028	-0.021	0.027	0.021	0.068	0.109	0.116	0.234	0.279	0.325	0.373	0.399	0.382	0.378	0.369	0.375	0.361	0.340	0.329	0.304	0.301	0.283	0.257	0.243	0.232	0.220	0.217	0.206	0.190
7.0	-0.026	0.017	0.023	0.004	-0.014	0.026	0.020	0.066	0.105	0.112	0.209	0.261	0.309	0.365	0.382	0.409	0.396	0.390	0.400	0.394	0.379	0.372	0.351	0.349	0.334	0.305	0.299	0.291	0.275	0.274	0.266	0.254
8.0	-0.027	0.020	0.019	-0.007	-0.029	0.008	0.004	0.050	0.089	0.097	0.188	0.244	0.299	0.357	0.378	0.396	0.410	0.399	0.417	0.411	0.397	0.392	0.375	0.371	0.358	0.329	0.323	0.317	0.300	0.299	0.291	0.279
9.0	-0.029	0.028	0.016	-0.025	-0.056	-0.024	-0.028	0.013	0.053	0.062	0.156	0.217	0.279	0.343	0.369	0.390	0.399	0.416	0.430	0.428	0.417	0.412	0.399	0.396	0.385	0.357	0.354	0.351	0.334	0.336	0.327	0.313
10.0	-0.009	0.044	0.031	-0.011	-0.057	-0.027	-0.029	0.016	0.050	0.055	0.135	0.206	0.278	0.342	0.375	0.400	0.417	0.430	0.485	0.476	0.470	0.475	0.468	0.460	0.452	0.422	0.412	0.417	0.401	0.393	0.391	0.382
11.0	0.004	0.059	0.048	-0.006	-0.062	-0.039	-0.042	-0.002	0.034	0.040	0.111	0.184	0.255	0.325	0.361	0.394	0.411	0.428	0.476	0.489	0.479	0.483	0.479	0.471	0.465	0.436	0.430	0.439	0.420	0.416	0.411	0.402
12.0	-0.007	0.067	0.046	-0.009	-0.073	-0.058	-0.061	-0.022	0.008	0.015	0.078	0.155	0.230	0.298	0.340	0.379	0.397	0.417	0.470	0.479	0.488	0.489	0.488	0.481	0.477	0.446	0.444	0.454	0.436	0.433	0.433	0.427
13.0	0.006	0.070	0.045	-0.009	-0.081	-0.064	-0.068	-0.027	0.000	0.005	0.062	0.143	0.219	0.288	0.329	0.372	0.392	0.412	0.475	0.483	0.489	0.508	0.504	0.495	0.492	0.464	0.458	0.470	0.453	0.446	0.450	0.444
14.0	0.027	0.082	0.048	-0.012	-0.093	-0.083	-0.088	-0.052	-0.025	-0.024	0.023	0.109	0.186	0.258	0.304	0.351	0.375	0.399	0.468	0.479	0.488	0.504	0.521	0.508	0.506	0.480	0.476	0.491	0.474	0.465	0.472	0.467
15.0	0.043	0.106	0.067	0.000	-0.088	-0.078	-0.088	-0.053	-0.025	-0.025	0.019	0.103	0.177	0.255	0.301	0.349	0.371	0.396	0.460	0.471	0.481	0.495	0.508	0.511	0.503	0.483	0.483	0.493	0.476	0.469	0.478	0.470
16.0	0.056	0.110	0.073	0.006	-0.081	-0.075	-0.083	-0.051	-0.026	-0.026	0.008	0.089	0.162	0.235	0.283	0.334	0.358	0.385	0.452	0.465	0.477	0.492	0.506	0.503	0.507	0.481	0.480	0.495	0.477	0.470	0.477	0.472
17.0	0.084	0.124	0.077	0.003	-0.089	-0.085	-0.095	-0.067	-0.041	-0.044	-0.015	0.065	0.136	0.210	0.257	0.305	0.329	0.357	0.422	0.436	0.446	0.464	0.480	0.483	0.481	0.474	0.471	0.484	0.467	0.458	0.466	0.458
18.0	0.103	0.167	0.110	0.024	-0.075	-0.080	-0.095	-0.071	-0.044	-0.047	-0.031	0.047	0.119	0.197	0.243	0.299	0.323	0.354	0.412	0.430	0.444	0.458	0.476	0.483	0.480	0.471	0.485	0.493	0.475	0.474	0.484	0.475
19.0	0.112	0.181	0.119	0.023	-0.079	-0.087	-0.102	-0.081	-0.056	-0.063	-0.050	0.028	0.100	0.178	0.232	0.291	0.317	0.351	0.417	0.439	0.454	0.470	0.491	0.493	0.495	0.484	0.493	0.517	0.493	0.493	0.498	0.491
20.0	0.087	0.158	0.087	0.003	-0.097	-0.102	-0.117	-0.094	-0.072	-0.075	-0.059	0.021	0.094	0.170	0.220	0.275	0.300	0.334	0.401	0.420	0.436	0.453	0.474	0.476	0.477	0.467	0.475	0.493	0.480	0.475	0.484	0.478
21.0	0.083	0.169	0.089	-0.006	-0.108	-0.115	-0.135	-0.114	-0.090	-0.092	-0.074	0.008	0.084	0.162	0.217	0.274	0.299	0.336	0.393	0.416	0.433	0.446	0.465	0.469	0.470	0.458	0.474	0.493	0.475	0.489	0.491	0.484
22.0	0.070	0.166	0.097	0.010	-0.103	-0.114	-0.134	-0.109	-0.088	-0.090	-0.085	-0.002	0.074	0.153	0.206	0.266	0.291	0.327	0.391	0.411	0.433	0.450	0.472	0.478	0.477	0.466	0.484	0.498	0.484	0.491	0.512	0.505
23.0	0.048	0.141	0.086	0.008	-0.105	-0.119	-0.135	-0.110	-0.095	-0.096	-0.096	-0.016	0.065	0.138	0.190	0.254	0.279	0.313	0.382	0.402	0.427	0.444	0.467	0.470	0.472	0.458	0.475	0.491	0.478	0.484	0.505	0.511

Table S5.3: Coregionalization matrix $\mathbf{P}^3$

f (Hz)	0.1	0.2	0.3	0.4	0.5	0.6	0.7	0.8	0.9	1.0	2.0	3.0	4.0	5.0	6.0	7.0	8.0	9.0	10.0	11.0	12.0	13.0	14.0	15.0	16.0	17.0	18.0	19.0	20.0	21.0	22.0	23.0
0.1	0.040	0.019	0.028	0.030	0.033	0.017	0.030	0.027	0.030	0.033	0.006	0.014	0.018	0.001	-0.002	-0.007	-0.010	-0.001	0.002	-0.002	-0.003	-0.003	-0.012	-0.014	-0.015	-0.009	-0.011	-0.010	-0.006	-0.008	-0.006	-0.006
0.2	0.019	0.021	0.021	0.030	0.026	0.012	0.016	0.010	0.016	0.009	0.001	0.008	0.010	0.005	0.001	0.010	0.004	0.003	-0.001	-0.002	0.003	0.005	0.005	0.002	0.002	0.000	-0.005	-0.002	0.001	-0.004	-0.001	-0.004
0.3	0.028	0.021	0.040	0.041	0.033	0.022	0.015	0.022	0.018	0.025	0.010	0.013	0.013	0.011	0.006	-0.003	-0.002	-0.004	-0.002	-0.004	-0.004	-0.004	-0.005	-0.008	-0.007	-0.015	-0.024	-0.020	-0.013	-0.013	-0.010	-0.010
0.4	0.030	0.030	0.041	0.086	0.058	0.048	0.037	0.047	0.037	0.035	0.020	0.021	0.018	0.018	0.016	0.020	0.011	0.009	0.000	-0.002	0.003	0.008	0.008	0.002	0.001	-0.002	-0.010	-0.008	0.002	-0.006	0.001	-0.007
0.5	0.033	0.026	0.033	0.058	0.090	0.049	0.049	0.044	0.037	0.035	0.015	0.032	0.025	0.016	0.014	0.006	0.005	0.005	-0.006	-0.010	0.000	-0.001	0.006	0.005	0.003	0.002	-0.002	-0.004	0.002	-0.002	0.003	0.000
0.6	0.017	0.012	0.022	0.048	0.049	0.083	0.041	0.040	0.030	0.038	0.027	0.028	0.017	0.012	0.008	-0.007	-0.010	-0.004	-0.011	-0.019	-0.019	-0.013	-0.010	-0.009	-0.011	-0.011	-0.018	-0.015	-0.012	-0.012	-0.013	-0.016
0.7	0.030	0.016	0.015	0.037	0.049	0.041	0.095	0.056	0.057	0.058	0.037	0.035	0.028	0.009	0.000	0.000	0.000	0.000	-0.014	-0.015	-0.014	-0.013	-0.012	-0.016	-0.013	-0.008	-0.007	-0.003	-0.003	-0.005	-0.007	-0.011
0.8	0.027	0.010	0.022	0.047	0.044	0.040	0.056	0.118	0.065	0.059	0.041	0.043	0.015	0.012	0.011	0.000	0.005	0.002	-0.014	-0.022	-0.026	-0.016	-0.020	-0.018	-0.021	-0.007	-0.010	-0.010	-0.014	-0.012	-0.015	-0.019
0.9	0.030	0.016	0.018	0.037	0.037	0.030	0.057	0.065	0.123	0.093	0.043	0.021	0.011	-0.005	-0.006	-0.006	-0.001	-0.010	-0.029	-0.027	-0.033	-0.027	-0.020	-0.025	-0.022	-0.010	-0.013	-0.009	-0.018	-0.018	-0.015	-0.024
1.0	0.033	0.009	0.025	0.035	0.035	0.038	0.058	0.059	0.093	0.164	0.058	0.029	0.016	-0.001	-0.002	-0.013	-0.005	-0.003	-0.026	-0.021	-0.031	-0.020	-0.024	-0.024	-0.024	-0.005	-0.002	-0.005	-0.007	-0.007	-0.010	-0.025
2.0	0.006	0.001	0.010	0.020	0.015	0.027	0.037	0.041	0.043	0.058	0.106	0.034	0.027	0.007	0.005	0.001	-0.005	-0.006	-0.015	-0.019	-0.022	-0.016	-0.017	-0.023	-0.017	-0.014	-0.017	-0.012	-0.024	-0.017	-0.022	-0.016
3.0	0.014	0.008	0.013	0.021	0.032	0.028	0.035	0.043	0.021	0.029	0.034	0.117	0.066	0.029	0.023	0.020	0.014	0.017	0.012	0.010	0.016	0.016	0.017	0.008	0.009	-0.006	0.002	0.003	-0.001	0.004	0.006	0.003
4.0	0.018	0.010	0.013	0.018	0.025	0.017	0.028	0.015	0.011	0.016	0.027	0.066	0.147	0.049	0.030	0.019	0.026	0.024	0.032	0.031	0.032	0.031	0.031	0.014	0.021	0.007	0.017	0.022	0.020	0.024	0.018	0.023
5.0	0.001	0.005	0.011	0.018	0.016	0.012	0.009	0.012	-0.005	-0.001	0.007	0.029	0.049	0.092	0.042	0.028	0.035	0.037	0.037	0.035	0.038	0.031	0.033	0.025	0.024	0.004	0.003	0.006	0.006	0.007	0.013	0.010
6.0	-0.002	0.001	0.006	0.016	0.014	0.008	0.000	0.011	-0.006	-0.002	0.005	0.023	0.030	0.042	0.109	0.054	0.053	0.048	0.053	0.042	0.040	0.033	0.032	0.030	0.028	0.019	0.015	0.014	0.012	0.010	0.022	0.019
7.0	-0.007	0.010	-0.003	0.020	0.006	-0.007	0.000	0.000	-0.006	-0.013	0.001	0.020	0.019	0.028	0.054	0.098	0.061	0.046	0.034	0.030	0.040	0.046	0.041	0.038	0.035	0.026	0.016	0.018	0.016	0.008	0.013	0.006
8.0	-0.010	0.004	-0.002	0.011	0.005	-0.010	0.000	0.005	-0.001	-0.005	-0.005	0.014	0.026	0.035	0.053	0.061	0.104	0.061	0.046	0.043	0.050	0.053	0.051	0.051	0.050	0.037	0.035	0.031	0.029	0.021	0.025	0.017
9.0	-0.001	0.003	-0.004	0.009	0.005	-0.004	0.000	0.002	-0.010	-0.003	-0.006	0.017	0.024	0.037	0.048	0.046	0.061	0.099	0.063	0.058	0.063	0.060	0.048	0.054	0.057	0.047	0.046	0.040	0.044	0.041	0.049	0.035
10.0	0.002	-0.001	-0.002	0.000	-0.006	-0.011	-0.014	-0.014	-0.029	-0.026	-0.015	0.012	0.032	0.037	0.053	0.034	0.046	0.063	0.103	0.070	0.072	0.067	0.058	0.057	0.057	0.043	0.039	0.038	0.044	0.045	0.049	0.050
11.0	-0.002	-0.002	-0.004	-0.002	-0.010	-0.019	-0.015	-0.022	-0.027	-0.021	-0.019	0.010	0.031	0.035	0.042	0.030	0.043	0.058	0.070	0.103	0.089	0.079	0.071	0.065	0.064	0.052	0.052	0.041	0.055	0.057	0.065	0.058
12.0	-0.003	0.003	-0.004	0.003	0.000	-0.019	-0.014	-0.026	-0.033	-0.031	-0.022	0.016	0.032	0.038	0.040	0.040	0.050	0.063	0.072	0.089	0.126	0.100	0.086	0.084	0.078	0.058	0.061	0.048	0.061	0.059	0.064	0.057
13.0	-0.003	0.005	-0.004	0.008	-0.001	-0.013	-0.013	-0.016	-0.027	-0.020	-0.016	0.016	0.031	0.031	0.033	0.046	0.053	0.060	0.067	0.079	0.100	0.119	0.089	0.087	0.074	0.059	0.055	0.044	0.057	0.054	0.059	0.048
14.0	-0.012	0.005	-0.005	0.008	0.006	-0.010	-0.012	-0.020	-0.020	-0.024	-0.017	0.017	0.031	0.033	0.032	0.041	0.051	0.048	0.058	0.071	0.086	0.089	0.115	0.092	0.084	0.060	0.058	0.054	0.058	0.054	0.059	0.050
15.0	-0.014	0.002	-0.008	0.002	0.005	-0.009	-0.016	-0.018	-0.025	-0.024	-0.023	0.008	0.014	0.025	0.030	0.038	0.051	0.054	0.057	0.065	0.084	0.087	0.092	0.111	0.093	0.072	0.068	0.060	0.066	0.065	0.064	0.055
16.0	-0.015	0.002	-0.007	0.001	0.003	-0.011	-0.013	-0.021	-0.022	-0.024	-0.017	0.009	0.021	0.024	0.028	0.035	0.050	0.057	0.057	0.064	0.078	0.074	0.084	0.093	0.107	0.074	0.069	0.063	0.069	0.068	0.071	0.063
17.0	-0.009	0.000	-0.015	-0.002	0.002	-0.011	-0.008	-0.007	-0.010	-0.005	-0.014	-0.006	0.007	0.004	0.019	0.026	0.037	0.047	0.043	0.052	0.058	0.059	0.060	0.072	0.074	0.091	0.077	0.072	0.078	0.073	0.073	0.066
18.0	-0.011	-0.005	-0.024	-0.010	-0.002	-0.018	-0.007	-0.010	-0.013	-0.002	-0.017	0.002	0.017	0.003	0.015	0.016	0.035	0.046	0.039	0.052	0.061	0.055	0.058	0.068	0.069	0.077	0.096	0.072	0.081	0.079	0.075	0.066
19.0	-0.010	-0.002	-0.020	-0.008	-0.004	-0.015	-0.003	-0.010	-0.009	-0.005	-0.012	0.003	0.022	0.006	0.014	0.018	0.031	0.040	0.038	0.041	0.048	0.044	0.054	0.060	0.063	0.072	0.072	0.082	0.075	0.077	0.071	0.065
20.0	-0.006	0.001	-0.013	0.002	0.002	-0.012	-0.003	-0.014	-0.018	-0.007	-0.024	-0.001	0.020	0.006	0.012	0.016	0.029	0.044	0.044	0.055	0.061	0.057	0.058	0.066	0.069	0.078	0.081	0.075	0.097	0.088	0.084	0.073
21.0	-0.008	-0.004	-0.013	-0.006	-0.002	-0.012	-0.005	-0.012	-0.018	-0.007	-0.017	0.004	0.024	0.007	0.010	0.008	0.021	0.041	0.045	0.057	0.059	0.054	0.054	0.065	0.068	0.073	0.079	0.077	0.088	0.107	0.091	0.080
22.0	-0.006	-0.001	-0.010	0.001	0.003	-0.013	-0.007	-0.015	-0.015	-0.010	-0.022	0.006	0.018	0.013	0.022	0.013	0.025	0.049	0.049	0.065	0.064	0.059	0.059	0.064	0.071	0.073	0.075	0.071	0.084	0.091	0.105	0.083
23.0	-0.006	-0.004	-0.010	-0.007	0.000	-0.016	-0.011	-0.019	-0.024	-0.025	-0.016	0.003	0.023	0.010	0.019	0.006	0.017	0.035	0.050	0.058	0.057	0.048	0.050	0.055	0.063	0.066	0.066	0.065	0.073	0.080	0.083	0.093

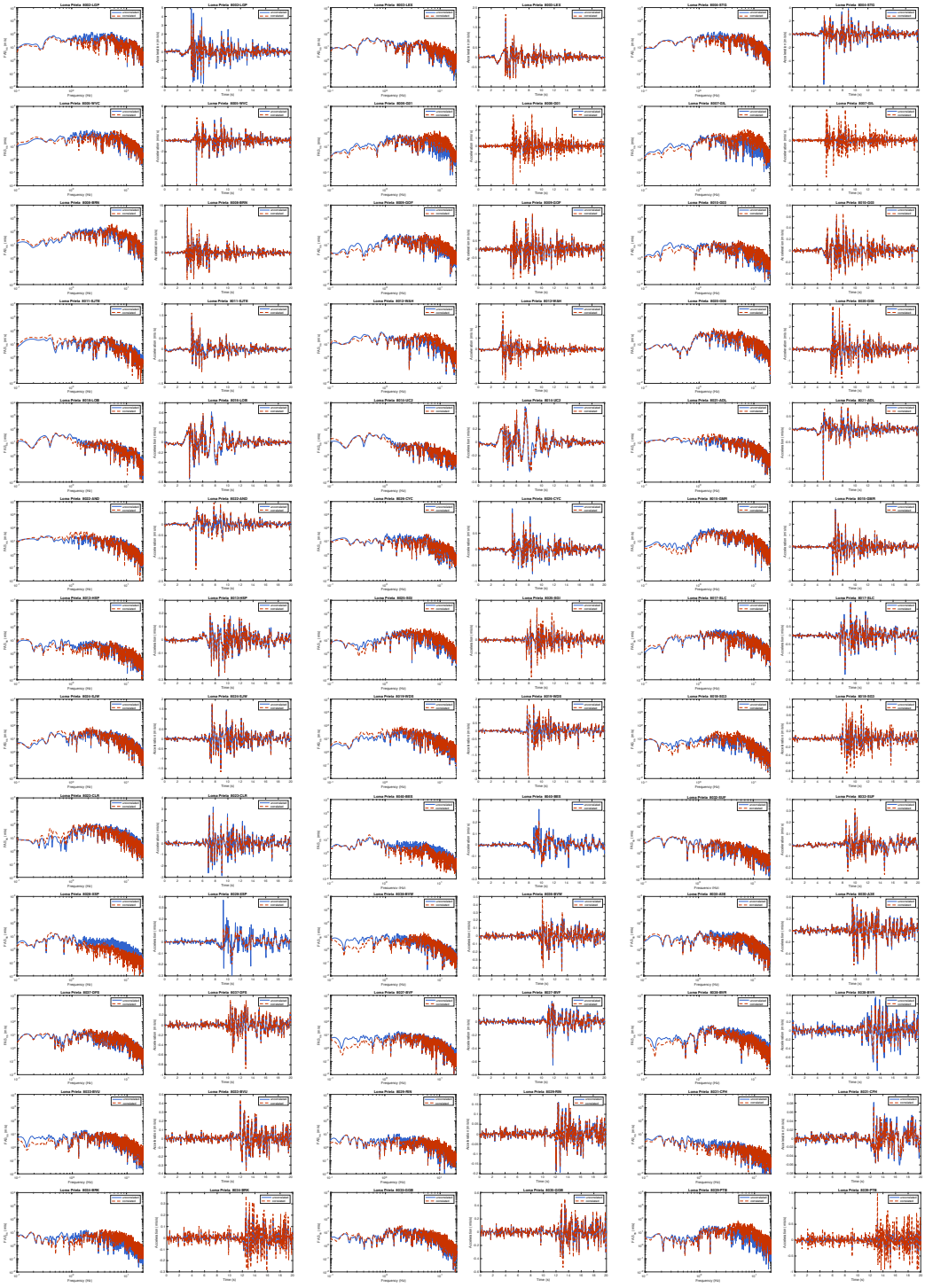

Figure S5.1: Examples of the north-south component of FAS (left) and acceleration time histories (right) for one simulation at 39 stations of the 40 considered stations for the Loma Prieta earthquake after (red dashed line) and before (blue solid line) applying our method to implement the proposed spatial correlation model (the plot for the remaining station is in Figure 5.8).

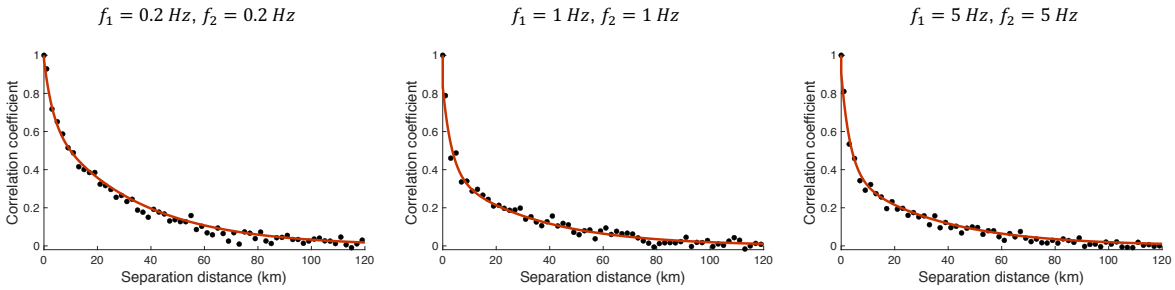

Figure S5.2: Spatial correlation coefficients of epsilon for EAS at the reference frequency pair $f_1 = f_2 = 0.2$ Hz (left), $f_1 = f_2 = 1$ Hz (middle) and $f_1 = f_2 = 5$ Hz (right) from the proposed model (red lines) and the SDSU SCEC BBP Module after applying our method with 50 source realizations (dots) for the 1992 M7.2 Landers earthquake.

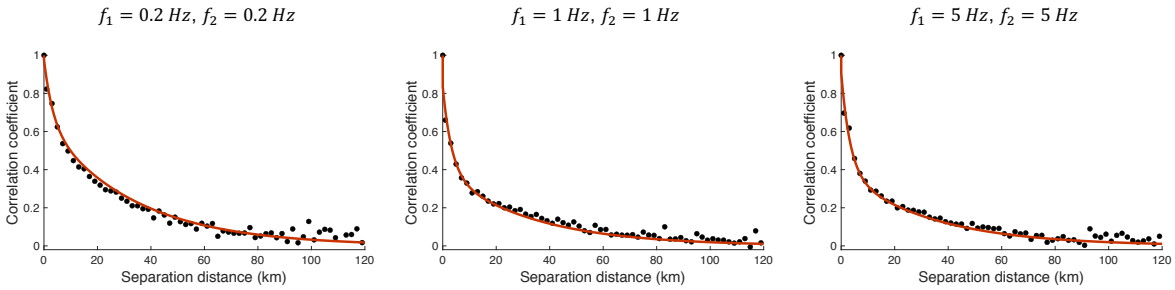

Figure S5.3: Same as Figure S5.2, but for the 1994 M6.7 Northridge earthquake.

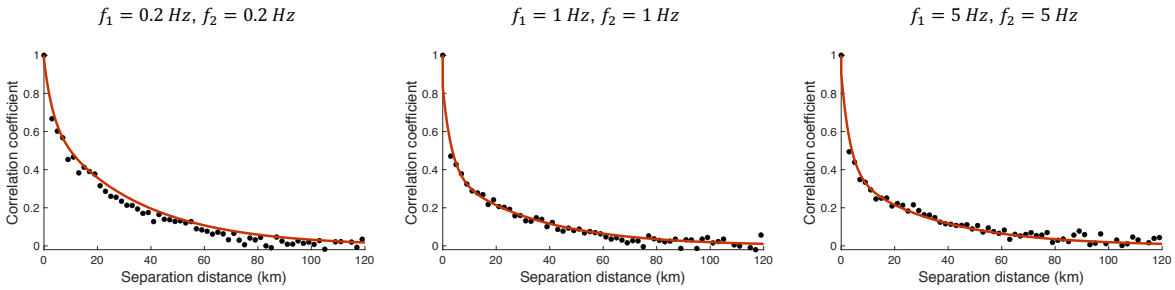

Figure S5.4: Same as Figure S5.2, but for the 1986 M6.1 North Palm Springs earthquake.

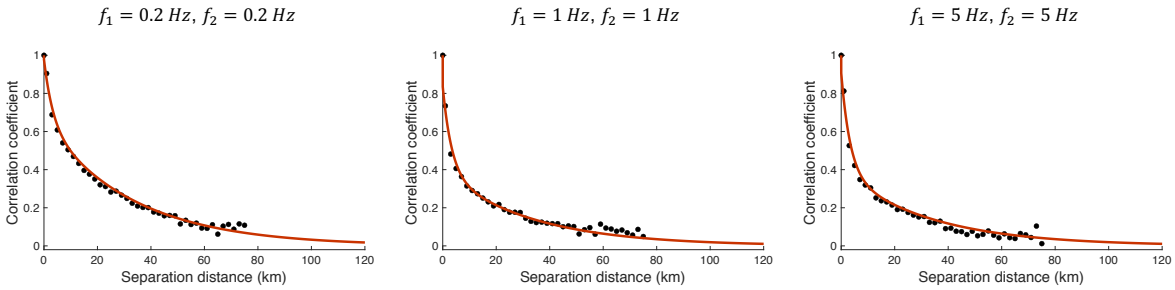

Figure S5.5: Same as Figure S5.2, but for the 1987 M5.9 Whittier-Narrows earthquake.

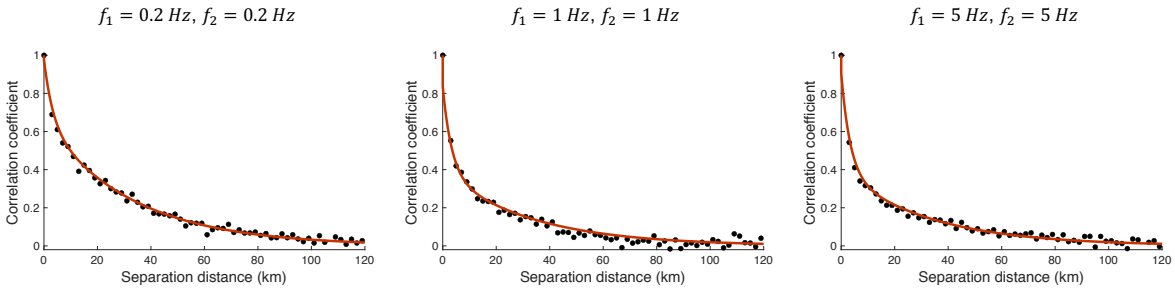

Figure S5.6: Same as Figure S5.2, but for the 2008 M5.4 Chino Hills earthquake.

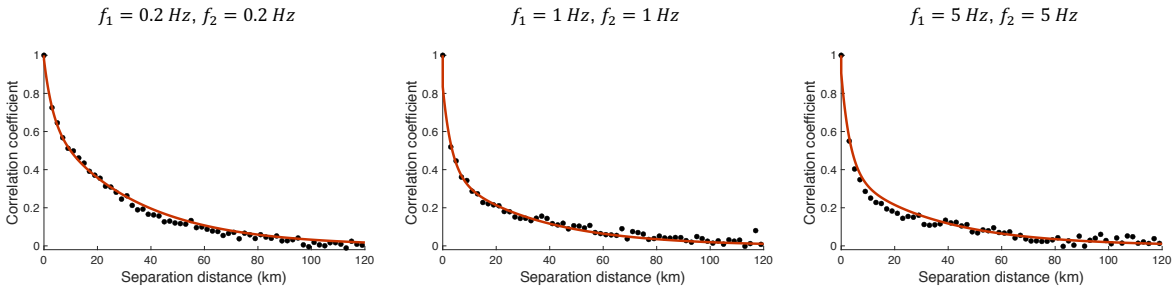

Figure S5.7: Same as Figure S5.2, but for the 2007 M5.5 Alum Rock earthquake.

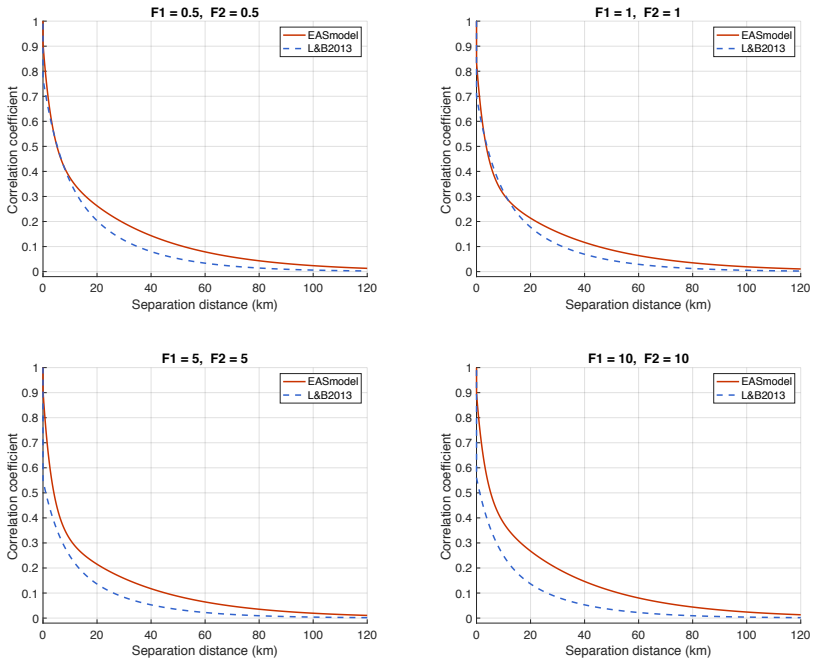

Figure S5.8: Comparison between our EAS within-event spatial correlation model (solid lines) and the PSA within-event spatial correlation model by Loth and Baker (2013) (dashed lines) at frequency pairs $f_1 = f_2 = 0.5$ Hz, 1 Hz , 5 Hz and 10 Hz.

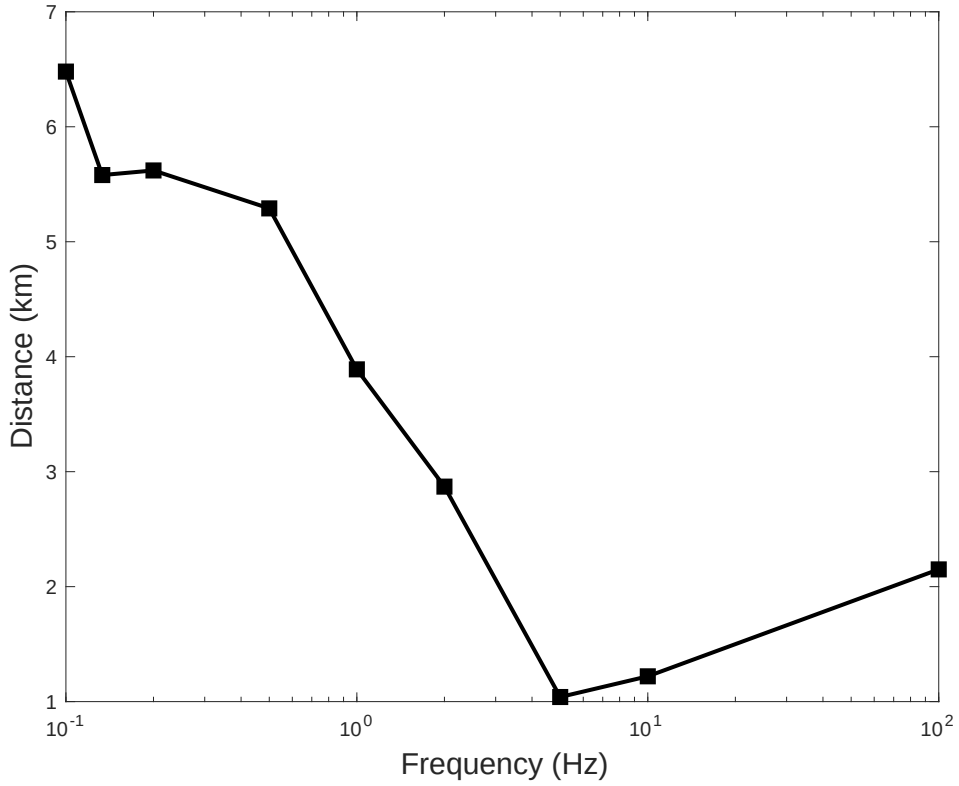

Figure S5.9: Separation distances where the correlation coefficient drops to 0.5 in the Loth and Baker (2013) model for spectral accelerations, using pairs of two identical frequencies.

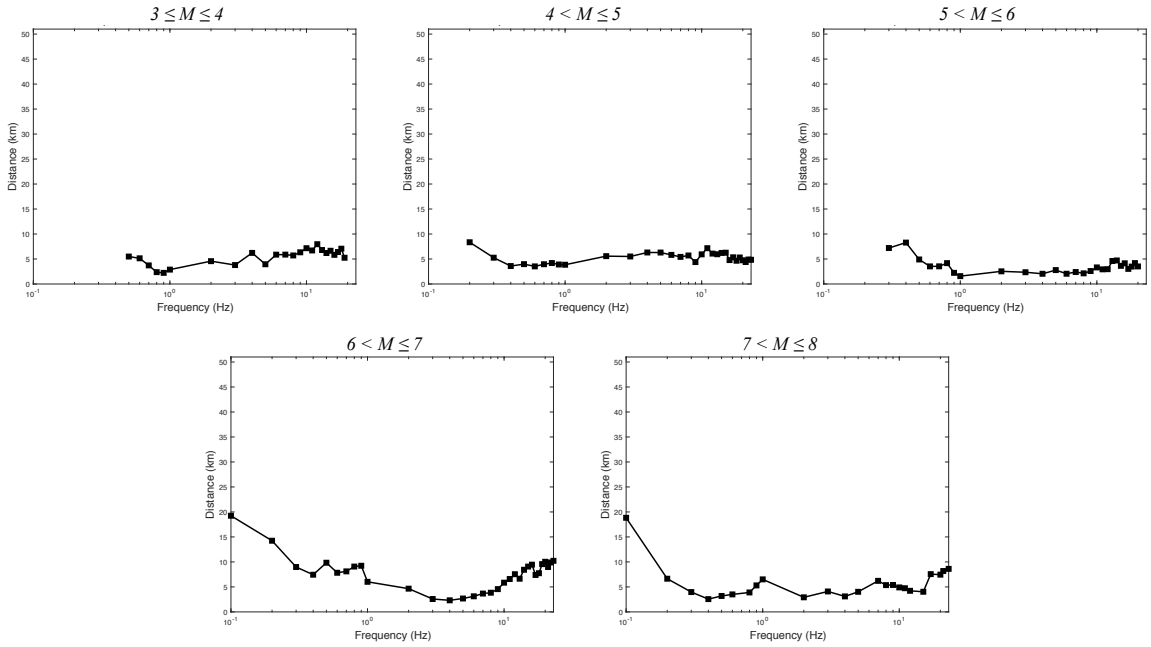

Figure S5.10: Separation distances where the empirical EAS correlation coefficient drops to 0.5, using pairs of two identical frequencies for different magnitude ranges. Note, that correlation coefficients are missing for frequencies with insufficient amounts of data available to regress a stable value.

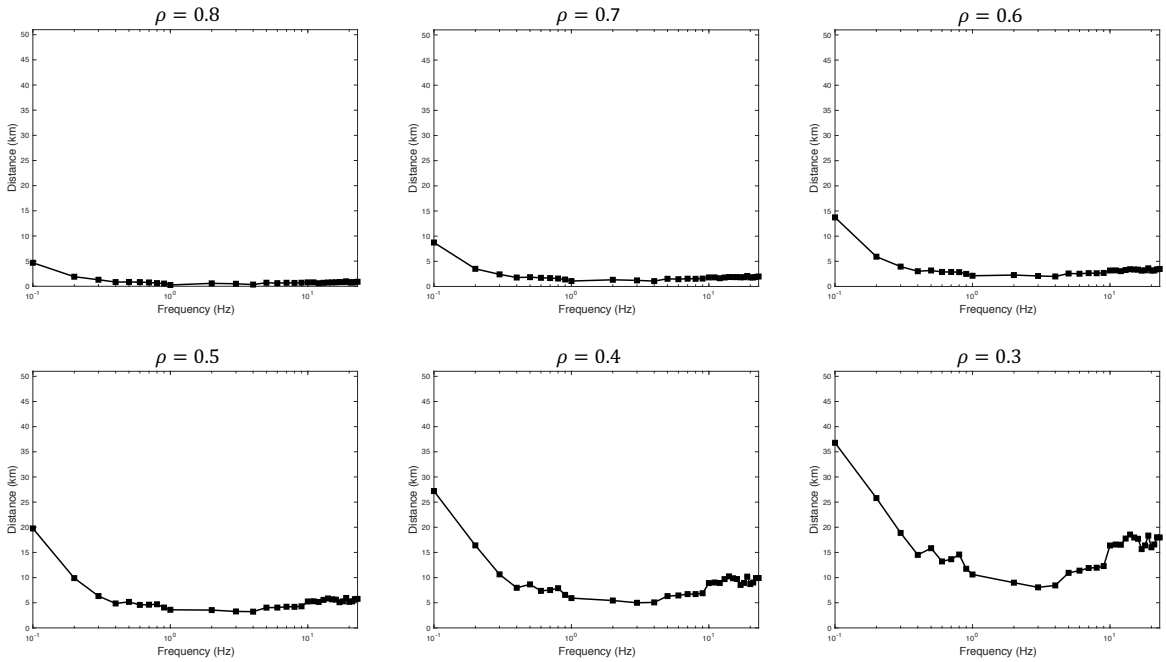

Figure S5.11: Separation distances where the empirical EAS correlation coefficient drops to 0.8, 0.7, 0.6, 0.5, 0.4 and 0.3, using pairs of two identical frequencies.